technische universität
dortmund

Biophysical Insights into the High Pressure Sensitivity of Biomolecules

Dissertation

For the achievement of the academic degree of the

Doctor rerum naturalium

(Dr. rer. nat.)

submitted to

Technical University Dortmund

Faculty of Chemistry and Chemical Biology

by

Mimi Gao

born in Tianjin, China

Dortmund 2017

technische universität
dortmund

Biophysikalische Einblicke in die Hochdruck-Sensitivität ausgewählter Biomoleküle

Dissertation

zur Erlangung des akademischen Grades

Doctor rerum naturalium

(Dr. rer. nat.)

eingereicht bei der

Technischen Universität Dortmund

Fakultät für Chemie und Chemische Biologie

vorgelegt von

Mimi Gao

geboren in Tianjin, China

Dortmund 2017

Die vorliegende Arbeit wurde im Zeitraum von Oktober 2014 bis Oktober 2017 am Lehrstuhl für Physikalische Chemie I (Biophysikalische Chemie) der Technischen Universität Dortmund unter Betreuung von Herrn Prof. Dr. Roland Winter angefertigt.

Dissertation eingereicht am:	23.10.2017
Tag der Disputation:	11.12.2017

Amtierender Dekan	Prof. Dr. Roland Winter

Prüfungskommission

Vorsitzender:	Prof. Dr. Carsten Strohmann
	Anorganische Chemie, CCB, TU Dortmund
Erster Gutachter:	Prof. Dr. Roland Winter
	Physikalische Chemie, CCB, TU Dortmund
Zweiter Gutachter:	Prof. Dr. Heinz Rehage
	Physikalische Chemie, CCB, TU Dortmund

Dedicated to my lovely parents.

A scientist in his laboratory is not a mere technician: he is also a child confronting natural phenomena that impress him as though they were fairy tales

---

(Marie Sklodowska Curie)

ACKNOWLEDGEMENT

Firstly, I would like to express my deepest gratitude to my supervisor **Prof. Dr. Roland Winter** for the continuous support of my doctorate and related research, for his patience, motivation, trust as well as the numerous and fruitful discussions. I thank you for giving me freedom in my research, demanding a high quality of work, and encouraging my attendance at various conferences. I gained a lot from your vast knowledge and scientific curiosity.

Besides my advisor, I would like to thank **Prof. Dr. Heinz Rehage** for his work as the second examiner of this thesis.

I sincerely acknowledge **Andrea Jeworrek** for the constant friendly support and help with all the administration problems during the three years, but also for the always quick orders of my chemicals. I am very grateful to **Simone Möbitz** for keeping our work in the lab running smoothly as well as for the countless funny moments in the office and lab.

I am also very grateful to **Dr. Janine Nicolai** and **Dr. Katrin Weise**, who are a tremendous source of support and encouragement throughout the three years. A special thank goes to my officemate **Nelli Erwin** for beeing an extraordinary source of advice and practical scientific knowledge. I admire her extremely relentless work ethic. I wish to thank **Loana Arns** and **Dr. Melanie Berghaus** for the many enjoyable and fruitful collaborations. I appreciate Loana for her constant willingness to help and the way how she always cheered me whenever I had a bad day in the lab. Further, I thank Melanie for introducing me into Synchrotron SAXS and being a good companion during the night shifts at DELTA. I appreciate **Dr. Irena Kiesel** for her knowledge of scattering and MATLAB, but much more for her social commitment in our group. I am also grateful to **Dr. Vitor Schuabb** and **Süleyman Cinar** for their help with the high pressure equipments and the FTIR instruments. Further, I thank **Prof. Dr. Claus Czeslik** for keeping his office door open and being available always when we need scientific and practical advice. I would also like to thank all other former and current members of our **PC I group** for a good and constructive working atmosphere.

All members of the mechanical and electronic workshop led by **Holger Konopka** and **Ralf**

Maserski are acknowledged for their many helps.

In addition, I have been very privileged to get to know and to collaborate with many other great people over the last three years.
First, I deeply acknowledge **David Gnutt** and **Prof. Dr. Simon Ebbinghaus** from the Ruhr University Bochum for working together on the RNA project. David, thank you for the many stimulating and fruitful discussions. I am also grateful to Simon for allowing me to finish my master project. I have greatly enjoyed the opportunity to work with **Dr. Julian von der Ecken** and **Prof. Dr. Stefan Raunser** from the Max Planck Institute in Dortmund on the actin bundle project. I also thank them for providing access to the ultracentrifuge. I thank **Dr. Balasubramanian Harish** and **Prof. Dr. Catherine A. Royer** from the Rensselaer Polytechnic Institute in Troy (USA) for the fruitful collaboration on the GMP project. Thanks go to **Karin Julius** for sharing her beam time at DLS. Also, I want to thank **Dr. Christian Sternemann** and **Dr. Michael Paulus** for their support at the DELTA in Dortmund. Many thanks to **Dr. José Fernando Díaz Pereira** from the Centro de Investigaciones Biologicas (CSIC) in Madrid (Spain) and **PD Dr. Leif Dehmelt** from the Max Planck Institute in Dortmund for introducing me to the tubulin world and teaching me how to work with this tricky protein. **Dr. Ulrike Hinssen** from Hypermol in Bielefeld is kindly acknowledged for sharing practical advice and knowledge of working with actin.

I thank **Loana Arns**, **Dr. Irena Kiesel** and **Juliana Rey** for proofreading this thesis.

I acknowledge the **Stiftung Stipendien-Fonds des Verbandes der Chemischen Industrie e.V.** for giving me with the *Chemiefonds-Stipendium für Doktoranden*, but also for the financial support for attending the 67th Lindau Nobel Laureate Meeting.

Last but not the least, I would like to thank my **family and friends** for supporting me spiritually throughout my studies, doctorate and my life in general.

PUBLICATIONS

Part of the work presented in this thesis is based on the following publications:

- M. Gao*, M. Berghaus,* J. von der Ecken, S. Raunser, and R. Winter. Condensation Agents Determine the Temperature-Pressure Stability of F-actin Bundles. *Angew. Chem. Int. Ed.* **54** (2015) 11088 -11092.

- M. Gao, and R. Winter. Kinetic Insights into the Elongation Reaction of Actin Filaments as a Function of Temperature, Pressure, and Macromolecular Crowding. *ChemPhysChem* **16** (2015) 3681-3686.

- M. Gao*, D. Gnutt*, A. Orban, B. Appel, F. Righetti, R. Winter, F. Narberhaus, S. Müller, and S. Ebbinghaus. RNA Hairpin Folding in the Crowded Cell. *Angew. Chem. Int. Ed.* **55** (2016) 3224-3228.

- M. Gao, L. Arns, and R. Winter. Modulation of the Thermodynamic Signatures of an RNA Thermometer by Osmolytes and Salts. *Angew. Chem. Int. Ed.* **56** (2017) 2302-2306.

- M. Gao, B. Harish, M. Berghaus, R. Seymen, L. Arns, S. A. McCallum, C. A. Royer, and R. Winter. Temperature and Pressure Limits of Guanosine Monophosphate Self-Assemblies. *Sci. Rep.* **7** (2017) 9864.

- M. Gao, C. Held, S. Patra, L. Arns, G. Sadowski, R. Winter. Crowders and Cosolvents - Major Contributors to the Cellular Milieu and Efficient Means to Counteract Environmental Stresses. *ChemPhysChem* (2017), DOI:10.1002/cphc.201700762.

- M. Gao, M. Berghaus, S. Möbitz, V. Schuabb, N. Erwin, M. Herzog, K. Julius, C. Sternemann, and R. Winter. On the Origin of Microtubules' High Pressure Sensitivity, *submitted*.

*As co-first authors

Furthermore, the author contributed to the following publications:

- P. H. Schummel, M. Gao, R. Winter. Modulation of the Polymerization Kinetics of α/β-Tubulin by Osmolytes and Macromolecular Crowding. *ChemPhysChem* **18** (2017) 189-197.

- M. Gao, and R. Winter. The Effects of Lipid Membranes, Crowding and Osmolytes on the Aggregation and Fibrillation Propensity of Human IAPP. *J. Diabetes Res.* (2015) Article ID 849017, 21 pages.

ABSTRACT

Accurate folding and dynamics of biomolecules are substantially important for the functionality of living systems. As life can also be found in the realm of environmental extremes, biomolecules as well as their homo- and heterotypic interactions must withstand different environmental stresses including a wide range of temperature, pressure and salinity. For example, extreme conditions including high temperature, high hydrostatic pressure (up to 100 MPa) and high salinity (up to 600 mM) can be found close to marine hydrothermal vents. Hence, adaptation strategies must exist to ensure life of extremophiles. Notably, globular proteins and double-stranded nucleic acids have been reported to be very pressure stable, whereas initial studies have shown that quaternary interactions of proteins and non-canonical structures of nucleic acids, being essential components of cellular entities, are rather pressure-sensitive. In particular, filamentous and biopolymeric components of the cytoskeleton, responsible for mechanical integrity and functional architecture of the cell, have been demonstrated to be one of the most pressure-sensitive structures. However, those early and initial studies do not provide any insight into the origin of the high pressure sensitivity.
The present work shed light on the origin of the pressure sensitivity of the eukaryotic cytoskeleton by focusing on the components actin filaments and microtubules. More importantly, it addressed the issue of molecular strategies for pressure resistance. In particular, it focused on the role of accessory proteins of the cytoskeleton as well as the effects of macromolecular crowding and osmolytes, phenomena easily encountered inside cells. Further, the latter aspect was also investigated for a functional and temperature-sensitive ribonucleic acid hairpin known to regulate the gene expression in bacteria. To fundamentally understand the pressure effect on nucleic acids, the self-assembly reaction of guanosine-monophosphate as a single nucleotide was focus of the present work as well.
Using a high hydrostatic pressure measuring platform based on spectroscopic, scattering and microscopic techniques, the following observations and conclusions have been drawn for the high pressure behavior of the eukaryotic cytoskeleton. First, it was found that microtubules at every structural level are less pressure stabile compared to actin filaments. Microtubules and their bundles are completely disintegrated at 150 MPa, whereas dissociation of actin filaments is completed beyond 400 MPa. Thereby, their pressure-induced disorganization exhibited distinct molecular mechanisms. Lateral and longitudinal contacts of microtubules were found to feature different pressure stabilities, which arise mainly from internal voids and packing defects at the interfaces of the self-assemblies. Conversely, the morphology and

stability of actin filaments are determined by the pressure stability limit of their monomeric building blocks shown by previous work. Further, binding partners of microtubules were found to decrease the pressure stability of longitudinal contacts of microtubules, most likely caused by forming additional packing defects in the proteins and at the longitudinal interfaces. In contrast, a protein crosslinker of actin filaments was revealed to enable the formation of pressure-resistant actin filament bundles, whereby their packing geometry and tightness are not affected by pressure values up to 100 MPa, which cover the physiologically relevant range encountered in the deep sea. A comparison to purely electrostatically induced actin bundles suggests that a chemically heterogeneous contact interface between actin and the crosslinker is the reason for the improved pressure resistance. Next, the effect of macromolecular crowding, a typical generic phenomenon of the cellular environment, could be shown to increase the pressure stability of both cytoskeletal components. Finally, distinct steps during the formation of both biopolymers appeared to be differently modulated by high hydrostatic pressure. While the initial nucleation step is very pressure-sensitive and largely retarded under high pressure conditions, the elongation kinetics is hardly affected by pressure. This highlights the importance and need of protein nucleators to bypass the otherwise highly pressure-sensitive *de novo* formation of actin filaments and microtubules.

Using the example of a functional and temperature-sensitive RNA hairpin, the present work revealed that studying biomolecules in isolation and dilute solution may not unveil the *in vivo* scenario because background molecules inside cells can actively modulate their dynamics and folding landscapes. Considering the effects of macromolecular crowding and osmolytes showed that (1) (de)stabilizing contributions from volume exclusion, nonspecific interactions and water activity change may modulate the folding stability of the RNA hairpin spatially and temporally even causing folding heterogeneities inside cells, and (2) a strong interplay between water, salt, and osmolyte drives the thermodynamics and defines the temperature and pressure stability limit of the RNA hairpin.

Finally, studying the self-assembly reaction of guanosine-monophosphate as a single nucleotide could shed light on the origin of the high pressure sensitivity of non-canonical nucleic acid structures such as G-quadruplexes. Hydration, stacking interactions and packing defects were revealed to play an important role in determining the pressure stability nucleotide of self-assemblies.

ZUSAMMENFASSUNG

Die Funktionalität von lebenden Systemen ist durch eine korrekte Faltung von Biomolekülen und deren Dynamiken gegeben. Weil Leben sich im Verlauf der Evolution erfolgreich an alle erdenklichen Habitate auf der Erde angepasst hat, müssen solche Biomoleküle sowie ihre homo- und heterotypischen Interaktionen unterschiedlichsten Umweltstressoren standhalten. Dazu gehören Faktoren wie Temperatur, hydrostatischer Druck und Salzkonzentration. Ein extremes Habitat bilden z.B. Hydrothermalquellen in der Tiefsee, deren Wasser eine Temperatur bis zu 400 °C, einen hydrostatischen Druck von 100 MPa und einen Salzgehalt von 600 mM aufweisen kann. Um Leben unter solchen Bedingungen zu ermöglichen, müssen sich Anpassungstrategien entwickelt haben. Es ist bekannt, dass globuläre Proteine und doppelsträngige Nukleinsäuren sehr druckstabil sind, während hingegen erste Studien zeigen, dass Quartärstrukturen von Proteinen und nicht-kanonische Strukturen von Nukleinsäuren, die wichtige Funktionen in zellulären Systemen einnehmen, vergleichsweise drucksensitiv sind. Es konnte beispielweise gezeigt werden, dass insbesondere filamentöse Komponenten des Zytoskelettes als nicht-kovalente Biopolymere eine der drucksensitivsten Strukturen darstellen. Diese frühen und anfänglichen Studien sind allerdings nicht hinreichend um den Ursprung der beobachteten Hochdruck-Sensitivität zu erklären.
Vor diesem Hintergrund befasst sich die vorliegende Arbeit mit der Ursache der Hochdruck-Sensitivität des eukaryotischen Zytoskelettes mit besonderem Fokus auf die Aktinfilamente und die Mikrotubuli als zentrale Elemente. Von besonderem Interesse ist ebenfalls das Aufzeigen von molekularen Strategien, die die Hochdruckresistenz von Biomolekülen gewährleisten. Dabei werden akzessorische Proteine des Zytoskelettes sowie zelluläre Phänomene wie das makromolekulare Crowding und die Anwesenheit von Osmolyten hinsichtlich ihrer Rolle als Regulator der Hochdruckresistenz untersucht. Des Weiteren wird der letztere Aspekt auch am Beispiel einer funktionellen und temperatursensitiven RNA-Haarnadel, die als Steuerelement für die Genexpression in Bakterien fungiert, untersucht. Um den Einfluss von Hochdruck auf Nukleinsäuren fundamental zu verstehen, ist die Selbstassemblierung eines Einzelnukleotides am Beispiel von Guanosinmonosphoshat ebenfalls Forschungsgegenstand der vorliegenden Arbeit.
Mit Hilfe spektroskopischer und mikroskopischer Techniken sowie der Röntgenstreuung in Kombination mit Hochdruck-Applikation wurde zunächst das Hochdruck-Verhalten des eukaryotischen Zytoskelettes untersucht. Die Ergebnisse dieser Studien haben u.a. gezeigt, dass Mikrotubuli auf jeder Strukturebene eine wesentliche geringere Stabilität als Aktinfilamente hinsichtlich des Hochdrucks aufweisen. Mikrotubuli und ihre Bündelstrukturen liegen bei 150 MPa vollständig dissoziiert vor, während ein vollständiger Zerfall der Aktinfilamente in ihre Monomere erst bei 400 MPa erreicht ist. Die druckinduzierten Dissoziationen der beiden Spezies verlaufen dabei nach unterschiedlichen molekularen Mechanismen. Laterale und longitudinale Kontakte der Mikrotubuli weisen u.a. unterschiedliche Hochdruck-

stabilitäten auf, die hauptsächlich durch intramokulare Hohlräume und Packungsdefekte an Kontaktstellen der Mikrotubuli verursacht werden. Dagegen hat eine frühere Untersuchung gezeigt, dass die Morphologie und die Stabilität der Aktinfilamente maßgeblich durch die Hochdruckstabilität der monomeren Bausteine bestimmt werden. Desweiteren konnte in der vorliegenden Arbeit gezeigt werden, dass bekannte Bindungspartner von Mikrotubuli die Hochdruckstabilität der longitudinalen Kontakte absenken, vorwiegend verursacht durch die Bildung von zusätzlichen Packungsdefekten in den Proteinen und an den longitudinalen Kontaktflächen. Im Gegensatz dazu konnte gezeigt werden, dass eine Quervernetzung von Aktinfilamenten durch ein Querverbindungsprotein die Bildung von hochdruckresistenten Aktinbündeln bewirkt, wobei die Packungsgeometrie und -dichte der Bündel bis zu einem Druckwert von 100 MPa, der im Bereich des hydrostatischen Drucks der Tiefsee liegt, nicht verändert wird. Ein Vergleich mit Aktinbündeln, die ausschließlich durch elektrostatische Kondensation gebildet werden, zeigt, dass eine chemisch heterogene Kontaktfläche zwischen Aktin und dem Querverbindungsprotein entscheidend zu der beobachteten Hochdruckresistenz beiträgt. Weiterhin konnte der Effekt des makromolekularen Crowding für beide Biopolymere des Zytoskelettes als eine weitere Anpassungsstrategie an hydrostatische Drücke identifiziert werden. Ebenfalls wurde für beide Biopolymere herausgefunden, dass verschiedene Schritte der Selbstassemblierungsreaktion durch hydrostatische Drücke kinetisch unterschiedlich moduliert werden. Während die anfängliche Keimbildung (Nukleation) einen sehr drucksensitiven Schritt darstellt und bei hohen Drücken retardiert wird, wird die Kinetik des Elongationsschrittes kaum durch Druck beeinflusst. Dies betont die Wichtigkeit und Notwendigkeit von Nukleationsfaktoren, die die andernfalls sehr drucksensitive De-novo-Bildung der Aktinfilamente und Mikrotubuli bei hohen Drücken gewährleisten.

Am Beispiel einer funktionellen und temperatursensitiven RNA-Haarnadel konnte die vorliegene Arbeit zeigen, dass eine isolierte Betrachtung und Untersuchungen von Biomolekülen in verdünnten Lösungen nicht die In-vivo-Situation widerspiegeln. Dies wird durch die Anwesenheit von Hintergrundmolekülen in Zellen, die die Dynamiken und Faltungslandschaften von Biomolekülen aktiv beeinflussen können, verursacht. Die Untersuchung der Effekte des makromolekularen Crowding und der Osmolyte hat ergeben, dass (1) (de)stabilisierende Beiträge resultierend aus Volumenauschlusseffekten, nichtspezifischen Wechselwirkungen sowie Veränderungen der Wasseraktivität die Faltungsstabilität der RNA-Haarnadel sowohl zeitlich als auch räumlich modulieren können, und sogar zu einer subzellulären Faltungsheterogenität führen und dass (2) Wasser, Salz und Osmolyte in einem engen Zusammenspiel die Thermodynamik und somit die Temperatur- und Hochdruckstabilitätsgrenzen der RNA-Haarnadel definieren.

Schließlich konnte die Untersuchung der Selbstassemblierung eines Einzelnukleotides am Beispiel von Guanosinmonosphoshat Licht auf die Ursache der Hochdruck-Sensitivität der nicht-kanonischen Strukturen von Nukleinsäuren, wie z.B. in G-Quadruplexen, werfen. Es konnte u.a. gezeigt werden, dass Hydratation, Basenstapelkräfte und Packungsdefekte die Hochdruckstabilität der selbstassemblierten Spezies maßgeblich bestimmen.

CONTENTS

LIST OF FIGURES

LIST OF TABLES

ABBREVIATIONS

(v/v)	(volume/volume)
(w/v)	(weight/volume)
ABP	Actin-binding protein
AFM	Atomic force microscopy
ADP	Adenosine diphosphate
ATP	Adenosine triphosphate
a.u.	Arbitrary units
BME	2-Mercaptoethanol
bp	Base pair
BSA	Bovine serum albumin
CASTp	Computed atlas of surface topography of proteins
CCD	Charge-coupled device
Da	Dalton
DLS	Dynamic light scattering
DMEM	Dulbecco's Modified Eagle's Medium
DMSO	Dimethyl sulfoxide
DNA	Deoxyribonucleic acid
DPBS	Dulbecco's phosphate buffered saline
DSC	Differential scanning calorimetry
DTT	Dithiothreitol
e.g.	Exempli gratia
EGTA	Ethylene glycol-bis(β-aminoethyl ether)-*N,N,N',N'*-tetraacetic acid
F-actin	Actin filament
FBS	Fetal bovine serum
FReI	Fast relaxation imaging
FRET	FÖRSTER resonance energy transfer

FSD	FOURIER self-deconvolution
FTIR	FOURIER-transform infrared spectroscopy
FWHM	Full-width half-maximum
G-actin	Globular actin
GDP	Guanosine diphosphate
GMP	Guanosine monophosphate
GMPCPP	Guanosine-5'-[(α,β)-methyleno]triphosphate
GTP	Guanosine triphosphate
h	hour
HeLa	Henrietta Lacks
HHP	High hydrostatic pressure
i.e.	Id est
EG	Ethylene glycol
MAP	Microtubule-associated protein
min	Minute
MT	Microtubule
NMR	Nuclear magnetic resonance
PDB	Protein data bank
PEG	Polyethylene glycol
PF	Protofilament
pH	pondus Hydrogenii
pI	Isoelectric point
PMT	Photomultiplier tube
PMSF	Phenylmethylsulfonyl fluoride
PPC	Pressure perturbation calorimetry
P/S	Penicillin/streptomycin
RBS	Ribosome-binding site
RNA	Ribonucleic acid
rpm	Revolutions per minute
RPMI	Roswell Park Memorial Institute
RT	Room temperature
s	Second

SASA	Solvent accessible surface area
SAXS	Small-angle X-ray scattering
SDS-PAGE	Sodium dodecyl sulfate polyacrylamide gel electrophoresis
S/N	Signal-to-noise ratio
SPT	Scaled-particle theory
TEM	Transmission electron microscopy
TMAO	Trimethylamine-*N*-oxide
Tris	Tris(hydroxymethyl)aminomethane
U	Unit

CHAPTER 1

MOTIVATION

The evolution of life has begun about four billion years ago when the building blocks of nucleic acids and proteins might possibly be formed under extreme conditions according to the primordial soup theory. Despite the fact that the origin of life could have taken place under extreme conditions like in the depth of the proto-ocean of the Hadean Earth,[1] nowadays less life can be found in the realm of environmental extremes, which represent the greatest portion of our biosphere on Earth, however. Nevertheless, few microorganisms but also more complex living beings can still be found in regions with conditions of high pressure and high temperature (close to hydrothermal vents) or of high pressure and low temperature (at the ocean floor where pressures up to about 100 MPa are reached). Hence, the important questions arise how they have adapted to such environmental extremes and what their strategies for pressure resistance are, particularly in the light of *in vitro* high pressure studies on biomolecules showing that quaternary interactions of proteins, being essentially important for the cellular functionality, are highly pressure-sensitive. Interestingly, non-covalent self-assemblies of proteins such as filamentous components of the cytoskeleton have been reported to be one of the most pressure-sensitive assemblies.[2,3] However, those early studies do not provide any insight into the origin of the pressure sensitivity.

Hence, the aim of this work is to shed light on the origin of the pressure sensitivity of the eukaryotic cytoskeleton by focusing on the components actin filaments and microtubules. More importantly, it will also address the issue of molecular strategies for pressure resistance. In particular, it will answer (1) if and how accessory proteins of the cytoskeleton can assist to improve and guarantee the mechanical strength of the cell under high pressure conditions, (2) if the cellular effect of crowding is an active contributor to counteract the pressure sensitivity, and (3) if and how small organic cosolutes can act as piezolytes to improve the pressure resistance.

The later two aspects will also be investigated for a functional ribonucleic acid (RNA) molecule known to regulate the gene expression in bacteria. To fundamentally understand the pressure effect on nucleic acids, the self-assembly reaction of guanosine-monophosphate as a single nucleotide will also be focus of this work.
All in all, this work will yield new biophysical insights into the molecular origin of the pressure sensitivity of biomolecules and possible mechanistic strategies for the pressure resistance found in living beings thriving under extreme environmental conditions. Such findings may also be valuable for pressure applications in biotechnology and food industry.

Outline of this thesis

The thesis is organized as follows: First, the scientific background of the high hydrostatic pressure effect and the different concepts for explaining the crowding and osmolyte effects will be introduced. In the following chapter, the theoretical background of the experimental methods used will be explained. The results obtained will be presented in the subsequent chapters. Studies presented in Chapter 4 describe the pressure sensitivity of the cytoskeletal actin and how different cellular factors can improve the pressure resistance of this very important component inside the eukaryotic cell. Chapter 5 provides detailed insights into the origin of the microtubules' pressure sensitivity in different morphological and dynamic states. Chapter 6 shows how the folding stability of a functional RNA hairpin is modulated by hydration, osmolytes and crowding. Chapter 7 focuses on fundamentals of nucleotide self-association. Hence, the thermodynamic stability of guanosine 5'-monophosphate self-assemblies is studied over a wide temperature and pressure range. Finally, Chapter 8 will summarize the results and provide a general conclusion about the effect of hydrostatic pressure on different biomolecules.

CHAPTER 2

SCIENTIFIC BACKGROUND

2.1 The Cellular Solvent

Today's living systems, both prokaryotes and eukaryotes, are organized in highly dynamic and structured functional units providing a platform for life. Thereby, a dynamic and protein composed cytoskeleton together with a complex membrane system is required to establish compartmentation, cell shape, to provide mechanical strength as well as to realize biological movements. To understand the underlying molecular mechanisms of life, individual biomolecules are usually investigated in isolation and in standard test tubes. However, an important difference between the cytoplasm and the test tube as reaction vessels is the chemical and physical properties of the aqueous solution, where the biomolecule of interest is situated in. Unlike a homogeneous solution in the test tube, the interior of a cell is highly structured, compartmentalized on many length scales, and highly crowded. Up to 40% of the total cellular volume is physically occupied by macromolecules, especially proteins, nucleic acids, lipids and carbohydrates (up to 400 g L^{-1}).[4–6] This phenomenon is also referred to as macromolecular crowding. Next to it, high concentrations of cosolvents such as osmolytes and denaturants can also affect the water activity inside the cell and the chemical potential of different biomolecules.[7] Therefore, the question arises whether experiments in the test tube, having been the gold standard for a long time, really unveil the *in vivo* scenario. Numerous studies have shown that both, osmolytes and macromolecular crowding, are crucial components to understand the thermodynamics and kinetics of biological processes in living system.[6,8,9] Both effects have been shown to affect the unfolding free energy of

The content of this section is published in [M. Gao, C. Held, S. Patra, L. Arns, G. Sadowski, R. Winter. Crowders and Cosolvents - Major Contributors to the Cellular Milieu and Efficient Means to Counteract Environmental Stresses. *ChemPhysChem* (2017), DOI: 10.1002/cphc.201700762] and has been rephrased for this thesis.

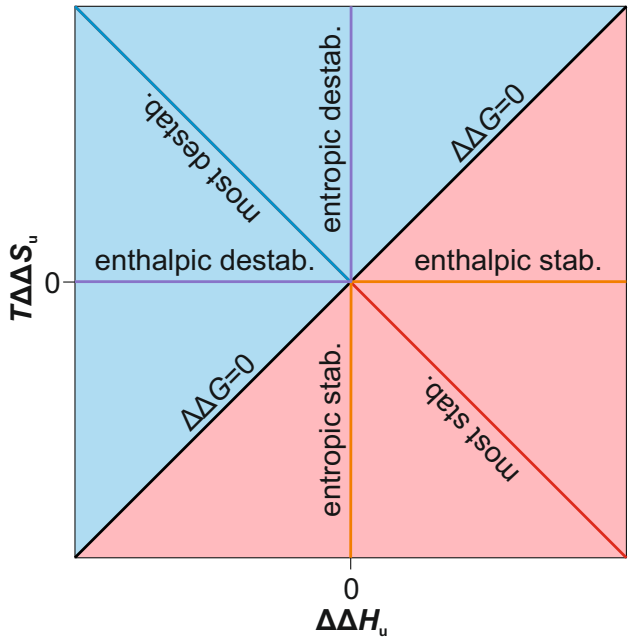

Figure 2.1 | Schematic plot for cosolvent-induced entropy and enthalpy contributions to the folding stability of biomolecules. The plot shows the different thermodynamic mechanisms for stabilization (red area) and destabilization (blue area) of biomolecules, with $\Delta\Delta X_{\mathrm{u}} = \Delta X_{\mathrm{u,c}} - \Delta X_{\mathrm{u,w}}$ (notation: u = unfolding, c = cosolvent solution, w = water). Reprinted from [M. Gao, C. Held, S. Patra, L. Arns, G. Sadowski, R. Winter (2017) Crowders and Cosolvents - Major Contributors to the Cellular Milieu and Efficient Means to Counteract Environmental Stresses, ChemPhysChem, DOI: 10.1002/cphc.201700762] with permission of John Wiley & Sons, Inc. Copyright ©2017 Wiley-VCH Verlag GmbH & Co. KGaA, Weinheim.

biomolecules, $\Delta G_{\mathrm{u}} = G_{\mathrm{unfolded}} - G_{\mathrm{folded}}$, thereby be either stabilizing or destabilizing on the folded state. Thermodynamically, those effects may be explained by enthalpy and entropy contributions (Fig. 2.1):

$$\Delta G_{\mathrm{u}} = \Delta H_{\mathrm{u}} - T\Delta S_{\mathrm{u}} \tag{2.1}$$

The mechanistic details are described below.

2.1.1 Macromolecular Crowding

The total concentration of macromolecules up to 400 g L^{-1} makes biological fluids to be highly volume-occupied or crowded, viscous, and heterogeneous solvents.[4] First systematic crowding studies were conducted in the 1950-60s.[10,11] In the 80s, Allen P. Minton and Edwin H. McConkey interpretated the crowding effect in a more biological context. Using different thermodynamic approaches, they proposed that intracellular processes may be significantly affected by the macromolecular crowding effect.[12,13] As the intracellular macromolecules are typically separated by 1-2 nm only,[14] Allen P. Minton focused on the steric

repulsions between such molecules and thus shaped the term "excluded volume effect". In 1981, Allen P. Minton predicted that the effect of excluded volume would favor compact protein conformations and association processes, as well as alter enzyme-catalyzed reactions.[12] In contrast, Edwin H. McConkey suggested in 1982 that weak and transient "quinary" interactions inside the cell may be responsible for the intracellular organization.[13] Since then, investigating the macromolecular crowding effect has become a growing and attractive research field.[6,8,15–20] However, as sophisticated techniques and analysis are required, until today *in vivo* or in-cell experiments on molecular thermodynamics and kinetics are very rare. Instead, synthetic polymers (e.g. the polysaccharides dextran and Ficoll or polyethylene glycol (PEG)) and easily available proteins (e.g. albumin, lysozyme and hemoglobin) are commonly employed as an alternative to mimic the intracellular crowding density *in vitro*. Such studies revealed that the cellular crowding effect is able to significantly modulate the stabilities, dynamics, conformational equilibria, reaction rates, and transport processes of biomolecules.[8,15,16]

The quantitative description of the macromolecular crowding effect is given by the crowding coefficient, Γ_{Cr}, which can be given as a function of the crowding-induced changes in standard GIBBS free energy, enthalpy, and entropy:[15]

$$\ln \Gamma_{\mathrm{Cr}} = \ln(K_{\mathrm{Cr}}/K_{\mathrm{bulk}}) = -\frac{\Delta\Delta G^0}{RT} = -\frac{\Delta\Delta H^0}{R}\left(\frac{1}{T}\right) + \frac{\Delta\Delta S^0}{R}, \tag{2.2}$$

with $\Delta\Delta X = \Delta X_{\mathrm{Cr}} - \Delta X_{\mathrm{bulk}}$. Therefore, the crowding effect can be dissected into enthalpic and entropic contributions. Numerous studies have shown that the crowding effect is diverse and cannot be generalized. There are studies reporting on the stabilizing effect of *in vitro* macromolecular crowding on folding equilibria, which ranges from modest to strong.[8] In contrast, cellular crowding was also shown to only weakly shift protein folding equilibria towards the folded state[21–25] or even to destabilize the folded state.[26–30] Such observations are commonly explained by steric and nonspecific chemical ("soft") interactions between solute and cosolvent (Fig. 2.2).[6,15,17,31]

Steric effect of excluded volume

The steric effect of mutual impenetrability of macromolecules and the consequential steric repulsive interactions can be described either by the ASAKURA-OOSAWA model or by

the scaled-particle theory (SPT) of hard-sphere fluids.[32] The more widely used SPT has been decisively coined by Allen P. Minton, a pioneer in the crowding field. To quantify the so-called excluded volume effect, in this model, macromolecules are treated as inert hard spheres and are transferred from a dilute bulk solution to a solution containing a certain concentration of other macromolecules. Thereby, the free energy of transfer is equal to the free energy of creating a space in the solution to incorporate the new macromolecule.[8,12,33] Hence, the excluded volume effect depends on the volume occupied by the crowding agent as well as the relative sizes and shapes of solute and cosolvent.[8] It was concluded that small molecules such as osmolytes, ions and water play a minor role in crowding effects. The temperature-independent effect of excluded volume is predicted to affect reaction equilibria by reducing the overall non-occupied volume of the system.[8]. Thermodynamically, volume exclusion causes an increased activity coefficient and thus affects the chemical potential of the solute.[34] In the case of folding, the excluded volume effect causes a reduction of the configurational entropy of biomolecules, primarily for the rather expanded unfolded state. Consequently, the folding equilibrium is shifted towards the more compact folded state (Fig. 2.2).[8] In the case of biomolecular association reactions, crowding can significantly enhance the association tendency, when the complex is more compact compared to the individual subunits. Hence, the effect of crowding also highly depends on the shapes of the crowding agent, the monomers and their assemblies.[8] Conversely, it was recently emphasized that not only large crowding molecules (protein, nucleic acids, crowding agents like PEG, and Ficoll), but also small molecules like ions and water do exclude.[35] When the steric contribution of water was taken into account, it could be shown that large molecules are less effective crowders than water. This originates from a reduced entropy change caused by the replacement of a large cosolute by multiple small water molecules.[35] Nevertheless, many *in vitro* crowding studies using artificial macromolecular agents such as Ficoll, dextran and PEG could show that the excluded volume effect is able to stabilize proteins,[36–38] stabilize RNA tertiary structure and increase ribozyme activity,[39–42] enhance protein-protein associations[43] as well as promote protein polymerization and aggregation.[44–51] However, in such crowding studies, a single crowder with a uniform size was commonly used, which does not represent the *in vivo* crowding scenario. Indeed, it was reported that the composition and the size heterogeneity of crowder molecules may play an important role in determining the crowding effect.[52,53]

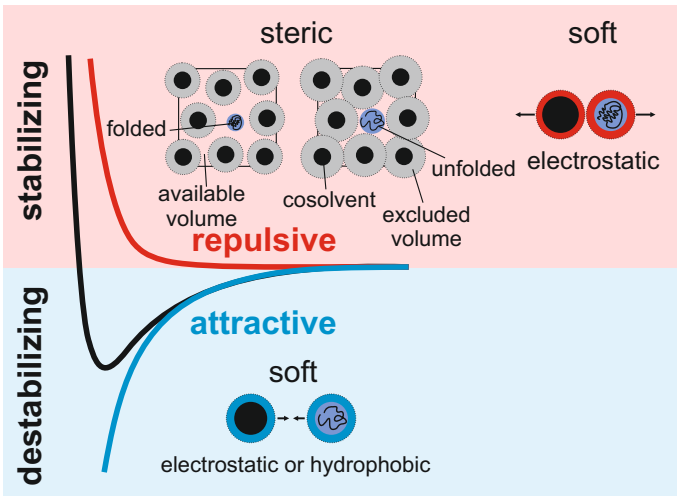

Figure 2.2 | Different contributions determining the effect of macromolecular crowding. The schematic overview is shown for the folding equilibrium of a biomolecule such as a protein or nucleic acid. Generally, the interactions between a biomolecule (solute) and the surrounding crowder molecules (cosolvents) can be divided into hard-core repulsion (entropically driven) and longer-ranged non-specific chemical ("soft") interactions (enthalpically driven). The steric contribution is mainly described by the effect of excluded volume, which favors the compact folded state. In contrast, the soft interactions between the solute and cosolvent can be attractive or repulsive, depending on their chemical properties. Attractive electrostatic and hydrophobic interactions usually cause a preference for the unfolded state with a maximal solvent accessible surface area (SASA), whereas repulsive electrostatic interactions reinforce the depletion force and thus act stabilizing on the folded state. Reprinted from [M. Gao, C. Held, S. Patra, L. Arns, G. Sadowski, R. Winter (2017) Crowders and Cosolvents - Major Contributors to the Cellular Milieu and Efficient Means to Counteract Environmental Stresses, ChemPhysChem, DOI: 10.1002/cphc.201700762] with permission of John Wiley & Sons, Inc. Copyright ©2017 Wiley-VCH Verlag GmbH & Co. KGaA, Weinheim.

Kinetics and increased viscosity

Another important aspect of crowding is the increased solvent viscosity, which can substantially affect the kinetics of biomolecular reactions as well.[6] For instance, the diffusion rate of biomolecules is significantly reduced under crowding conditions.[16,31,54] Consequently, their reaction rates for folding and association reactions are expected to be affected. If a reaction is diffusion-controlled, increased crowding is expected to decrease the reaction rates. Thereby, the slowdown of diffusion in crowded environment can originate from collisions with the crowders as well as nonspecific reversible binding to the crowders.[55] In contrast, in the reaction-controlled regime, crowding is expected to increase the effective concentrations and lower the energy barrier, if the transition state is more compact than the ground state.[8,56] Hence, protein folding kinetics is markedly affected by highly crowded environments.[36,37,57–59] Moreover, the microscopic spatial heterogeneity of a crowded solution can also cause solvent microviscosities that can be much less viscous than the bulk.[56,60] This

solvent-induced dynamics change has also been shown to drive protein folding kinetics.[36]

Nonspecific chemical interactions

The experimentally observed discrepancies from the predictions made by the excluded volume effect have led to the introduction of the so-called nonspecific chemical ("soft") interactions between solute and cosolvents, which are of enthalpic nature (Fig. 2.2).[20,25,26,31,61–69] As indicated by Eq. 2.2, this enthalpic contribution is temperature-dependent. Furthermore, its extent also depends on the chemical make-up of the biomolecule, the crowder and the solvent.[61,63,64,67,70,71] Such soft interactions can increase or decrease the folding stability of biomolecules depending on the interaction types (Fig. 2.2). For instance, electrostatic repulsions may enhance the stabilizing effect of excluded volume,[22] whereas attractive interactions including electrostatic, hydrophobic interactions and H-bonding may favor the unfolded state, because unfolding is accompanied by an increase of the solvent accessible surface area (SASA).[18] Therefore, protein crowders and cell lysates featuring a chemically heterogeneous surface have been increasingly used to mimic the in-cell scenario and to explore the enthalpic contribution of crowding. Pioneering works by Gary J. Pielak demonstrated that the enthalpic contribution of crowding can even dominate and destabilize globular proteins and impede their diffusion inside cells.[63,67,72]

Crowding-induced hydrational effect

The comparative use of crowding agents such as Ficoll and dextran and their monomeric building blocks sucrose and glucose, which are known as osmolytes (see section 2.1.2), has shown that the crowding agents can affect biomolecules in a similar way like their monomers,[49,55,61,73] thus suggesting an enthalpy-dependent and hydration-mediated mechanism.[61,70] MD simulations reported on an altered water structure mostly beyond the first hydration shell, a slowdown of the diffusion and a decreased dielectric constant of interstitial hydration water, suggesting highly constrained water in crowded environments.[74,75] As a consequence, the hydrodynamic properties of biomolecules and the strength of different intramolecular interaction types including hydrogen bonding as well as electrostatic and VAN-DER-WAALS interactions may be affected and modulated.[6,75] Furthermore, the picosecond hydration dynamics of hydrational water has been shown to be perturbed by protein self-crowding. Thereby, the reduction of the interprotein distances below a threshold of

3-4 nm is accompanied by a collective hydration and thus a dramatic extension of hydration layers.[76] It was concluded that only a small amount of the intracellular water behaves "bulk-like".[76] However, the hydration shell and thus the crowding-induced perturbation may be protein-specific.[77] Another aspect is the decrease of the water activity caused by the high content of biomolecules, osmolytes and salts,[20,78] which may affect the reaction equilibria of biomolecules as well.

In-cell crowding

The crowding effect in the biological cell is even more complex due to the high degree of intracellular heterogeneity, which can be both, of spatial and temporal nature.[25,79–82] Moreover, effects like confinement (membrane-enclosed organelles),[83] adsorption (on membranes and cytoskeleton),[84] and liquid-liquid phase separation[85] have to be taken into consideration as well. In the last decades, new techniques and approaches including in-cell nuclear magnetic resonance,[30,86] temperature-jump experiments in combination with fluorescence microscopy,[87] dye labelling experiments,[28] and *in silico* whole-cell models[31,88] have been established and revealed that nonspecific interactions may be the dominating contribution of macromolecular crowding and may prevail over the steric repulsion, resulting in negligible or even destabilizing effects of in-cell crowding.[18] Such transient and weak interactions may organize the fifth level of protein structure and thus the cellular interior.[89–91] Moreover, the presence of sophisticated protein machines such as chaperones, proteasomes and the ubiquitination machinery is another level of modulating folding and stability of proteins, which is not considered in in-cell crowding studies.[6]

2.1.2 Osmolytes and Denaturants as Cosolvents

Osmolytes are small and neutrally charged organic molecules accumulated in biological fluids and include classes such as carbohydrates (e.g. trehalose), amino acids (e.g. glycine and proline), polyols (e.g. glycerol, sorbitol, sucrose, and inositol), and methylamines (e.g. trimethylamine-*N*-oxide, betaine, and sarcosine).[7] Osmolytes are commonly used by organisms to combat different osmotic catastrophes like high salinity, dehydration, high hydrostatic pressure or the presence of the denaturant urea.[7,92,93] For instance, marine animals utilize an intracellular concentration of osmolytes up to 600 mM to counteract the

osmotic pressure of ocean water.[94,95] The preferred accumulation of osmolytes over inorganic ions to regulate the intracellular osmolality is due to their compatibility with macromolecular structures and functions, which means that they feature non-perturbing or even stabilizing effects.[7,96] Hence, osmolytes are even referred to as chemical chaperones.[97] Osmolytes do double duty: they maintain cellular volume and counteract water stress-induced biomolecular denaturation.[98,99] Moreover, it has been shown that methylamine osmolytes like trimethylamine-*N*-oxide (TMAO) act as an antagonist of urea and thus can counteract its denaturing effect on macromolecules.[100]

To understand the working mechanisms of such cosolvents, concepts of "direct" and "indirect" mechanism have emerged for osmolytes and denaturants.[9] Consequently, their stabilizing and destabilizing effects would originate from either direct interactions or perturbation of water structure. Therefore, numerous experimental and theoretical approaches have been undertaken to investigate aqueous solutions of such cosolvents, with TMAO and urea as the most studied candidates.

So far, it was found that urea does not perturb the tetrahedral hydrogen-bond network of liquid water, can substitute for a water dimer,[101] and does not affect the water dynamics beyond its first hydration shell.[102] In contrast, within the hydration shell of urea only one water molecule per urea molecule is strongly immobilized, featuring a six times slower orientational dynamics compared to bulk water, whereas the other water molecules of the hydration shell behave bulk-like.[102] This strong retardation was explained by a doubly hydrogen-bonded water molecule to a urea molecule.[102,103] However, water-urea interactions were found to become unfavored with increasing urea concentration,[104] thus leading to self-aggregation of urea.[104,105] From those observations it was concluded that urea is a better solvent than water and denatures biomolecules by direct interactions owing to its favorable interactions with the peptide backbone and amino acid side chains of proteins or nucleobases of nucleic acids, resulting in preferential binding to them over water.[106–113] Consequently, urea entropically and enthalpically prefers and stabilizes the unfolded state by maximizing the biomolecule's SASA. Enthalpic gain originates from the preferential binding of urea over water, whereas entropic gain is caused by the displacement of two water molecules by one urea molecule upon binding (Fig. 2.1).[114,115]

In contrast, the hydration picture of TMAO is more complex and still far from completely understood. So far, simulations and experiments reported on the formation of strong hydro-

gen bonds in the hydration shell of TMAO, in terms of shorter atomic distances, increased hydrogen-bond energy, and retarded dynamics.[116–129] The retardation might originate either from the three hydrophobic methyl groups, which are proposed to immobilize water molecules via hydrophobic hydration,[120,125,130–132] or from the highly polar and hydrophilic N-O group, which has been shown to accept up to three hydrogen bonds forming very stable TMAO-water clusters.[116–118,132–135] Based on those observations, the stabilizing effect of TMAO on biomolecules is commonly explained by an indirect mechanism, in which the osmolyte is a poor solvent for the biomolecule, but prefers strong interaction with water molecules over biomolecules. In fact, it was found that interactions between TMAO and backbones of proteins and nucleic acids are unfavored.[121,129,136–139] Consequently, the so-called preferential hydration effect favors conformational states that feature compactness and less dynamics with a minimal SASA.[9,20,140] Thereby, the water structure enhancement and thus an optimization of the hydrogen-bond network of the biomolecule's hydration shell are believed to cause an enthalpic gain.[61,70,141] However, the underlying entropic and enthalpic contributions to the net stabilizing effect of different stabilizing osmolytes may vary for different osmolyte systems (Fig. 2.1).[32] For instance, TMAO was also suggested to act entropically as a nano-crowding agent through steric depletion from the biomolecular surface.[141–143]

As mentioned before, TMAO is an antagonist of urea and acts in an additive way, whereby full counteraction is typically found at an 1:2 concentration ratio of TMAO and urea.[7,120,144] Although neutron scattering experiments reported on direct interactions between the oxygen atom of TMAO and urea at high concentrations,[116,145] an indirect, water-mediated mechanism has been assumed for the compensatory effect.[123,129,146–150] It was suggested that TMAO would strengthen the hydrogen bonds between water molecules as well as between urea and water, leading to an attenuated interaction between urea and the biomolecule.[123] Consequently, the counteraction is realized by removing the denaturant from the biomolecule's surface.[123,149,150]

Thermodynamic description of the cosolvent effect

To describe the thermodynamics of a system containing water (W), cosolvent (C) and biomolecule (B), two different models have been established and are often used in parallel (Fig. 2.3). In general, each component is defined by its chemical potential, $\mu_i = \mu_i^0 + RT \ln(\gamma_i m_i)$,

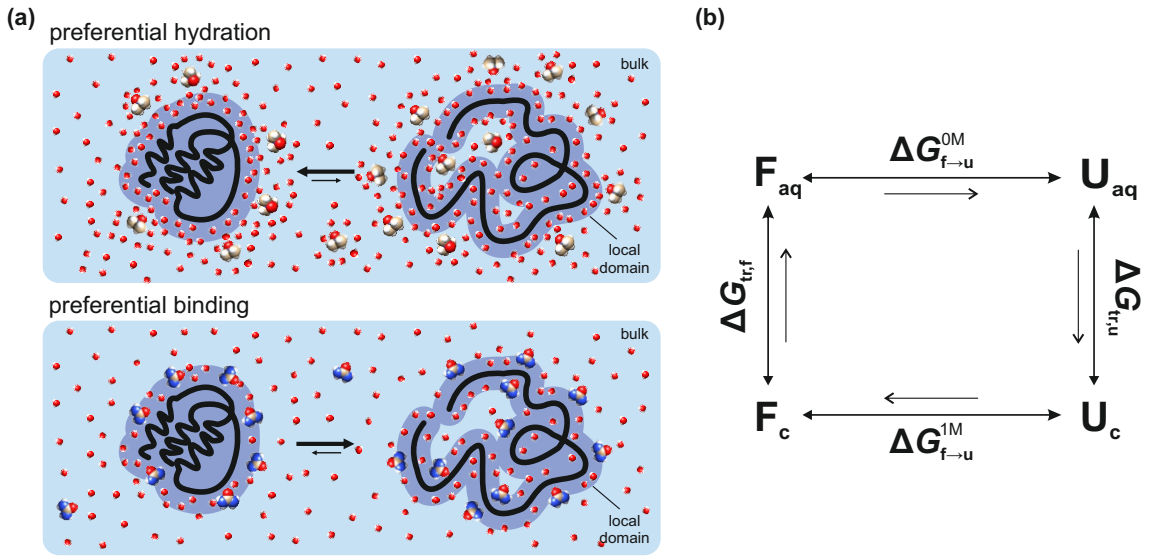

Figure 2.3 | Two common models describing the effect of osmolytes on folding equilibria of biomolecules. (a) Model of preferential hydration (TMAO as cosolvent) and preferential binding (urea as cosolvent) at the surface of a protein (local domain) in the folded and unfolded state. Of note, the quantity and the relative sizes of the molecules do not correspond to reality. (b) The transfer model according to Tanford is based on a thermodynamic cycle, which describes the difference of the unfolding free energies in 1 M cosolvent and in aqueous buffer. Reprinted from [M. Gao, C. Held, S. Patra, L. Arns, G. Sadowski, R. Winter (2017) Crowders and Cosolvents - Major Contributors to the Cellular Milieu and Efficient Means to Counteract Environmental Stresses, ChemPhysChem, DOI: 10.1002/cphc.201700762] with permission of John Wiley & Sons, Inc. Copyright ©2017 Wiley-VCH Verlag GmbH & Co. KGaA, Weinheim.

with activity coefficient γ_i, molal concentration m_i, and standard chemical potential μ_i^0. Usually, the activity of the biomolecule is assumed to be unity (at infinite dilution). At constant temperature and pressure, the addition of a cosolvent of concentration m_C to water perturbs the folding equilibrium of the biomolecule as follows:[6]

$$\left(\frac{\partial \Delta G_{\mathrm{C}}^0}{\partial \mu_{\mathrm{C}}}\right)_{T,p,m_{j\neq \mathrm{C}}} = \left(\frac{\partial \Delta \mu_{\mathrm{B}}^0(m_{\mathrm{C}})}{\partial \mu_{\mathrm{C}}}\right)_{T,p,m_{j\neq \mathrm{C}}} = -\left(\frac{\partial \ln K}{\partial \ln a_{\mathrm{C}}}\right)_{T,p,m_{j\neq \mathrm{C}}}, \tag{2.3}$$

where $\Delta\mu_{\mathrm{B}}^0(m_{\mathrm{C}}) = \mu_{\mathrm{C,U}}^0 - \mu_{\mathrm{C,F}}^0$ is the difference in the standard chemical potentials of the biomolecule in its unfolded (U) and folded (F) state.

To restore the chemical equilibrium of the system, the chemical potential and in this case the concentration of the cosolvent around the biomolecule must be adjusted accordingly.[151] This is the fundamental idea of the model of preferential binding and hydration pioneered by Serge N. Timasheff. The thermodynamic quantification of the mutual perturbation of the chemical potentials of cosolvent and biomolecule, but indirectly also that of water, is given

by:[6]

$$\Gamma_{\mathrm{BC}} = -\left(\frac{\partial\mu_{\mathrm{B}}/\partial m_{\mathrm{C}}}{\partial\mu_{\mathrm{C}}/\partial m_{\mathrm{C}}}\right)_{m_{\mathrm{B}}} = \left(\frac{\partial\mu_{\mathrm{B}}}{\partial\mu_{\mathrm{C}}}\right)_{\mu_{\mathrm{B}}} = \left(\frac{\partial m_{\mathrm{C}}}{\partial m_{\mathrm{B}}}\right)_{\mu_{\mathrm{C}}}, \tag{2.4}$$

when the WYMAN linkage relation, $(\partial\mu_{\mathrm{C}}/\partial m_{\mathrm{B}})_{m_{\mathrm{C}}} = (\partial\mu_{\mathrm{B}}/\partial m_{\mathrm{C}})_{m_{\mathrm{B}}}$ (at constant T and p), is taken into account. Γ_{BC} is the experimentally accessible preferential binding coefficient and a measure for the interaction between the biomolecule and the cosolvent.[151] It can be related to the number of cosolvent molecules, which diminish ($\Gamma_{\mathrm{BC}} < 0$, preferential exclusion) or accumulate ($\Gamma_{\mathrm{BC}} > 0$, preferential binding) around the biomolecule. Simultaneously, the number of water molecules is also affected. From the perspective of water, the coefficient of preferential hydration, Γ_{BW}, is used.[151,152] Therefore, the Γ_i does not represent the actual number of cosolvent or water molecules that are in physical contact with the biomolecule, but rather their excess numbers in the local surface domain of the biomolecule over the bulk, $\Delta N_{\mathrm{BC}} = N_{\mathrm{C}}^{\mathrm{loc}} - N_{\mathrm{C}}^{\mathrm{bulk}}$ and $N_{\mathrm{BW}} = N_{\mathrm{W}}^{\mathrm{loc}} - N_{\mathrm{W}}^{\mathrm{bulk}}$ (Fig. 2.3a):[151,153,154]

$$\Gamma_{\mathrm{BC}} = \Delta N_{\mathrm{BC}} - \left(\frac{N_{\mathrm{C}}^{\mathrm{bulk}}}{N_{\mathrm{W}}^{\mathrm{bulk}}}\right)\Delta N_{\mathrm{BW}} \quad \text{and} \quad \Gamma_{\mathrm{BW}} = \Delta N_{\mathrm{BW}} - \left(\frac{N_{\mathrm{W}}^{\mathrm{bulk}}}{N_{\mathrm{C}}^{\mathrm{bulk}}}\right)\Delta N_{\mathrm{BC}}. \tag{2.5}$$

Hence, the preferential exclusion of cosolvent is a consequence of preferential hydration and vice versa. Generally, stabilizing osmolytes feature negative values of Γ_{BC} and denaturants positive values.[152] In the case of unfolding reactions, a negative value of $\Delta\Gamma_{\mathrm{BC}} = \Gamma_{\mathrm{BC,U}} - \Gamma_{\mathrm{BC,F}}$ is assigned to stabilizing osmolytes favoring the folded state, whereas denaturants such as urea, cause positive values of $\Delta\Gamma_{\mathrm{BC}}$ and interact preferentially with the biomolecule favoring unfolded conformations with maximal SASA.[9]

The second model is the transfer model developed by Charles Tanford and established by Matthew Auton and D. Wayne Bolen.[106,155] This model is based on the quantitative description of the solvent quality for the backbone and side chains of proteins, which is quantified by the transfer free energy, ΔG_{tr}, of a protein from water to a second solvent system.[106,140] To predict the effect of cosolvents on protein stability, a thermodynamic cycle is used to calculate the difference between the folding equilibrium in 1 M cosolvent and in buffer solution, which is equal to the transfer free energy difference between the unfolded and folded state (Fig. 2.3b). Individual transfer free energies of side chains and the peptide backbone are known from experimental determinations and are assumed to contribute in an additive manner.[106,140] In the case of osmolytes, the transfer free energy of the unfolded biomolecule with

a more expanded SASA is more positive than that of the folded state, whereas the transfer of the unfolded biomolecules is more favored in the case of denaturants due to the maximized SASA.[140] In general, this model shows that the (un)favorable interactions between the cosolvent and the peptide backbone determine the extent of the (de)stabilizing effect of the cosolvent, whereas the interactions with the side chains play a minor role or even might give opposite effect.[106,140] In contrast, in the first model of preferential binding the major contribution comes from the side chains, rather than from the backbone.[9] Hence, more precise predictions based on structural information are needed and might be possible in the near future since very recently the strengths of amide-amide and amide-hydrocarbon interactions in water have been experimentally estimated with atomic resolution.[156]

In experiments, the GIBBS free energy of unfolding has often been observed to depend linearly on the cosolvent concentration. Thereby, the slope of the linear fit is referred to as the m-value.[157] Both, the preferential interaction coefficient and the transfer free energy can be related to the m-value.[9] That means that the m-value depends on the change in SASA upon unfolding as well as on the strength of the favorable interactions of the cosolvent with the different moieties of the biomolecule.[158,159] Hence, the underlying mechanism responsible for the biomolecule's stability depends not only on the physical and chemical nature of the cosolvent, but also on the chemical surface of the biomolecule.[6] In case of RNAs, the m-value may further depend on the length of the duplex, the degree to which RNA structures fold, and the ionic strength.[139,160–163]

2.2 High Hydrostatic Pressure

Hydrostatic pressure is not only an environmental condition that can be easily encountered at the ocean floor, but is also a powerful tool for studying the thermodynamics and kinetics of biomolecules.[164] The story of pressure studies on biomolecular systems started about 100 years ago, when Nobel prize laureate Piercy Bridgman reported on coagulation of egg white under high hydrostatic pressure (HHP) at room temperature.[165] The driving forces underlying the HHP perturbation on biomolecules are essentially the release of packing defects/voids and changes in hydration resulting in a reduced partial molar volume.[166–169] During heat-induced unfolding driven by entropy, the hydrophobic core of a biomolecule is exposed to the solvent. Conversely, upon pressurization, water penetrates into the biomolecular interior

causing filling of the voids and swelling of the core.[164,166,170–172] While perturbations by temperature and denaturing agents are commonly applied to study the folding pathways of proteins and nucleic acids, the pressure variable was less considered in the past, but interest in the use of HHP as a valuable variable has been considerably growing in physico-chemical studies of biomolecules in recent years.

2.2.1 Advantages, Biological Relevance and Impact on Biomolecules

For many aspects, hydrostatic pressure is a more elegant tool to study the thermodynamics and kinetics of biomolecules compared to temperature and detergents:

1. Compared to temperature-dependent and detergent-dependent studies, increase of pres-

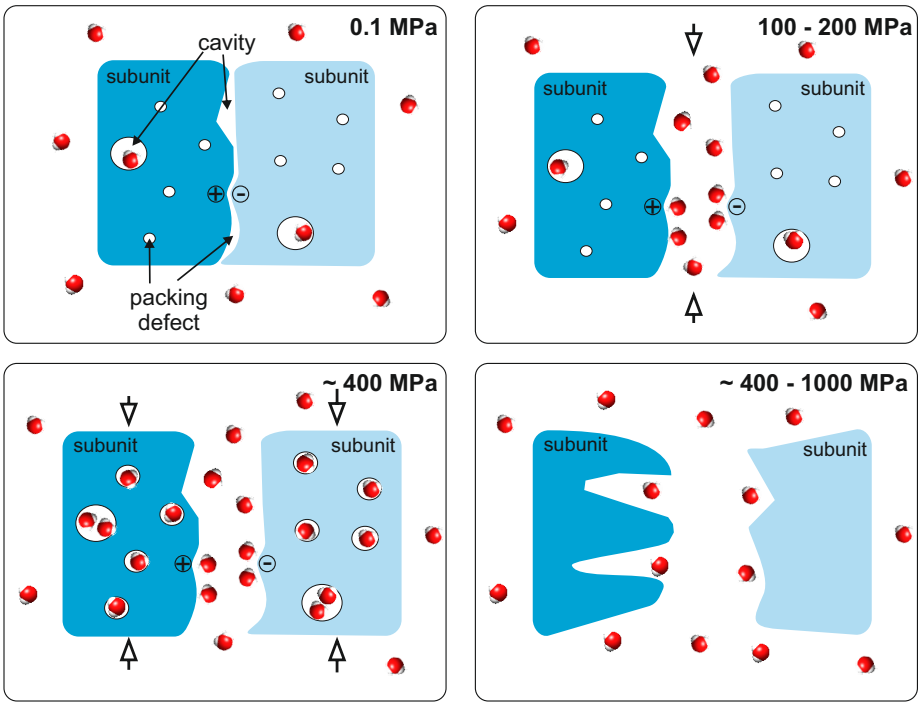

Figure 2.4 | Schematic representation how pressure induces dissociation and unfolding of a protein dimer. A native protein dimer contains packing defects and cavities both at the interface and within the subunits. Packing defects are water-inaccessible spaces, whereas cavities are large enough to host water molecules, which might have only very short dwell times due to the dynamics of proteins. Upon application of relatively low pressures, water molecules penetrate into the dimer interface and cause dimer dissociation by releasing void volumes arising from cavities and packing defects at the interface. In addition, hydration of ionic residues weakens electrostatic contacts (known as electrostriction). Further pressurization leads to water penetration into the interior of both subunits resulting in filling of the cavities and packings defects. Finally, the swelling of the protein core leads to disruption of tertiary/secondary structures, that means unfolding of the protein. Next to cavities and packing defects, changes in hydrogen bond properties and hydration shells also contribute to the volume change associated with the unfolding reaction.

sure causes solely a density effect, whereas the thermal energy and chemical properties remain unchanged.[172] According to the LE CHÂTELIER's principle,[173] conformations occupying smaller volumes and reactions, for which the transition state has a smaller volume than the ground state, are favored under HHP conditions.[164] Thus, pressure allows mechanistic insights into a reaction through volumetric information, whereas temperature generally only changes the frequency of the motions. Additionally, HHP is useful to study the hydration of a biomolecule as its partial molar volume consists of an intrinsic and a hydrational contribution (see section 2.2.2).[167,169]

2. Pressures up to 2 GPa affect primarily non-covalent interactions,[164] which are substantial for biomolecules. Ionic interactions are generally weakened under high pressure conditions because dissociation of ion pairs results in electrostriction, which means rehydration of the ions and thus contraction of water.[171] It was reported that the pressure-induced dissociation of ion pairs is accompanied by a volume decrease in the range of 10-30 mL mol^{-1}.[174] In contrast, hydrogen bonds are stabilized with increasing pressure.[171] Furthermore, it was reported that pressure even induces shortening of hydrogen bonds.[171] However, the effect of pressure on hydrophobic interactions is still under debate. Initially, it was believed that the hydration of non-polar residues results in a negative volume change,[175] but this weakening of the hydrophobic effect could not explain the relatively small negative or even positive volume changes of unfolding observed experimentally. Therefore, the discrepancy between the experimental volume changes and the void volumes obtained from protein structures gives rise to the "Protein Volume Paradox".[169,175] Recently, Chen et al. pointed out that the model used to describe hydrophobic hydration, in which protein unfolding was modelled as a transfer from non-polar solvent to aqueous solution, might overestimate the volume changes due to the larger size of the non-polar solvent compared to water. Using a transfer model from gas phase to water, they found that the hydration volume upon unfolding is accompanied by a positive volume change.[167]

3. Pressures relevant for studies of biomolecules generally range from 0.1 MPa to 1 GPa and allow a gradual and controlled fine-tuning of intra- and intermolecular interactions (Fig. 2.4).[164,172] In the range below 100-300 MPa, pressure impacts the quaternary structure of proteins.[172] Dissociation of complexes is favored due to packing defects

and cavities at the interfaces, resulting in negative volume changes. In the range beyond about 400 MPa, secondary and tertiary structures are affected, resulting in reversible unfolding of a protein due to changes in hydration and packing properties upon protein unfolding. Thereby, the volume changes upon protein unfolding are typically on the order of -10 to -100 mL mol^{-1}.[176] In contrast, high pressure resistance was found for DNA double helices and the phenylalanine transfer RNA.[177–179] This is because pressure decreases the extent of charge neutralization by cations, reduces the Watson-Crick hydrogen-bond distance and favors base stacking.[177,178,180] Conversely, non-canonical DNA structures, such as G-quadruplex DNA and a DNA hairpin with an oversized poly-dA loop, were found to be more sensitive to pressure.[160,181]

4. Kinetic studies under pressure are of additional advantage to explore protein folding landscapes including transition states. In most cases, pressure has been found to decrease the folding rate and increase the unfolding rate.[182–184] Some enzymatic reactions have been demonstrated to be accelerated under high pressure conditions.[185]

5. HHP is well-suited for investigating protein dynamics and its functional role.[164,186,187] Protein dynamics means conformational fluctuations, whereby the ensemble of nearly isoenergetic conformers could differ in their volumes and are pressure-sensitive. Further, HHP is able to increase the roughness of the folding energy landscape and shifts the chemical equilibrium towards populations of high-energy conformers or transient conformational substates, which are often difficult to detect at ambient pressure.[188] This is due to decreased conformational diffusion upon compression. Therefore, pressure could populate rare, but functional conformational substates.[187]

6. At marine hydrothermal vents, microbial growth can be found up to 122 °C and 130 MPa.[172] Interestingly, bacterial survival was even found at 2 GPa.[189] Under abyssal conditions (1-4 °C, <100 MPa), even more complex organisms can be encountered.[190] As oceans cover about 70% of the surface of the Earth with an average depth of 3.8 km and consequently an average pressure of 38.5 MPa,[191] pressure studies are also important for understanding the adaptation strategies of life in a pressurized world.

7. Life on Earth emerged under primitive conditions, but its early stages might have also evolved under harsh environmental conditions like in the depth of the proto-ocean of

the Hadean Earth, that means including high temperature and pressure.[1] Therefore, pressure is also a core element in studies of prebiotic chemistry and origin-of-life.

8. Pressure application is also considered in a broad range of other disciplines including food science (e.g. high pressure food processing),[192] biotechnology (e.g. baroenzymology)[193] and biomedicine (e.g. inactivation of viruses).[194] For instance, pressure application in food industry has its origin in Japan in the 1980-1990s, where pressure was considered as an alternative to radiation processing.[191]. Compared to thermal sterilization, pascalization is a much more gentle method to guarantee food safety (to kill pathogens and spoilage organisms) and taste (to maintain bioactive molecules).[191,195]

So far, simple biomolecular systems such as monomeric proteins and nucleic acids have been extensively investigated in HHP studies.[164,172] There are also pressure studies on lipid bilayers, model biomembranes, and a few reconstituted membrane-protein systems.[172,186,196] Additionally, pressure-induced protein folding reactions and protein disaggregation have been studied.[197–199] However, the effect of pressure to perturb and modulate more complex biochemical structures and processes is still largely unexplored, in particular in combination with the effects of osmolytes and crowding.

2.2.2 Thermodynamic Description

To quantitatively describe the effect of pressure on any chemical equilibrium and reaction rate, the following equations are given:

$$\left(\frac{\partial \ln K}{\partial p}\right)_T = -\frac{\Delta V}{RT}, \quad \left(\frac{\partial \ln k}{\partial p}\right)_T = -\frac{\Delta V^{\#}}{RT}, \tag{2.6}$$

where K is the pressure-dependent equilibrium constant, k is the rate constant of a reaction, and ΔV and $\Delta V^{\#}$ are the reaction and activation volumes, respectively. According to the LE CHÂTELIER's principle,[173] those equations indicate that only reactions associated with a negative ΔV and $\Delta V^{\#}$ are favored and accelerated under high pressure conditions.
According to Tigran V. Chalikian, ΔV can be described as the sum of an intrinsic, thermal,

and hydration contribution, that is:[169]

$$\Delta V = \Delta V_{\mathrm{M}} + \Delta V_{\mathrm{T}} + \Delta V_{\mathrm{h}}. \tag{2.7}$$

The intrinsic volume, ΔV_{M}, originates from the VAN-DER-WAALS volume of the molecule plus the volume of interior voids, which are water-inaccessible. This means that such voids are much smaller than 18 mL mol^{-1}. The thermal volume, ΔV_{T}, represents the voids formed by the solute and the solvent at their interface. It depends on the biomolecule's SASA and the thermally induced molecular vibrations and reorientations.[200] The hydrational term, ΔV_{h}, describes the volume change of solvent molecules involved in hydrating solvent-accessible atomic groups of the biomolecule with respect to the bulk. As the density of hydrational water is higher compared to that of bulk water, hydration processes may reduce the partial molar volume.[168] In the studies of Chen et al. the thermal and hydrational volumes are combined. They showed that the change of the intrinsic volume upon protein unfolding is relatively large and negative due to the voids, whereas the volume change due to hydration is positive resulting in relatively small, either negative or positive, total volume change upon unfolding.[167] Hence, the main driving forces for pressure-induced unfolding are the presence of packing defects located inside biomolecules and their hydration behavior.
To consider both factors, temperature and pressure, the thermodynamic stability of a biomlecule ($\Delta X = X_{\text{unfolded}} - X_{\text{folded}}$) is described as follows:[6]

$$\mathrm{d}\Delta G = -\Delta S \mathrm{d}T + \Delta V \mathrm{d}p, \tag{2.8}$$

where ΔS and ΔV are the changes in entropy and volume upon unfolding, respectively. Integration of Eq. 2.8 with respect to some reference point T_0, p_0, gives:

$$\begin{aligned} \Delta G =& \Delta G_0 + \Delta V_0(p - p_0) - \frac{\Delta\kappa'}{2}(p - p_0)^2 + \Delta\alpha'(p - p_0)(T - T_0) \\ & - \Delta C_p \left[T \left(\ln \frac{T}{T_0} - 1 \right) + T_0 \right] - \Delta S_0 (T - T_0), \end{aligned} \tag{2.9}$$

where κ', α', C_p are the second order terms of the TAYLOR expansion and are referred to as the compressibility factor, the thermal expansivity factor, and the heat capacity at constant p, respectively. Assuming pressure- and temperature independence, they are defined as

follows:[169,172]

$$\begin{aligned} \Delta\kappa' &= -(\partial\Delta V/\partial p)_T \\ \Delta\alpha' &= (\partial\Delta V/\partial T)_p = -(\partial\Delta S/\partial p)_T \\ \Delta C_p &= T(\partial\Delta S/\partial T)_p. \end{aligned} \tag{2.10}$$

The compressibility factor, κ' is related to the isothermal compressibility, $\kappa'_T = -V^{-1}(\partial V/\partial p)_T$, which describes the pressure dependence of V, via $\kappa' = V\kappa'_T$. Usually, below 200 MPa, the compressibility term is negligibly low, leading to a linear pressure dependence of ΔG as in Eq. 2.6.[164] The thermal expansivity factor, α' is related to the coefficient of thermal expansion, $\alpha = -V^{-1}(\partial V/\partial T)_p$, which describes the temperature dependence of V, via $\alpha' = V\alpha$. Depending on the experimental methods, the partial molar volume changes of biomolecules upon unfolding are obtained either at their melting temperatures or at the set temperature. Therefore, comparison of volumetric data reported in literature is quite difficult when the change in thermal expansivity is not known.

CHAPTER 3

EXPERIMENTAL METHODS

The scope of this chapter is to introduce the underlying theory of the experimental methods used in this thesis.

3.1 Fluorescence Spectroscopy and Microscopy

Fluorescence-based methods are commonly used in molecular biology and exhibit advantages including providing information on dynamic processes on the nanosecond time scale, structural information of molecules as well as on the molecular environment. Fluorescence is very sensitive and allows applications with subnanomolar concentrations and even single-molecule detection.[201,202]

3.1.1 Fluorescence

A fluorophore owns the property to absorb energy in the form of electromagnetic radiation with a certain wavelength. During absorption, energy of the photon is transferred to an electron causing excitation of the electronic state. This excitation causes the MORSE potential of the molecule (see section 3.3.1) in the excited electronic state to shift to a new equilibrium position of the nuclei. As the electronic transitions are much faster compared to nuclear motions (according to the BORN-OPPENHEIMER approximation), electronic transitions are most likely to occur when the position and vibrational momenta of the nuclei thereby are not changed (known as the FRANCK-CONDON principle).[173,201] That means, when a vibrational transition occurs during an electronic excitation, the new vibrational state in the excited electronic state has to be compatible with the original vibrational state of the ground electronic state. As a consequnce, vertical electronic transitions are allowed, only, where the nuclear coordinates are not changed during the transition. The FRANCK-CONDON factor is

proportional to the square of the overlapping integral between the two vibrational wavefunctions that are involved in the transition and thus describes their transition probability.[173,201] The electronically excited molecule is able to release the absorbed energy in multitude radiative and non-radiative ways (Fig. 3.1).[201,202] However, the molecule has first to relax to the ground vibrational state of the excited electronic state. This occurs within the first 10^{-11} s and is known as internal conversion (IC). During this process energy is released by collisions with surrounding solvent molecules. In the ground vibrational state of the excited electronic state, the molecule can electronically relax into the ground electronic state via IC again. However, a competing pathway is the radiative process termed fluorescence, where the transition from the first excited electronic state to the ground state occurs with a rate constant of 10^{8} s^{-1} by emitting a photon. The probability to which the vibrational state in the ground electronic state the molecule is relaxed is again determined by the FRANCK-CONDON factor. The wavelength of the emitted photon is usually red shifted (referred to as STOKE shift) compared to that of the absorbed photon.[201,202] At higher excited states, the fast non-radiative processes occur more likely. The third pathway of electronic relaxation is called intersystem crossing (ISC), where the electron changes the spin multiplicity from the singlet state to the triplet state. In a simple quantum-mechanical view, this is forbidden, but becomes likely when the energy difference between the singlet and triplet state is small. ISC leads to an alternative radiative process termed phosphorescence, where the electron transitions from an excited triplet state to a singlet ground state with a rate constant of 10^{-2} to 10^{2} s^{-1}. Finally, the relaxation energy can also be transferred to an adjacent molecule in a non-radiative way known as quenching.

Interactions between the fluorophore and the solvent molecules can significantly affect the fluorescence spectrum of the fluorophore. The polarity and the inhomogeneity of the solvent cause broadening and red shift of the emission spectrum.[201,202] In a polar solvent, the dipole moments of the solvent and the fluorophore are aligned in an anti-parallel fashion at the equilibrium state. The absorption of a photon causes the electric dipole moment of the fluorophore to change direction and strength. As a consequence, the solvent molecules have to adapt to the new equilibrium, a process which is completed within 10^{-10} s upon excitation of the fluorophore. This causes a stabilisation and thus an decreased energy level for the excited electronic state of the fluorophore, which is expressed in a red shifted emission spectrum. This red shift ranges from 20 to 50 nm and depends on the polarity of the solvent.[201]

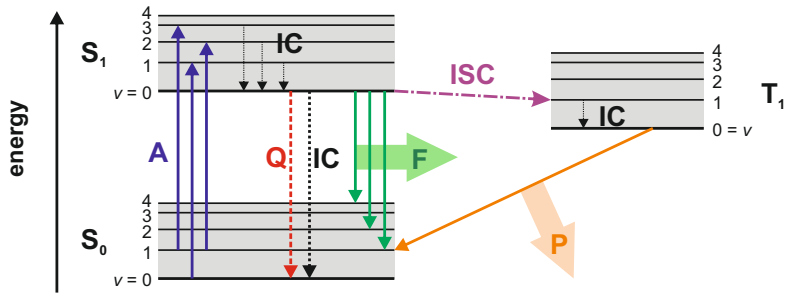

Figure 3.1 | JABLONSKI diagram showing excitation and relaxation of a fluorophore. After absorbing (A) a photon the molecule transitions from the singlet ground state (S_0) to the first (S_1) excited singlet state with various vibrational energy states. During relaxation, the energy is dissipated through multitude radiative and non-radiative processes including internal conversion (IC), quenching (Q), fluorescence (F), intersystem crossing (ISC) and phosphorescence (P).

Usually, the more polar the solvent is, the more significant the red shift is. In nonpolar and highly viscous solvents, the red shift is much less pronounced and can even cause a blue shift of the emission spectrum.[201] One example is the extrinsic dye pyrene, which is covalently bound to a biomolecule to probe its microenvironment.[203] For instance, pyrene is a well established probe to monitor the polymerization reaction of actin. Upon polymerization, the microenvironment of pyrene-labeled actin is changed from a polar (exposed to the aqueous solvent) to a hydrophobic microenviroment (burried in the actin filament). This causes the vibronic band at 385 nm of the fluorescence spectrum of pyrene to be significantly enhanced.[203]

3.1.2 FÖRSTER Resonance Energy Transfer (FRET)

In addition to fluorescence, relaxation of excited molecules can also occur through a non-radiative energy transfer from one excited fluorophore (donor) to an adjacent fluorophore (acceptor) via dipole dipole coupling (referred to as FÖRSTER resonance energy transfer, FRET).[204] Upon transfer, the acceptor gets excited and emits the energy subsequently via fluorescence. Thereby, the transfer efficiency depends strongly on the spectral overlap of the donor's emission spectrum and the acceptor's excitation spectrum (Fig. 3.2b), the distance of the two fluorophores (< 8 nm), and the relative orientation of their transition dipole moments. The energy of the dipole-dipole interaction is given by:[201,202]

$$E_{\mathrm{DD}} = \frac{1}{4\pi\epsilon_0 n_{\mathrm{L}}^2 R^3} \cdot \left\{ \vec{\mu}_{\mathrm{D}} \vec{\mu}_{\mathrm{A}} - \frac{3}{R^2} (\vec{\mu}_{\mathrm{D}} \vec{R})(\vec{\mu}_{\mathrm{A}} \vec{R}) \right\}, \tag{3.1}$$

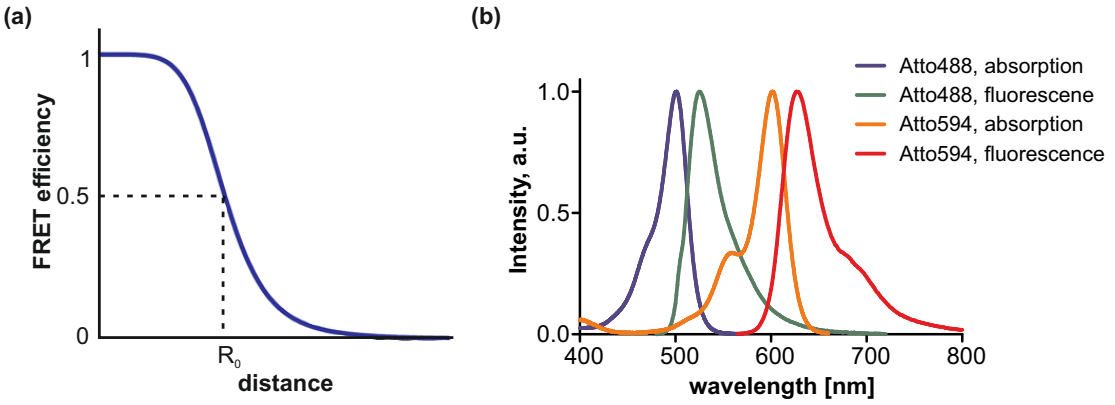

Figure 3.2 | Schematic mechanism of FRET. a) FRET efficiency as a function of inter-fluorophore distance, with R_0 as the FÖRSTER radius. b) Absorption and fluorescence spectra of Atto488 and Atto594, a FRET-pair used in this thesis.

with n_L as the refractive index of the solution, ϵ_0 as the vacuum permittivity, and R as the distance between the donor and acceptor. The rate constant for the energy transfer is proportional to the square of E_DD and depends on the spectral overlap, J. If both fluorophores rotate freely and are isotropically oriented, the rate constant for the energy transfer, k_trans, can be described as:[201]

$$k_\mathrm{trans} = \text{const.} \cdot \frac{\frac{2}{3} J Q_\mathrm{F,D}}{n_\mathrm{L}^4 R^6 \tau_\mathrm{D}}, \tag{3.2}$$

where $Q_\mathrm{F,D}$ is the quantum yield and τ_D is the life time of the donor in the absence of acceptor. The constants in Eq. 3.2 can be summarized to the so-called FÖRSTER radius, R_0:[201]

$$k_\mathrm{trans} = \frac{1}{\tau_\mathrm{D}} \cdot \left(\frac{R_0}{R}\right)^6. \tag{3.3}$$

To determine the distance between the donor and the acceptor, the FRET or transfer efficiency, E_trans, has to be known:[201,202]

$$E_\mathrm{trans} = \frac{k_\mathrm{trans}}{k_\mathrm{trans} + k_\mathrm{F} + k_\mathrm{IC} + k_\mathrm{ISC}} = 1 - \frac{Q_\mathrm{F,D+A}}{Q_\mathrm{F,D}} = \frac{1}{1 + \left(\frac{R}{R_0}\right)^6}. \tag{3.4}$$

Thereby, the FÖRSTER radius is the distance at which the energy transfer efficiency is 50%. Due to the strong distance-FRET efficiency relationship (Fig. 3.2a), FRET is widely used as a molecular ruler to investigate the structural dynamics and interactions of macromolecules.

3.1.3 Confocal Laser Scanning Microscopy

Optical microscopy is commonly used to magnify and thus to investigate tissues and cells in a non-invasive way. Since the establishement of efficient fluorescent probes, which can be covalently labeled to the molecule of interest, the application of fluorescence microscopy has been substantially increased. However, the spatial resolution of a conventional fluorescence microsope is restricted by the ABBE diffraction limit:[201]

$$d = \frac{0.61\lambda}{n \sin \alpha}, \tag{3.5}$$

where λ is the wavelength of the light source, n the refractive index of the imaging medium, α is the half angle over which the objective gathers light from the specimen. $n \sin \alpha$ is also known as the numerical aperture (NA) of the objective. d describes the minimal distance between two objects, which can be optically distinguished. Owing to the wave nature of light, diffraction and thus blurring always occur when light is focused through lenses. Instead of a single point, imaging of a point light at the focal lane produces an AIRY disk, a bright region in the center of a series of concentric rings (AIRY pattern). The numerical aperture correlates with the radius of the AIRY disk. The smaller the numerical aperture of the ojective is, the larger the AIRY disk and thus the lower the optical resolution is. The resolution of an optical microscope can also be characterized by the point-spread function (PSF), which describes the probability for an area where a given point can appear. The lateral full-width half-maximum (LFWHM) of the PSF for a conventional microscope is given by:[205]

$$\text{LFWHM}_{\text{conv}} = 0.51\frac{\lambda}{\text{NA}}. \tag{3.6}$$

As all parts of the specimen in the optical path are excited, the axial resolution is even worse:[205]

$$\text{AFWHM}_{\text{conv}} = 0.89\frac{\lambda}{n - \sqrt{n^2 - \text{NA}^2}}. \tag{3.7}$$

Confocal laser scanning microscopy (CLSM) is an optical imaging technique allowing improved resolution and contrast compared to conventional optical microscopy. CLSM was pioneered by Marvin Minsky in 1955.[206] The key components of a confocal microscope are two pinhole apertures, which enable point-by-point illumination of the specimen and re-

jection of out-of-focus light (Fig. 3.3).[207] The first pinhole is located in front of the light source in order to minimize the area of the specimen, which is illuminated. This allows the objective lens of the confocal microscope to focus a point of light at the desired focal plane in the specimen. As a consequence, light sources of very high intensity like lasers are neccessary. Further, to build an image of the specimen, the focused point of light has to be scanned across the specimen. Usually, vertically and horizontally scanning mirrors switched in sequence and motor-driven are utilized to move the laser spot across the specimen. The emitted fluorescence light from the dyes in the specimen is filtered by a dichromatic mirror and focused by a second objective lens at the second pinhole placed in front of a photomultiplier as the detector. This second pinhole prevents the detection of out-of-plane unfocused light and allows only in-plane focused light to pass through. As the focal plane of the objective lens and the pinhole are conjugate planes, the name 'confocal' pinhole is assigned to the second pinhole. As a result, the resolution of a confocal microscope is improved to:[205]

$$\begin{aligned} \mathrm{LFWHM_{conf}} &= 0.37\frac{\lambda}{\mathrm{NA}} \\ \mathrm{AFWHM_{conf}} &= 0.64\frac{\lambda}{n-\sqrt{n^2-\mathrm{NA}^2}}. \end{aligned} \tag{3.8}$$

The improved axial resolution allows the three-dimensional reconstruction of the specimen by recording a series of images obtained along the vertical axis (optical sectioning).

3.1.4 Fast Relaxation Imaging

Fast relaxation imaging (FReI) is a recently developed technique allowing the study of biomolecular thermodynamics inside living cells.[87]. FReI combines FRET microscopy and temperature-jump relaxation to record biomolecular dynamics with a high spatio-temporal resolution. In the 1950s, chemical relaxation methods were established by Manfred Eigen.[208] They provide the possibility to study thermodynamics and kinetics with time scales in the range of μs and ms[209]. As chemical equilibrium constants depend on external factors such as temperature and pressure, such factors can be rapidly changed to perturb the equilib-

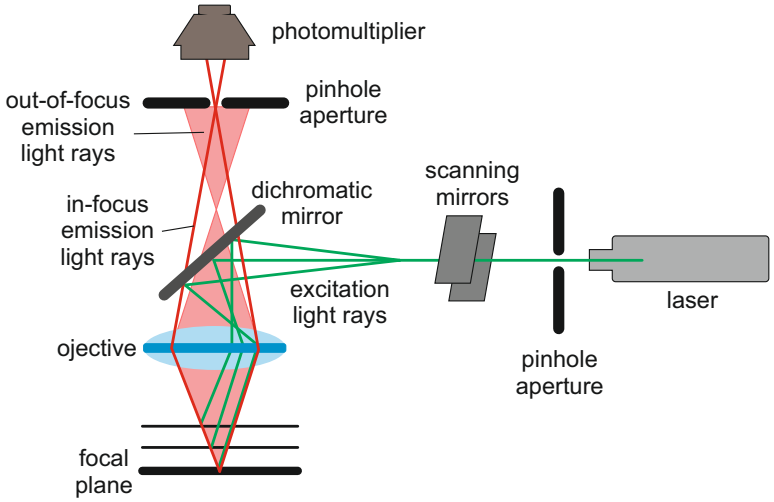

Figure 3.3 | Schematic of a confocal laser scanning microscope. The laser light (green) is sent through a pinhole aperture, reflected by a dichromatic mirror to the objective and focused at the focal plane of the specimen. The emitted fluorescence light (red) from the specimen is focused by the objective and goes through the dichromatic mirror and the second pinhole to the photomultiplier. Thereby, only in-focus emission light rays will be detected. The vertically and horizontally scanning mirrors enable a point-by-point scanning across the specimen.

rium:[201]

$$\left(\frac{\partial \ln K}{\partial T}\right)_p = \frac{\Delta H}{RT^2}$$
$$\left(\frac{\partial \ln K}{\partial p}\right)_T = -\frac{\Delta V}{RT}. \tag{3.9}$$

The relaxation of a parameter x to the new equilibrium follows an exponential course if the perturbation is not too large:[173]

$$x = x_0 \exp(-t/\tau). \tag{3.10}$$

In case of a single-step and reversible reaction of first-order, the relaxation time constant, τ, can be related to the rate constants of the reaction at the new equilibrium:[173]

$$\frac{1}{\tau} = k_{\text{for}} + k_{\text{back}} \tag{3.11}$$

with $K = k_{\text{for}}/k_{\text{back}}$. Hence, such chemical perturbation methods allow the determination of equilibrium and rate constants of a reaction.

For FReI, an infrared laser (λ = 2,200 nm) is utilized to induce temperature-jumps allowing fast and homogeneous equilibration in aqueous solutions.[87]

3.2 Stopped-Flow Methodology

To monitor chemical reactions in real time and thus to analyze their kinetics, different experimental techniques have been developed over time scales ranging from hours down to few femtoseconds. Reactions occruing on time scales of milliseconds to seconds are commonly studied using flow techniques.[173,201] Such kinetical experiments consist of mixing of reactants, initiating the reaction on a time scale that is negligible relative to that of the reaction (dead time), and monitoring the reaction as a function of time. The vanish of the reactants or the rise of the product is usually detected by UV/Vis absorption, circular dichroism, turbidimetry, small-angle X-ray scattering or fluorescence emission.[201] The simplest flow method is the continuous-flow technique, where the two reactants, each filled in a pneumatically driven syringe, are injected into a mixing chamber with the same and a constant velocity (Fig. 3.4a).[173] Subsequently, the homogeneously mixed solution passes from the mixing chamber to an observation chamber situated at one or more positions along the flow tube. The distinct positions of the oberservation chamber correspond to different time points of the chemical reaction after initiation and thus allow time-dependent detection of the reaction mixture composition. The disadvantage of this technique is the relatively high sample consumption due to the large reaction volume required. Moreover, high flow velocities are needed to study fast reactions. Those disadvantages are avoided in the stopped-flow technique (Fig. 3.4b).[173,201] In this mode, an additional piston is installed to the end of the flow tube. This allows to stop the sample flow after being injected into the mixing and observation chamber. As a result, a defined but small volume of reactants is required. The observation chamber is located at a fixed position and allows e.g. a spectroscopic monitoring of the reaction as a function of time.[173] Thus, the stopped-flow method has become popular for the study of biochemical kinetics. The time resolution is usually limited by the used mixing mode, which is in the range of milliseconds.

Usually, the reaction rate of a chemical reaction depends on the concentrations of the reactants and can be described as:[173]

$$v = k[A]^a[B]^b[C]^c..., \tag{3.12}$$

where the rate is proportional to the concentrations of the reactants each raised to some power

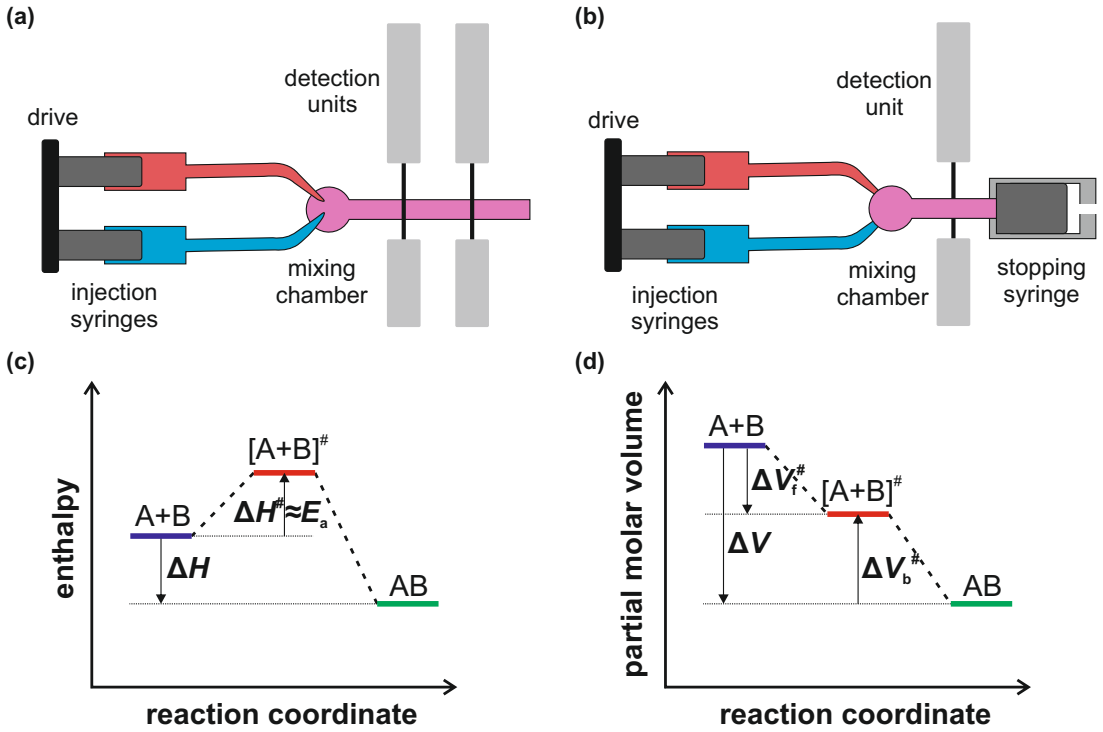

Figure 3.4 | Flow techniques and kinetic parameters. a) Schematic of a continuous-flow capillary mixing apparatus with several detection units. b) Schematic of a stopped-flow capillary mixing apparatus with one stationary detection unit. c) Enthalpy and d) volume profile of a biomolecular reaction.

and k is the rate constant. The sum of the powers is termed the overall order of the reaction. To determine the reaction order, the method of isolation is commonly used. In this method, the dependence of the reaction rate on the concentration of reactants is reduced to one by putting all other reactants present in a large excess. As a consequence, their concentrations remain essentially constant during the reaction and the reaction rate depends only on the concentration of one reactant:[173]

$$v = k[A]^a[B]^b \approx k_{\text{obs}}[A]^a \tag{3.13}$$

with $k_{\text{obs}} = k[B]_0^b$ as the effective or observed rate constant.

For reactions with a non-zero activation energy and volume, the rate constant depends on temperature and pressure (Fig. 3.4c-d). The temperature dependence can be described by the ARRHENIUS equation:[173]

$$k = A \exp[-E_a/RT] \tag{3.14}$$

with E_a as the activation energy required to form the transition state and A as the pre-exponential factor, a measure for the collision rate. Hence, reactions are accelerated with increasing temperature when the activation energy is positive. In terms of enthalpy, the temperature dependence of the rate constant is defined as:[164]

$$\left(\frac{\partial \ln k}{\partial T}\right)_p = -\frac{\Delta H^{\#}}{RT^2} \tag{3.15}$$

with $\Delta H^{\#}$ as the activation enthalpy.
The pressure dependence is given by:[164]

$$\left(\frac{\partial \ln k}{\partial p}\right)_T = -\frac{\Delta V^{\#}}{RT}, \tag{3.16}$$

where $\Delta V^{\#}$ is the activation volume of the reaction. If the transition state has a smaller volume than the reactants, that is a negative $\Delta V^{\#}$, the reaction is accelerated under high pressure conditions according to the LE CHÂTELIER's principle. Hence, temperature- and pressure-dependent studies on the reaction kinetics allow insight into the reaction mechanisms.

3.3 Infrared Spectroscopy

Proteins and nucleic acids play key roles in living organisms. Knowing their structures is essential to understand how they work. To obtain structural information about them, a resolution at atomic level is necessary. However, the resolution of the far-field optical microscopy is limited by the ABBE limit $\sim \lambda$/NA due to light diffraction. Three-dimensional structures of biomolecules can be resolved by X-ray diffraction (XRD). Limitations of this technique are that the biomolecule of interest has to be crystallizable and only static structures are determinable. An alternative to X-ray crystallography is multi-dimensional nuclear magnetic resonance spectroscopy (NMR), which allows studies in solutions and thus provides dynamic information of biomolecules. Due to a complex data analysis, line broadening and extensive isotopic labeling, NMR is limited to relative small biomolecules (<$30\,\mathrm{kDa}$). In contrast, infrared spectroscopy is a popular technique to study biomolecules' structure and interactions. It offers short recording times, requires less sample material, allows non-perturbative and

label-free extraction of biomolecular information, and can be used under different physicochemical conditions. However, it does not provide atomic resolution.

3.3.1 Vibrations and Rotations

Infrared spectroscopy is a technique measuring the absorption of different infrared frequencies of a sample. Thereby, either the transmission ($T = (I/I_0) \cdot 100\%$) or the extinction/absorption ($E = -\log T$)) of the incident beam light is recorded as a function of the wavenumber ($\tilde{\nu} = 1/\lambda$). The infrared region spans a section of the electromagnetic spectrum from 800 to 10^6 nm, which can be divided into three subareas: near infrared (NIR, 800-2500 nm), mid infrared (MIR, 2.5-50 μm), and far infrared (FIR, 50-10^3 μm).[201]
All atoms in a molecule are in vibration and rotation at temperatures above absolute zero. If the frequency of the infrared radiation is equal to the frequency of a specific vibrational/rotational transition, the molecule absorbs the radiation. Due to the BORN-OPPENHEIMER approximation, the wave function of molecules can be separated into discrete electronic and nuclear (vibration and rotation) components. The fine structure of an infrared absorption spectrum corresponds to vibrational and rotational transitions of a molecule.

Vibrations

Vibrations of molecules can be described in first approximation by harmonic oscillators. In classical physics, they are treated as springs experiencing a restoring force, when displaced from the equilibrium position. The restoring force is described by the HOOK's law:[173]

$$F = -kx, \tag{3.17}$$

where k is the force constant.
The equation for the motion of the harmonic oscillator is then:[173]

$$m\frac{\partial^2 x}{\partial t^2} + kx = 0, \tag{3.18}$$

where m is the mass of the oscillator and gives:[173]

$$x(t) = A\cos(2\pi\nu t + \Phi) \tag{3.19}$$

as the solution. Thereby, ν is the frequency of the oscillator, which depends on k and m:[173]

$$\nu = \frac{1}{2\pi}\sqrt{\frac{k}{m}}. \tag{3.20}$$

The potential energy of the oscillator is given by:[173]

$$V(x) = \frac{1}{2}kx^2. \tag{3.21}$$

From a quantum-mechanical point of view, the SCHRÖDINGNER equation for the harmoic oscillator consisting of two masses is:[173]

$$-\frac{\hbar^2}{2\mu}\frac{\mathrm{d}^2}{\mathrm{d}x^2}\Psi + \frac{1}{2}kx^2\Psi = E\Psi \tag{3.22}$$

with μ as the reduced mass and the energy eigenvalues of the oscillator can be obtained from the time-independent SCHRÖDINGNER equation:[173]

$$E_v = h\nu_0(v + \frac{1}{2}) \tag{3.23}$$

with $v = 0, 1, 2, 3, ...$ and ν_0 is:[173,201]

$$\nu_0 = \frac{1}{2\pi}\sqrt{\frac{k}{\mu}} \quad \text{with} \quad \mu = \frac{m_1 \cdot m_2}{m_1 + m_2}. \tag{3.24}$$

Thus, harmonic oscillators have equidistant energy levels ($\Delta E = h\nu$) and the selection rule for a transition is:[173,201]

$$\Delta v = \pm 1. \tag{3.25}$$

The physical meaning of this selection rule is that the electric dipole moment of the molecule has to change in course of the vibrational motion ($\partial\mu_{\mathrm{el}}/\partial r \neq 0$).[201]

For large values of the vibrational quantum number, v, the vibrations can not longer be described by a harmonic oscillator because repulsive forces between nuclei and the dissociation limit are not considered. However, those properties are described in the MORSE potential:[173,201]

$$V(r) = D_{\mathrm{e}}[1 - \exp(-d(r - r_{\mathrm{e}}))]^2 \tag{3.26}$$

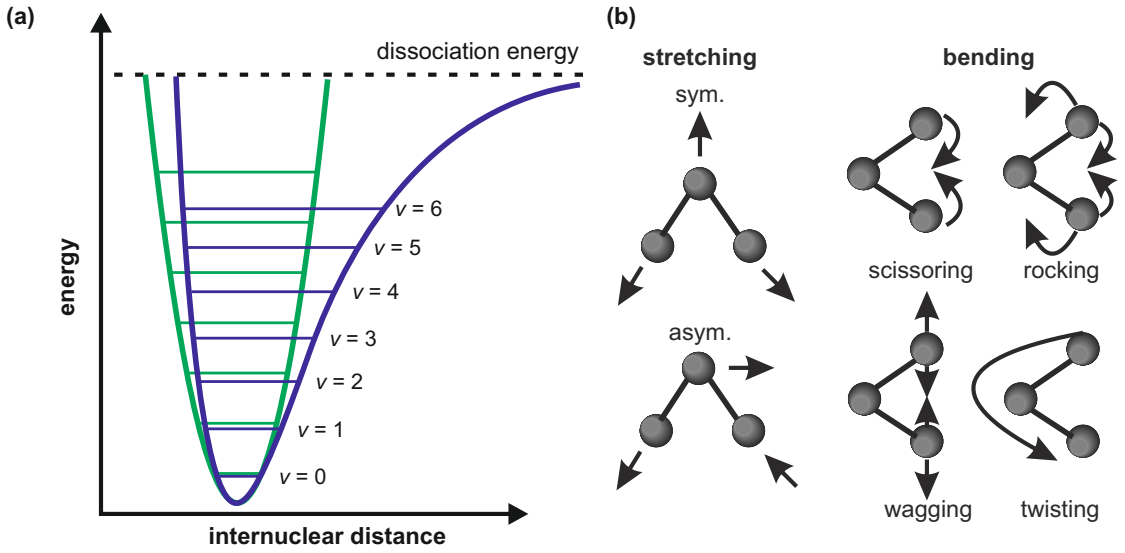

Figure 3.5 | Principle of infrared spectroscopy. a) Potential curve for a harmonic (green) and an anharmonic (blue) oscillator. b) Overview of major vibrational modes for a typical CH_2-group. Stretching causes changes in the inter-atomic distannce along the bond axis. Bending is accompanied by changes in the angle between two bonds.

with D_e as the spectroscopic dissociation energy, d as a molecule-specific constant and r_e as the equilibrium internuclear distance. Compared to the harmonic oscillator, the MORSE potential is steeper than parabolic when the bond length is compressed and less steep when the bond length is expanded (Fig. 3.5a). Additionally, the vibrational energy levels become closer with increasing vibrational quantum number, v:[210]

$$E_v = h\nu_0(v + \frac{1}{2}) - \frac{h^2\nu_0^2}{4D_e}(v + \frac{1}{2})^2. \tag{3.27}$$

Moreover, the selection rule allows the anharmoic oscillator to undergo fundamental vibration ($\Delta v = \pm 1$) as well as overtones ($\Delta v = \pm 2, 3, ...$).[201]

Each atom of a molecule has three degrees of freedom. Considering translation and rotation, a molecule of n atoms has in total $3n - 6$ normal modes for non-linear molecules and $3n - 5$ for linear molecules.[201] Normal modes are independent vibrations of a molecule and can be superposed to describe the most general motion of a molecule. During a normal mode, all atoms of the molecule move sinusoidally with the same frequency and usually also the same phase. Translations and rotations must not occur during a normal mode. The major types of molecular vibrations are stretching and bending (Fig. 3.5b).

Rotation

Vibrational motions are commonly accompanied by rotational motions of the molecule. These motions are described by rigid rotors and exhibit quantized energy levels as well:[210]

$$E_{\text{ges}} = E_{\text{vib}} + E_{\text{rot}} = h\nu(v + \frac{1}{2}) + BJ(J+1) \tag{3.28}$$

with B as the rotation constant and J as the rotational quantum number for a two-atomic molecule. $\Delta J = 0, \pm 1$ is allowed. The combination of vibrational and rotational motions of molecules in solution as well as solute-solvent interactions lead to significant band broadening in the absorption spectrum.

3.3.2 FOURIER-Transform Infrared Spectroscopy

A disperse absorption spectrometer measures how well a sample absorbs light at each wavelength. In principle, a monochromatic light beam is guided through a sample and the intensity of the transmitted light is measured. This is repeated at different wavelength. However, due to the time-consuming recording time and noisy spectra, the technique termed FOURIER-transform infrared spectroscopy (FTIR) has been developed. The advantages of FTIR include simultaneous collection of spectral data in a wide spectral range, higher light intensity (JACQUINOT's advantage), high signal-to-noise ratios (FELLGETT's advantage) as well as higher wavelength accuracy (CONNES' advantage). The core element of a FTIR is the so-called MICHELSON interferometer containing a beam splitter, a stationary and a moving mirror (Fig. 3.6). A light beam from a polychromatic infrared source is guided to the beam splitter, which splits ideally 50% of the light towards the fixed mirror and 50% towards the moving mirror. Due to the moving mirror, the difference in optical path length between the two mirrors can be varied. Light from the two mirrors is reflected back to the beam splitter, where 50% of the original light is recombined. Depending on the difference in the optical length, x, constructive ($x = n\lambda$) and destructive ($x = (n + 1/2)\lambda$) interference may occur. This light beam is directed into the sample chamber. The detector measures the light intensity as a function of the position of the moving mirror, which is known as the interferogram. The polychromatic intereference can be described as:[201,211]

$$I(x) = \int_0^\infty B(\tilde{\nu})(1 + \cos(2\pi\tilde{\nu}x))\mathrm{d}\tilde{\nu} \tag{3.29}$$

with x as the length path of the mirror, $\tilde{\nu} = 1/\lambda$ as the wavenumber and B considers the intensity of the incident light beam as well as the transmission and reflexivity of the beam splitter. The function of the interferogram is:[201]

$$F(x) = I(x) - I(\infty) = \int_0^\infty B(\tilde{\nu}) \cos(2\pi\tilde{\nu}x) \mathrm{d}\tilde{\nu}. \tag{3.30}$$

At zero retardation (zero path difference), there is constructive interference for all wavelength and thus the light intensity is maximal. Using an algorithm called FOURIER transform the time domain in the interferogram (light absorption for each mirror position) is tranformed into the frequency domain in order to obtain the typical absorption spectra. Thus, the spectral intensities, $B(\tilde{\nu})$, is obtained after FOURIER transforming the intergerogram, $F(x)$:[201]

$$B(\tilde{\nu}) = 4 \int_0^\infty F(x) \cos(2\pi\tilde{\nu}x) \mathrm{d}x. \tag{3.31}$$

$B(\tilde{\nu})$ does not correspond to the transmission spectrum of the sample, but rather represents a single beam spectrum. To obtain the transmission or absorption spectrum of a sample, the single beam spectrum of the sample, $B(\tilde{\nu})$, has to be divided by the single beam spectrum of the reference (e.g. background), $B_0(\tilde{\nu})$:[201]

$$A(\tilde{\nu}) = -\log T(\tilde{\nu}) = -\log \frac{B(\tilde{\nu})}{B_0(\tilde{\nu})}. \tag{3.32}$$

Although the integration range for the expression above is from 0 to infinity, that is an infinite range of movement for the moving mirror, the moving range of the mirror is limited in reality. Hence, in practice the integration has to be cut off in a finite range. As each data point of the interferogram contributes to some information about all the data points in the FOURIER transformed spectrum, a finite range of the optical path difference would cause errors in the FOURIER transformed spectra, which are in particular the ringing or the GIBBS phenomenon of the instrumental line shape. Apodization is a mathematical technique used to reduce such ringing effect in a truncated interferogram.[212] The interferogram is multiplied with an apodization function before FOURIER transformation to smooth the transition at the boundaries of the truncated interferogram. Outsite of the finite range, the apodization function is defined to be zero. However, the attenuation of the GIBBS phenomenon is accompanied by a reduced resolution of the actual spectrum (lower and broader peaks).

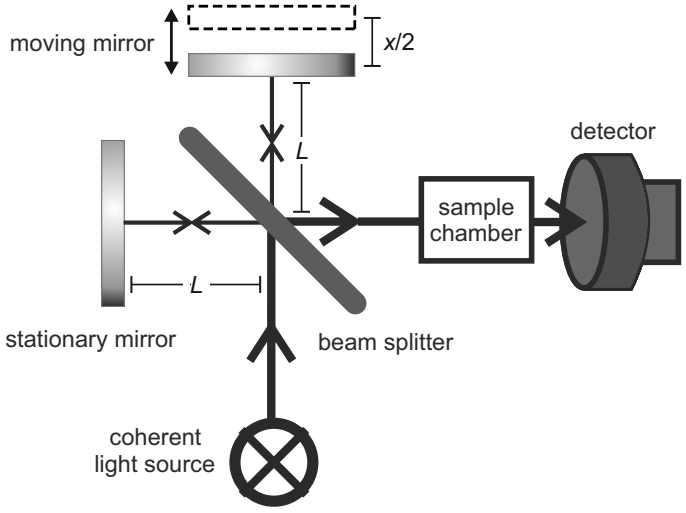

Figure 3.6 | Schematic setup of a FTIR spectrometer. The main component of a FTIR spectrometer is the MICHELSON interferometer consisting of a stationary and a moving mirror.

The HAPP-GENZEL apodization function, $D_{\mathrm{HG}}(x)$, is often used in FTIR data processing to give a good balance betwen resolution and ringing size:[212]

$$D_{\mathrm{HG}}(x) = \begin{cases} 0.54 + 0.46\cos\left(\frac{\pi x}{x_{\max}}\right) & \text{for} |x| \leq x_{\max} \\ 0 & \text{for } |x| > x_{\max}. \end{cases} \tag{3.33}$$

3.3.3 Biomolecular Applications

Nuleic Acids

The spectral range relevant for nucleic acids (DNA and RNA) in aqueous solution is 1800-800 cm^{-1} and can be divided into four sections. The 1800-1500 cm^{-1} region is assigned to nucleobase vibrations, in particular from in-plane double bond stretch vibrations (C=C, C=N, C=O). Hence, such bands are sensitive to base pairing and stacking and can be used to monitor structural changes of nucleic acids. Usually, base pairing causes a blue shift and intensity decrease of such bands.[213] The 1500-1250 cm^{-1} region corresponds to base-sugar vibrations and thus is sensitive to glycosidic bond rotation, backbone conformation and sugar puckering mode.[213] The 1250-1000 cm^{-1} region originates from sugar-phosphate vibrations and can be used to distinguish between different nucleic acid backbone conformations in the helical state (A-, B-, Z-form).[213] The 1000-800 cm^{-1} region is due to sugar vibrations and thus a marker for the sugar conformation (C2'- or C3'-*endo*).[213] Hence, FTIR is a powerful

method to study the structure and interaction of nucleic acids.

Proteins

FTIR is also commonly applied for the examination of protein secondary structures and dynamics in aqueous solution. The IR spectrum of a polypeptide can be interpreted in terms of vibrations of the protein backbone, which can be seen as structural repeat units. In total, nine IR absorption bands are well characterized for proteins, namely amide A, B and I-VII (Tab. 3.1). The most prominent bands are the amide I and II bands corresponding to C=O

Table 3.1 | Characteristic infrared bands of protein repeat units measured in D_2O.[214].

designation	wavenumbers (cm^{-1})	description
amide A	3300	N-H stretching
amide B	3100	N-H stretching
amide I	1690-1600	C=O stretching
amide II	1575-1480	C-N stretching, N-H bending
amide III	1301-1129	C-N stretching, N-H bending
amide IV	767-625	O=C-N bending
amide V	800-640	out-of-plane N-H bending
amide VI	606-537	out-of-plane C=O bending
amide VII	200	skeletal torsion

stretching, C-N stretching and N-H bending of the protein backbone. In particular, the amide I band, which arises mainly from the C=O stretching (70-85 %), the C-C-N deformation and the N-H in-plane bending, is most sensitive to protein secondary structures and is hardly affected by the side chains.[201] The amide I band is a superposition of subbands caused by the different secondary structural elements of a protein (Tab. 3.2).[215] Secondary structures such as α-helices and β-sheets form hydrogen bonds via C=O and N-H of the polypeptide backbone and thus generate coupled oscillators in the polypeptide backbone. Therefore, amide I band assignment is commonly used to study the secondary structure content of a protein as a function of different physico-chemical factors.

As the amide I band is usually broad and featureless due to the overlap of the subbands, it hampers a direct evaluation of the secondary structures. However, band narrowing and curve-fitting are two well established mathematical approaches to calculate the secondary structure content of a protein in FTIR spectroscopy.[215]

Table 3.2 | Correlation between the amide I band wavenumbers and the secondary structure elements of proteins in D_2O buffer.[201]

wavenumbers (cm^{-1})	assignment
1690-1660	β-turn
1680-1670	β-sheet
1658-1650	α-helix
1650-1640	random coil
1640-1620	β-sheet

There are two common ways to narrow infrared bands. In the first one, band narrowing is achieved by calculating the second-derivative of the area-normalized amide I band:[216]

$$\frac{\mathrm{d}^2 A(\tilde{\nu})}{\mathrm{d}\tilde{\nu}^2} = -\int (2\pi x)^2 F(x) \cos(2\pi\tilde{\nu}x)\mathrm{d}x. \tag{3.34}$$

Hence, $(2\pi x)^2$ results as a weighting function and reduces the line width of the second-derivative of a band. Thereby, the minima in the second-derivative spectrum can be assigned to distinct secondary structure elements.

The second method to reduce bandwidth is called FOURIER self-deconvolution (FSD).[216,217] To enhance the intensity of the individual subbands, the data are manipulated in the FOURIER domain. The inferograms can be seen as damped cosine trains, whereby the degree of damping increases with increasing bandwidth. The key concept of FSD is to reduce the degree of damping. To this end, the vibrational bands are treated as LORENTZ functions:[216,218]

$$A(\tilde{\nu}) = A_0 \frac{\gamma^2}{(\tilde{\nu} - \tilde{\nu}_0)^2 + \gamma^2} \tag{3.35}$$

with A_0 as the maximal absorption of the band, $\tilde{\nu}_0$ as the corresponding wavenumber and γ as the half-width at half-height (HWHH). By inserting Eq. 3.35 into Eq. 3.30, one obtains:[216,218]

$$F(x) = 0.5 A_0 \gamma \cos\left(2\pi\tilde{\nu}_0 x\right) \exp\left(-2\pi x\gamma\right). \tag{3.36}$$

Hence, the exponential decay is determined by γ. In a second step, Eq. 3.35 is multiplied with a rising exponential function:[216,218]

$$F'(x) = F(x) \cdot \exp\left(2\pi\gamma' x\right) = 0.5 A_0 \gamma \cos\left(2\pi\tilde{\nu}_0 x\right) \exp\left[-2\pi\left(\gamma - \gamma'\right) x\right]. \tag{3.37}$$

Further, $F'(x)$ is multiplied with an apodization function. After FOURIER transformation of $F'(x)$ to $A'(\tilde{\nu})$, the HWHH is reduced to $(\gamma - \gamma')$. Thereby, the resolution enhancement factor, K, is defined as:[216]

$$K = \gamma/\gamma'. \tag{3.38}$$

As FSD also enhances the noise in a spectrum, the K value is limited in practice to approximately $K < \log(\text{S/N})$.[216] The maxima in a FSD spectrum correspond to the positions of the subbands. Usually, second-derivative and FSD are performed simultaneously to verify the number and position of the subbands.

To quantify the content of secondary structure elements, curve-fitting can be performed. Thereby, the subbands can be treated as GAUSSIAN, LORENTZ or VOIGT functions with initial parameters obtained from the second derivative and FSD, and are subsequently linear combined to be fitted to the area-normalized absorbance spectrum.[215]

3.4 Light Scattering

Scattering techniques are powerful tools to investigate molecular structures and organisations within colloidal systems. They can provide quantitative information on size, shape and strucure of biomolecules in solution by studying their interactions with incident radiation (from e.g. light, X-ray or neutrons).[201] Depending on whether energy is transferred, scattering can be distinguished between elastic (e.g. RAYLEIGH scattering), quasielastic and inelastic (e.g. RAMAN scattering).

One of the most prominent elastic scattering types is the RAYLEIGH scattering. It describes the interaction between electromagnetic radiation and particles, whose size is much smaller than the wavelength of the incident radiation. The scattered electromagnetic waves originate from the electronic polarizability of the particles (i.e. bound electrons) and their scattered intensity, I_s, is proportional to the square of the electric field, E:[201]

$$\frac{I_\mathrm{s}}{I_\mathrm{i}} = \frac{N}{V}\frac{\pi^2\alpha^2}{\epsilon_0^2 r^2 \lambda^4}\frac{1+\cos^2 2\theta}{2} \tag{3.39}$$

with I_i as the intensity and λ as the wavelength of the incident beam. Further, α is the electronic polarizability of the molecule, N/V the particle number density, r the sample-to-detector distance, and 2θ the scattering angle. Considering the CLAUSIUS-MOSOTTI

equation, the polarizability, α, can be converted into the refractive index of the solution, n:[201]

$$\frac{N}{V}\left(\alpha - \alpha_{\text{solvent}}\right) = \epsilon_0 \left(n^2 - n^2_{\text{solvent}}\right). \tag{3.40}$$

Hence, the intensity of RAYLEIGH scattering decays with the 4th power of the incident wavelength and is a function of the particle's refractive index.

3.4.1 Turbidimetry

The scattering effect of macromolecules suspended in aqueous solutions causes an intensity attenuation of the transmitted light. The turbidity can be described as follows:[201]

$$I = I_{\text{i}} \exp(-\tau_{\text{s}} d), \tag{3.41}$$

where I_{i} is the intensity of the incident light beam and d the path length of the light beam in the supsension. τ_{s} is the turbidity coefficient and correlates with the RAYLEIGH ratio, $R_0 = \pi^2\alpha^2/2\epsilon_0^2\lambda^4$:[201]

$$\tau_{\text{s}} = \frac{16\pi}{3} R_0. \tag{3.42}$$

Thus, the shorter the wavelength of the incident light beam is, the more pronounced the turbidity is. The intensity of scattered light depends also on the concentration and size of the particles. Hence, turbidimetry is suited to monitor, for example, the formation of large particles such as microtubules.

3.4.2 Dynamic Light Scattering

Dynamic light scattering (DLS) is a scattering technique for measuring temporal fluctuations of scattered light in suspensions of particles. Thereby, DLS provides information about the dynamics of the suspended particles (translation, rotation, intramolecular motions) through their BROWNIAN motion and relates those to their size.[201]

A monochromatic and coherent light source like a laser is commonly used for DLS measurements. The light passes through a polarizer and illuminates the sample cell and the scattered light passes through a second polarizer and is collected at an 173° scattering angle (2θ, back angle) by a photomultiplier.

When light hits the suspended particles ($\lambda >> d$), the light will be elastically scattered in all directions (RAYLEIGH scattering). Thereby, the incident beam interacts with the electric field of the particle and induces an oscillating dipole in the electron cloud. As a consequence, secondary electromagnetic waves as scattered light will be emitted. The scattered light caused by the different scatterers can interfere constructively and destructively depending on the angle. As the molecules and thus the scatterers undergo BROWNIAN motion, the distances between the scatterers vary and the interference pattern changes with time. As a consequnce, the number of photons detected at 2θ also fluctuates with time. To extract information about the diffusional properties of the sample, intensity auto-correlation functions of the measured photon counts are computed. Thereby, the scattered intensity at time point t is compared to that at time point $t + \tau$, with τ as the correlation time:[201,219]

$$C(\tau) = \frac{1}{n}\sum_{i=1}^{n} I_{\mathrm{s}}(t_i) \cdot I_{\mathrm{s}}(t_i + \tau), \tag{3.43}$$

whereby n is the number of sequential scattering signals.

For $\tau = 0$, the intensity auto-correlation functions corresponds to the mean square intensity of the scattered light, $< I_{\mathrm{s}}^2 >$, which is the maximum value of $C(\tau)$. The intensity fluctuations lose their correlations (or similarities) for increasing τ-values and thus $C(\tau)$ corresponds to the square of the averaged intensity, $< I_{\mathrm{s}} >^2$. For non-periodical fluctuations, $C(\tau)$ decays exponentially from $< I_{\mathrm{s}}^2 >$ to $< I_{\mathrm{s}} >^2$. The normalized auto-correlation function is:[201,219]

$$g_2(\tau) = \frac{C(\tau)}{< I_{\mathrm{s}} >^2}. \tag{3.44}$$

To convert the intensity auto-correlation function to the field-correlation function for the electric field amplitude of the scattered light, the SIEGERT relationship holds:[201,219]

$$g_2(\tau) = 1 + A|g_1(\tau)|^2, \tag{3.45}$$

where A is a constant. For small magnitudes of the momentum transfer, q, and monodisperse systems, the field auto-correlation function can be described by a single exponential function:[201,219]

$$g_1(\tau) = \exp(-Dq^2\tau), \tag{3.46}$$

whereby D is the translational diffusion coefficient and $q = n(4\pi/\lambda)\sin\theta$ is the momentum transfer.

The STOKES-EINSTEIN equation describes the relationship between the diffusion and the hydrodynamic radius, R_h, of spherically symmetric particles:[201,219]

$$D = \frac{k_\mathrm{B}T}{6\pi\eta R_\mathrm{h}} \tag{3.47}$$

with k_B as the BOLTZMANN constant and η as the viscosity of the solvent.

In the case of polydisperse systems, the field auto-correlation functions needs to be described by multiple and weighted exponential functions, which overlap:[219]

$$g_1(\tau) = \sum_{i=0}^{n} \gamma_i \exp(-D_i q_i^2 \tau), \tag{3.48}$$

whereby n is the number of differently sized particles.

One method to determine the width of the size distribution is the cumulant analysis:[219]

$$\ln g_1(\tau) = -K_1\tau + \frac{1}{2!}K_2\tau^2 - \frac{1}{3!}K_3\tau^3 + ..., \tag{3.49}$$

whereby K_1 corresponds to the mean diffusion coefficient, $< D >= K_1/q^2$, and K_2 provides information about the polydispersity. The index of polydispersity is defined by PDI $= K_2/K_1$. For PDI $= 0$, the suspension is monodisperse. The cumulant analysis is suitable for samples with a PDI < 0.3. Otherwise, multiple exponential fits such as non-negative least squares (NNLS) or CONTIN need to be performed.[219]

3.4.3 Small-Angle X-Ray Scattering

Small-angle X-ray scattering (SAXS) is a non-invasive technique allowing the investigation of structure in the range of 1 to 100 nm by measuring scattering intensity at small scattering angles 2θ. Compared to X-ray diffraction of crystalline materials, SAXS of dissolved and disordered materials provides only structural information averaged over the entire scattering volume and a large number of scattering units. As SAXS and transmission electron microscopy (TEM) cover the same dimensional range, they are referred to as complementary techniques. TEM allows direct, local and detailed imaging in real space, whereas SAXS

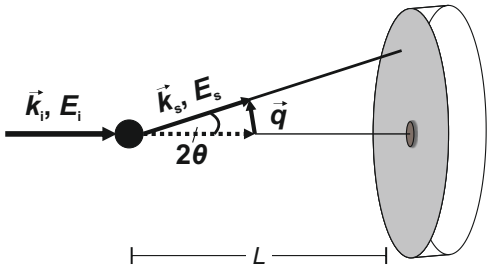

Figure 3.7 | Schematic setup of a SAXS experiment. An incident X-ray beam with wave vector $\vec{k}_\mathrm{i}$ and energy E_i is scattered by the sample. This causes emission of secondary electromagnetic waves ($\vec{k}_\mathrm{s}$, E_s) at a scattering angle 2θ. The scattered intensity is detected at a distance L from the sample.

enables *in situ* studies and yields global parameters as well as their distributions in the reciprocal space.

3.4.3.1 THOMSON Scattering

In SAXS, X-rays are elastically scattered by the electrons of an object. When a collimated and monochromatic X-ray beam hits an object, its electrons will oscillate at the same frequency and emit secondary electromagnetic waves with the same wavelength as that of the incident wave. Such coherent and spherical waves interfere with each other and the resulting scattering intensity is detected as a function of the scattering angle 2θ at a distance L from the sample (Fig. 3.7).[220] Thereby, the kinematic approximation is presumed. That means that the interactions between the incident wave and the electrons are of very weak magnitude. The incident beam crosses the sample with a nearly unchanged incident intensity, the proportion of scattered intensity is very small compared to the incident intensity, and the excitation of electrons to other energy levels as well as multiple scattering are unlikely.[201] Hence, a beamstop in front of the detector is neccessary to absorb the transmitted primary beam. Moreover, the entire flight path of the X-ray beam before and after the sample needs to be evacuated to prevent absorption or scattering by air.

Owing to the elastic scattering behavior, the magnitude of the incident ($|\vec{k}_\mathrm{i}|$) and scattered ($|\vec{k}_\mathrm{s}|$) wave vectors are equal:[201]

$$|\vec{k}_\mathrm{i}| = |\vec{k}_\mathrm{s}| = \frac{2\pi}{\lambda}. \tag{3.50}$$

Hence, the magnitude of the momentum transfer, q, is given by:[201]

$$q = |\vec{q}| = 2|\vec{k_{\mathrm{i}}}| \sin\theta = \frac{4\pi}{\lambda} \sin\theta. \tag{3.51}$$

A relationship between the q-range and the dimension of the real space, D, is given by:

$$q = \frac{2\pi}{D}. \tag{3.52}$$

Hence, the typical q-range covered by Synchrotron SAXS ($0.006 < q < 6$ nm^{-1}) corresponds to 1 μm to 1 nm in the real space dimension.[220]

The scattered intensity of a free electron (THOMSON scattering) is described as:[220]

$$I_e = I_{\mathrm{i}} r_e^2 \frac{1 + cos^2\theta}{2}, \tag{3.53}$$

where r_e is the THOMSON scattering length, also known as the classic electron radius.

Owing to the high intensity of the incident X-ray beam, all electrons of an atom are excited to oscillate. As SAXS cannot resolve atomic details, the scattering amplitude of an atom can be described by its electron density, $\rho(\vec{r})$:[201]

$$A(\vec{q}) = \int \rho(\vec{r}) \exp(i\vec{q}\vec{r}) \mathrm{d}\vec{r}. \tag{3.54}$$

The scattered intensity depends on the solid angle, $\Delta\Omega$, that the detector covers, and the size of the incident beam intensity that hits the sample. Therefore, a normalized scattered intensity or the so-called differential scattering cross-section, $\mathrm{d}\sigma/\mathrm{d}\Omega$ is used to describe the interaction between the incident beam and the scattering behavior of the sample:[201]

$$\frac{\mathrm{d}\sigma}{\mathrm{d}\Omega} = \frac{I_{\mathrm{s}}/\Delta\Omega}{I_{\mathrm{i}}/A_0}, \tag{3.55}$$

where A_0 is the cross-section of the incident beam. Hence, the measured scattering intensity is given as the mean square of the scattering amplitude averaged over all orientations of the scattering object:[201]

$$I(q) = \frac{\mathrm{d}\sigma}{\mathrm{d}\Omega} = \langle |A(\vec{q})|^2 \rangle = \left\langle \left| \int \rho(\vec{r}) \exp(i\vec{q}\vec{r}) \mathrm{d}\vec{r} \right|^2 \right\rangle. \tag{3.56}$$

3.4.3.2 Macromolecules in dilute solutions

Macromolecules in infinitely diluted solutions can be treated as isolated and non-interacting particles. The distance between macromolecules is much larger than the distance between atoms within a macromolecule. Further, the electron density of biomolecules can be considered as homogeneously distributed and thus is independent of the electron location within the macromolecule. As the macromolecules are embedded in a solvent, the term contrast, K, needs to be introduced:[201]

$$K = V_{\mathrm{m}} \left(\rho_{\mathrm{m}} - \rho_0\right), \tag{3.57}$$

where V_{m} is the volume of the macromolecule. ρ_{m} and ρ_0 are the electron densities of the macromolecule and the solvent, respectively.
The scattering intensity of N_{m} independent macromolecules in a solution is equal to:[201]

$$I(q) = N_{\mathrm{m}} \left(\rho_{\mathrm{m}} - \rho_0\right)^2 \left\langle \left| \int \exp(i\vec{q}\vec{r}) \mathrm{d}\vec{r} \right|^2 \right\rangle. \tag{3.58}$$

Considering the definition of the form factor of the macromolecule, $F(\vec{q})$:[201]

$$F(\vec{q}) = \frac{1}{V_{\mathrm{m}}} \int \exp(i\vec{q}\vec{r}) \mathrm{d}\vec{r}, \tag{3.59}$$

the measured intensity as a function of q can be simplified to:[201]

$$I(q) = N_{\mathrm{m}} K^2 \langle |F(\vec{q})|^2 \rangle = N_{\mathrm{m}} K^2 \langle P(\vec{q}) \rangle = N_{\mathrm{m}} K^2 P(q) \tag{3.60}$$

with $P(q)$ as the intra-particle structure factor. Hence, the scattering intensity only depends on the geometry of the macromolecule. Analytical and numeric solutions for different form factors (or intra-particle structure factors) are listed in the literature.[221]

3.4.3.3 Data evaluation

The radial pair-distance distribution function

The form factor, $F(\vec{q})$, is the FOURIER transform of the electron density, $\rho(\vec{r})$. Hence, the distance distribution between two scattering centers within a macromolecule can be calculated from the measured scattering intensity. In this context, the characteristic function of

the electron density, $\gamma(\vec{r})$, is introduced:[222]

$$\gamma(\vec{r}) = \int \rho(\vec{r'})\rho(\vec{r'} + \vec{r})\mathrm{d}\vec{r'}. \tag{3.61}$$

Thus, the characteristic function can be referred to the intra-particle structure factor:

$$P(\vec{q}) = \int \gamma(\vec{r}) \exp(i\vec{q}\vec{r})\mathrm{d}\vec{r}. \tag{3.62}$$

Spherical averaging over all orientations gives:[222]

$$P(q) = 4\pi \int_0^\infty \gamma(r) r^2 \frac{\sin qr}{qr}\mathrm{d}r = 4\pi \int_0^\infty p(r) \frac{\sin qr}{qr}\mathrm{d}r. \tag{3.63}$$

Thereby, $p(r)$ is the pair-distance distribution function. By inverse FOURIER transformation, $p(r)$ can be obtained from the measured scattering intensity:[201]

$$p(r) = \frac{r^2}{(2\pi)^3} \int_0^\infty I(q) \frac{\sin qr}{qr} 4\pi q^2 \mathrm{d}q. \tag{3.64}$$

For macromolecules with a homogeneous electron density, $p(r)$ describes the distribution of the paired-set of distances between all of the electrons within the macromolecule. Thus, $p(r)$ provides a visual access to the shape and the maximum dimension of a macromolecule. In addition, the radius of gyration, R_G, of the macromolecule, which is the root mean square distance between all scattering centers within the macromolecule and its gravity, can be calculated from $p(r)$:[201]

$$R_\mathrm{G}^2 = \frac{1}{V_\mathrm{m}} \int r^2 \mathrm{d}\vec{r} = \frac{\int r^2 p(r)\mathrm{d}r}{2\int p(r)\mathrm{d}r}. \tag{3.65}$$

GUINIER approximation

Alternatively, R_G can also be obtained from the so-called GUINIER approximation, which is only valid for the section of $I(q)$ at small angles ($qR_\mathrm{G} < 1.3$)[223] and relies on the assumption of a monodisperse and infinitely diluted solution:[201]

$$I(q) = I(0)\left[1 - \frac{1}{3}q^2 R_\mathrm{G}^2\right] \approx I(0)\exp(-q^2 R_\mathrm{G}^2/3). \tag{3.66}$$

Hence, plotting $\ln I(q)$ against q^2 gives the GUINIER plot with a linear course featuring the

slope $-R_G^2/3$. Any derivation from a linear course indicates the presence of aggregates, interacting macromolecules and polydispersity.

KRATKY plot and the compactness

To obtain information about the compactness or the degree of disorder in a macromolecule, the scattering data can be presented in a so-called KRATKY plot, i.e. $I(q) \cdot q^2$ versus q.[201] As a globular structure has a GAUSSIAN-like shape at small q and follows the POROD's law ($I(q) \propto q^{-4}$) at high q, it shows a bell-shaped curve in the KRATKY plot. For an expanded structure, $I(q)$ decays approximately as q^{-2}. In contrast, $I(q)$ becomes proportional to q^{-1} for GAUSSIAN chains. Their KRATKY plot exhibits an inital increase, which is followed by a plateau in the central q-range and a final linear increase at high q. Hence, such dinstict shapes of the curve in the KRATKY plot can give hints on the conformation of a macromolecule.

3.4.3.4 Polydispersity

Sample polydispersity causes smearing of sharp structures of the intra-particle structure factor, $P(q,r)$, such as minima. To consider polydisperse systems, $P(q,r)$ can be multiplied by a distribution function, $D(r)$:[220]

$$I(q) \propto \int_0^\infty D(r) \cdot P(q,r) \mathrm{d}r. \tag{3.67}$$

3.4.3.5 Partially ordered systems

Near and far orders of biomolecules and their assemblies lead to characteristic reflections in the scattering profile. Such peaks originate from BRAGG diffraction, i.e. constructive interference of waves, which are scattered from lattice planes separated by an interplanar distance, d:[201]

$$2d \sin\theta = n\lambda. \tag{3.68}$$

Combining Eq. 3.51 with the BRAGG equation (Eq. 3.68) yields:[201]

$$q_n = \frac{4\pi}{\lambda} \sin\theta_n = n\frac{2\pi}{d_{\mathrm{lam}}}. \tag{3.69}$$

This enables the calculation of the lattice constant, d_{lam}, of a lamellar and one-dimensional lattice. For a hexagonal lattice, the lattice constant, d_{hex}, can be obtained by:[201]

$$q_{h,k} = \frac{4\pi}{\sqrt{3}d_{\text{hex}}}\sqrt{h^2 + k^2 + hk}, \tag{3.70}$$

where h and k are the MILLER indices.

3.5 Vapor Pressure Osmometry

Osmosis describes the effort of a solvent to move across a semipermeable membrane (permeable to the solvent, but not to the solute molecules) to equalize the solute concentrations on the two sides of the membrane. Thereby, the osmotic pressure, Π, is defined as the equilibrium pressure required so that there is no net movement of solvent across the membrane.[173,201] Assuming a system consisting of pure solvent on the left side and solutes dissolved in the solvent on the right side, the chemical potential of the solvent at both sides has to be equal in case of equilibrium:[173]

$$\begin{aligned} \mu_{\text{solvent}}(p) &= \mu_{\text{solvent}}(x_{\text{solvent}}, p + \Pi) \quad \text{with} \\ \mu_{\text{solvent}}(x_{\text{solvent}}, p + \Pi) &= \mu_{\text{solvent}}(p) + \int_p^{p+\Pi} V_{\text{m}}\text{d}p + RT \ln x_{\text{solvent}} \\ -RT \ln x_{\text{solvent}} &= \Pi\, V_{\text{m}}, \end{aligned} \tag{3.71}$$

where x_{solvent} is the mole fraction of the solvent, and V_{m} is the molar volume of the solvent. Assuming a dilute solution,[173]

$$\begin{aligned} \ln(1 - x_{\text{solute}}) &\approx -x_{\text{solute}} \\ x_{\text{solute}} &\approx n_{\text{solute}}/n_{\text{solvent}}, \end{aligned} \tag{3.72}$$

the osmotic pressure of a dilute solution, Π, is given by:[173]

$$\Pi = RTc_{\text{solute}}, \tag{3.73}$$

also known as the VAN'T HOFF equation. Π depends on the molar concentration of the solute, c_{solute}, but not on its identity, and thus is a colligative property. However, due to

the size as well as interactions between solvent and solute, solutions of macromolecules behave non-ideally. Therefore, a second virial coefficient, B, is introduced to describe the non-ideality:[173,201]

$$\Pi = RT\left(c_{\text{solute}} + Bc_{\text{solute}}^2\right). \tag{3.74}$$

Notably, B is used as a measure to distinguish between poor and good solvents ($B < 0$ poor solvent, $B > 0$ good solvent).[148,201] Further, by knowing the osmotic pressure/osmotic strength of a solution, information about the total molality of osmotically active solutes in a solution (osmolality, mol per kg solvent), the water activity of a solution, and the molecular weight of unknown compounds may be obtained.

To measure the osmotic strength of a solution, several techniques including membrane osmometry, vapor pressure osmometry, and freezing point osmometry are known. The membrane osmometer determines the osmotic pressure of a solution by separating it from pure solvent by a semipermeable membrane. A freezing point osmometer utilizes the phenomenon of freezing point depression induced by the osmotically active solutes. In case of vapor pressure osmometers, the reduced vapor pressure of a solution caused by the osmotically active solutes is measured. According to RAOULT's law, the vapor pressure of a solution is given by:[173]

$$p = x_{\text{solvent}} \cdot p^0_{\text{solvent}} = (1 - x_{\text{solute}}) \cdot p^0_{\text{solvent}}, \tag{3.75}$$

where p^0_{solvent} is the vapor pressure of the pure solvent.

Hence, the degree of vapor pressure reduction, $\Delta p = p - p^0_{\text{solvent}}$ depends only on the mole fraction of the solute:[173]

$$\Delta p = -x_{\text{solute}} \cdot p^0_{\text{solvent}}. \tag{3.76}$$

Nowadays, a thermocouple hygrometer is the key component of modern vapor pressure osmometers. The reduction of the dew point instead of the vapor pressure is measured and correlated with the osmolality of the solution. The dew point is defined as the temperature at which the air is saturated with water vapor and the relative humidity is 100%. Any cooling would lead to condensation of the water vapor. The advantage of this technique is that the physical state of the specimen needs not to be changed. The mode of operation of a hygrometer-based vapor pressure osmometer is sketched in the following.

10 μL of the sample solution is pipetted onto a paper disc and introducted into a sealed sam-

ple chamber. First, the temperature and vapor pressure of the sample are equilibrated in the chamber and a reference temperature (T_{A}) is established for the measurement. In a next step, the chamber is cooled to a temperature below the dew point and water condenses from the air in the chamber onto the surface of the thermocouple. Subsequently, the temperature is gradually increased again until water stops to condense (dew point) and the temperature of the thermocouple stabilizes (T_{D}).[224] The relationship between the vapor pressure depression and dew point depression is given by:[224]

$$\begin{aligned} \Delta T &= \Delta p / \left(\mathrm{d}p/\mathrm{d}T\right)_{T_{\mathrm{A}}} \quad \text{with} \\ \Delta T &= T_{\mathrm{A}} - T_{\mathrm{D}} \\ \Delta p &= p^0_{\text{solvent}} - p \\ \left(\mathrm{d}p/\mathrm{d}T\right)_{T_{\mathrm{A}}} &= \frac{\Delta H}{R} \frac{p^0_{\text{solvent}}}{T^2}, \end{aligned} \tag{3.77}$$

where p^0_{solvent} is the saturation vapor pressure and p is the chamber vapor pressure. $\left(\mathrm{d}p/\mathrm{d}T\right)_T$ describes the slope of the vapor pressure-temperature function at the chamber temperature, T_{A}. Due to the linearity of RAOULT's law, standards are used to calibrate the instrument and to convert the voltage-based signal for ΔT into osmolality with mmol kg^{-1} as unit.

CHAPTER 4

PRESSURE SENSITIVITY OF THE CYTOSKELETAL ACTIN AND ITS STRATEGIES FOR PRESSURE RESISTANCE*

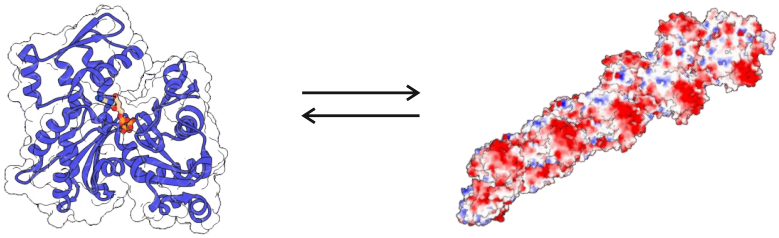

Abstract

The cytoskeleton is an essential platform for the structure, dynamics and function of prokaryotic and eukaryotic cells. *In vivo* experiments revealed that, compared to other cellular components, the temperature and pressure stability of the cytoskeleton is extremely limited. Actin is a highly conserved and the most abundant protein in eukaryotes. Its polymerization reaction is essential to provide driving force for cellular motility and mechanical resistance for cell shape. In this chapter, polymerization and further bundling of actin are studied. The results illustrate the importance of actin-binding proteins and the effect of macromoleculuar crowding for maintaining the stability and dynamics of the cytoskeleton in a pressurized world.

The protein images were prepared and modified with UCSF Chimera v1.11.2[225] using pdb:1NWK and pdb:3G37.

* The work herein described has been published in the following peer-reviewed research articles and subsequently reprinted in parts with the permission of the journals. Contributions of co-authors are either dinstinctly marked or not shown as results of this thesis.

1. M. Gao, M. Berghaus, J. von der Ecken, S. Raunser, and R. Winter. Condensation Agents Determine the Temperature-Pressure Stability of F-actin Bundles. *Angew. Chem. Int. Ed.* **54** (2015) 11088-11092

   was published online on August 5th, 2015 and the DOI is 10.1002/anie.201504247. In this chapter, the publication is partially reproduced in sections 4.3 and 4.4.2 with the permission by John Wiley & Sons, Inc. Copyright ©2015 Wiley-VCH Verlag GmbH & Co. KGaA, Weinheim. The used text paragraphs and figures were reformatted to the format of the thesis (e.g. text font, reference numbering, figure numbering). Some phrases in active voice were changed to those in passive voice. In addition, the supplementary figures were moved to the main text and splitted to improve the quality of reading.

   Author contribution: R.W. designed the research, M.G., M.B. and J.v.d.E. performed research, M.G., M.B. and J.v.d.E. analyzed data, S.R. contributed analytic tools, M.G., M.B. and R.W. interpretated the results and wrote the paper with refinement by all coauthors.

2. M. Gao, and R. Winter. Kinetic Insights into the Elongation Reaction of Actin Filaments as a Function of Temperature, Pressure, and Macromolecular Crowding. *ChemPhysChem* **16** (2015) 3681-3686

   was published online on November 13th, 2015 and the DOI is 10.1002/cphc.201500633. In this chapter, the publication is reproduced in sections 4.3 and 4.4.1 with the permission by John Wiley & Sons, Inc. Copyright ©2015 Wiley-VCH Verlag GmbH & Co. KGaA, Weinheim. The used text paragraphs and figures were reformatted to the format of the thesis (e.g. text font, reference numbering, figure numbering). Some phrases in active voice were changed to those in passive voice. In addition, the supplementary figures and tables were moved to the main text and splitted to improve the quality of reading.

   Author contribution: M.G. and R.W. designed the research, M.G. performed research and analyzed data, M.G. and R.W. interpretated the findings and wrote the paper.

4.1 Introduction

A dynamic and protein-composed cytoskeleton is essential to establish cell shape, to provide mechanical strength as well as to realize biological movements. It consists of three main kinds of filaments, which are microfilaments, intermediate filaments and microtubules (Fig. 4.1a).[226] Microfilaments are the thinnest filaments within cells and were described for the first time in 1942.[227] Globular actin (G-actin) is the monomeric building block of the microfilaments. Hence, it is the most abundant protein in eukaryotic cells and is also highly evolutionarily conserved.[228] It belongs to the protein class of ATPases and supports cells with a diversity of fundamental cellular processes such as cytokinesis, phagocytosis, cell adhesion and intracellular transports.[229,230] Spontaneous self-assembly of G-actin leads to the formation of filamentous actin (F-actin) with a double-stranded and helical arrangement of subunits and owing a diameter of 7 nm. The polymerization depends on the concentration of divalent cations, ATP, actin nucleation factors and G-actin.[229,231–235] *In vivo*, more than hundred cytoplasmic actin-binding proteins act in concert to tightly regulate the formation of actin filaments considering concentration, length distribution, location and rate of turnover.[236,237]

The 42 kDa G-actin consists of 375 amino acid residues, which fold into two domains each subdivided further into two subdomains (Fig. 4.1b). Two binding sites are formed between those two domains. One is responsible for binding of adenosine diphosphate (ADP) or adenosine triphosphate (ATP) and divalent cations, whereas the other mediates contacts between actin and actin-binding proteins (ABPs).[238] G-actin is not an effective ATPase and is most able to polymerize in the ATP-bound state.[239] During polymerization, the G-to-F-transition is accompanied by large conformational changes within the monomer that resembles a flattening of the monomer (Fig. 4.1c).[240,241] The polymerization of G-actin occurs in kinetically discriminable steps. The spontaneous *de novo* polymerization is kinetically unfavorable due to the thermodynamic instability of actin dimers/trimers during nucleation, which is followed by a fast elongation phase, in which more actin monomers associate to both ends of the filament than dissociate.[228] In cells, several protein-based nucleators exist to accelerate actin assembly by uncapping of pre-existing filaments, severing of filaments, or bypassing the *de novo* nucleation.[236,242] At steady state, when the concentration of G-actin is in equilibrium with F-actin (denoted as critical concentration), no further net extension

of the actin filaments is observable.[228,243] As all actin monomers in a filament point in the same direction, F-actin is a polar structure with a fast-growing barbed and a slow-growing pointed end (Fig. 4.1b).[228] Those ends exhibit different association/dissociation rates and thus different critical concentrations, leading to a non-equilibrium behavior termed treadmilling, which is described by dissociation of ADP-actin from the pointed end, ADP-ATP exchange in G-actin and association of ATP-G-actin at the barbed end, resulting in a directed movement of the filament (Fig. 4.1d).[244,245] Upon polymerization, ATP hydrolyzes within the F-actin with a half time of 2 s, whereas the γ-phosphate dissociates slowly with a half time of 360 s.[229] In the ADP-bound state, actin is highly unstable and dissociates from the pointed end more rapidly than from the barbed end.[230] Thus, the transition from ATP to ADP state determines the turnover of actin filaments. For Mg^{2+}-bound actin, the critical concentrations in the ATP-bound state were estimated as 0.1 μM and 0.7 μM at the barbed and pointed end, respectively, whereas in the ADP-bound state the critical concentrations are 0.5 μM and 0.6 μM.[244]. If the actin monomer concentration is beyond 0.7 μM, association

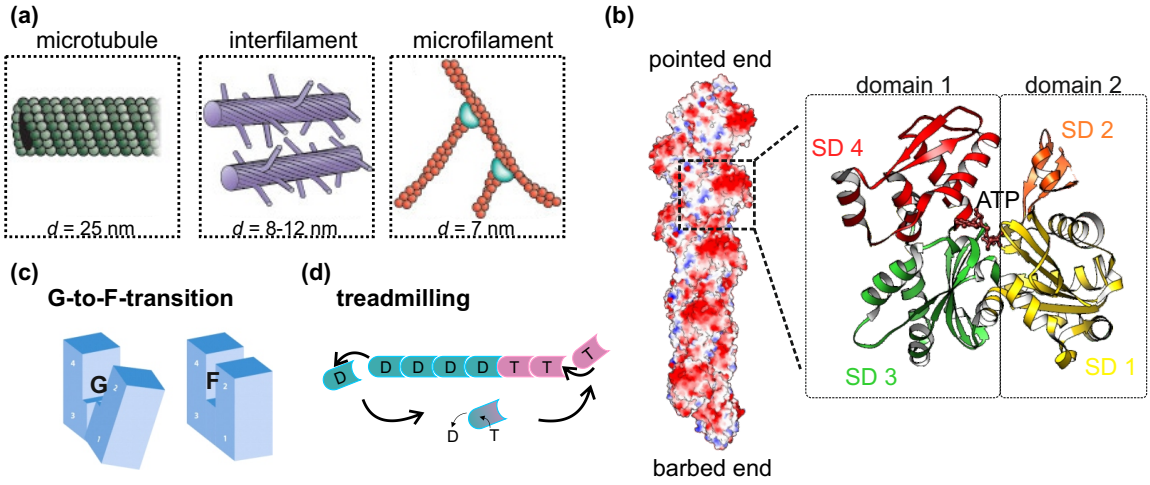

Figure 4.1 | Structure and function of actin. (a) The eukaryotic cytoskeleton consists of three different filament types: microtubules, interfilaments and microfilaments. Adapted from [D. Fletcher, R. Mullins (2010) Cell Mechanics and the Cytoskeleton, Nature, 463, 485-491, DOI: 10.1038/nature08908] by permission from Macmillan Publishers Ltd: Nature. Copyright ©2010, Nature Publishing Group. (b) Orientation and secondary structure of G-actin in F-actin. The F-actin structure is shown in an electrostatic surface potential map. Blue represents a positive surface and red a negative surface. The protein images were prepared and modified with UCSF Chimera v1.11.2[225] using pdb:1NWK and pdb:3G37. SD: subdomain. (c) Conformational flattening of the monomer during the G-actin to F-actin transition. Modified from [R. Dominguez, K.C. Holmes (2011) Actin Structure and Function, Annu. Rev. Biophys., 40, 169-186, DOI: 10.1146/annurev-biophys-042910-155359] (d) Treadmilling effect: ATP hydrolysis-driven non-equilibrium behavior of F-actin, which is described by dissociation of ADP-actin from the pointed end, ADP-ATP exchange in G-actin and association of ATP-G-actin at the barbed end.

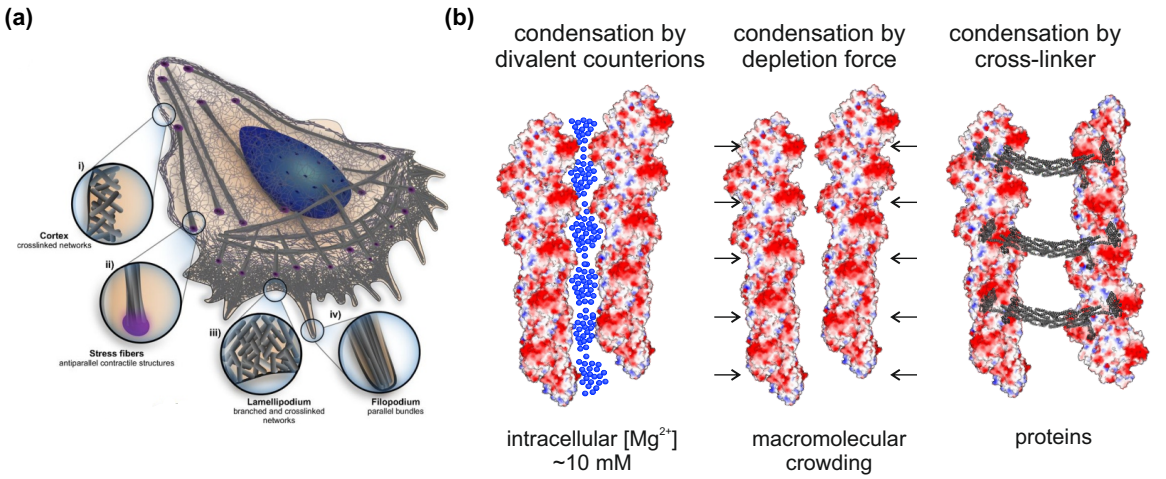

Figure 4.2 | Architectural organization of F-actin. (a) Schematic representation of a eukaryotic cell with different architectural organizations of F-actin. Taken from [L. Blanchoin, R. Boujemaa-Paterski, C. Sykes, J. Plastino (2014) Actin Dynamics, Architecture, and Mechanics in Cell Motility, Physiol. Rev. 94, 235-263, DOI:10.1152/physrev.00018.2013] Copyright ©2014, the American Physiological Society. (b) Schematic representation for the lateral condensation of F-actin induced by different forces. The protein images were prepared and modified with UCSF Chimera v1.11.2[225] using pdb:4S1E and pdb:3G37.

of ATP-bound G-actin is dominating at both ends, whereas below 0.1 μM dissociation is favored.

Actin filaments can organize themselves further into different architectures generating a diversity of cellular organizations including branched or crosslinked networks, parallel bundles, and antiparallel structures in contractile and stress fibers (Fig. 4.2a). The lateral condensation and thus bundling of F-actin plays a key role in the formation of filopodia, invadopodia, microvilli, stress fibers and hair cells.[246] Depending on the cellular function, parallel and antiparallel bundles can be observed. For cellular protrusion, stiff and parallel bundles are needed in order to push the membrane by the collective treadmilling phenomenon of actin filaments within the bundles, whereas antiparallel bundles of F-actin are required for cell integrity and myosin-induced contraction.[246] The geometries and the mechanical properties of bundles highly depend on the shape and size of the cross-linking agent.[247] F-actin features a surface charge density of $0.15e/\text{nm}^2$ at pH 8.[248,249] *In vivo*, the like-charge attraction between F-actin as polyelectrolytes is realized with the aid of specific binding proteins,[250], whereas *in vitro* it can be observed in the presence of multivalent counterions and polymers (Fig. 4.2b).[251]. Those condensation agents are thought to balance the local charge and to induce attractive interactions between the biopolymers.

Filopodia are thin, finger-like membrane protrusions acting as antennae for cells to sense

the environment. Thus, filopodia are involved in cell migration as well as wound healing, adhesion to the extracellular matrix and formation of neurite outgrowth.[252] A key bundling protein in filopodia is fascin.[253–256] The 55 kDa protein consists of four β-trefoil domains with a pseudo-2-fold symmetry.[254,255] Although the molecular mechanism of fascin-induced bundling of F-actin is not fully understood, mutagenesis studies revealed that positively charged actin binding sites are present allowing cooperative binding of F-actin.[255] Saturation of bundling occurs when approximately every fourth actin is bound to fascin.[253,256]. Upon bundling, fascin induces a maximal overtwist of 0.9° per monomer in the native F-actin helix (13/6 monomers/turn) in a concentration-dependent manner.[257]

In contrast, in aqueous solution in the absence of actin-binding proteins, repulsive interactions between actin filaments as polyelectrolytes would be expected according to the POISSON-BOLTZMANN formalism.[258] However, high concentrations of divalent ions have been found to induce like-charge attractions between polyelectrolytes and thus to bundle F-actin. Small-angle X-ray scattering (SAXS) studies revealed that the divalent ions condense into ripple-like charge layers coating the actin filaments. Interestingly, these layers do not follow the native symmetry of F-actin, but rather form a 1D charge density wave forcing F-actin to adapt a new 36/17 symmetry with a 3.8° per monomer overtwist.[251,259] In cells, the concentration of Mg^{2+}, a potential condensation agent, can reach up to 10 mM.[260] Further, the cytoplasm of cells is typically filled up to a volume of 30-40% by different macromolecules.[4] Inert and water soluble synthetic polymers including Ficoll, polyethylene glycol and dextran are often used to mimic the cellular environment and thus to study the effect of steric repulsion on different cellular processes.[8] This holds also true for the lateral aggregation of F-actin. Independent studies revealed that depletion forces induced by highly concentrated poly(ethylene glycol) solutions feature bundling activity without incorporating the polymer into the actin bundles.[249,261] This observation raises the question why cells actively use proteins rather than depletion forces and divalent ions for F-actin bundling which are ubiquitously presented in the cytoplasm.

After more than 60 years of study and about 111,500 entries in PubMed, however, still many questions about the structure and dynamics of actin have remained elusive. In particular, the knowledge about the molecular mechanisms underlying the polymerization process of G-actin in organisms thriving in physically or geochemically extreme conditions is very limited. In fact, *in vivo* and *in vitro* studies have demonstrated the high pressure sensitivity of filamen-

tous structures.[2,3,262–270] In particular, the critical concentration for actin polymerization has been shown to be elevated when pressure is increased up to several hundred bars, conditions that are easily encountered in the deep sea.[2,263,264] In 1966, Ikkai and Ooi described for the first time a gradual denaturation of F-actin modulated by pressure.[2] F-actin denatures irreversibly above 150 MPa without ATP and above 250 MPa with ATP. In the presence of ATP, F-actin reversibly depolymerizes with exchange of ADP to ATP in the range between 0.1 and 250 MPa. The volume change for the F- to G-actin transition has been estimated to be about -67 mL mol^{-1}.[267] Above 250 MPa, F-actin depolymerizes irreversibly due to rapid release of ADP from the monomers upon dissociation.[267] Recently, a pressure-temperature diagram of G-actin, F-actin and bundled F-actin (B-actin) demonstrated that G-actin is the least temperature-stable and also the least pressure-stable actin species (Fig. 4.3).[270] Under typical deep sea conditions (1-4 °C, <150 MPa) G-actin was shown to become unstable, whereas F-actin can withstand pressure up to 300-400 MPa. Therefore, pressure-induced conformational changes and even unfolding of the monomeric building block were concluded to be responsible for the dissociation of F-actin.[270] The calculated void volume from the crystal structure of G-actin is about 24 mL mol^{-1}, and consistently the volume change for the unfolding of G-actin has been determined to be $\sim$ -20 mL mol^{-1} (at 20 °C).[270] However, the mechanistic strategies of pressure resistance to ensure the formation of the actin cytoskeleton in piezophilic organisms are largely unknown.

4.2 Aim

The polymerization and depolymerization process of actin has been shown to be one of the most pressure-sensitive processes. Even though intact and well-formed cytoskeletons can be found in deep sea organisms. Hence, the aim of the study presented in this chapter is to provide insights into the molecular principles underlying the mechanistic strategy of pressure resistance for actin polymerization and bundle formation as found in piezophilic species. As the cellular composition (i.e., the presence of cosolutes and binding partners) and environment (i.e., the effect of macromolecular crowding) is linked to the structure, dynamics and hence function of biomolecules, pressure studies on the effect of macromolecular crowding as well as the effect of various accessory proteins on the assembly/disassembly reaction of actin are focus of this work. The use of spectroscopic, scattering and microscopic techniques

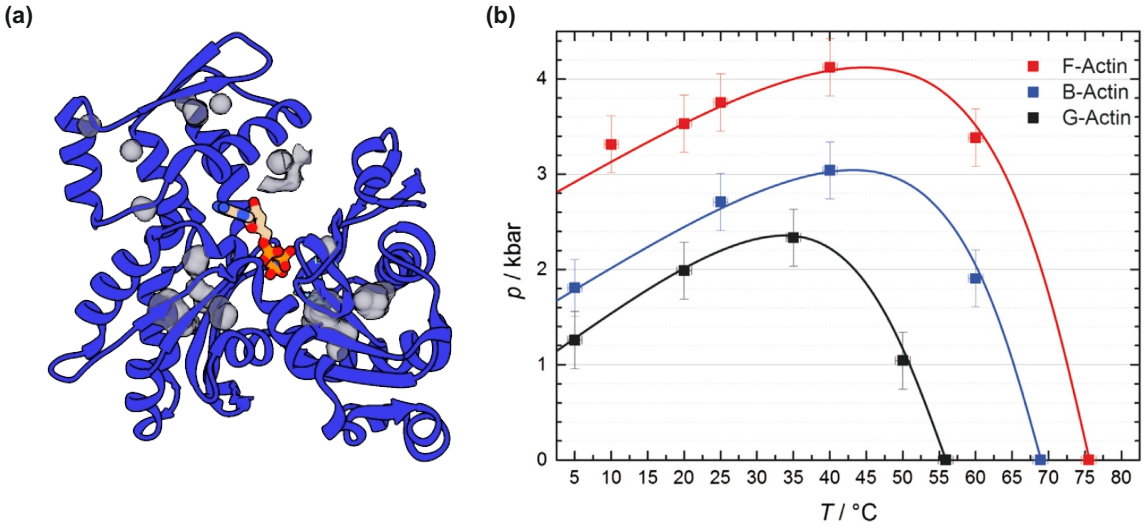

Figure 4.3 | Pressure and temperature stability of actin. (a) 3D crystal structure of G-actin with the molecular surface of voids (burried, water-inaccessible space) shown in grey. The voids are calculated using the CASTp server[271], and thereby the probe radius was 1.4 Å. The protein image was prepared and modified with UCSF Chimera v1.11.2[225] using pdb:1NWK. (b) Pressure-temperature diagram of G-actin. F-actin and B-actin. Reprinted from [C. Rosin, M. Erlkamp, J. von der Ecken, S. Raunser, R. Winter (2014) Exploring the Stability Limits of Actin and its Suprastructures, Biophys. J. 107, 2982-2992, DOI: 10.1016/j.bpj.2014.11.006] Copyright ©2014, with permission from Elsevier.

allowed me to study the pressure effect thermodynamically, kinetically and structurally and to answer (1) if cellular crowding is an active contributor to counteract the pressure sensitivity, and (2) how different actin-binding proteins can assist and ensure the formation of the actin cytoskeleton.

4.3 Materials and Methods

4.3.1 Chemicals and Sample Preparation

$MgCl_2$, sucrose, Ficoll ®PM 70, BSA and lysozyme were obtained from Sigma-Aldrich (Germany), G-actin (α-skeletal muscle actin from rabbit), fascin (human, recombinant) and gelsolin (cytoplasmic from porcine smooth muscle) were purchased from Hypermol (Germany). For kinetic experiments, 1 mg mL^{-1} G-actin solution was dialyzed against G-buffer containing 2 mM Tris-HCl (pH 8.2), 0.4 mM ATP, 0.1 mM DTT (dithiothreitol), 0.08 mM $CaCl_2$ overnight, and subsequently centrifuged at 60,000 rpm (Beckman TLA-100.4, USA) and 4 °C for 1 h to remove aggregates. Gelsolin (1 mg mL^{-1}) was dissolved in 10 mM imidazole (pH 7.0), 0.2 mM DTT, 0.2 mM EGTA, 2 mM NaN_3 and 1% disaccharides. Fascin

(1 mg mL^{-1}) was dissoveld in 150 mM NaCl, 20 mM HEPES (pH 7.4), 1 mM DTT and 5% sucrose.

For the kinetic experiments on F-actin elongation, 20 μM dialysed G-actin (10 mol% pyrene-labeled) and the appropriate amount of gelsolin were preincubated in the presence of 0.2 mM $CaCl_2$ at room temperature and for at least 10 min to form the nucleation complex. The filament elongation reaction was induced by adding F-buffer containing 10 mM imidazole (pH 7.4), 100 mM KCl, 2 mM $MgCl_2$,and 1 mM ATP (final concentration) to the solution.

For the sedimensation experiments on actin bundles, 10 mg mL^{-1} G-actin dissolved in 20 mM Tris-HCl (pH 8.2), 4 mM ATP, 1 mM DTT, 0.8 mM $CaCl_2$ (10x G-buffer) was directly polymerized by adding F-buffer (10 mM imidazole pH 7.4, 100 mM KCl, 2 mM $MgCl_2$, 1 mM ATP) to the solution. After 30 min of incubation at room temperature, F-actin was further bundled either by adding appropriate amounts of fascin (molar ratio of 1:4 fascin to G-actin) or 50 mM $MgCl_2$ to the solution. For transmission electron microscopy imaging, 2 mg mL^{-1} G-actin was dialyzed against 1x G-buffer overnight and subsequently centrifuged at 100,000 g and 4 °C for 1 h prior to polymerization. In order to remove G-actin and minor aggregates, F-actin was sedimented at 100,000 g and 4 °C for 2 h. The pellet of F-actin was resuspended in F-buffer and further bundled with fascin and $MgCl_2$, respectively. The bundles were stored at 0 °C and analyzed within one week after preparation.

4.3.2 Fluorescence Spectroscopy

To investigate the intrinsic effects of temperature and pressure on the fluorescence properties of pyrene, preformed F-actin (capped with gelsolin) containing pyrene-labeled actin monomers (10 mol%) was stabilized by incubation with phalloidin (Sigma, Germany) in a molar ratio of 1:1 or 1:2 (G-actin to phalloidin). The temperature- and pressure-dependent fluorescence spectroscopic measurements were carried out on a PerkinElmer LS 55 (Perkin Elmer, USA) and a K2 multifrequency phase and modulation fluorometer (ISS Inc.,USA), respectively. The fluorescence intensity was detected at 401 nm with an excitation wavelength of 365 nm. Temperature-dependent measurements were performed using a quartz cuvette. For the pressure-dependent measurements, a high pressure cell from ISS Inc. (USA) containing a quartz bottle sealed with a pressure-transmitting Dura Seal film was used. Hydrostatic pressure was generated using a screw type hand pump. Data were normalized to the intensity

values at 20 °C and 0.1 MPa.

4.3.3 Stopped-Flow Experiments

Temperature-dependent stopped-flow measurements from 20 to 45 °C were carried out on a Hi-Tech Scientific SHU-61SX2 stopped-flow fluorimeter, and high-pressure stopped-flow experiments up to 160 MPa using a Hi-Tech Scientific HPSF-56 stopped-flow apparatus with a mercury-xenon light source (both TgK Scientific, UK). In both cases, 20 μM G-actin solution containing 0.1 μM nucleation complex (syringe 1) and 2x F-buffer (syringe 2: 20 mM imidazole (pH 7.4), 200 mM KCl, 4 mM $MgCl_2$, 2 mM ATP) were mixed in the ratio 1:1. To study the effect of macromolecular crowding, appropriate amounts of the crowding agent was added to the F-buffer. The pyrene fluorescence intensity was measured using a 390 nm cut-off filter at an excitation wavelength of 365 nm. The data were offset corrected. For normalization, the intensity values were divided by the average intensity in the last second of each measurement.

4.3.4 Confocal Laser Scanning Microscopy

Upon preincubation with 50 nM gelsolin, 10 μM G-actin (10 mol% labeled with Atto488) were polymerized by adding F-buffer that contained the appropriate crowding agent. For fluorescence microscopic visualization, the actin filaments were further bundled in the presence of 50 mM $MgCl_2$. Images were recorded by a Nikon Eclipse TE300 inverted microscope equipped with a Biorad MRC 1024 confocal laser scanning system. Atto488 was excited by the 488 nm line of a krypton argon laser which was focused by a 100x oil immersion objective (Nikon CFI P-Apo l NA 1.45) on the sample. An emission band pass filter 522 nm/FWHM 35 nm was placed in front of the PMT. The images were background corrected, and the contrast was enhanced.

4.3.5 Transmission Electron Microscopy

The effect of temperature and pressure on the morphology of B-actin was visualized by TEM imaging. A JEOL JEM-1400 electron microscope equipped with a LaB6 filament and operated at 120 kV was used. Images were recorded on a TVIPS TemCam-F416 CMOS camera.

10-20 μL B-actin samples were either heated or pressurized up to the appropriate value and incubated for 10 min. A home-built high pressure autoclave was used for the hydrostatic compression.[270] After compression/heating, the samples were immediately placed on ice. For subsequent TEM imaging, 4 μL of each sample was adsorbed on glow-discharged carbon grids before negative staining with 0.75% uranyl formate.[241] The final actin concentration was adjusted empirically.

4.3.6 Sedimentation Assay

After temperature- and pressure-treatment, the B-actin samples were immediately centrifuged at 20,000 g and 0 °C for 60 min to separate bundles and large aggregate clusters from smaller actin species. Equal volumes of pellet and supernatant were analyzed by 12% SDS-PAGE and silver stained (PlusOne Silver Staining Kit, GE Healthcare).

4.4 Results and Discussion

4.4.1 Kinetic Insights into the Elongation Reaction of Actin Filaments as a Function of Temperature, Pressure and Macromolecular Crowding

Despite regulation and mediation by actin-binding proteins, the cytosolic environment itself may be a significant modulator of the actin polymerization reaction. In particular, the concentration of macromolecules in the cytosol can reach 400 g L^{-1}, resulting in a reduction of the accessible cellular volume up to 30-40% and thus often causing an entropic effect on folding and association equilibria of biomolecules (termed excluded volume effect).[4,8,272] Studies in diluted solutions have yielded essential information about the dynamics of actin. However, very little is known about the effect of the cytosol as a solvent on actin dynamics, as macromolecular crowding includes additional factors such as increased viscosity,[16,55,67,273] and non-specific interactions between solute and cosolute that are of enthalpic nature.[27,61,63,73,274,275] It has been shown by using synthetic crowding agents that the excluded volume effect accelerates actin nucleation[48] and equalizes the critical concentrations of ATP- and the less stable ADP-actin.[276]

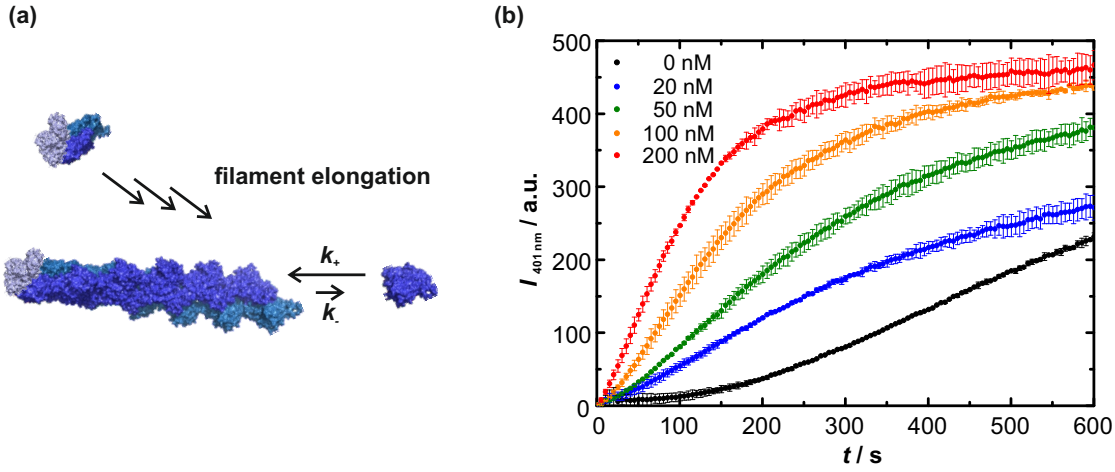

Figure 4.4 | The GA_2 complex as an actin nucleator for filament elongation at the pointed end. (a) A schematic of the GA_2 complex consisting of one gelsolin (light blue) and two monomeric actin (blue and cyan) molecules, acting as a template for polymerization of actin towards the pointed end. (b) Concentration-dependent effect of the preformed GA_2 complex on the polymerization reaction of actin (10 μM G-actin, 20 °C), monitored by the pyrene fluorescence assay (I, fluorescence intensity). The data were offset corrected. n=2-3, error bars indicate mean±standard deviation (s.d.).

Here, a comprehensive kinetic study was performed to reveal quantitatively the effect of macromolecular crowding on actin polymerization, thereby focusing on the growth of actin filaments at the pointed end as a function of temperature and pressure. Together with previous studies, these data shed also new light on the effect of pressure on the various steps of the polymerization reaction of actin, which is of significant biological relevance.[277]

By using preformed gelsolin-actin nuclei and stopped-flow methodology in combination with fluorescence detection, the elongation kinetics at the pointed end of actin filaments was studied. Gelsolin is a Ca^{2+}-dependent multifunctional actin-binding protein that can initiate actin nucleation, cap and sever actin filaments.[278–280] In the presence of excess G-actin, gelsolin forms a complex with two G-actin monomers, that is, the GA_2 complex, which acts as a stable elongation-competent nucleus.[281] As gelsolin remains attached to the barbed end of the growing actin filament (Tab. 4.1), the time course of filament elongation at the slow-growing pointed end can be monitored by a pyrene (which is covalently attached to the Cys374 of G-actin) fluorescence assay upon salt-based initiation (Fig. 4.4a).[243,282]

Owing to the sensitivity of pyrene to microenvironmental polarity change during filament formation, its fluorescence intensity, I, increases proportionally with the concentration or length of F-actin.[203,288] In the absence of preformed GA_2 nuclei, a sigmoidal-shaped pyrene fluorescence intensity profile for G-actin (10 μM; 10% pyrene-labeled) can be observed,

thus indicating initial *de novo* actin nucleation followed by filament elongation.[48,48] The addition of gelsolin, and hence, increased concentration of preformed GA_2 nuclei leads to the nucleation phase being bypassed, and thus to a progressively single exponential time-course in a gelsolin concentration-dependent manner, reflecting filament elongation toward the pointed end (Fig. 4.4b). Hence, a simple first-order kinetic model can be employed, in which actin polymerizes onto a constant concentration of filaments ($[GA_2]$),[281] where it is assumed that in the presence of excess G-actin, gelsolin is almost completely bound to actin (omitting gelsolin-induced fragmentation) and that the elongation rate is much faster than the formation of *de novo* actin nuclei (no filament growth at barbed end).[277] As the slow *de novo* nucleation step is bypassed by the GA_2 complex, the impact of the less frequent spontaneous fragmentation of F-actin on the elongation kinetics can be neglected (Tab. 4.1).[289] The rate

Table 4.1 | Literature rate and equilibrium constants for gelsolin-actin interaction and actin polymerization onto GA_2 nuclei.

Parameter	Value	Condition
Rate constant of GA_1 formation[245,283]	$2.5{\cdot}10^{-2}$ $\mu M^{-1}s^{-1}$	pH 7.0, 37 °C, 0.15 mM $CaCl_2$, 1 mM $MgCl_2$, 100 mM KCl
Rate constant of GA_2 formation from GA_1[284]	20 $\mu M^{-1}s^{-1}$	pH 7.5, 37 °C, 0.1 mM $CaCl_2$, 1 mM $MgCl_2$, 100 mM KCl
Rate constant of dissociation of GA_2 to GA_1[284]	0.02 s^{-1}	pH 7.5, 37 °C, 0.1 mM $CaCl_2$, 1 mM $MgCl_2$, 100 mM KCl
Equilibrium constant for GA_2 formation from GA_1[284]	10^9 M^{-1}	pH 7.5, 37 °C, 0.1 mM $CaCl_2$, 1 mM $MgCl_2$, 100 mM KCl
Binding affinity of G for the barbed end[285]	$4{\cdot}10^9$ M^{-1}	pH 7.6, 23 °C, 0.1 mM $CaCl_2$, 2 mM $MgCl_2$, 150 mM KCl
Association rate of ATP-actin at pointed end[244]	1.3 $\mu M^{-1}s^{-1}$	pH 7.0, 22 °C, 1 mM $MgCl_2$, 50 mM KCl, 1 mM EGTA
Dissociation rate of ATP-actin at pointed end[244]	0.8 s^{-1}	pH 7.0, 22 °C, 1 mM $MgCl_2$, 50 mM KCl, 1 mM EGTA
Nucleation rate[277]	$2{\cdot}10^{-9}$ $\mu M^{-2}s^{-1}$	pH 7.4, 20 °C, 2 mM $MgCl_2$, 100 mM KCl
Spontaneous fragmentation[286,287]	10^{-8} s^{-1}	pH 7.4, 37.1 °C, 1 mM $MgCl_2$, 100 mM KCl

of the polymerization reaction can then be analyzed using:

$$I(t) = I_0 + \Delta I \left[1 - \exp(-k_{\text{obs}} t)\right]. \tag{4.1}$$

Here, I_0 is the initial fluorescence value, ΔI is the overall change in fluorescence intensity and $k_{\text{obs}} = k_+[\text{G}]$ is the observed rate constant for polymerization at the pointed end [$n > 2$]:

$$\text{GA}_n + \text{A} \overset{k_+}{\rightarrow} \text{GA}_{n+1}, \tag{4.2}$$

where [G] is the total gelsolin concentration, and k_+ is the second-order association rate constant (the reverse reaction, k_-, can be neglected, as $k_+ \cdot [G] >> k_-$). Hence, the molar ratio of gelsolin to G-actin was kept constant at a ratio of 1:200 to explore the effect of macromolecular crowding on the monomer addition rate at the pointed end of actin filaments by using synthetic and protein crowding agents, and how such an effect is modulated by temperature and pressure. The temperature- and pressure-dependent measurements provided additional information on the transition state during the G-to-F-transition through the determination of the activation energy and activation volume, respectively. From the temperature dependence of the rate constant, k_+, the activation energy, E_a, can be obtained, and the pressure dependence of the rate constant enables the activation volume, $\Delta V^{\#}$, of the elongation process to be calculated by using:

$$\frac{\partial \ln k_+}{\partial (1/T)} = -\frac{E_a}{R}, \qquad \frac{\partial \ln k_+}{\partial p} = -\frac{\Delta V^{\#}}{RT}. \tag{4.3}$$

In an aqueous solution at 20 °C, an association rate, k_+, of (0.76±0.01)·10^5 $\text{M}^{-1}\text{s}^{-1}$ for ATP-G-actin was determined. A 7-fold acceleration of the reaction could be observed upon increasing the temperature up to 45 °C (Fig. 4.5a; 4.6a). These reaction rates are in the range of those reported in the literature.[244,281] The critical actin concentration is not affected by temperature under any conditions (Fig. 4.7). The macromolecular crowding agent Ficoll 70 is a large globular highly branched polysaccharide with a Stokes radius of about 5 nm. Here, it causes crowding agent concentration-dependent acceleration of the filament elongation, which again raises with increasing temperature (Fig. 4.5e,f; Fig. 4.6d,e). At 20 °C, the elongation reaction is accelerated 1.6-fold (at 100 g L^{-1} Ficoll 70) and 2.5-fold (at 200 g L^{-1} Ficoll 70) with respect to the diluted condition. A maximum association rate

of (12.5±0.01)·10^5 M^{-1} s^{-1} is measured at 45 °C and in the presence of 200 g L^{-1} Ficoll 70. In contrast, the addition of sucrose, the monomeric equivalent of Ficoll, results in cosolute concentration-dependent retardation of the elongation reaction (Fig. 4.5c,d; Fig. 4.6b,c), which is probably due to the elevated viscosity of the solution. For example, 1.3-fold (at 100 g L^{-1} sucrose) and 2-fold (at 200 g L^{-1} sucrose) retardation were found in the temperature range of 25-45 °C with respect to the diluted conditions; these findings are in line with literature data for the temperature-dependent viscosities of water in the absence and presence of sucrose.[290,291] However, at 20 °C, additional enthalpic effects of weak nature might be involved, leading to 2.2- and 5.5-fold retardation of the elongation reaction in the presence

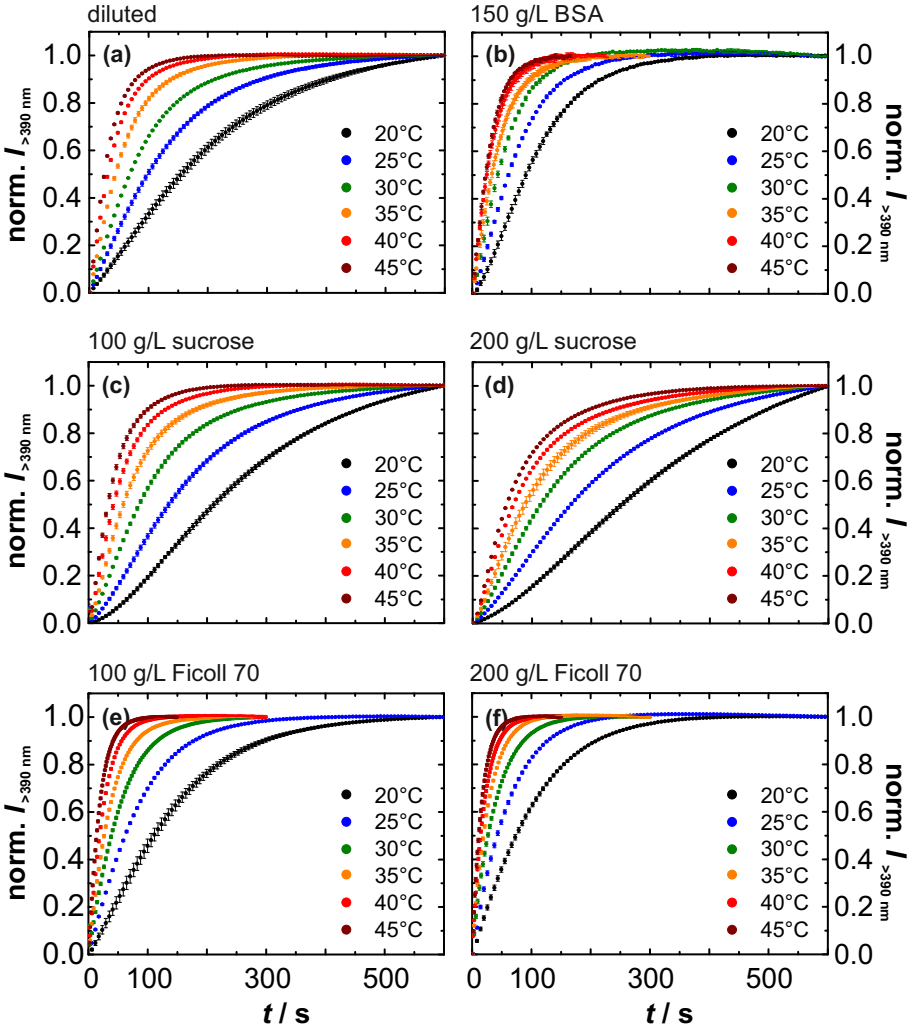

Figure 4.5 | The accelerative effect of temperature and macromolecular crowding on the elongation reaction of F-actin. Temperature-dependent elongation time course of F-actin (10 μM G-actin) onto 50 nM GA_2 complex at 0.1 MPa (a) in the absence of crowding agent, (b) in 150 g L^{-1} BSA, (c) in 100 g L^{-1} sucrose, (d) in 200 g L^{-1} sucrose, (e) in 100 g L^{-1} Ficoll 70, and (f) in 200 g L^{-1} Ficoll 70 monitored by pyrene fluorescence spectroscopy with normalized intensities. n=3-4, error bars indicate mean±s.d.

of 100 and 200 g L^{-1} sucrose, respectively. Interestingly, the same retarding effect of sucrose on the elongation rate of human islet amyloid polypeptide (IAPP) fibrils was found.[49] These findings imply that monomer addition to the pointed end is a concentration-controlled process and its acceleration under macromolecular crowding is predominantly controlled by the excluded volume effect of Ficoll, and thus the elevated effective protein concentration rather than by changes of viscosity or effects of an enthalpic nature (due to "soft" interactions).[61,73,292,293] *In vitro*, the elongation of actin has been previously shown to be weakly dependent on the viscosity, and thus not diffusion limited at the pointed end, but at the barbed end.[294]

In contrast to synthetic and often inert polymers, globular proteins exhibit a chemically heterogeneous surface, allowing local intermolecular interactions such as electrostatic interactions, hydrogen bonding, or attraction mediated by the hydrophobic effect.[6] Hence, to mimic such cellular environments *in vitro*, the proteins bovine serum albumin (BSA) and lysozyme as protein crowding agents were used. In the case of BSA, electrostatic repulsion is expected to reinforce the effect of excluded volume (steric repulsion), as both the solute and cosolute are anionic proteins at pH 7.4 [pI(BSA) = 4.7 and pI(G-Actin) = 5.3; pI = isoelectric point]. A similar accelerative impact of BSA compared to Ficoll 70 (Fig. 4.5b; Fig. 4.6f) is observed. At 20 °C, the association rate in the presence of BSA (150 g L^{-1}) is twice of that in the diluted solution. However, with increasing temperature, the association rates approach similar values. The repulsive electrostatic contribution of BSA to the excluded volume effect might be (partially) compensated by the viscosity (eventually including electroviscous effects)[295] or other (enthalpic) retarding forces compared with the pure buffer solution. Conversely, 100 g L^{-1} lysozyme causes complete inhibition of actin elongation, as indicated by the rapid decay of pyrene fluorescence (Fig. 4.6g). In a Mg^{2+}-induced F-actin bundling assay, only amorphous agglomerates are observed in the presence of lysozyme, whereas actin bundles are formed under all other solution conditions (Fig. 4.8). This effect is probably due to nonspecific electrostatic binding of lysozyme to the unlike-charged pyrene-labeled G-actin, as the isoelectric point of lysozyme is 11.4.[296]

To gain further insights into the G-to-F-transition, the activation energy, E_a, was calculated from the temperature-dependent elongation rate constants. From the ARRHENIUS plot (Fig. 4.9a), an activation energy of E_a =(56±4) kJ mol^{-1} ($\approx 23 k_B T$) was obtained for the actin association at the pointed end and in diluted buffer. Drenckhahn and Pollard

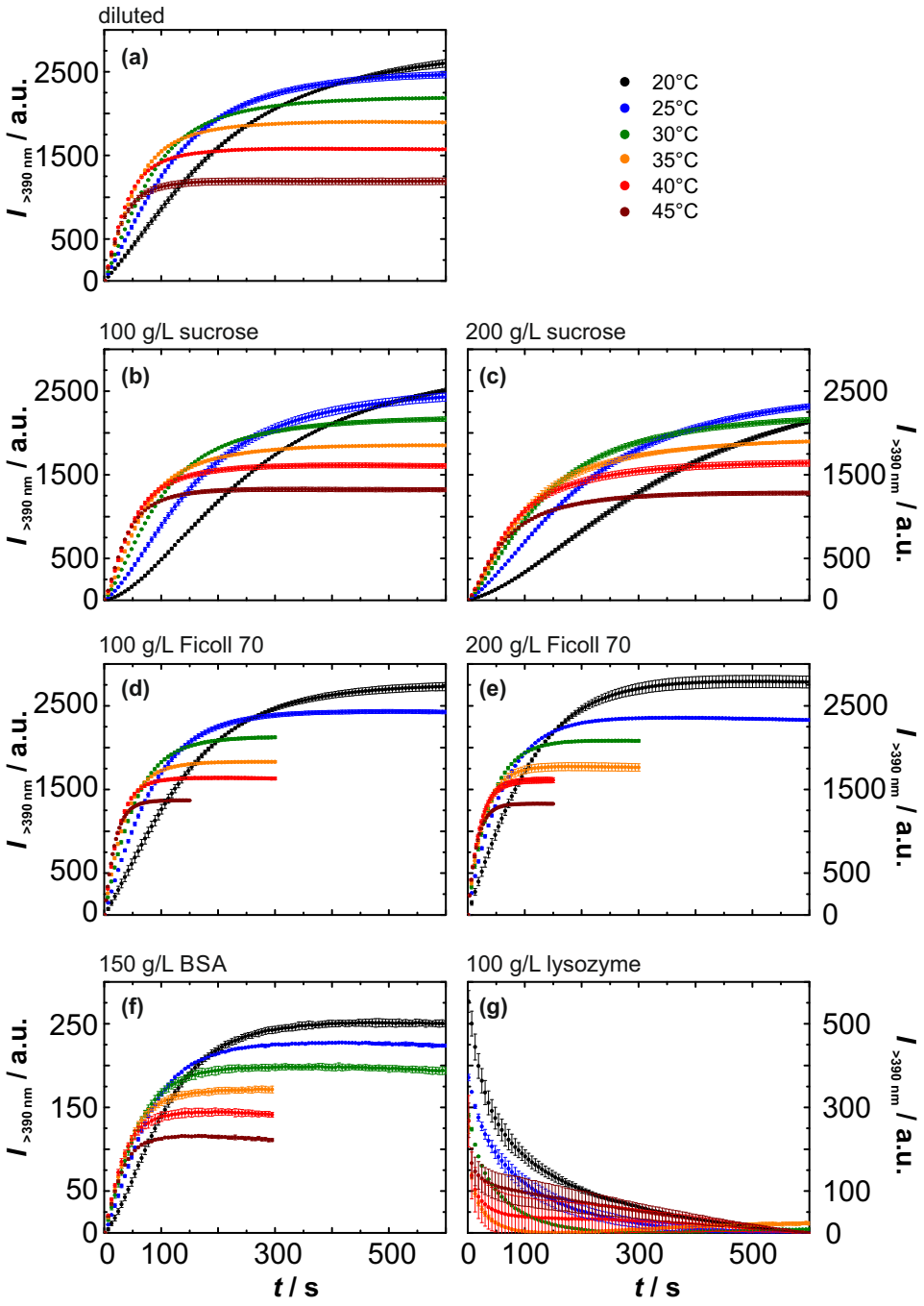

Figure 4.6 | The accelerative effect of temperature and macromolecular crowding on the elongation reaction of F-actin. Temperature-dependent elongation time course of actin filaments (10 μM G-actin) onto 50 nM GA_2 complex at 0.1 MPa, (a) in the absence of crowding agent, (b) in 100 g L^{-1} sucrose, (c) in 200 g L^{-1} sucrose, (d) in 100 g L^{-1} Ficoll 70, (e) in 200 g L^{-1} Ficoll 70, (f) in 150 g L^{-1} BSA or (g) in 100 g L^{-1} lysozyme monitored by pyrene fluorescence spectroscopy with absolute intensities. The data were offset corrected, except for (g). n=3-4, error bars indicate mean$\pm$s.d.

measured E_a =(36$\pm$6) kJ mol^{-1} for filament elongation at both ends.[294] These data indicate that a slightly higher activation energy is needed for initial binding and for the G-to-F transformation at the pointed end compared with the barbed end. This would be consistent

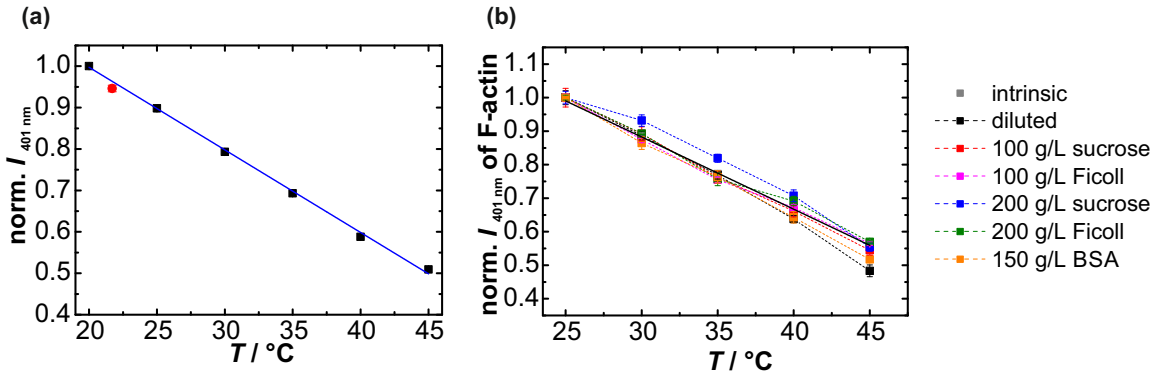

Figure 4.7 | Pyrene fluorescence displays intrinsic response to temperature. (a) Normalized fluorescence intensities of pyrene bound to F-actin:phalloidin and dissolved in F-buffer as a function of temperature show a linear decrease. The red point indicates fluorescence recovery after cooling to room temperature. (b) Normalized fluorescence plateau values obtained from the average intensity in the last second of each polymerization measurement are plotted against temperature. Since the polymerization does not reach steady state under every condition at 20 °C, the plateau values from 25 to 45 °C are considered, only. For each condition, the temperature dependence follows almost the intrinsic behavior of pyrene, indicating that the critical concentration for actin polymerization is not affected by temperature. The solid line represents a linear fit for the intrinsic behavior of pyrene, and dashed lines connect data points to guide the eye.

with a recently suggested model that the G-to-F-transition is induced by a pulling movement of the D-loop upon its own docking to the hydrophobic cleft of the neighboring subunit,

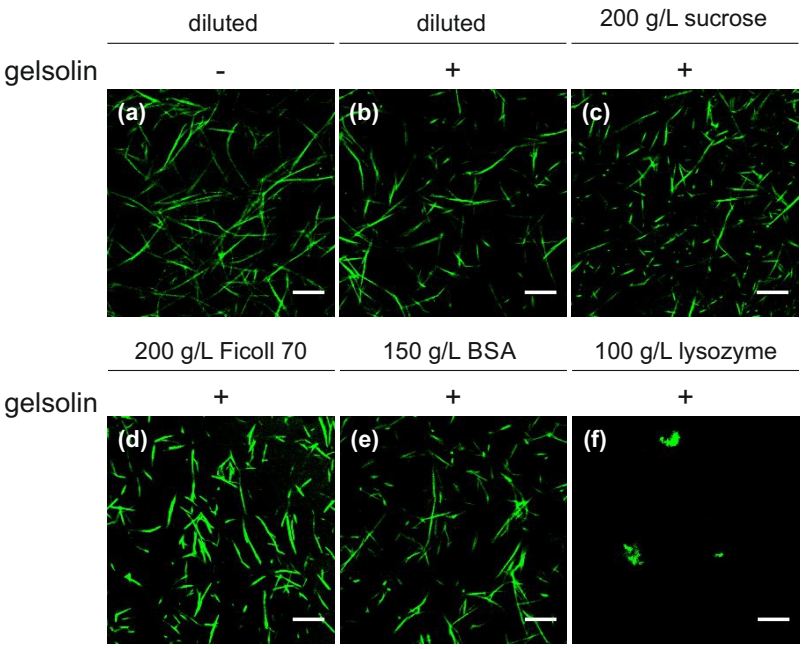

Figure 4.8 | Actin species (10 mol% labeled with Atto488) formed under different crowding conditions upon polymerization and further Mg^{2+}-induced bundling. In the presence of gelsolin, shortened actin filaments and thus bundles are abundant (a-b). Formation of actin filaments and thus bundles is not disturbed by the crowding agents (c-e), except for lysozyme (f). Amorphous agglomerates are observed here, only. Scale bar, 10 μm.

which differs at both ends.[238,241] At the barbed end, the flexible D-loop of G-actin traps the hydrophobic cleft of F-actin and induces an intramolecular conformational change upon pulling. In contrast, at the pointed end the less flexible D-loop of F-actin has to interact with and to pull the hydrophobic cleft of G-actin to induce an intermolecular conformational change. Of note, significant less energy input is required for such conformational and hydrational changes during the elongation of actin compared with that of Aβ fibrillization, which has been determined to be (95$\pm$5) kJ mol^{-1}.[297] The addition and increase in concentration of Ficoll 70 do not significantly affect the activation energy of the elongation reaction, suggesting that the transition state is as compact as the ground state. In the presence of BSA (150 g L^{-1}), however, the activation energy is diminished by $\sim$7 $k_{\mathrm{B}}T$ (Fig. 4.9c). This is probably a result of the (electro)viscous effect modulating the elongation kinetics at the pointed end, and its temperature dependence, which is expected to display a different temperature dependence than the bulk viscosity of the diluted solution.

The temperature mainly modulates the frequency of the motion, whereas an increase of pressure causes a change in density (or volume), thus revealing information about the activation volume change of the elongation reaction.[172] Hence, pressure-dependent kinetic studies on the elongation of F-actin were also performed. A marked decelerating effect of pressure on the *de novo* nucleation process of actin polymerization has been reported in the literature, indicating a volume expansion of the transition state during nucleation.[277] Here, hydrostatic pressure is found to hardly affect the elongation kinetics in diluted buffer, that is, $\Delta V^{\#} \approx 0$ (Fig. 4.9b; Fig. 4.11a) but causes the equilibrium to shift towards the monomeric state, and thus increases the critical concentration at the pointed end (Fig. 4.10a), similar to previous findings.[263] This is reflected in the pressure-dependent decrease of the fluorescence plateau values, which differ from the intrinsic response of pyrene fluorescence to pressure (Fig. 4.12). Therefore, the transition state of the elongation reaction is not accompanied by an expansion or compaction of the ground state through formation or elimination of hydrophobic cavities and packing defects, or by a marked change in hydration.[270,298]

Interestingly, the macromolecular crowding agent Ficoll 70 and the protein crowding agent BSA seem to stabilize polymerizable G-actin against pressure, and thus counteract the deteriorating effect of pressure in a concentration- and type-dependent manner as indicated by increased fluorescence plateau values with respect to the diluted buffer scenario (Fig. 4.10; Fig. 4.12b). The elongation kinetics is not modulated by pressure in the presence of BSA

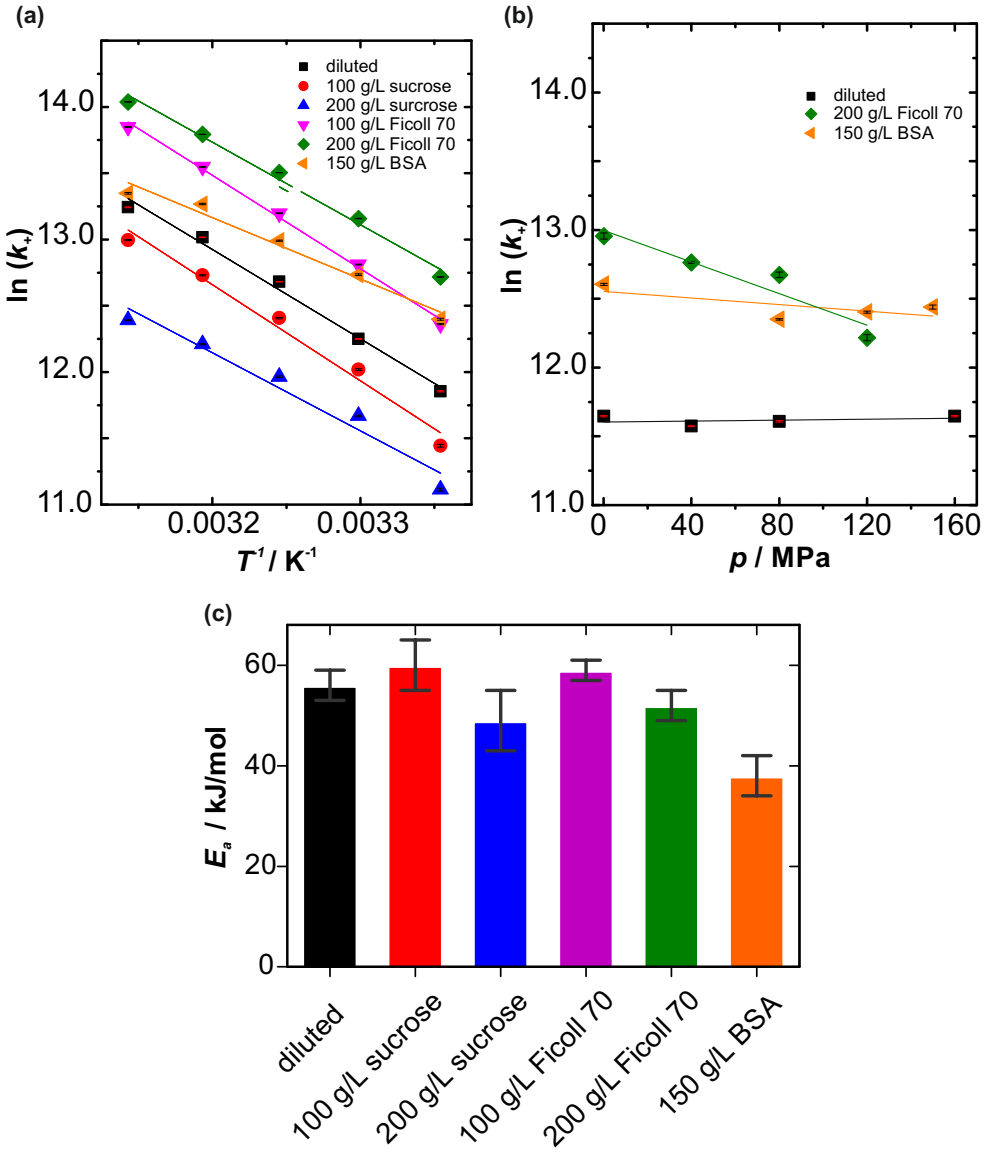

Figure 4.9 | The effect of macromolecular crowding on the activation energy and activation volume of the elongation reaction of F-actin at the pointed end. (a) Arrhenius plot [$\ln(k_+)$ vs. T^{-1}] for actin filament elongation under different crowding conditions. (b) Plot of $\ln(k_+)$ versus p of actin in diluted buffer and in BSA (150 g L^{-1}) and Ficoll 70 (200 g L^{-1}). Error bars indicate mean±s.d. (c) Activation energies of the elongation reaction at the pointed end of actin filaments in the presence of different cosolutes.

(Fig. 4.9b; Fig. 4.11b). However, in the presence of 200 g L^{-1} Ficoll 70, with increasing pressure, a loss of the exponential shape of the elongation curve and a slight retardation of the elongation kinetics are observed. The retardation is equivalent to a small positive activation volume, $\Delta V^{\#}$, of about (15±3) mL mol^{-1}, which corresponds roughly to one water molecule (Fig. 4.9b; Fig. 4.11c,d), and might be the consequence of minor changes to the transition state structure, owing to weak actin-Ficoll interactions and/or minor hydration changes in the presence of the macromolecular crowding agent. The same activation volume is estimated in

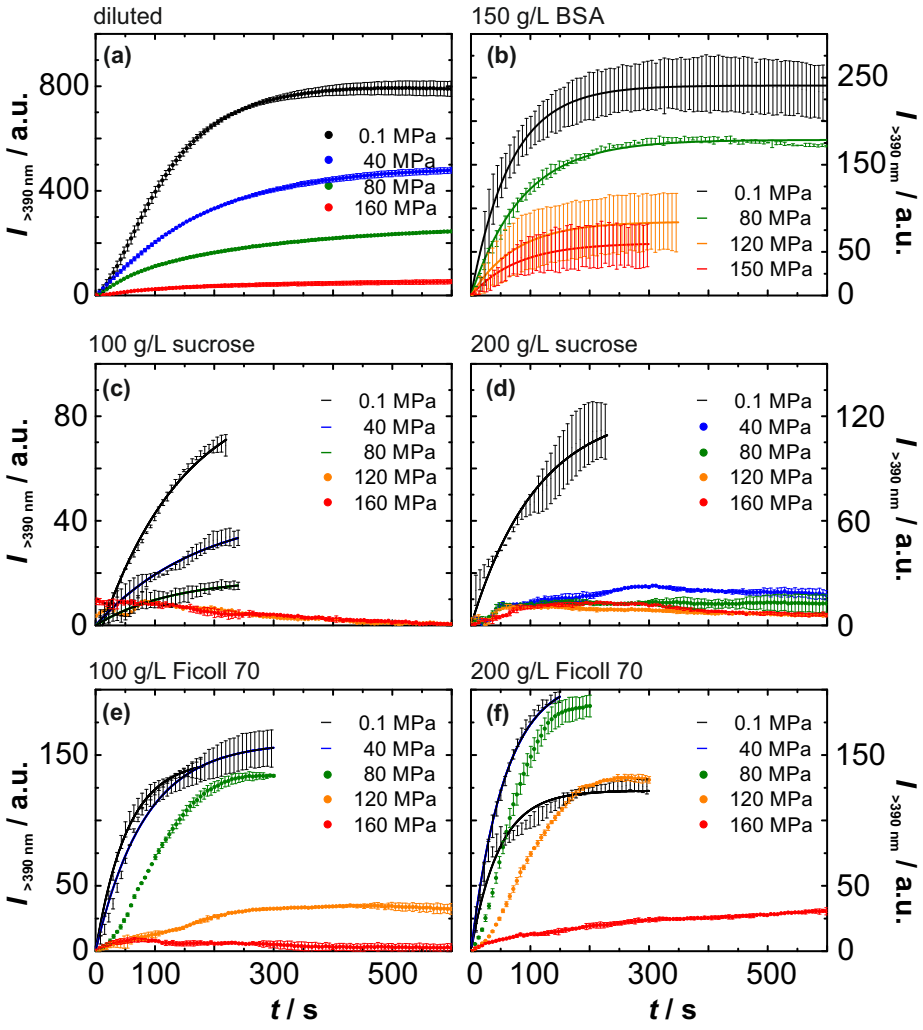

Figure 4.10 | The combined effect of hydrostatic pressure and macromolecular crowding on the elongation reaction of F-actin. Pressure-dependent elongation time course of F-actin (10 μM G-actin) onto 50 nM GA_2 complex at 30 °C (a) in the absence of crowding agent, (b) in 150 g L^{-1} BSA, (c) in 100 g L^{-1} sucrose, (d) in 100 g L^{-1} sucrose, E) in 100 g L^{-1} Ficoll 70, and (f) in 200 g L^{-1} Ficoll 70 monitored by pyrene fluorescence spectroscopy. The data were offset corrected. n=2-3, error bars indicate mean±s.d. Due to the viscosity increase of the solutions, and thus less efficient mixing in the stopped-flow cell, the obtained curves from fitting instead of data points are shown in some cases (solid line).

the presence of 100 g L^{-1} Ficoll 70, thus indicating that the pressure-dependent retardation is not caused by an increase in viscosity of the polymer solution upon pressurization.[299] On the contrary, the addition and increase in concentration of sucrose cause a drastic inhibition of the actin polymerization from 0.1 to 40 MPa (Fig. 4.10c,d). Hence, the sucrose control confirms that the stabilizing effect of Ficoll 70 with respect to pressure originates from the excluded volume effect, that is, an increase in the effective actin concentration (i.e., activity). In summary, this study has shown how the elongation of actin filaments at the pointed end is affected in different crowding environments over a wide range of temperatures and pres-

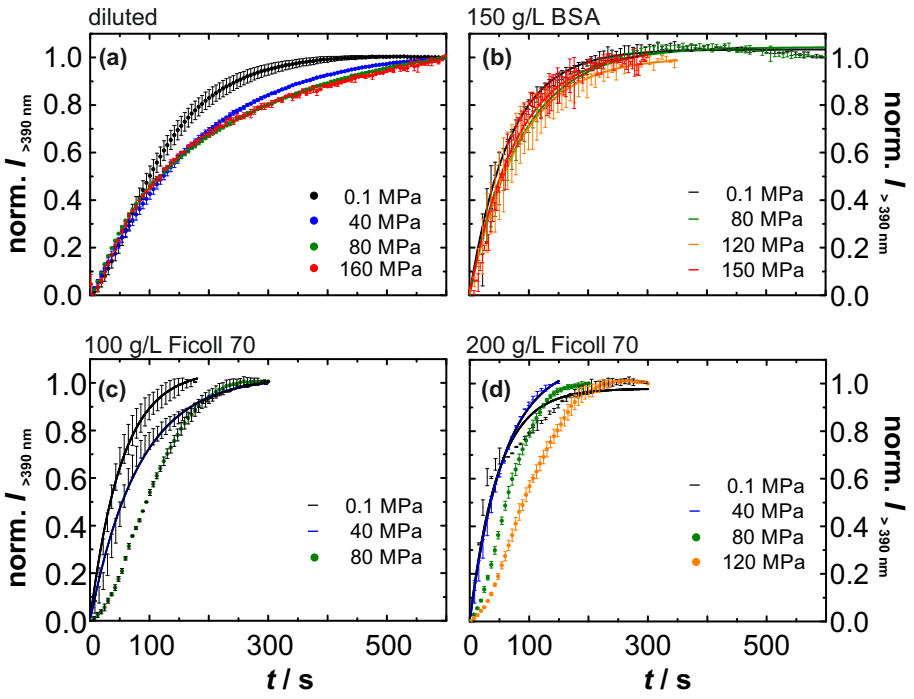

Figure 4.11 | The combined effect of hydrostatic pressure and macromolecular crowding on the elongation reaction of F-actin. Pressure-dependent elongation time course of F-actin (10 μM G-actin) onto 50 nM GA_2 complex at 30 °C (a) in the absence of crowding agent, (b) in 150 g L^{-1} BSA, (c) in 100 g L^{-1} Ficoll 70 or (D) in 200 g L^{-1} Ficoll 70, monitored by pyrene fluorescence spectroscopy with normalized intensities. n=2-3, error bars indicate mean±s.d. Due to the viscosity increase of the solutions, and thus less efficient mixing in the stopped-flow cell, the obtained curves from fitting instead of data points are shown in some cases (solid line).

sures. The elongation rate, k_+, is accelerated under macromolecular crowding conditions (100-200 g L^{-1} Ficoll 70), owing to the entropic effect of excluded volume. However, the use of different protein crowding agents (BSA and lysozyme) reveals that the enthalpic contribution of the crowding effect, which is here essentially electrostatic in nature, can retard or even inhibit the polymerization of actin in the case of unlike-charge protein pairs. In the case of like-charge protein pairs, the (electro)viscous effect of the concentrated BSA solution is shown to modulate the excluded volume effect and its temperature dependence. Macromolecular crowding can significantly alter the polymerization kinetics of actin inside the cell, therefore, the effect of the native solvent itself on the elongation rate is expected to be more complex, as its enthalpic contribution depends on the chemical nature of each individual macromolecule present.

Moreover, the temperature- and pressure-dependent studies on the elongation kinetics reveal that the association of actin monomers to the pointed end of F-actin proceeds via a transition state, where a thermal energy input of 56 kJ mol^{-1} for conformational and/or hydration rear-

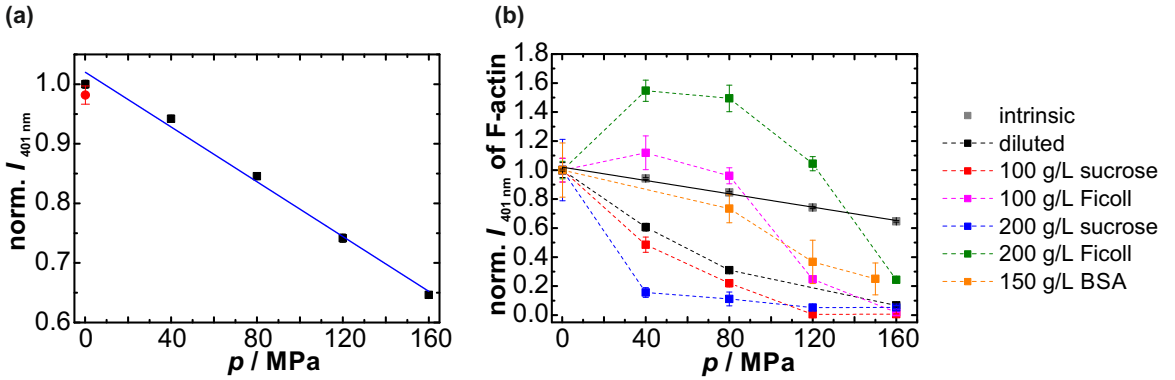

Figure 4.12 | Pyrene fluorescence displays intrinsic response to pressure. (a) Linear pressure response of pyrene bound to F-actin:phalloidin and dissolved in F-buffer. The red point indicates fluorescence recovery after pressure release. (b) Normalized fluorescence plateau values obtained from the average intensity in the last second of each polymerization measurement are plotted against pressure. The pressure dependences feature an individual behavior and do not follow the intrinsic pressure response of pyrene, indicating that pressure modulates the critical concentration for actin polymerization.The solid line represents a linear fit for the intrinsic behavior of pyrene, and dashed lines connect data points to guide the eye.

rangement is required. However, the reaction is not accompanied by formation or elimination of hydrophobic cavities and void volume, which is reflected in a negligible activation volume of the elongation step. Both, the activation energy and activation volume are not markedly affected by the excluded volume effect, thus indicating that the formation of the transition state is not associated with a significant conformational expansion or compaction. Several pressure studies on the depolymerization of F-actin revealed that the G-to-F-transition is accompanied by a reaction volume change, ΔV, of about 60-80 mL mol^{-1}.[2,263,264] In contrast to the elongation reaction, it was previously found that high pressure dramatically decreases the *de novo* nucleation rate of actin polymerization, by about two orders of magnitude per kbar, which corresponds to a large positive activation volume, $\Delta V^{\#}$, of 104 mL mol^{-1}.[277] Moreover, a 2.5-fold higher activation energy (139$\pm$20 kJ mol^{-1}) is required for the *de novo* nucleation reaction compared with the elongation process at the pointed end.[277] Hence, these data imply that the high-pressure sensitivity of the kinetics of the polymerization process of actin is essentially due to the initial *de novo* nucleation event. As volume changes arise mainly from packing and hydration changes, these data suggest that the initial assembly of actin oligomers creates void volumes at the contact sites of the G-actin molecules, thus rendering nuclei formation to be the most pressure-sensitive process of actin polymerization. Therefore, those findings highlight the importance and need for actin nucleation factors (e.g. gelsolin, formin and Arp2/3) to bypass the energetically costly and pressure-sensitive *de novo*

nucleation *in vivo* ensuring formation of the cytoskeleton, also under extreme environmental (high hydrostatic pressure) conditions.

4.4.2 Condensation Agents Determine the Temperature-Pressure Stability of F-Actin Bundles

Biological cells provide a large variety of rodlike filaments. These filaments are semiflexible polymers with a large persistence length and can assemble into different morphologies.[246] Actin filaments have persistent lengths of $\sim$ 10 μm and can hence form meshworks and bundles.[246] As the interfilament attraction is mediated by crosslinkers, the formation of F-actin bundles is reversible and can be controlled by the crosslinker concentration and their stability.[246] Owing to the polyelectrolyte nature of F-actin, bundling can also be achieved by unspecific electrostatic attractions via counterion condensation, e.g. by Mg^{2+} ions.[251] To shed light on the question, why cells actively use proteins rather than the ubiquitously present divalent ions for F-actin bundling, small-angle X-ray scattering (SAXS) and transmission electron microscopy (TEM) were used to compare the morphology, packing geometry of fascin- and Mg^{2+}-induced F-actin bundles and to determine their stability over a wide range of temperatures and pressures. The SAXS experiments have been mainly performed by Melanie Berghaus (TU Dortmund). Hence, the obtained SAXS data is referred to the published research article and only briefly discussed in this thesis.

Transmission electron microscopy (TEM) reveals significant differences between the morphology of the bundles formed by fascin and Mg^{2+} ions, respectively, thus indicating different underlying molecular interaction mechanisms (Fig. 4.13a,b). At ambient conditions, fascin induces the formation of rigid and planar bundles with a homogenously distributed thickness. In contrast, more flexible, tubular and differently sized bundles are formed in the presence of Mg^{2+} ions. By exhaustive screening of several prepared specimens at low magnification, significantly shorter bundles are observable in the presence of fascin compared to Mg^{2+}. However, in both cases the bundles feature periodic transverse banding patterns indicating orderly and hexagonal packing. At a molar ratio of 1:4 of fascin and G-actin, all actin filaments are bundled, whereas in the presence of 50 mM Mg^{2+} ions, isolated F-actin molecules are still detectable. From complementary SAXS measurements, a hexagonal lattice constant (interfilament distance) of d = 12.4 nm and 8.5 nm are found for the fascin-induced and

Mg^{2+}-induced F-actin bundles, respectively.[300]

Increasing the temperature up to 55 °C causes dissociation of the fascin-induced bundles into F-actin, whereas the morphology of the Mg^{2+}-induced species is not significantly affected (Fig. 4.13c,d). Further, the dissociation leads to formation of free actin filaments which are longer than those within the bundles, indicating immediate assembly of short actin filaments along their long axis. This behavior reflects the intactness of F-actin upon dissociation from the bundles. At 65 °C, no bundles are present, but shrunk filaments and first amorphous aggregates are formed for the fascin-induced species (Fig. 4.13e). In contrast, during thermal denaturation Mg^{2+}-induced bundles directly aggregate into amorphous protein clusters rather than dissociate into filamentous actin (Fig. 4.13f), which is consis-

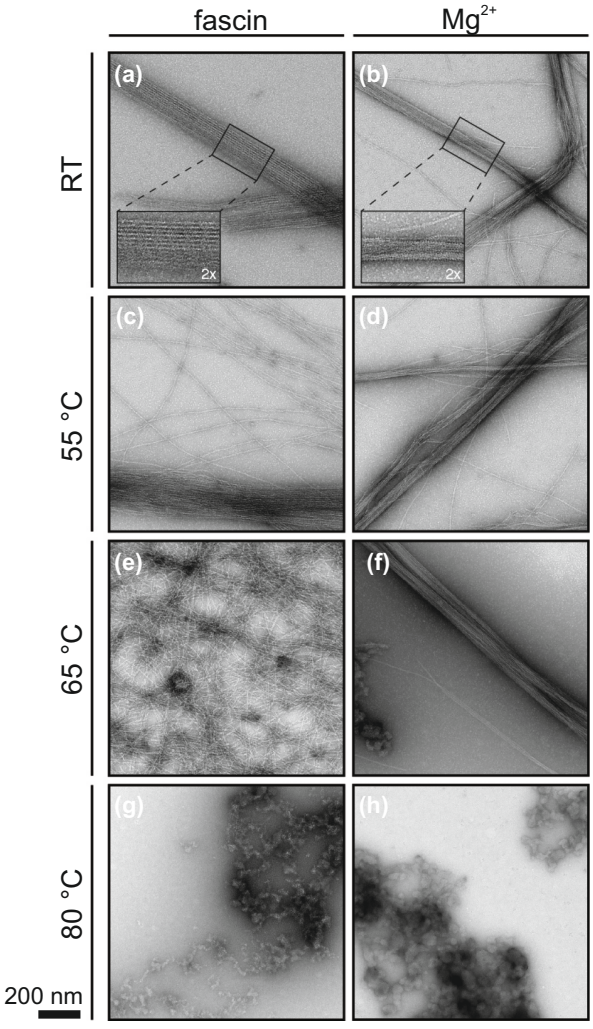

Figure 4.13 | Thermal stability of F-actin bundles condensed by fascin and Mg^{2+}. Representative transmission electron micrographs show the morphology of B-actin at room temperature (a and b) and after heating up to 55 (c and d), 65 (e and f), and 80 °C (g and h) for 10 min. The TEM images were taken in collaboration with Dr. Julian von der Ecken (MPI, Dortmund).

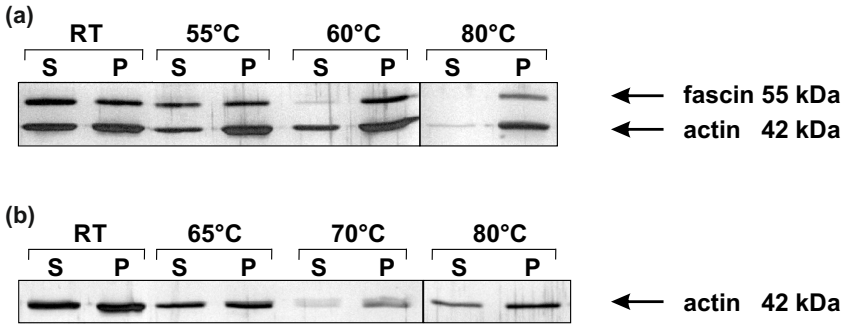

Figure 4.14 | Temperature-dependent stability of actin bundles studied by a sedimentation assay at 20,000 g. Supernatant (S) and pellet (P) fractions were analyzed by gel electrophoresis and silver stained. Sedimentation behavior of fascin- (a) and Mg^{2+}-induced (b) bundles after 10 min incubation at the denoted temperature.

tent with the complementary SAXS data.[300] Those data confirm that fascin-induced F-actin bundles dissociate between T_m = 52.5-55 °C, whereas the Mg^{2+}-induced bundles denature between T_m = 65-57.5 °C.[300] Further, low speed (20,000 g) sedimentation assays revealed that thermal denaturation of both bundles leads to a continuous growth of the pellet fraction, thus indicating direct aggregation upon denaturation (Fig. 4.14). Taken together, these observations imply that the interfilament interactions of electrostatic nature are stronger than the intrafilament interactions. Finally, when heating up to 80 °C, both bundle types aggregate completely (Fig. 4.13g,h).

Studying the response of fascin- and Mg^{2+}-induced actin bundles to high hydrostatic pressure reveals that they feature significantly different and even opposite pressure-temperature stabilities. Hydrostatic compression from 0.1 MPa up to about 150 MPa does not significantly affect the morphology of both bundle types (Fig. 4.15a-d). Only a slight thinning and extension of the fascin-formed bundles can be observed (Fig. 4.15c). Interestingly, although highly ordered Mg^{2+}-induced bundles can be only found *in situ* up to a pressure of $\sim$125 MPa obtained by SAXS,[300] TEM reveals no morphological changes up to 150 MPa, thus indicating reversible pressure dissociation and therefore reassembling upon pressure release (Fig. 4.15d). Such finding can be explained by the pressure effect on electrostatic interactions. Since dissociation of internal salt bridges leads to a reduction in the overall volume caused by electrostrictive effects of water molecules,[188,193,301] attenuation of such interactions and thus an increase of the interfilament distance as observed in SAXS occurs upon pressure increase.[300] Further pressure increase leads to complete and irreversible lateral dissociation of fascin-induced bundles into F-actin and finally formation of denatured protein clusters after

pressure release (Fig. 4.15e,g). Similar to the temperature-dependent behavior, F-actin is always present in the Mg^{2+}-induced assemblies and its concentration does not change below the denaturation pressure. Instead, a direct transformation from bundles to smaller protein clusters is observed *ex situ* (Fig. 4.15f,h). These results indicate that hydrostatic compression causes denaturation of actin monomers directly within the bundles or after dissociation from the bundles. However, in comparison to the fascin-induced species, some Mg^{2+}-formed bundles can still be observed after pressurization up to 350 MPa (Fig. 4.15g,h). In the low speed (20,000 g) sedimentation assays, pressure denaturation causes initial reduction of the pellet fraction and an increase again at higher pressure values, thus suggesting dissociation of intermediate species from the bundles which only aggregated above certain pressure values and after pressure release (Fig. 4.16).

In summary, this study has shown that fascin-induced bundles are stable up to ≈ 54 °C at ambient pressure and up to a pressure of $p_M \approx 250$ MPa at $T = 20$ °C, whereas the Mg^{2+}-induced actin bundles display an about 12 °C higher melting temperature ($T_M \approx 66$ °C), but a much lower dissociation pressure of the bundles of $p_M \approx 125$ MPa at $T = 20$ °C. The differences in temperature and pressure stability of the two bundle types can be explained by different types of intermolecular interactions involved in bundling the filaments. High hydrostatic pressure is known to lead to a weakening of electrostatic interactions (due to the electrostrictive effect, i.e., the reduction in volume due to formation of a dense hydration shell around the solvent-exposed ions).[188,193,301] As for Mg^{2+}-induced bundles electrostatic interactions are the only interaction type involved in the lateral condensation of F-actin, a pressure-induced weakening is expected to lead to the dissociation of the bundle structure. In addition, the release of void volume at the contact interfaces of the interacting filaments upon dissociation of the bundles will also lead to a negative volume change, hence in agreement with LE CHÂTELIER's principle, also favoring dissociation of the actin bundles at rather low pressures. However, it has been recently shown that the pressure-induced volume changes upon disintegration of Mg^{2+}-bundles, ΔV, at 25 °C amounts to -9 mL mol^{-1}, thus indicating very compact packing.[270] This indicates that packing defects (void volumes) are likely to be a minor component in the pressure-induced dissociation of the Mg^{2+}-induced bundles. Notably, the SAXS data show that starting from 0.1 MPa the interfilament distance increases continuously and divergently (Δ = 0.6 nm in total) before dissociation of the Mg^{2+}-induced bundles into the filaments.[300] The findings that the interfilament distance of the fascin-

induced bundles is not affected upon pressurization up to about 100 MPa,[300] and that the dissocation of the bundles starts above $\sim$ 250 MPa imply that additional interaction types are operative for the fascin-crosslinking mechanism. The pressure-induced lateral dissociation is very likely due to destabilization of the tertiary structure of fascin and its local interaction site with F-actin because the stability of F-actin has been found to be in the pressure range of $\sim$350 MPa.[270] As the fascin-induced bundles feature a significantly higher pressure stability compared to the purely electrostatically stabilized bundles, one might conclude that protein-based crosslinking of F-actin might fit better the requirements inside cells for organisms living under extreme environmental conditions, such as those encountered in the deep sea and sub-seafloor, where pressures up to about 100 MPa and beyond are reached.[1,172] In

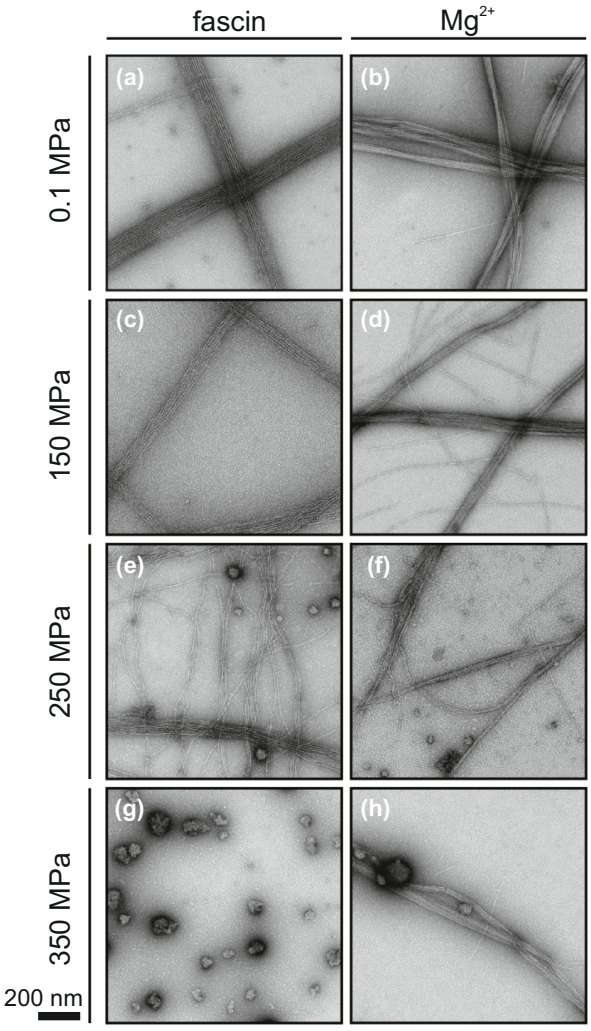

Figure 4.15 | Pressure stability of F-actin bundles condensed by fascin and Mg^{2+}. Representative transmission electron micrographs show the morphology of B-actin at ambient conditions (a and b) and after hydrostatic compression up to 150 (c and d), 250 (e and f), and 350 MPa for 10 min. The TEM images were taken in collaboration with Dr. Julian von der Ecken (MPI, Dortmund).

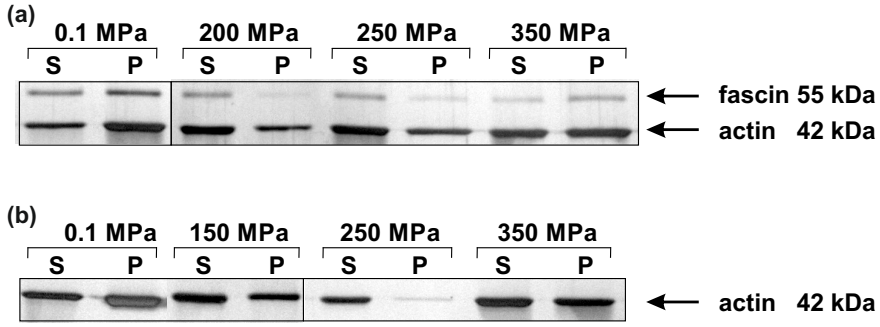

Figure 4.16 | Pressure-dependent stability of actin bundles studied by a sedimentation assay at 20,000 g. Supernatant (S) and pellet (P) fractions were analyzed by gel electrophoresis and silver stained. Sedimentation behavior of fascin- (a) and Mg^{2+}-induced (b) bundles after 10 min incubation at the denoted pressure.

addition, fascin and actin are evolutionarily highly conserved.[302,303]

4.5 Conclusions

In summary, the results presented in this chapter unveil that despite the observed pressure sensitivity of the cytoskeletal actin, several ways exist inside cells to improve its pressure resistance. It could be shown that actin can benefit significantly from its accessory proteins as well as the cellular environment itself. First, the nucleator gelsolin can assist to bypass the most pressure-sensitive step during actin polymerization, namely the initial *de novo* nucleation event and thus ensure the formation of actin filaments under high pressure conditions. Compared to the nucleation step, the elongation step was found to be much more pressure resistant due to its highly compact transition state. Second, the crosslinker fascin was shown to enable the formation of pressure-resistant actin bundles. Their packing geometry and tightness are not affected by pressure values up to 100 MPa, which cover the physiologically revelant range found in the deep sea. Third, the crowded environment inside cells, as simulated by high concentrations of synthetic polymers and proteins *in vitro*, was shown to counteract the deteriorating effect of pressure by increasing the stability limit of the actin monomer and shifting the equilibrium towards the polymerized state. Taken together, those observations indicate that several strategies, active and passive ones, exist to ensure the formation and the dynamics of the cytoskeletal actin. However, the aspect of amino acid sequence variation was not considered in this work. Although the amino acid sequences of actin are highly conserved across different species, minor or even single changes of residues

could modulate the conformational dynamics of actin at high pressure conditions as well.[304]

CHAPTER 5

WHAT IS THE ORIGIN OF THE MICROTUBULES' HIGH PRESSURE SENSITIVITY?*

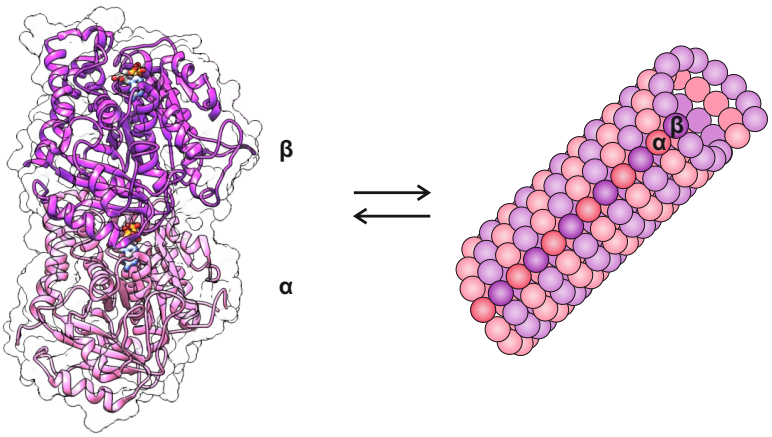

Abstract

Although it has been known for over 50 years that the mitosis of eukaryotic cells is inhibited already at HHP conditions of 30 MPa due to disorganization of microtubules as the main component of the spindle apparatus, the structural details of the depolymerization and the origin of the pressure sensitivity have remained elusive. In this chapter, the pressure stability of microtubules is studied at different structural levels and for distinct dynamic states. In particular, the results show that lateral and longitudinal contacts of microtubules feature different pressure stabilities, and they define also the pressure stability of microtubule bundles. In addition, it can be demonstrated that the cellular environment itself as a crowded place and accessory proteins can increase the pressure stability of microtubules and accelerate their otherwise highly pressure-sensitive formation.

The protein image was prepared and modified with UCSF Chimera v1.11.2 [225] using pdb:1JFF.

*Parts of this chapter form the basis for a manuscript in preparation by M. Gao, M. Berghaus, S. Möbitz, V. Schuabb, N. Erwin, M. Herzog, K. Julius, C. Sternemann, and R. Winter.

Author contribution: M.G. and R.W. designed the research. M.G. performed research. M.B., S.M., N.E., and M.H. assisted with protein purification or at the beamline. M.G. and R.W. analyzed data. V.S., C.S., and K.J. contributed analytic tools. M.G. and R.W. wrote the article. All authors discussed the results and commented on the manuscript.

Addendum: A revised version of the following chapter has been published in "M. Gao, M. Berghaus, S. Möbitz, V. Schuabb, N. Erwin, M. Herzog, K. Julius, C. Sternemann, and R. Winter. On the Origin of Microtubules' High Pressure Sensitivity. *Biophys. J.* (2018), https://doi.org/10.1016/j.bpj.2018.01.021"

5.1 Introduction

Microtubules, as a component of the eukaryotic cytoskeleton, are another class of non-covalently built-up biopolymers and are mainly involved in developing and maintaining cell shape and polarization, providing platforms for intracellular transport, and are crucial for cell signaling and mitosis.[305,306] To fulfill those functions, the heterodimer consisting of α- and β-tubulin ($\alpha\beta$-tubulin) polymerizes into hollow tubes of about 25 nm in diameter, whereby they form linear protofilaments in a head-to-tail fashion, and 10-15 of them then associate laterally to form a hollow and polar cylinder (Fig. 5.1a).[306–308] The subunits share about 50% amino acid sequence identity.[309] Each tubulin monomer binds a guanine nucleotide and has a molecular mass of about 50 kDa (Fig. 5.1b).[310] Thereby, the nucleotide bound to α-tubulin (N-site) is buried at the intradimer interface, is non-exchangeable and is not hydrolyzed upon polymerization, whereas GTP bound to β-tubulin (E-site) is exchangeable in solution, but becomes hydrolyzed and non-exchangeable upon association to the microtubule ends.[306,311] Hence, tubulin is a GTPase, whose activity is induced by the polymerization reaction.[312] Upon association of an $\alpha\beta$-tubulin molecule to the plus end, the catalytic domain of the incoming α-tubulin interacts with the previous E-site and completes the binding pocket enabling hydrolysis of the GTP bound to the previous β-tubulin.[313] Due to that asymmetry, microtubules are polar structures owning different polymerization rates at the two ends.[314] Within each protofilament the heterodimers are oriented with their β-subunit pointing towards the faster-growing plus end and with their α-subunit towards the slower-growing minus end of the microtubule (Fig. 5.1a).[306,314,315] *In vivo*, the microtubule minus end is stabilized by the microtubule-organizing center (MTOC), which allows microtubule formation with only 13 protofilaments.[316] Lateral interactions between protofilaments occur between adjacent α-tubulins and adjacent β-tubulins (homotypic contacts) with a seam in which α-tubulin and β-tubulin interact laterally (heterotypic contacts).[317,318]

The microtubule assembly *in vitro* and *in vivo* are distinguished by the energetically unfavored and time-consuming nucleation step, which is bypassed *in vivo* by microtubule templates such as γ-tubulin ring complexes localized at the MTOC.[316,319] Spontaneous polymerization of tubulin *in vitro* requires a stable oligomer/nucleus consisting of several tubulin dimers.[320,321] Once such nuclei are formed, they will elongate rapidly in both longitudinal and lateral direction.[322–324] Since sheet-like structures of protofilaments have been observed

at the tip of growing microtubules,[325] it is believed that the microtubule growth includes the step of sheet closure.[326] At steady state, microtubules undergo rapid cycles of growing and shrinking, a non-equilibrium behavior named dynamic instability (Fig. 5.1a,c),[327] which is crucial for their cellular functions and is energetically realized by the polymerization-triggered hydrolysis of GTP bound to β-tubulin. Hydrolysis of GTP and phosphate release have been believed for a long time to induce a bent conformation of $\alpha\beta$-tubulin with a kink between both subunits resulting in curvature of the otherwise straight protofilaments and thus destabilization of the microtubules.[305,328–330] However, a recent cryo-EM study revealed that the GTP hydrolysis provokes a lattice compaction around the interdimer interface along the

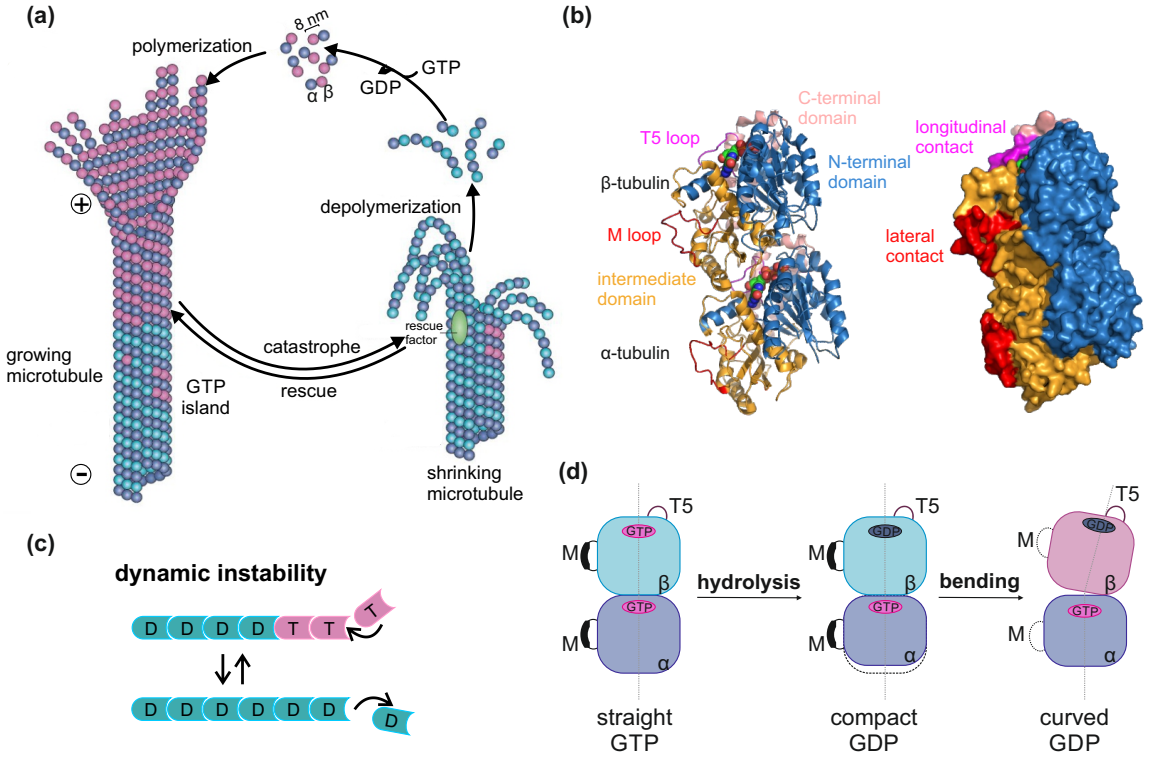

Figure 5.1 | Structure and dynamics of tubulin. (a) A dynamic cycle of polymerization and depolymerization is characteristic for the dynamic instability of microtubules. Reprinted from [A. Akhmanova, M. Steinmetz (2015) Control of Microtubule Organization and Dynamics: Two Ends in the Limelight, Nat. Rev. Mol. Cell Bio., 16, 711-726, DOI:10.1038/nrm4084] by permission from Macmillan Publishers Ltd: Nature Reviews Molecular Cell Biology. Copyright ©2015, Nature Publishing Group. (b) Secondary structure elements and surface topology of $\alpha\beta$-tubulin. Each subunit is divided into three main domains. GTP is buried in the longitudinal contact interface. The T5 loop and M loop are responsible for longitudinal and lateral contacts within the microtubule, respectively. The structure was generated with PyMol using pdb:1JFF. (c) Dynamic instability describes the stochastic switch between growth and shrinking of microtubules. The main driving force is believed to be the GTP hydrolysis. (d) The schematic illustrates the straight-to-bent transition of the tubulin heterodimer upon GTP hydrolysis. GTP hydrolysis provokes a lattice compaction around the interdimer interface of α-tubulin along the protofilament axis, which is proposed to cause conformational strain that would be released by breaking of the lateral contacts and bending of the protofilaments during depolymerization.

protofilament axis, which is proposed to cause conformational strain that would be released by breaking of the lateral contacts and bending of the protofilaments during depolymerization (Fig. 5.1d).[318,331] Interestingly, the structural compaction induced by GTP hydrolysis is inhibited in the presence of taxol, an antimitotic drug, which binds to a pocket in β-tubulin and is known to prevent microtubules from depolymerization.[331–333] However, a detailed molecular mechanism by which GTP hydrolysis controls the microtubule dynamics is still elusive.

To fullfill the manifold functions *in vivo*, myriad of microtubule-associated proteins (MAPs) are known to regulate the formation and the non-equilibrium dynamics of microtubules.[334–336] MAPs bind to microtubules in a nucleotide-independent fashion to modulate their dynamic instability, mostly by stabilizing them against depolymerization. However, they are also shown to be involved in inducing bundle formation of microtubules.[337–341] MAPs like tau and MAP2 assist microtubules to form dense parallel arrays in order to grow and maintain neuronal projections such as axons and dendrites.[342] Interestingly, such proteins do not directly crosslink the microtubules within the bundle, but control spacing between them by long-range repulsive forces reminiscent of polyelectrolyte polymer brushes.[343] Those MAPs feature two distinct domains: a C-terminal microtubule-binding domain, which is highly positively charged and contains three or four 18-residue microtubule binding repeats allowing electrostatic binding to the microtubule surface, and a N-terminal projection domain, which varies in length for different isoforms and is highly negatively charged keeping microtubules at distance.[344–346] MAP2 and tau bind longitudinally along the microtubule protofilaments with each binding repeat bound to one tubulin monomer.[347] This binding mode allows longitudinal stabilization of microtubules by bridging the interdimer interfaces and prevents them from depolymerization.[347–349] Furthermore, the abilities of bridging and charge-shielding of tau have been reported to accelerate the steps of nucleation and elongation during microtubule formation.[349–351] However, the mechanism by which MAP2 and tau mediate attractive interactions between microtubules within bundles is largely unknown. Recently, the Safinya group proposed a mechanism in which the projection domains of tau on opposing microtubules mediate the spacing by a balance between repulsive forces and transient sub-$k_{\mathrm{B}}T$ cationic/anionic charge-charge attractions.[341] *In vitro*, like-charge attraction between the negatively charged microtubules and formation of tightly packed hexagonal bundles have been observed in the presence of multivalent counterions (electrostatic conden-

sation) and concentrated polymer solutions (depletion attraction).[352–354]
Pioneering works by Salmon, Zimmerman and Marsland showed that elevated hydrostatic pressure induces mammalian epithelial cells to round-up or marine eggs to arrest in the cell-cycle, which are largely caused by disorganization of actin stress fibers and spindle microtubules, respectively.[262,355,356] Pressures up to 30 MPa have been shown to induce rapid and reversible depolymerization of microtubules in a variety of eukaryotic cell types and thus to inhibit mitosis. Similar effects have also been reported for cooling of microtubules.[357] However, details and the underlying mechanism of their pronounced pressure sensitivity are largely unknown. In contrast, actin filaments, another important component of the eukaryotic cytoskeleton, have been shown to be stable up to $\sim$150-200 MPa (see chapter 4).[267,270]

5.2 Aim

Despite the pressure and temperature sensitivity of the cytoskeleton, life has invaded the cold- and high-pressure habitats of marine depths. Hence, this raises the questions (1) what the origin of this pressure sensivitiy is and (2) which strategies deep sea organisms have evolutionarily established at a molecular level to improve the pressure resistance of their cytoskeleton. Hence, the aim of the study presented in this chapter is to study the pressure stability of microtubules at different structural levels and for distinct dynamic states and thus to provide biophysical insights into the origin of such pressure sensitivity. Further, it will be tested whether the molecular strategies, which were found to improve the pressure resistance of actin filaments (see chapter 4), are also valid for the microtubules.

5.3 Materials and Methods

5.3.1 Reagents

$\alpha\beta$-Tubulin purified from calf brain was obtained from the Centre of Biological Research, CSIC (Madrid, Spain) as lyophilized powder. PIPES (1,4-piperazinediethanesulfonic acid), spermidine and spermine were purchased from Sigma-Aldrich. Taxol from *Taxus brevifolia* was purchased from Sigma-Aldrich as dry powder and was dissolved in DMSO with a stock concentration of 2 mM.

5.3.2 Purification of MAP2c

Rat MAP2c was purified as described previously.[358] The cDNA encoding full length rat MAP2c was subcloned from pEGFP-N3 into the NdeI and BamHI sites of the pET15b vector for bacterial expression (GenScript, USA). pET15brMAP2c was transformed into competent *Escherichia coli* strain BL21(DE3) (Novagen) and grown in LB media supplemented with 100 μg mL^{-1} ampicillin to an A_{600} of 0.6-0.8. Upon addition of IPTG (0.4 mM), the cells were grown at 25 °C overnight and then harvested by centrifugation at 5000 g. The bacterial pellet was resuspended in 50 mM Tris-HCl (pH 8.0), containing 300 mM NaCl, 0.1% Triton X-100, 1 mM PMSF, protease inhibitor cocktail (Sigma-Aldrich), and DNase. Cells were lysed through sonication and centrifuged for 30 min at 75,600 g. The supernatant was brought to pH 7.5, supplemented with additional 450 mM NaCl and 2 vol% β-mercaptoethanol, and boiled for 8 min. After cooling on ice for 10 min, the solution was centrifuged for 25 min at 75,600 g. The supernatant was loaded onto a Ni-NTA column and washed with 10 mM imidazole. The MAP2c protein was eluted with 60-80 mM imidazole and further purified on a HiLoad 26/600 Superdex 75 column using 50 mM Tris-HCl (pH 7.0) and 300 mM NaCl. Purified MAP2c was dialyzed against 80 mM PIPES (pH 6.8), 1 mM EGTA, 1 mM DTT, 6 mM $MgCl_2$, and 50 mM KCl prior to experiments. The identity and purity of MAP2c were checked by 15% SDS-PAGE and electrospray mass spectrometry (observed: 51,334 Da; estimated: 51,332 Da).[359] Protein concentration was determined by UV absorbance at 280 nm (ϵ_{280} = 12950 M^{-1} cm^{-1}).

5.3.3 Sample Preparation

Microtubules were polymerized from about 10 mg mL^{-1} tubulin dissolved in 80 mM PIPES (pH 6.8), 1 mM EGTA, 1 mM DTT, 6 mM $MgCl_2$, 1 mM GTP, and 30 wt% glycerol by incubation at 37 °C for 30 min and then stabilized by the addition of 50 μM taxol. After further incubation of 30 min at 37 °C, to remove unpolymerized tubulin, microtubules were sedimented through a sucrose cushion (40 wt% sucrose in 80 mM PIPES, 1 mM EGTA, 6 mM MgC_2, 50 μM taxol, and 1 mM GTP) at 120,000 g and 30 °C for 15 min (Beckman TLA-120.1, USA). The microtubule pellet was carefully washed in 80 mM PIPES (pH 6.8) containing 20 μM taxol and resuspended in 80 mM PIPES (pH 6.8), 6 mM $MgCl_2$, 1 mM EGTA, 50 μM taxol, and 1 mM GTP. After resting for 30 min, the microtubule sample was

diluted with an equal volume of cation or PEG solution in 80 mM PIPES (pH 6.8) and incubated at least for 30 min. As a final step, the sample was centrifuged at 21,000 g and 25 °C for 1 h and the pellet was used for the SAXS measurements.

To form GTP-dependent active microtubules for the SAXS and FTIR measurements, lyophilized tubulin was dissolved in 80 mM PIPES (pH 6.8), 1 mM EGTA, 1 mM DTT, 6 mM $MgCl_2$, and 5 wt% glycerol to a concentration of about 20 mg mL^{-1} and put on ice for 10 min before centrifuging at 11,000 rpm and 2 °C for 2 min to remove potential aggregates. Tubulin was then polymerized at a concentration of about 100 μM by the addition of 3 mM GTP and incubation at 37 °C for 40 min. In case of MAP2c, additional 25 mM KCl and 20 μM MAP2c were added. To increase the protein density suitable for SAXS and FTIR, the sample was centrifuged at 11,000 g and 37 °C for 30 min prior to the measurement. For the FTIR measurements, buffers prepared in D_2O were used and MAP2c was added in lyophilized form. Previous experiments have shown that the steady-state microtubules are not structurally perturbed by centrifugation and are stable over time ($>$ 24 h).[341]

For the experiments on $\alpha\beta$-tubulin, the lyophilized powder was dissolved in 80 mM PIPES (pH 6.8), 1 mM EGTA, and 1 mM DTT to a concentration of 10-20 mg mL^{-1} and put on ice for 10 min before centrifuging at 11,000 rpm and 2 °C for 2 min to remove potential aggregates.

5.3.4 High Pressure Synchrotron SAXS

SAXS experiments were performed at the beamline BL9 of DELTA in Dortmund, Germany, and the beamline I22 of the Diamond Light Source in Didcot, UK. At BL9, the X-ray energy was 10 keV, which corresponds to a wavelength, λ, of 0.12 nm, and the sample-detector distance was 1.103 m (calibrated with a silver behenate control), covering a momentum transfer (q) range between 0.02 and 0.55 $Å^{-1}$. The scattering curves were recorded using a MAR345 imaging plate (D = 345 mm with 100 μm pixel size) and the exposure time was 15 min. The relatively long acquisition time did not affect the stability of taxol-stabilized microtubules. At I22, the X-ray energy was 18 keV (λ = 0.07 nm). The scattering curves were recorded in a distance of 3.752 m (calibrated with a silver behenate control) using a Pilatus P3-2M detector (W x H = 253.7 x 288.8 with 172 μm pixel size) in a q-range between 0.007 and 0.66 $Å^{-1}$. Samples of active microtubules were exposed to the beam for 0.5 s for each mea-

surement. No radiation damage was detected within the total exposure time of a complete pressure series. Pressure-dependent measurements were performed in a home-built pressure cell with diamond windows of 1 mm thickness (type IIa quality, Drukker, Cuijk, The Netherlands).[360] Water was used as pressurizing medium and hydrostatic pressure was generated either by a screw type hand pump or by a motor driven high pressure pump.[361] The sample volume was 10 μL. Pressurization up to 300 MPa at steps of 15 MPa was performed at 25 °C or 37 °C. The scattering profiles as a function of q were obtained by azimuthal integration over the whole active detector area. Subsequently, the scattering data was background corrected using the buffer measurement as reference and the SAXSutilities software package.[362] The software packages SASfit and ATSAS were used for further analysis.[363,364] All measurements were performed in duplicate.

5.3.5 High Pressure FTIR

Pressure-dependent FTIR spectra were collected using a Nicolet 6700 FTIR spectrometer (Thermo Fisher Scientific, USA) equipped with a liquid-nitrogen-cooled MCT detector (HgCdTe) in the wavenumber range of 4000-650 cm^{-1}. Pressure up to 400 MPa was applied using a P-series diamond anvil cell (DAC) with type IIa diamonds (High Pressure Diamond Optics Inc., Tucson, USA). A 50 μm thick gasket of CrNi steel with a 0.45 mm drilling was placed between the two diamonds holding 2.5 μL of the sample. The temperature of the DAC was controlled by an external water bath and set to 37 °C. Owing to the pressure-dependent stretching vibration of SO_4^{2-} (at about 983 cm^{-1}), $BaSO_4$ was used as an internal pressure gauge.[365] 128 scans were collected with a spectral resolution of 2 cm^{-1} and averaged for each pressure value. Data analysis was carried out using the GRAMS software (Thermo Electron). After buffer subtraction and baseline correction, the area of the amide I band (1700-1600 cm^{-1}) was normalized to one. All measurements were performed at least in duplicate. In addition, upon completion of the pressure-dependent measurement series, an IR spectrum of the unpressurized sample of the same preparation was recorded to check the time-dependent stability of the protein sample.

5.3.6 Turbidimetry

Lyophilized tubulin was dissolved in 80 mM PIPES (pH 6.8), 1 mM EGTA, 1 mM DTT, and 30 wt% glycerol to a concentration of about 2 mg mL^{-1} and put on ice for 10 min before centrifuging at 11,000 rpm and 2 °C for 2 min to remove potential aggregates. The exact protein concentration was determined by UV absorbance at 280 nm (ϵ_{280} = 1.15 mL mg^{-1} cm^{-1}) using a 1:200 dilution in 10 mM sodium phosphate (pH 6.8) and 1 wt% SDS. Prior to the experiments, 1 mM $MgCl_2$ and 1 mM GTP were added to 30 μM tubulin and put on ice. For experiments with MAP2c, 1 mM $MgCl_2$ and 1 mM GTP, 25 mM KCl and 6 μM rat MAP2c were added to 30 μM tubulin. To start the polymerization, 100 μL of the sample was placed in a prewarmed 96-well (37 °C). The polymerization process was followed by measuring the absorbance increase at 340 nm at 37 °C every 30 s after shaking for 3 s using a TECAN M200 multiplate reader. For high-pressure turbidimetry experiments, a home-built pressure cell equipped with two sapphire windows was used. The sample solution was directly filled into the cell and separated from the pressure-transmitting medium by a drop of immersion oil. To start the polymerization reaction, the pressure cell was quickly heated from 2 °C to 37 °C using a water bath prewarmed to 65 °C. A temperature of 37 °C could be reached within 2 min. During the measurement, the pressure cell was kept at 37 °C and every 5 s the absorbance at 340 nm was recorded (PerkinElmer Lambda 25). The absorbance change during the heating process was recorded as well to determine the dead time of the measurement.

5.3.7 Determination of Void Volumes

Void volumes are defined as water-inaccessible space inside proteins after removing all hetero atoms and were calculated using the CASTp server.[271] Water molecules were modeled as a spherical probe with a radius of 1.4 Å. The calculations were based on the PDB structures 3J6E, 3J6F and 3J6G,[331] and visualized using UCSF Chimera.[225]

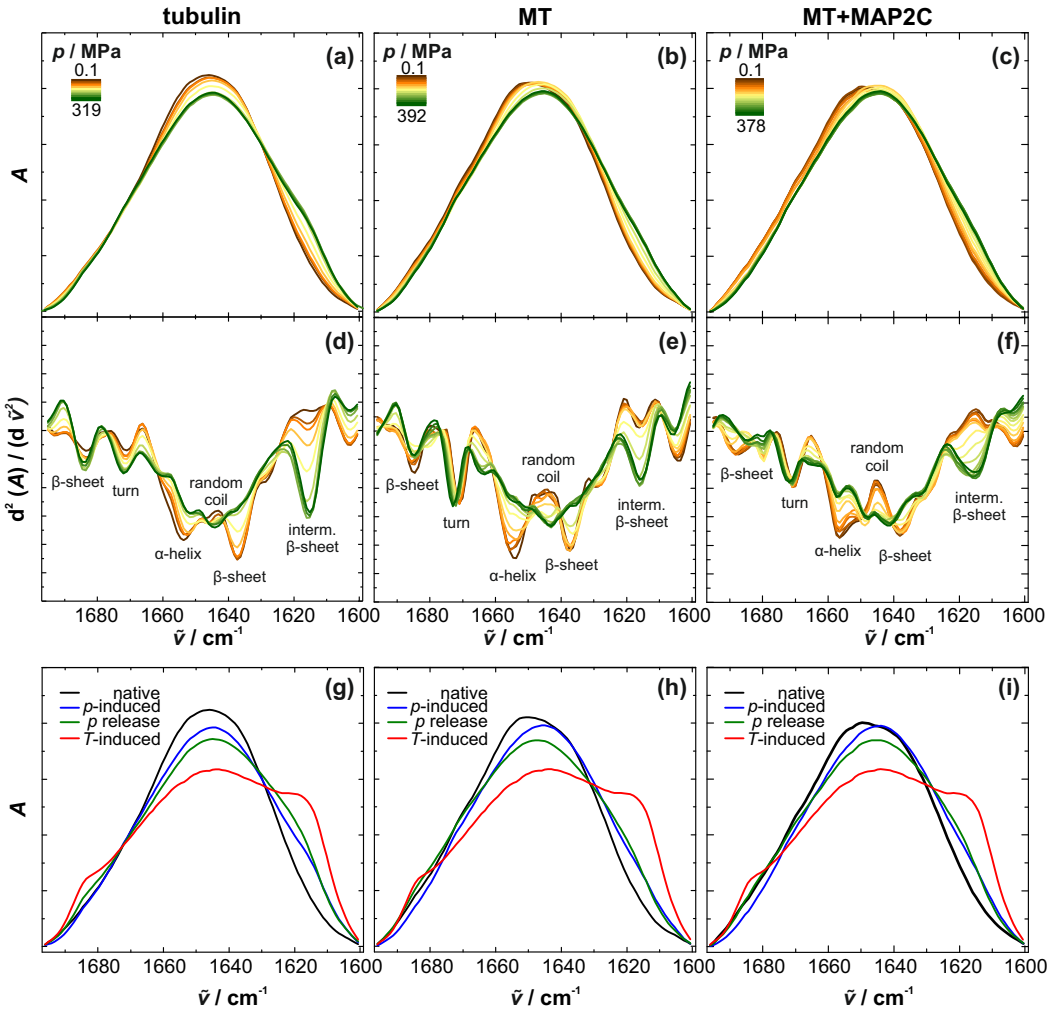

Figure 5.2 | Effect of pressure on the secondary structure of microtubules in distinct morphological states. Pressure-dependent (a-c) normalized FTIR absorbance spectra and (d-f) second-derivative spectra of the amide I' band (1700-1600 cm^{-1}) for $\alpha\beta$-tubulin, microtubules and MAP2c-bound microtubules at 37 °C. Temperature- and pressure-induced secondary structure changes shown in normalized absorbance spectra (g-i).

5.4 Results

5.4.1 Stability of Secondary Structure

To explore the pressure stability of microtubules, first the secondary structures of tubulin were examined in distinct morphological states as well as in the absence and presence of MAP2c, an isoform of MAP2 with a relatively short projection domain. To this end, the microtubules were polymerized in the presence of MAP2c at a 1:5 molar ratio of MAP2c to $\alpha\beta$-tubulin. Figure 5.2 shows the pressure-dependent FTIR spectra of $\alpha\beta$-tubulin, microtubules and MAP2c-bound microtubules. At atmospheric pressure, the area-normalized absorbance

spectra of their amide I' bands (1700-1600 cm^{-1}) are very similar in shape (Fig. 5.2a-c). Only small differences are visible in the corresponding second-derivative spectra, which originate mainly from the different contents of secondary structure elements such as α-helices, β-sheets, turns and random coils (Fig. 5.2d-f).[366] Upon pressurization up to $\sim$400 MPa, only marginal but still significant changes in spectral shape are visible, indicating no global unfolding of the protein. Conversely, high temperatures above 80 °C lead to unfolding with subsequent aggregation as indicated by the intermolecular β-sheet bands appearing at 1684 and 1618 cm^{-1} (Fig. 5.2g-i). The second-derivative spectra of $\alpha\beta$-tubulin, microtubules and MAP2c-bound microtubules reveal that the most affected region by pressure ranges from 1660 to 1630 cm^{-1}, which is assigned to α-helices, β-sheets, and random coils (Fig. 5.2d-f). Pressure induces vanishing of the minima at 1653 and 1637 cm^{-1} suggesting partial unwinding and unfolding of α-helices and intramolecular β-sheets. This is also consistent with the concomitant rise of the subband at 1644 cm^{-1}, which is assigned to random coils.[367] In case of $\alpha\beta$-tubulin and microtubules, the additional pressure-induced shift towards lower wavenumbers can be ascribed to enhanced exposure of such secondary structure elements to the solvent and thus strengthened hydrogen bonds between backbone carbonyl groups and the solvent molecules.[368] This observation might not only originate from partial unfolding, but also from disassembly of the heterodimers and microtubules leading to increased solvent-exposed secondary structure elements. By contrast, the presence of MAP2c causes a blue shift of such subbands, which can be ascribed to the pressure-induced elastic compression of chemical bonds.[369] This indicates that those structural elements may interact with MAP2c and thus are shielded from the solvent, also upon a pressure increase up to $\sim$400 MPa. In contrast, the minima at 1684 and 1671 cm^{-1} assigned to β-sheets and β-turns shift slightly in all three cases to higher wavenumbers. Hence, those secondary structure elements are buried inside the protein and are hardly affected by pressure. However, the increase of the subband around 1616 cm^{-1} gives evidence of intermolecular β-sheet formation and thus partial aggregation induced by pressure,[370] which is less pronounced compared to the thermally induced aggregation upon protein unfolding (Fig. 5.2g-i). The secondary structure of MAP2c itself is not affected by pressure in the investigated range (Fig. 5.3).

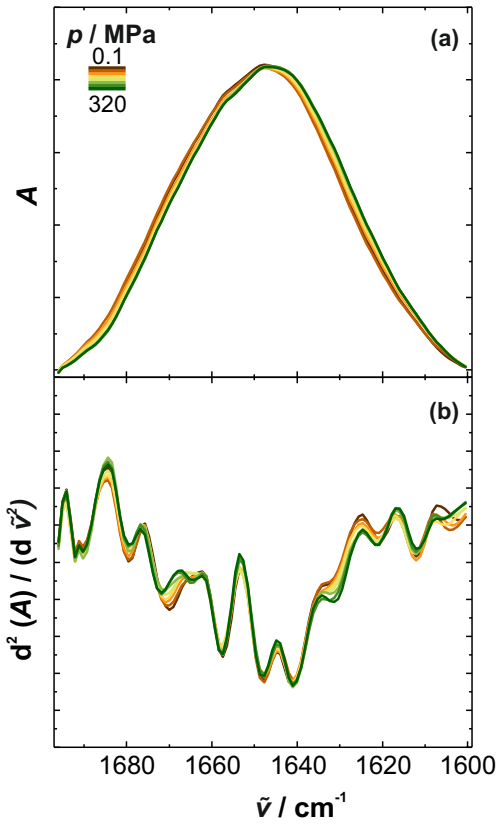

Figure 5.3 | Effect of pressure on the secondary structure of MAP2c. Pressure-dependent (a) normalized FTIR absorbance spectra and (b) second-derivative spectra of the amide I' band (1700-1600 cm^{-1}) for MAP2c at 37 °C.

5.4.2 Pressure Effect on the Quaternary Structure

Complementary high pressure Synchrotron SAXS studies were performed to obtain structural information of the microtubules on the Å-scale. Figure 5.4 exhibits the pressure-dependent and background-subtracted SAXS intensity profiles of microtubules in the active (in the presence of excess GTP) and non-dynamic (stabilized by taxol) state, respectively. At atmospheric pressure, the shape of the scattering data is in both cases typical for the form factor of hollow cylinders.[352] A qualitative fit shows that the active microtubules can be modeled as hollow cylinders with a wall thickness of 49 Å and an inner radius of 89-90 Å, which corresponds to the dimension of microtubules mainly consisting of 14 protofilaments (Fig. 5.4a).[371] This is in agreement with literature data.[306] In case of the taxol-stabilized microtubules, the inner radius is reduced to 84 Å when keeping the wall thickness constant (Fig. 5.4b). This is also consistent with the observation that taxol binding shifts the radial distribution to mostly 13 protofilaments.[332,372] Upon pressurization, the intensity of the

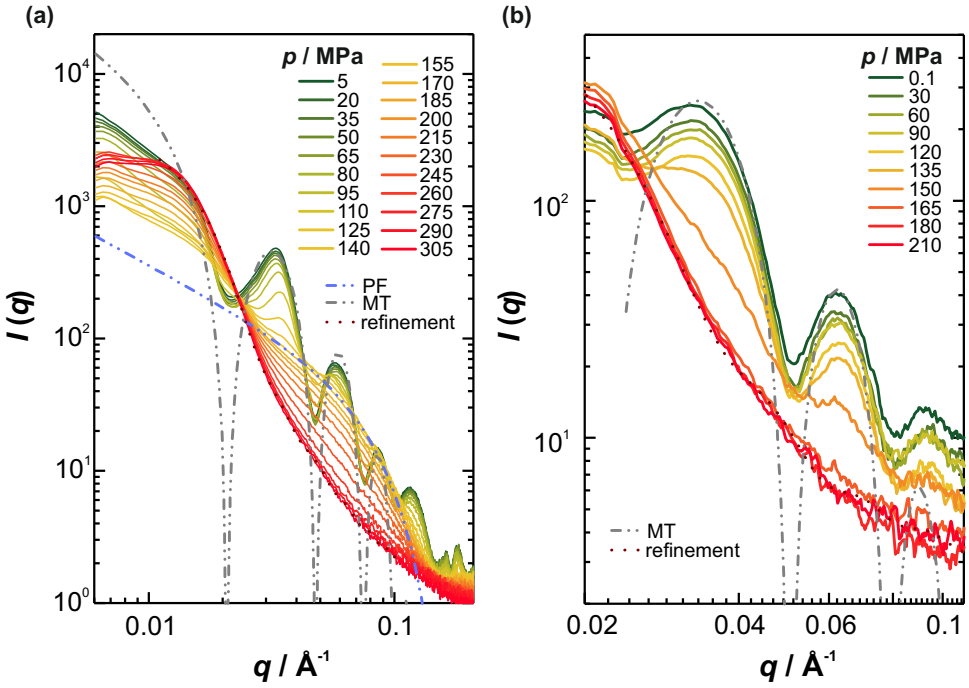

Figure 5.4 | Effect of pressure on the quaternary structure of active and non-active microtubules. Pressure-dependent and azimuthally averaged Synchrotron SAXS data of (a) active microtubules at 37 °C, and (b) taxol-stabilized microtubules at 25 °C. The dotted lines show the fits for calculation of the pair-distance distribution function (refinement). The dash-dotted lines indicate the fitted model scattering curves for microtubules (MT) and protofilaments (PF).

scattering maxima decreases, indicating disintegration of both microtubule species (Fig. 5.4). For the active microtubules, an intermediate species is observed at 155 MPa. Its scattering profile is characteristic for the protofilaments featuring a diameter of about 48 Å. Upon further compression up to 305 MPa, such protofilaments vanish and dissociate into oligomeric species. The pair-distance distribution function, $p(r)$, indicates a globular form for such oligomers with an average radius of gyration, R_g, of 130 Å (Fig. 5.4a; Fig. 5.5). In contrast, pressure induces the taxol-stabilized and non-active microtubules to dissociate directly into oligomeric species with a smaller R_g value of 90 Å (Fig. 5.4b; Fig. 5.5). At 150 MPa, the microtubules are completely dissociated without forming an intermediate species. This finding suggests that binding to taxol destabilizes protofilaments against pressure and causes simultaneous disintegration of lateral and longitudinal contacts of microtubules.

Next, it was tested whether MAP2c, known to longitudinally bridge tubulin subunits along the protofilaments, thereby inhibiting dynamic instability,[347] is able to stabilize the longitudinal contacts of active microtubules against pressure (Fig. 5.6a). At ambient conditions, the shape of the scattering pattern is entirely determined by the form factor of non-interacting

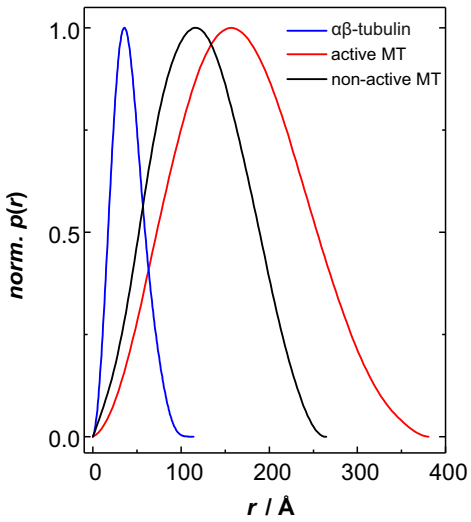

Figure 5.5 | Oligomeric species upon disintegration of microtubules. Pair-distance distribution functions, $p(r)$, of active microtubules at 37 °C and 305 MPa and non-active microtubules at 25 °C and 210 MPa indicate oligomeric species. The corresponding radii of gyration, R_g, are 130 Å (active) and 90 Å (non-active), respectively. The $p(r)$ function of $\alpha\beta$-tubulin (with R_g = 31 Å) calculated from the PDB structure 1JFF is shown as well. For better comparison, the pair-distance distribution functions are normalized to equal peak heights.

microtubules indicating that MAP2c does not induce formation of microtubule bundles unlike it does *in vivo*.[337] However, the SAXS profile is shifted to lower q in the presence of MAP2c, indicating an increase of the radial size of microtubules (Fig. 5.6b). Both, an increased protofilament number and a wall thickening due to MAP2c binding can contribute to the observed radial expansion of microtubules. Qualitative fits suggest that either the mean protofilament number is increased from 14 to 16 or MAP2c binding causes an 18 Å thick layer on the microtubule surface (Fig. 5.6b). As the electron density contrast between the region containing MAP2c relative to water is expected to be small,[347,373] the latter scenario seems to be unlikely. Again, a simultaneous disintegration of lateral and longitudinal contacts was found upon pressurization, but with $\alpha\beta$-tubulin dimers as the dominating species at 155 MPa, which denature and vanish upon further compression up to 305 MPa (Fig. 5.6a; Fig. 5.7). When starting from the unpolymerized state, a similar pressure-dependent behavior is observed for $\alpha\beta$-tubulin, exhibiting less pressure stability, however (Fig. 5.7). Hence, binding to MAP2c does not improve, but impairs the pressure resistance of the microtubule's longitudinal organization.

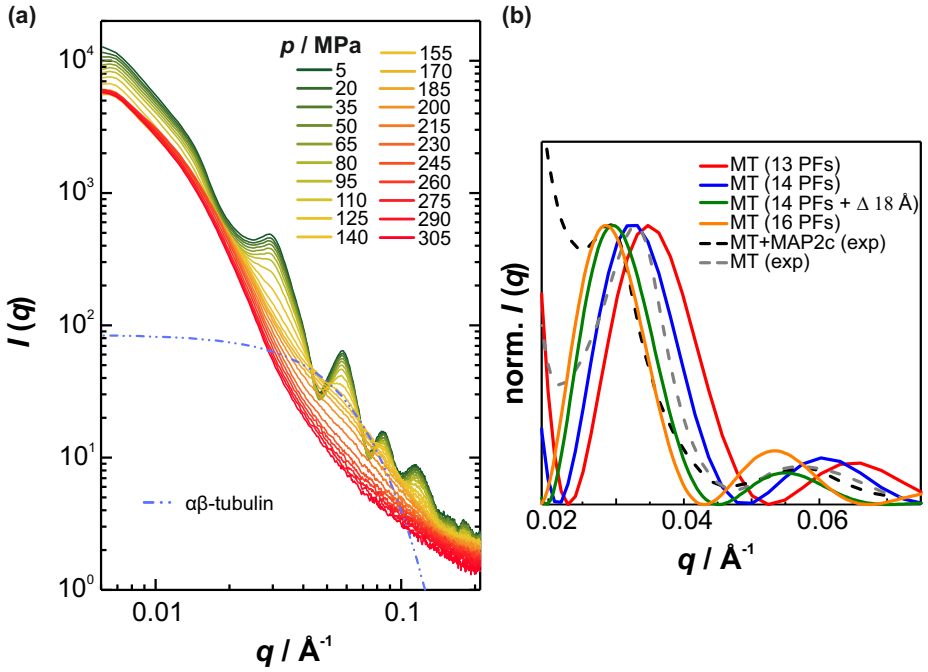

Figure 5.6 | Effect of MAP2c on the pressure stability of active microtubules. (a) Pressure-dependent and azimuthally averaged Synchrotron SAXS data of active microtubules at 37 °C and bound to MAP2c. The microtubules are polymerized in the presence of MAP2c with a 1:5 molar ratio of MAP2c to $\alpha\beta$-tubulin. The dash-dotted line shows the theoretical scattering profile of $\alpha\beta$-tubulin (pdb:1JFF). (b) Comparison between experimental scattering profiles of active microtubules in the absence and presence of MAP2c and theoretical form factors of microtubules consisting of different numbers of protofilaments or featuring increased wall thickness. For better comparison, the scattering profiles are normalized to equal height of the first peak maxima.

5.4.3 Pressure Stability of Microtubule Bundles

Further, the pressure stability of microtubule bundles, tubulin's next level of supramolecular self-assembly, was investigated, whereby the like-charge attraction between the taxol-stabilized microtubules was induced either by electrostatic condensation or by depletion attraction. Multivalent cations such as spermidine (3+) and spermine (4+) have been reported to condense onto microtubules as polyanions, thereby partially neutralizing their charge and thus inducing attractive interaction between them.[352] Depletion attraction can be found in crowded environments like those encountered in cells, where up to 40% of the cellular volume is occupied by different macromolecules.[5] As the ensuing effect of excluded volume increases the osmotic pressure and entropy penalty,[374] attractive forces between macromolecules such as microtubules are facilitated.[353] To mimic the intracellular crowding density, polyethylene glycol (PEG) 20k was used as a crowding agent. Figure 5.8a shows that both, electrostatic and depletion forces, are able to induce the formation of microtubule bundles, which are packed into a hexagonal lattice as indicated by the BRAGG peak positions

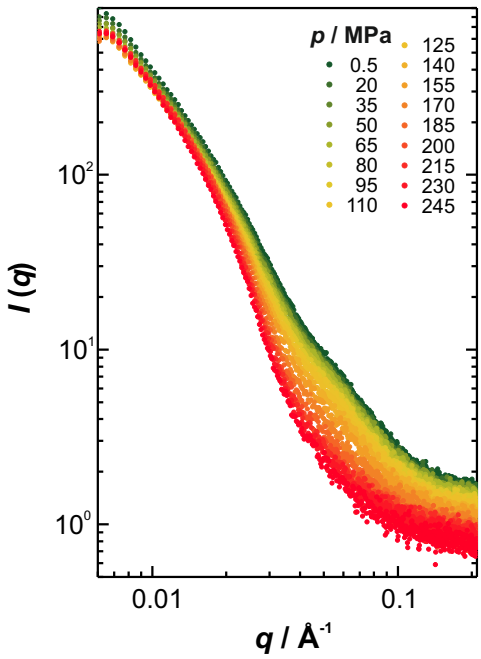

Figure 5.7 | Pressure stability of the $\alpha\beta$-tubulin dimer. Pressure-dependent and azimuthally averaged Synchrotron SAXS data of $\alpha\beta$-tubulin at 37 °C. Owing to the high sample concentration used, oligomers of tubulin already formed contribute to the scattering profiles.

at q_{10}, $q_{11} = \sqrt{3}q_{10}$, $q_{20} = 2q_{10}$, $q_{21} = \sqrt{7}q_{10}$, $q_{30} = 3q_{10}$, $q_{31} = \sqrt{13}q_{10}$, with a center-to-center distance of $a_{\mathrm{H}} = 4\pi/(\sqrt{3}q_{10})$. The peak maxima were obtained from LORENTZ fits. Some diffraction peaks are not apparent due to the overlapping form factor minima of microtubules at those positions.[352] In case of the cations spermidine and spermine, the center-to-center distances amount to 303 and 295 Å, respectively, whereas the presence of 10 and 20 wt% PEG 20k causes center-to-center distances of 303 and 292 Å, respectively. Hence, the tightness of the hexagonal bundles increases with the valence of the counterion as well as the crowding density, findings that are consistent with literature data.[352,353] When applying pressure, we observed a direct dissociation of the bundles into denatured oligomers of tubulin with the exception of spermidine-induced bundles, indicating that the pressure stability of the bundle phase is predominantly determined by the pressure limits of microtubules (Fig. 5.8c-e). In case of spermidine, pressurization up to 90 MPa induces a gradual dissociation of the bundles into individual microtubules, before those disintegrate completely at 150-165 MPa (Fig. 5.8b). This can be explained by the weakening effect of pressure on electrostatic interactions (referred to as the electrostrictive effect) because dissociation of ion pairs results in rehydration of the ions, which is accompanied by formation of a compact

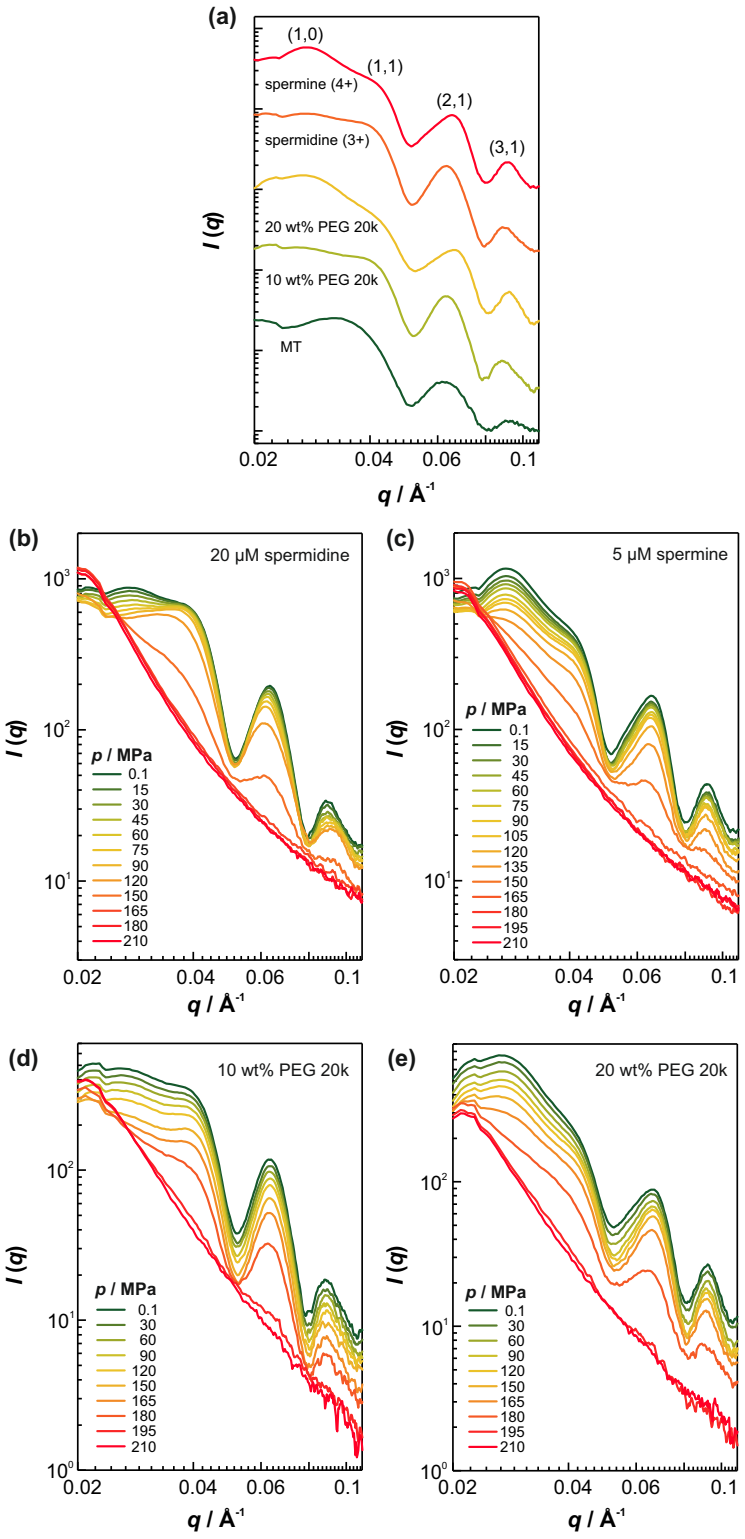

Figure 5.8 | Pressure stability of microtubule bundles. (a) Synchrotron SAXS data of various bundle types of taxol-stabilized microtubules at 25 °C and atmospheric pressure. Pressure-dependent scattering profiles of microtubule bundles induced by (b) 20 μM spermidine, (c) 5 μM spermine, (d) 10 wt% PEG 20k, and (e) 20 wt% PEG 20k.

hydration layer and thus reduction in the overall volume.[171] A similar pressure sensitivity was also observed for the Mg^{2+}-induced actin filament bundles (see section 4.4.2).[300] In contrast, the charge density of the tetravalent cation spermine seems to be high enough to overcome the electrostrictive effect and to maintain the electrostatic condensation of the microtubules up to 150-165 MPa, where pressure causes complete disintegration of taxol-stabilized microtubules. It is interesting to note that the crowding effect induced by PEG 20k elevates the pressure stability of microtubules to 180-195 MPa.

5.4.4 Pressure Sensitivity of the Microtubule's Polymerization Kinetics

By performing pressure-dependent turbidimetric measurements at 37 °C, the polymerization kinetics of microtubules was studied as a function of pressure as well (Fig. 5.9). In addition, using MAP2c as a nucleator, the initial nucleation step could be bypassed allowing one to distinguish between the events of nucleation and elongation (Fig. 5.9a). In the absence of MAP2c, a sigmoidal-shaped polymerization profile is observed, where small elongation-competent tubulin oligomers have first to be formed in the nucleation step for further lateral and longitudinal growth in the elongation phase (Fig. 5.9a). The addition of MAP2c leads to the nucleation phase being bypassed resulting in an exponentially shaped time course of polymerization (Fig. 5.9a). Increasing pressure modulates the kinetics of the nucleation and elongation events differently (Fig. 5.9b-e). While the *de novo* polymerization of tubulin is already retarded at 60 MPa and nearly inhibited at 90 MPa within the measured time range (Fig. 5.9b,c), the elongation kinetics is hardly affected by pressure up to 90 MPa (Fig. 5.9d,e). Owing to the relatively high dead time of the high-pressure set-up, the data are interpreted in a qualitative manner, only. However, the pressure-dependent decrease of the plateau values of the unnormalized turbidimetry data in both cases indicates that less amounts and/or shorter microtubules are formed under high pressure conditions. Such findings render the initial oligomer formation to be the most pressure-sensitive process of microtubule formation.

5.5 Discussion

According to LE CHÂTELIER's principle, an increase of pressure shifts a chemical equilibrium towards conformations occupying smaller volumes, commonly realized by release of defect volumes in biomolecules or at intermolecular interfaces.[172,193] In particular, pressure-

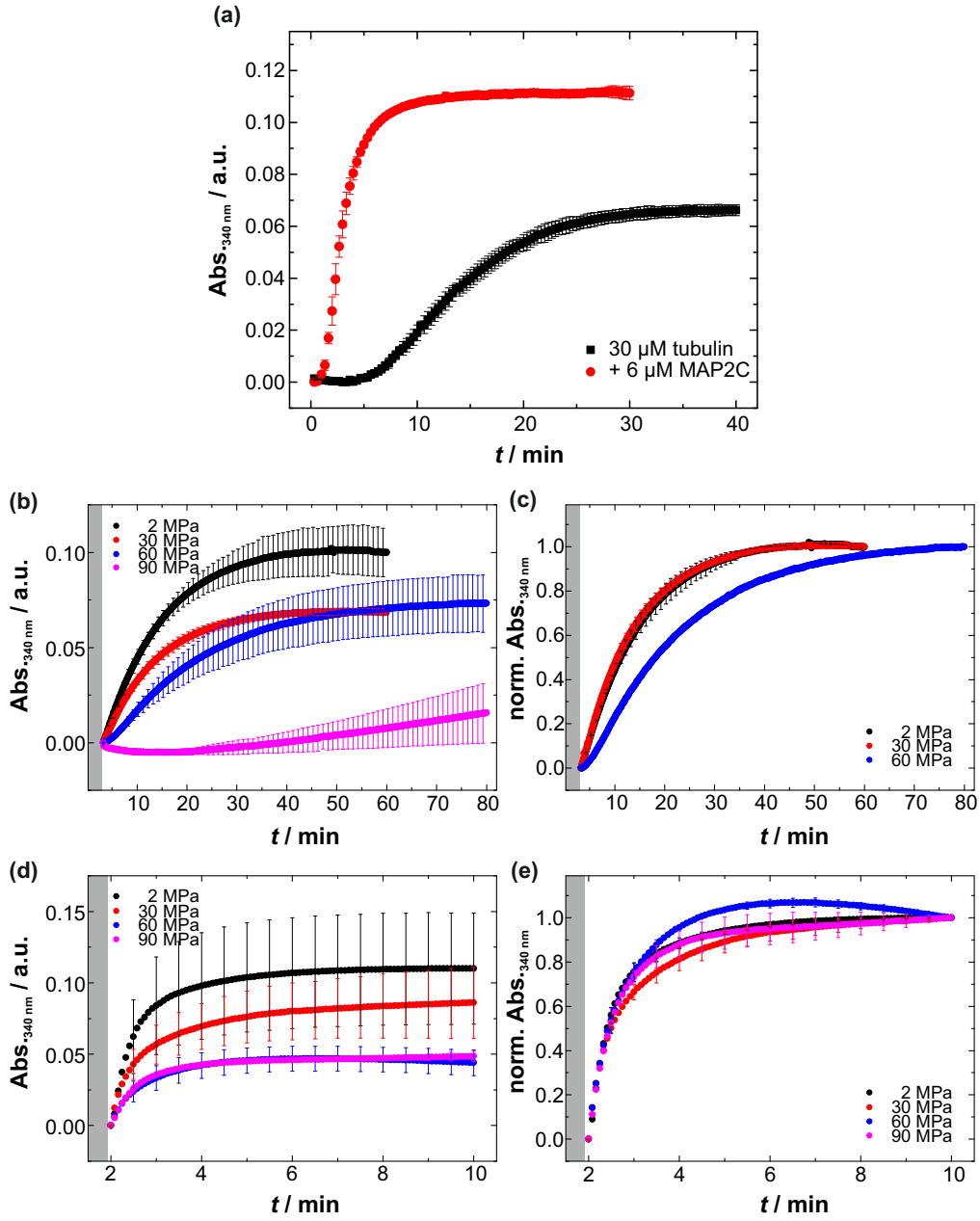

Figure 5.9 | Pressure effect on the microtubule formation. (a) Effect of 6 μM MAP2c on the polymerization of 30 μM $\alpha\beta$-tubulin at 37 °C and atmospheric pressure monitored by turbidimetry (at λ=340 nm). Pressure-dependent time course of the *de novo* polymerization and the elongation of tubulin at 37 °C and in the (b) absence and (d) presence of MAP2c. For better comparison of the underlying kinetics, the corresponding normalized turbidimetry data are shown in (c) and (e).

induced unfolding of proteins is mainly determined by the presence of internal cavities and voids.[166,167,170] To reveal the molecular origin of microtubules' pressure sensitivity, the water-inaccessible voids (without mouth openings to the outside bulk solution) located inside microtubules based on cryo-EM structures were calculated using CASTp.[271] Significant voids in the tubulin subunits and packing defects at the contact sites along the protofilaments are found, whereas the lateral contacts between the protofilaments do not contribute to any significant defect volumes. Such interfilament contacts are only created by a single point, where a tyrosine or histidine residue of one subunit is sandwiched by two loops of the adjacent subunit, resembling a lock-and-key configuration.[318] Despite a high degree of identity, α-tubulin shows increased internal void volumes compared to β-tubulin (Fig. 5.10a). Notably, events like GTP hydrolysis and binding to taxol lead to an increase of voids within the α-subunit (Fig. 5.10c). In contrast, packing defects along the protofilaments are more pronounced for the intradimer than for the interdimer interface (Fig. 5.10b,c). Therefore, such voids and packing defects can significantly impair the stability of microtubules under high pressure conditions.

Hence, the results presented here clearly show that the lateral contacts are the most pressure-sensitive interactions in active microtubules. Such phenomenon can be explained by the fragile lock-and-key configuration forming the lateral contact, which is susceptible to perturbation by the high local compressibilities of internal voids of the tubulin subunits. Thus, any minor structural change of this contact site, most likely induced by the partial unfolding and unwinding of secondary structure elements of tubulin as observed by FTIR spectroscopy, can cause lateral dissociation of the microtubules into protofilaments. The subsequent disintegration of the protofilaments observed upon further pressurization can be interpreted as a consequence of release of packing defects at the longitudinal contact interfaces. This is further facilitated by the pressure-induced weakening of salt bridges and polar interactions, which are involved in forming the intra- and interdimer contacts.[313] Another possibility is the release of the nucleotide at the E- and/or N-site, which has been demonstrated to cause disintegration of filaments formed by actin and its prokaryotic homologue ParM upon pressurization.[267,375] In case of taxol-stabilized microtubules, the pressure stability of the microtubule protofilaments was found to be decreased. Although taxol binds to a pocket in β-tubulin and restores the GDP lattice to a GTP-like extended state by swelling its binding site and expanding longitudinally the interdimer interface,[331] the void analysis shows that

taxol binding is also accompanied by significantly increased formation of packing defects in α-tubulin (Fig. 5.10c). This could explain the simultaneous dissociation of lateral and longitudinal contacts of taxol-bound microtubules under high pressure conditions. In contrast to taxol, the decreased pressure stability of protofilaments observed in the presence of MAP2c is more likely caused by additional packing defects at the longitudinal interfaces provoked by lattice constraints, which are a result of MAP2c acting on the protofilament conformation. Interestingly, although taxol and MAP2c modulate the number of protofilaments and thus the lattice of microtubules, distinguishable pressure stabilities for the lateral organization among the microtubule types were not found.

Owing to the observed pressure sensitivity of the lateral and longitudinal contacts in microtubules, they also determine the pressure stability of the bundle phase, which is in stark contrast to the effect of pressure on actin filament bundles. As described in section 4.4.2,

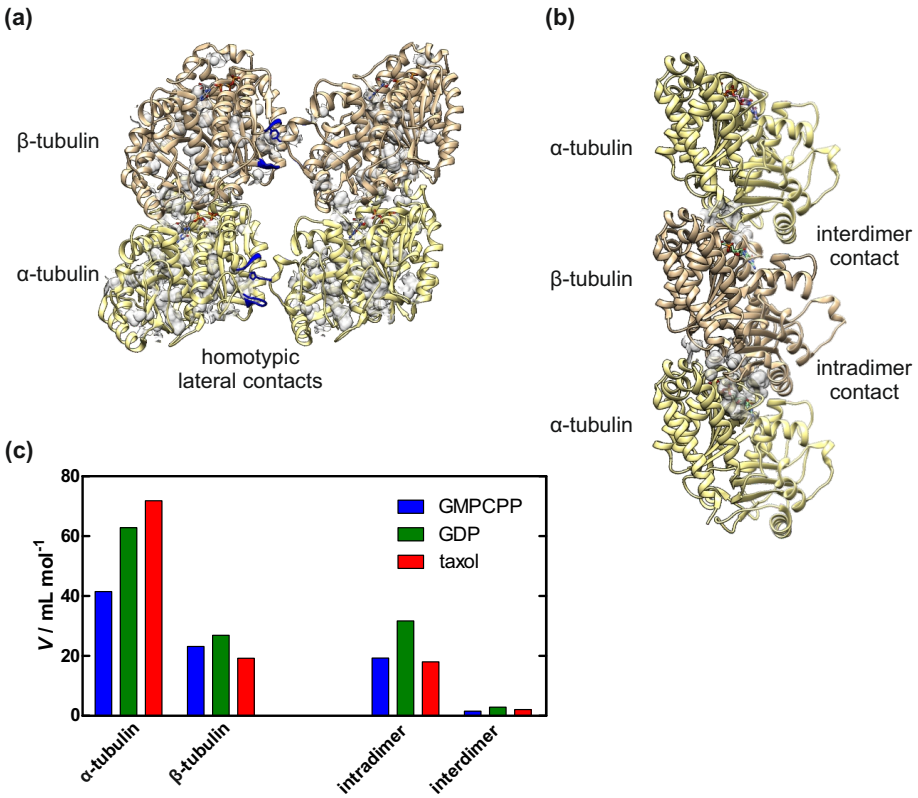

Figure 5.10 | Water-inaccessible voids located in microtubules. A spherical probe for H_2O with a radius of 1.4 Å was used for the calculations. (a) 3D structure of the GMPCPP-bound microtubule showing the voids located in the α- and β-subunits (marked in grey) as well as the homotypic lateral contacts between the protofilaments (marked in blue). (b) Packing defects (voids) formed at the inter- and intradimer contact sites along the protofilament. The images were prepared and modified with UCSF Chimera v1.11.2[225] using pdb:3J6E.[225] (c) Comparison of the total volumes of voids/packing defects within the subunits and at the contact sites of microtubules for distinct chemical states: bound to GMPCPP, GDP or taxol.

the interfilament interactions between actin filaments realized by electrostatic condensation (induced by Mg^{2+}) and a protein crosslinker (fascin) are gradually diminished by pressure leading to a decreasing tightness of the bundle phase and thus a continuously increasing interfilament distance before complete dissociation into actin filaments occurs.[300] In case of microtubule bundles, pressure does not modulate the packing tightness before complete disintegration of the bundles into denatured oligomers. Hence, actin filaments and microtubules, as the most important components of the eukaryotic cytoskeleton, exhibit not only differences in the morphology and function, but also in the pressure stability. At 150 MPa, the upper limit of the physiologically relevant pressure range, when the microtubules and their bundles are completely disintegrated, actin filaments start to deform, and their dissociation is completed beyond 400 MPa.[270]

Despite the high pressure sensitivity of such cytoskeletal components, life has invaded the high-pressure habitats of marine depths. This raises the question which strategies deep sea organisms have evolutionarily established at a molecular level to improve the pressure resistance of their cytoskeleton. For microtubules, the effect of macromolecular crowding, a typical generic phenomenon of the cellular environment, was found to increase the pressure stability of microtubules by 15-45 MPa. The high content of macromolecules inside cells restricts the accessible volume by the excluded volume effect (steric repulsion; see section 2.1.1) and thus entropically stabilizes proteins as well as enhances their associations by favoring more compact and folded structures.[8] In addition, it was found that accessory proteins like MAP2c can also assist to ensure the formation of microtubules under high pressure stress, thereby acting as a nucleator to bypass the pressure-sensitive nucleation step, the initial event of tubulin self-assembly. The pressure-dependent retardation of the nucleation step corresponds to a positive activation volume, which reflects the formation of large defect volumes and the release of hydration water during the assembly of tubulin oligomers as elongation-competent nuclei. Similar observations were also made for the polymerization reaction of actin filaments (see section 4.4.1).[277,376]

5.6 Conclusions

In summary, the results presented in this chapter show that microtubules are hardly stable under abyssal conditions, where pressures up to at least 100 MPa are reached. This pres-

sure sensitivity can be mainly attributed to the internal voids and packing defects in the microtubules. Most importantly, at every structural level, microtubules were found to be less pressure stabile compared to actin filaments. In particular, lateral and longitudinal contacts were shown to feature different pressure stabilities in case of dynamic microtubules. The more pressure-labile lateral interactions cause a progressive disintegration of the microtubules into protofilaments upon initial pressurization. The longitudinal dissociation starts from 150 MPa. This is consistent with the *in vivo* observation that pressures up to 30 MPa induce rapid and reversible depolymerization of spindle microtubules in a variety of eukaryotic cell types and thus inhibit mitosis.[262,355,356] Hence, the intactness of both contact types is necessary for the functionality of microtubules *in vivo*. Further, it could be shown that such contacts also define the pressure stability of the bundle phase. The dynamic instability of microtubules is commonly explained by thermodynamically labile associations of $\alpha\beta$-tubulin, next to conformational changes driven by GTP hydrolysis. Both, taxol and MAP2c are known to bind to microtubules and prevent them from depolymerization. However, here it was found that the pressure instability of the contact sites does not correlate with the dynamics of microtubules. In contrast, binding to taxol or MAP2c causes a decreased pressure stability of the protofilaments compared to the active microtubule protofilaments. Hence, owing to the high pressure sensitivity of the microtubules, adaptation strategies, both intrinsic and extrinsic, must exist in nature to improve the pressure resistance of cellular dynamics and movements found in living organisms thriving under extreme pressure conditions. In this study, the cellular environment itself as a crowded place and accessory proteins (e.g. MAP2c as nucleator) were found to increase the pressure stability of microtubules and accelerate their otherwise highly pressure-sensitive *de novo* formation. However, further adaptation strategies need to be unravelled in order to fully understand how the range of extreme environments that organisms can successfully inhabit could expand.

CHAPTER 6

FOLDING STABILITY OF AN RNA HAIRPIN - THE ROLE OF HYDRATION, OSMOLYTES, AND CROWDING*

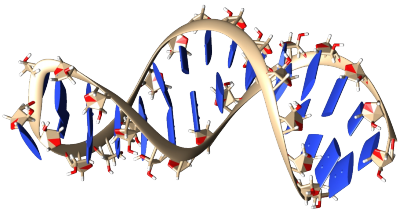

Abstract

Folding of ribonucleic acids (RNAs) is driven by several interrelated factors, such as base pairing and stacking, chain entropy, and ion-mediated electrostatics, which have been studied in great detail. However, the power of background molecules in the cellular milieu is often neglected. In this chapter, the effects of osmolytes and macromolecular crowding on the folding stability of a hairpin-structured RNA thermosensor is studied. First, the crowding study shows that the folding stability of the RNA inside the cell is comparable with that in the dilute buffer, despite a strong destabilization of the RNA that is suggested by the comparative *in vitro* experiments. Second, the effect of common osmolytes in modulating the stability of the RNA is found to depend strongly on the interplay between water, salt and osmolyte. The findings demonstrate the importance of the biological fluid in driving the thermodynamics and thus the function of RNA secondary structures.

* The RNA image was prepared and modified with UCSF Chimera v1.11.2 [225] using pdb:2GIO.

* The work herein described has been published in the following peer-reviewed research articles and subsequently reprinted in parts with the permission of the journals. Contributions of co-authors are either dinstinctly marked or not shown as results of this thesis.

1. M. Gao, D. Gnutt, A. Orban, B. Appel, F. Righetti, R. Winter, F. Narberhaus, S. Müller, and S. Ebbinghaus. RNA Hairpin Folding in the Crowded Cell. *Angew. Chem. Int. Ed.* **55** (2016) 3224-3228

   was published online on February 2nd, 2016 and the DOI is 10.1002/anie.201510847. In this chapter, figures and text are partially reproduced in sections 6.3 and 6.4.1. Copyright ©2016 The Authors. Published by Wiley-VCH Verlag GmbH & Co. KGaA. The used text paragraphs and figures were reformatted to the format of the thesis (e.g. text font, reference numbering, figure numbering). In addition, supplementary figures and tables as well as equations used for fitting were moved to the main text to improve the quality of reading.

   Author contribution: S.M., F.N and S.E. designed the research, M.G., D.G., A.O., B.A. and F.R. performed research, M.G., D.G., R.W. and S.E. analyzed data and interpretated the results, M.G., D.G. and S.E. wrote the paper. All authors discussed the results and commented on the manuscript.

2. M. Gao, L. Arns, R. Winter. Modulation of the Thermodynamic Signatures of an RNA Thermometer by Osmolytes and Salts. *Angew. Chem. Int. Ed.* **56** (2017) 2302-2306

   was published online on January 19th, 2017 and the DOI is 10.1002/ange.201611843. In this chapter, the publication is partially reproduced in sections 6.3 and 6.4.2 with the permission by John Wiley & Sons, Inc. Copyright ©2017 Wiley-VCH Verlag GmbH & Co. KGaA, Weinheim. The used text paragraphs and figures were reformatted to the format of the thesis (e.g. text font, reference numbering, figure numbering). Some phrases in active voice were changed to those in passive voice. In addition, supplementary figures and tables as well as equations used for fitting were moved to the main text to improve the quality of reading.

   Author contribution: M.G. and R.W. designed the research, M.G. and L.A. performed research and analyzed data, M.G. and R.W. interpretated the findings and wrote the paper.

6.1 Introduction

Nucleic acids participate in a wide range of cellular functions including information storage and translation, gene regulation and biochemical catalysis both in prokaryotes and eukaryotes (Fig. 6.1a).[377,378] Thereby, the three most important and prominent RNA types are messenger RNA (mRNA), transfer RNA (tRNA) and ribosomal RNA (rRNA), forming together the translation machinery (Fig. 6.1c). However, they are not only passive carrier with a random conformation as for the mRNA or a scaffold for the essential ribosomal proteins in the ribosomes or simply an adapter delivering the amino acid to the ribosome, but nowadays it is known that they can adopt diverse but defined structures and have also regulatory and catalytic functions.[379–381] For instance, microorganisms use so-called RNA thermometers to coordinate temperature-dependent gene expression.[380] Thereby, the translation of cold- and heat-shock proteins is very often involved. Such hairpin-structured thermometers are usually located at the 5'-untranslated region of the mRNA blocking the ribosome-binding site (RBS) and function either as a zipper or as a switch to regulate the ribosome access in a temperature-dependent manner.[380] The hairpin structure changes its secondary structure in response to temperature. In the case of the RNA zipper, the hairpin "melts" upon temperature increase and exposes the RBS allowing translation. This kind of built-in biosensor is commonly used in microorganisms to probe and to adapt to an altering environmental temperature.[380] Therefore, understanding the folding mechanism and the structure-function releationship of nucleic acids is essential in every aspect.

Both, DNA and RNA are biopolymers consisting of nucleotides linked by phosphodiester bonds (Fig. 6.1b). The secondary structure of hairpins and duplexes is largely guided by the hydrogen bond formation between complementary pyrimidine and purine nucleobases. The pyrimidine bases include cytosine (C), thymine (T) and uracil (U), whereas guanine (G) and adenine (A) belong to the purine bases.[377] The thymine base, the 5-methyl derivative of uracil, is exclusively used in DNA, whereas uracil is found only in RNA.[377] In DNA, A·T and G·C base pairs can be only found, while non-canonical base pairs are more frequently formed in RNA. The only chemical difference between RNA and DNA is the pentose sugar. DNA contains 2'-deoxyribose, whereas RNA is composed of ribose.[377] The consequences of the additional 2'-OH group include the conformation of the helical structure and the hydration level of the nucleic acid. Upon base pairing, two antiparallel polynucleotide strands

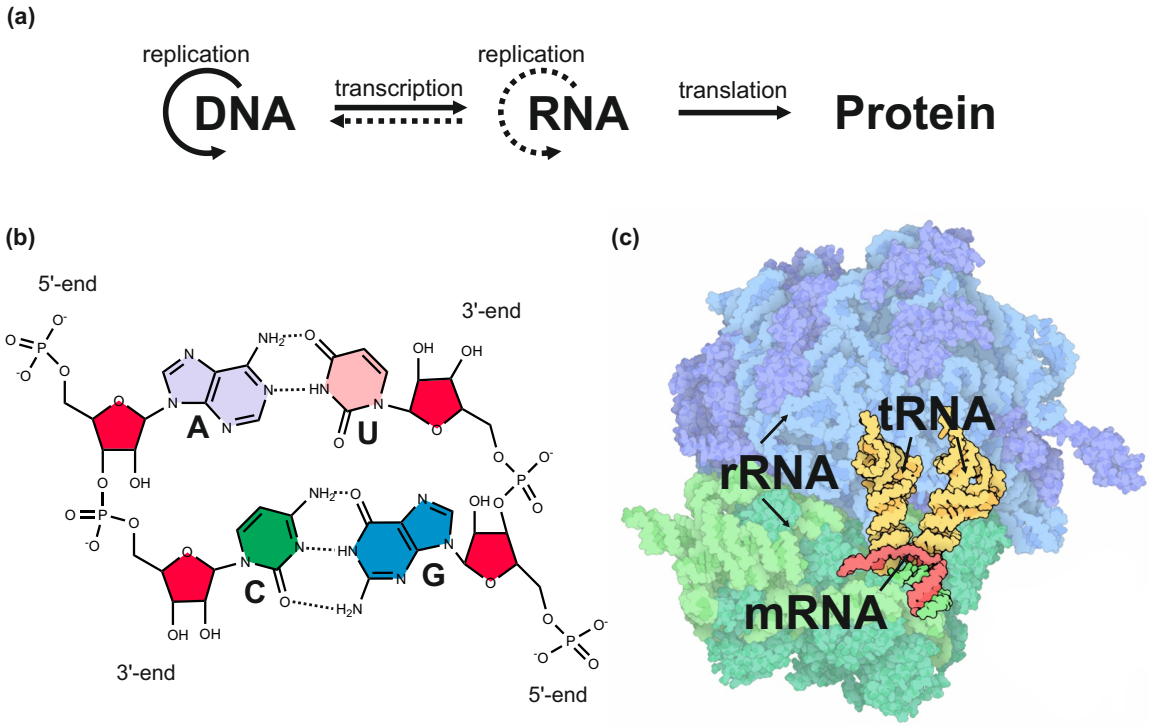

Figure 6.1 | The role of RNA in the central dogma of molecular biology. (a) Information flow in a biological system. Sequential information can be transferred from nucleic acid to nucleic acid and to protein, but not from protein to protein or to nucleic acid. (b) RNA is a polymer of nucleotides consisting of a ribose, a phsophate, and bases such as adenine (A), cytosine (C), guanine (G) and uracil (U). Base pairs are formed between A and U or between C and G via hydrogen bonds. (c) The three most abundant RNA types are messenger (m), ribosomal (r) and transfer (t) RNA. The mRNA contains the genetic code copied from the DNA during transcription. The rRNA is part of the ribosome which is responsible for the translation and thus the protein synthesis. The tRNA functions as an adapter between the mRNA and the protein by carrying an amino acid to the ribosome. The image is taken from `http://pdb101.rcsb.org/motm/121`.

do not simply form a side-by-side arrangement, but rather a helical structure. Thereby, the geometry of the sugar-phosphate backbone forces the duplex to adapt a right-handed helical structure. In the case of DNA, the B-conformation is preferred, in which the helix makes a complete turn every 3.4 nm (corresponds to 10 base pairs per turn).[382] In the case of RNA, due to the additional 2'-OH group, duplexes and helices can only adapt the A-conformation, which is a thicker helix with shorter distances between the base pairs. The structural differences are mainly caused by the two different conformations of sugar: C2'-*endo* in B-form and C3'-*endo* in A-form.[382] Another important feature of the helical structure of nucleic acids is the existence of major and minor grooves along the helical axis. They arise from the position of the glycosidic bonds relative to the interface between the base pairs.[383]. Furthermore, the additional 2'-OH group in RNA helical structures has been shown to attract water molecules as well as to function as a scaffold for the water network in the minor groove.[384]

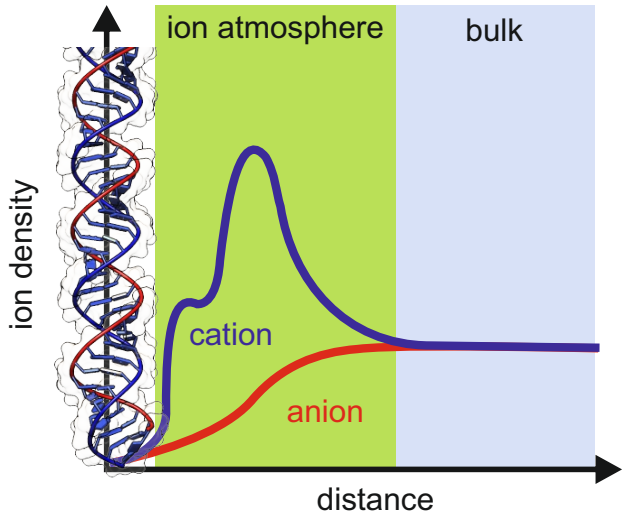

Figure 6.2 | Ions surrounding nucleic acids described by an ion atmosphere. Schematic representation of the ion density around a nucleic acid helix as a function of distance from the molecule. Cations are accumulated and anions are excluded near to the nucleic acid. The layered profile of the cations indicates its accumulation in the grooves and in the immediate vicinity of phosphates. The green area comprises the ion atmosphere, whereas the bulk is described by the blue area. Such density profiles are typically obtained from nonlinear POISSON-BOLTZMANN predictions.[386]

In contrast to DNA, RNAs appears usually as single-stranded molecules and thus can fold into specific tertiary structures. Thereby, folding of secondary and tertiary structures is driven by several interrelated factors consisting of WATSON-CRICK base pairing and stacking, chain entropy, ion-mediated electrostatics, and non-canonical interactions.[385]

Nucleic acids can be seen as polyanions and feature a high charge density as adjacent phosphate groups are only separated in the sub-nanometer range.[387] Therefore, the free energy of nucleic acid folding and interactions are strongly affected by electrostatics. As a consequence, nucleic acid-ion interactions are an essential component to ensure structure and function of nucleic acids by counterion screening. Screening describes the reduction of long-range electrostatic interactions between like-charged molecules.[388] These nucleic acid-ion interactions can be at least divided into two classes.[389] There are specifically bound ions, which are visible to traditional structural techniques and partially dehydrated, but the majority of interacting ions are part of an ion atmosphere, which is a dynamically and diffusely associated sheath of ions surrounding the nucleic acid polyanion.[388,390] Those ions do not directly interact with the nucleic acid surface and their hydration is not perturbed.[389] The ion atmosphere is characterized by a counterion accumulation and a co-ion depletion (Fig. 6.2).[388,391] Overall, charge neutrality must prevail, that means that the sum of the charges

from the ion atmosphere must be equal and opposite to that of the nucleic acid:[391,392]

$$\sum_i q_i \Gamma_i = -q_{\text{nucleic acid}}, \tag{6.1}$$

whereby q_i describes the charge of ionic species i, $q_{\text{nucleic acid}}$ the net charge of the nucleic acid, and Γ_i is the preferential interaction coefficient indicating the number of associated ions. Interestingly, it was reported that the salt types determine the extent of anion exclusion and cation inclusion within the ion atmosphere.[391] Further, it was found that salts with low activity coefficients exhibit greater inclusion of both, cations and anions, within the ion atmosphere, which gives evidence for cation-anion correlation effects inside the ion atmosphere.[391] However, the fluctuating nature of the ion atmosphere makes its experimental description difficult. In contrast, many theoretical models exist to characterize the ion atmosphere.[387,388] The two prominent and influential models are the MANNING counterion condensation theory and the POISSON-BOLTZMANN theory. In the counterion condensation theory, the nucleic acid is modeled as a cylindrical polyelectrolyte featuring a linear charge density. Its high charge density induces cation condensation at the surface of the polyanion until the effective charge is reduced below a critical value. Counterion condensation takes place when the so-called MANNING parameter $\xi = l_{\text{B}}/b > 1$, where b is the distance between charges, and l_{B} is the BJERRUM length with $l_{\text{B}} = e^2/4\pi\epsilon_0\epsilon k_{\text{B}}T$.[393] The counterion condensation is driven by the favorable electrostatic enthalpy for the ion-nucleic acid interactions. When $\xi < 1$, the unfavorable entropy change, arising from the loss of their translational freedom in solution, dominates and condensation is prevented.[387] However, the MANNING model might be oversimplified because atomic-level properties and interactions of the ions, solvent properties and hydration of the polyanion are not considered.[387]
In contrast, the non-linear POISSON-BOLTZMANN theory is more comprehensive and widely used to quantitatively predict the composition and shape of the ion atmosphere:[387]

$$\nabla^2\Phi(\vec{r}) = -\frac{1}{\epsilon\epsilon_0}\left[\rho_{\text{nucleic acid}}(\vec{r}) + \sum_i c_{i,\,\text{bulk}} q_i \exp\left(\frac{-q_i\Phi(\vec{r})}{k_{\text{B}}T}\right)\right], \tag{6.2}$$

whereby $\Phi(\vec{r})$ is the electrostatic potential and $\rho_{\text{nucleic acid}}$ the fixed charge density of the nucleic acid, and the summation describes the charge density of all species of mobile ions in solution. Thereby, the ions are treated as a continuous charge density and not as dis-

crete particles and thus their average potential is determined by the BOLTZMANN factor, which is the exponential term in Eq. 6.2. Hence, the nonlinear POISSON-BOLTZMANN equation describes the mean-field electrostatic interactions of ions with the nucleic acid in solution.[388] Atomic-level properties of the ions including their size, polarizability and solvation are neglected, however.[388]

In addition, water has been found to be a vital part in forming duplexes and hairpins of nucleic acids. For instance, it displays ordered hydration patterns in both grooves of A-RNA helices with longitudinally bridging water molecules between the ionic phosphate oxygens in the major groove and transversal hydration linking adjacent 2'-hydroxyl groups in the minor groove.[384] Moreover, the extent of hydration in the helix state has been shown to determine the thermodynamic stability of the nucleic acid.[384] A greater hydration is correlated with a higher thermodynamic stability. To determine the change in macromolecular hydration accompanied by macromolecular reactions and conformational transitions, osmotic stress experiments have been frequently used.[154,394] In such experiments, inert (non-interacting) cosolvents are used to modulate the chemical activity of water. The water activity of a cosolvent-containing solution can be determined by measuring its osmotic strength, which is related to the reduced vapor pressure of water above the solution compared to that above pure water.[394] The osmotic stress method is based on the GIBBS-DUHEM equation:[154]

$$0 = -S\mathrm{d}T + V\mathrm{d}p - \sum_i n_i \mathrm{d}\mu_i, \tag{6.3}$$

where S is entropy, V volume, T temperature, p pressure, μ_i the chemical potential and n_i the number of moles of species i. Usually, an equilibrium dialysis experiment is used as model to describe the direct and indirect impacts of cosolvent and water on the nucleic acid at constant temperature and pressure. A semipermeable membrane separates a solution containing a macromolecule with N_w and N_cs molecules of water and cosolvent and a reference solution containing n_w and n_cs molecules of water and cosolvent. Both solutions are in equilibrium:[154]

$$\begin{aligned} \mathrm{d}\mu_\mathrm{M} + N_\mathrm{w}\mathrm{d}\mu_\mathrm{w} + N_\mathrm{cs}\mathrm{d}\mu_\mathrm{cs} &= 0 \\ n_\mathrm{w}\mathrm{d}\mu_\mathrm{w} + n_\mathrm{cs}\mathrm{d}\mu_\mathrm{cs} &= 0. \end{aligned} \tag{6.4}$$

For the GIBBS free energy change of the macromolecule, it means:[154]

$$\mathrm{d}G_{\mathrm{M}} = -N_{\mathrm{w}} \left(1 - \frac{n_{\mathrm{w}}/n_{\mathrm{cs}}}{N_{\mathrm{w}}/N_{\mathrm{cs}}}\right) \mathrm{d}\mu_{\mathrm{w}} \equiv -N_{\mathrm{ew}} \mathrm{d}\mu_{\mathrm{w}}. \tag{6.5}$$

N_{ew} is the excess or deficit number of waters at the surface of the macromolecule compared to those in bulk. As μ_{w} and μ_{cs} are coupled, a similar equation can be obtained from the point of view of the cosolvent.[154]

In osmotic stress experiments, N_{w} is equated with the actual number of water molecules that are physically in contact with the macromolecule. Hence, in the case of a reaction, such as the unfolding equilibrium, the equilibrium constant, K, can be expressed as follows:

$$\Delta N_{\mathrm{w}} = \frac{\partial \ln K}{\partial \ln a_{\mathrm{w}}}, \tag{6.6}$$

where ΔN_{w} is the stoichiometric number of water associated with the unfolding reaction, and a_{w} is the water activity. The equation is based on the WYMAN linkage.[395] Osmotic stress experiments have revealed that a change in water activity can significantly affect the conformational preferences of nucleic acids to form base pairs and thus helical structure. Generally, the cosolvent-induced decrease of water activity is reported to be unfavorable for the formation of WATSON-CRICK base pairs.[69,396,397] This is commonly explained by the release of water molecules upon unfolding. Thereby, ΔN_{w} is commonly interpretated as the actual or stoichiometric number of water involved in the reaction. However, Serge N. Timasheff criticizes that the concepts of preferential binding and hydration (see section 2.1.2) are ill-used in the interpretation of osmotic stress experiments because cosolvents cannot be non-interacting (inert).[151] Therefore, solute-cosolvent interactions, cosolvent-induced hydration perturbation and the fact that the unfolding event is accompanied by an increase in SASA, are neglected.[110,398,399]

As *in vivo* the water activity and polarity inside cells are reduced due to the high content of biomolecules, osmolytes and salts, it is necessary to understand the role of hydration in dictating the thermodynamics of nucleic acids. Understanding the hydration change during nucleic acid folding is also important to understand and to predict how natural osmolytes affect secondary and tertiary structures of nucleic acids *in vivo*. While the effect of osmolytes on protein folding and association has been studied largely (see section 2.1.2), only

few attempts have been made for nucleic acids. Those investigations suggest that the stabilizing effect of TMAO on proteins might be not valid for nucleic acids. Thermal melting experiments reported on stabilization of RNA tertiary structures, whereas the effect on secondary structure is marginal and destabilizing.[139,161,400,401] These findings are explained by weak favorable interactions of TMAO with nucleobases and strong exclusion from the phosphate backbone.[139] Conversely, denaturants such as urea seem to work universally for proteins and nucleic acids via direct interactions. As a consequence of the preferential binding effect, urea stabilizes the unfolded state of a biomolecule in trying to maximize its SASA.[111–113,161,163,402] Conclusions on the impact of osmolytes on the secondary structure level are mainly drawn from model nucleic acid duplexes and hairpins with perfectly matched WATSON-CRICK base pairs. However, mismatches and non-canonical base pairs are naturally occurring and important RNA secondary structure motifs serving as binding and recognition sites for metals, small ligands or other biomolecules.[403] They often cause large helical perturbations and changed hydration patterns of the A-form helix of RNAs.[404,405] Moreover, the intricate interplay between water, salt and cosolvents in driving the thermodynamics of nucleic acids is also still far from understood.

In addition, the effect of macromolecular crowding has also been shown to affect the folding equilibrium of nucleic acids.[20] Thereby, the crowding effect on tertiary and quaternary nucleic acid structures can be generalized to be stabilizing,[39,42,161,406,407] whereas its impact on secondary hairpin structure is mostly destabilizing.[69,161,396,397,408] Such findings can be explained by three major contributions of crowding. First, the crowding-induced effect of excluded volume (see section 2.1.1) shifts the folding equilibrium towards the more compact folded native state relative to the unfolded more extended state.[8,20] Thereby, the magnitude of this effect depends on the relative size of the RNA and the crowder.[8,69,409] Second, crowding means high concentration of different macromolecules. As a consequence, the water activity inside cells is expected to be reduced as discussed above.[78] Following osmotic stress experiments, a reduction in water activity would destabilize RNA secondary structures.[69,396,397,408] Third, specific surface interactions between the nucleobases and commonly used crowding agents do exist, thus leading to an enthalpic stabilization of the unfolded state with nucleobases exposed to the solvent.[161,410,411] However, those conclusions were drawn from *in vitro* experiments using artificial crowding agents to mimic the cellular environment. Therefore, it is unclear whether the same scenarios can be found inside cells.

6.2 Aim

Existing knowledge about the effect of osmolyte and crowding on the secondary structure level of nucleic acids is mainly obtained from artificial models and systems. However, a detailed and complete conformational and energy landscape of natural and functional RNA secondary structure elements, including the consideration of fundamental physico-chemical effects of the cellular environment, such as macromolecular crowding and osmolytes, are important to understand the functional complexity of RNAs *in vivo*, but this is still largely underexplored. Hence, the aim of the study presented in this chapter is to investigate the thermodynamics of a natural and functional RNA secondary structure element and how it is modulated by the "real" crowding effect inside living cells, but also by the interplay of water, salt and osmolytes. As a model system, a well-studied bacterial RNA thermometer, a temperature-sensitive RNA structure, was utilized. The *Salmonella* fourU RNA thermometer (4U) is located in the 5'-untranslated region (5'-UTR) of the agsA (aggregation-suppression protein) gene and functions as a temperature-sensitive control element of gene expression of a small heat shock protein at the mRNA level.[412,413] At low temperature, four consecutive uracil nucleotides base pair with the ribosome binding site, known as the SHINE-DALGARNO motif, and form a temperature-sensing hairpin. At elevated temperatures, this hairpin melts and renders the ribosome binding site accessible for translation initiation. If the thermodynamics of the RNA thermometer highly depends on the degree of crowding, cosolvents and hydration, their intracellular fluctuations are very likely to be relevant as a regulator for the structural transition of the hairpin structure and thus the temperature sensitivity of the 4U RNA thermometer.

6.3 Materials and Methods

6.3.1 Chemicals and Sample Preparation

Betaine, glycine, L-leucine, sarcosine, TMAO, and urea were purchased from Sigma-Aldrich (Germany). The crowding reagents sucrose, Ficoll ®PM 70, EG, PEG 200, PEG 400, PEG 6k, and PEG 20k were obtained from Sigma-Aldrich as well. HPLC-purified and FRET-labeled 4U RNA was either synthesized by the Sabine Müller Group (University of Greifswald, Germany) or custom synthesized by IBA (Germany). In the first case, the 5'-terminus

of the RNA was labeled with Atto488 (NHS-ester) via a C6 amino linker and the uracil base at 3'-terminus was replaced by 2'-O-propargyluridine for click labeling with Atto565 (azide). In the second case, the 5'-terminus of the RNA was labeled with Atto488 (NHS-ester) via a C6 amino linker and the uracil base at 3'-terminus was replaced by 5-C8-alkyne-dU for click labeling with Atto594 (azide). Nuclease-free water and RNase AWAY surface decontaminant were purchased from Omega Bio-tek (USA) and Thermo Fischer Scientific (USA), respectively. Different osmolyte-containing solutions were prepared in 15 mM Tris-HCl buffer (pH 7.4) and filtered through a 0.02 μm Whatman Anotop 25 Plus syringe filter (GE Healthcare Life Sciences, Germany). The shallow osmolyte mixture contains 30 mM betaine, 30 mM sarcosine, 10 mM L-leucine, 410 mM glycine, and 170 mM TMAO, whereas the deep sea osmolyte mixture consists of 20 mM betaine, 20 mM sarcosine, 20 mM L-leucine, 100 mM glycine, and 590 mM TMAO. Differently concentrated crowding solutions were prepared in Dulbecco's phosphate-buffered saline (DPBS, pH 7.4).

6.3.2 Vapor Pressure Osmometry

The change in water activity due to the presence of salts and osmolytes was determined by vapor osmometry.[414] Briefly, 10 μL of the buffer solution were applied to a Wescor 5520 or 5600 vapor pressure osmometer (Wescor, USA). The measurements were performed at room temperature. For each condition, the measurement was repeated three times. The water activity, a_{w}, can be calculated from the measured osmolality ($mOsm$ [10^{-3} mol kg^{-1}]) using the equation: $mOsm = -(10^6 \ln a_{\mathrm{w}})/M_1$ with M_1 being the molecular mass [g mol^{-1}] of water.

6.3.3 Cell Culture and Microinjection

HeLa cells were grown in 35-mm glass-bottom dishes (FluoroDish, WPI) in DMEM supplemented with 10% FBS, 100 U mL^{-1} penicillin, and 0.1 mg mL^{-1} streptomycin. Prior to microinjection and imaging, the medium was removed and replaced by Leibovitz's L15 medium supplemented with 30% FBS. Semi-automatic microinjections were performed using an Eppendorf FemtoJet attached to Eppendorf InjectMan NI2 micromanipulator. 3 μL of 200 μM FRET-labeled 4U RNA dissolved in ddH_2O were loaded to a Femtotips II glass-capillary (Eppendorf) from the back using microloader capillaries (Eppendorf). Injection

pressure was adjusted to 100-250 hPa for 0.2-0.7 s so that no visible expansion of cell volume was observed during injection.

6.3.4 Fast Relaxation Imaging

An inverted fluorescence microscope (AxioObserver Z1, Zeiss) with a Colibri excitations system was used. The monochromatic light was guided through a 90° reflection using a beamsplitter (DFT 490+575, Zeiss) to a 40x objective (N.A. = 0.95, Zeiss) and focused on the sample. Emitted fluorescence of Atto488 and Atto565 was transmitted through the first beamsplitter and was reflected by a prism to the second beamsplitter (BC 565, Zeiss), where donor and acceptor/FRET fluorescence light were separated and reflected onto different CCD cameras (AxioCam HS, Zeiss) with appropriate emission filters (BP512/30 and BP630/98, Zeiss). A diode laser (m2k laser; λ = 2200 nm) was used to induce fast 2.4 °C temperature jumps, heating the cells and the entire field of view (40x objective; N.A. = 0.95) homogenously. For each jump the temperature was equilibrated for 20 s. The temperature jumps were calibrated using the temperature-sensitive dye rhodamine B. During temperature jump stepping, the power profile of the diode laser was controlled by a custom-written LabView template. The LED excitation intensity was kept constant for all experiments. Images were recorded with 2 fps using the imaging software AxioVision 4.8 (Zeiss).
Stock solution of FRET-labeled 4U RNA sample was heated up to 70 °C for 5 min and slowly cooled down to RT to ensure correct folding of the RNA hairpin structure. For *in vitro* measurements, 5 μM samples were prepared by mixing the RNA with different crowding solutions. 20 μL of each mixture were placed between 100 μm imaging spacer (SigmaAldrich). The dish was then placed on the microscope stage and the excitation light was focused onto the imaging spacer which represents the solution layer. Comparative in-cell measurements were performed in the same way. After removing the medium, a glass cover slip with 80 μL Leibovitz's L15 medium supplemented with 30% FBS was mounted via an imaging spacer onto the glass bottom dish which contained microinjected cells. The RNA stock solution was used directly as microinjection sample.

6.3.5 High Pressure Fluorescence Spectroscopy

Stock solution (100 μM) of FRET-labeled 4U RNA was heated up to 75 °C for 5 min and slowly cooled down to room temperature to ensure correct folding of the RNA hairpin structure. For the high pressure experiments, the RNA concentration was adjusted to 1 μM by mixing the RNA with different osmolyte-containing solutions. Iso-hyperbaric and temperature-dependent melting measurements of 4U RNA were carried out on a K2 multifrequency phase and modulation fluorometer (ISS Inc., USA). A 250 μL quartz bottle was filled with the sample solution, sealed with a pressure-transmitting Dura Seal film and placed into a high-pressure cell from ISS Inc. Hydrostatic pressure up to 200 MPa was generated using a screw type hand pump. Fluorescence of Atto488 was excited at 488 nm and an emission spectrum between 500 and 690 nm was recorded. The temperature was regulated using a circulating bath (Julabo, Germany) and monitored by a thermocouple that is fixed to the high pressure cell and connected to a digital thermometer. To validate any RNA degradation during the melting experiments, the FRET signal was recorded upon cooling the sample to the initial temperature.

6.4 Results and Discussion

6.4.1 RNA Hairpin Folding in the Crowded Cell

Numerous crowding studies exist and have provided mechanistic insights into how artificial crowding agents modulate thermodynamics and folding events of RNA molecules. However, the remaining question is whether the concentrated aqueous solutions of such synthetic polymers adequately mimic the cellular environment and report on in-cell RNA structure and functionality. Interestingly, experiments on folding of tertiary RNA structures have demonstrated that various *in vitro* crowding agents, such as PEG, dextran, Ficoll and BSA, lead to different crowding behaviors compared to the cell extract prepared from *Xenopus laevis* eggs.[415–417]. Those results point out that the use of *in vitro* crowding agents could lead to a misinterpretation of the *in vivo* scenario and thus the in-cell functionality of RNAs. In case of protein folding, there is also clear experimental evidence that crowding agents do not always reflect the folding behavior observed in the living cell.[26,90,418]

Therefore, in this work, the thermal stability of the hairpin-structured *Salmonella* fourU

RNA thermometer (4U) was studied directly in living cells and the results were interepreted by comparative studies with artificial crowding agents. To shed light on how intracellular crowding and hydration alter the folding landscape of such a biosensor, the recently developed technique fast relaxation imaging (FReI) was used to study the thermal unfolding of 4U in living mammalian cells and under different *in vitro* corwding conditions.[87,419] FReI combines fast laser-induced temperature jumps with FRET microscopy and thus allows the study of biomoleular kinetics and thermodynamics in single living cells (Fig. 6.3a). To study the thermal unfolding of the 4U RNA thermometer, a tailored temperature jump protocol that consisted of 2.4 °C consecutive temperature jumps was applied. This protocol enables thermal titration measurements to be completed within 300 s avoiding cytotoxic effects and cell damage.[419] The step-shaped temperature rises with a fast upward jump and a 20 s dwell time shifting the investigated system to a new equilibrium (Fig. 6.3a).

To investigate the thermal unfolding of 4U by FRET, the 4U RNA was functionalized by end-group labeling using Atto488 and Atto565 via orthogonal N-hydroxysuccinimide (NHS) and click chemistry (Fig. 6.3b). The synthesis and labeling were conducted by Axel Orban and Dr. Bettina Appel in collaboration with Prof. Dr. Sabine Müller from University of Greiswald (Germany). Upon temperature increase, donor (D, Atto488) fluorescence increased and acceptor (A, Atto565) fluorescence diminished with increasing temperature resulting in the increase of the D/A FRET signal (Fig. 6.3d,e), indicating unfolding of the hairpin structure. The intrinsic response of the D/A FRET signal to temperature was marginal (Fig. 6.4). During temperature stepping, the equilibration of the sample was completed within the 20 s dwell time (Fig. 6.5). The thermal unfolding process of 4U was fully reversible and the RNA was intact upon refolding (Fig. 6.3c; Fig. 6.6a).
Owing to the cooperativity of 4U RNA unfolding,[413] a two-state transition for the RNA hairpin unfolding process (hairpin-to-coil transition) was assumed. The fraction of unfolded state is given by:

$$f_{\mathrm{u}} = \frac{1}{1 + K_{\mathrm{u}}} \tag{6.7}$$

with K_{u} as the equilibrium constant for the unfolding reaction. To account for the intrinsic temperature dependence of both dyes, Atto488 and Atto565 (Fig. 6.4), two linear baselines with the same slope representing the folded $(a_{\mathrm{f}} + b(T - T_{\mathrm{min}}))$ and unfolded $(a_{\mathrm{u}} + b(T - T_{\mathrm{min}}))$

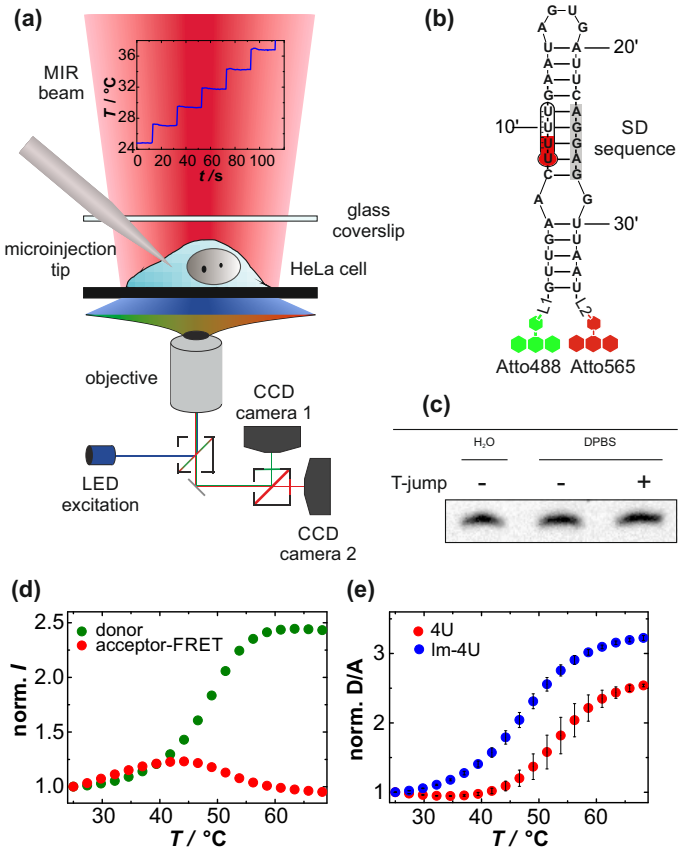

Figure 6.3 | 4U RNA thermal unfolding studied by Fast Relaxation Imaging (FReI). (a) Representation of the FReI setup. (b) 4U structure labeled with FRET-capable dyes Atto488 and Atto565. SD=SHINE-DALGARNO. (c) Gel electrophoresis and EtBr staining reveal the intactness of the hairpin after temperature stepping in DPBS buffer. Those experiments were conducted by Dr. Francesco Righetti (Ruhr-University Bochum, Germany). (d) Normalized donor- and acceptor-FRET fluorescence intensities for 4U RNA in DPBS buffer studied by FReI. (e) Normalized D/A FRET signal as a function of temperature for 4U RNA and its low-melting variant G12A-C23U (lm-4U) *in vitro*. n=4. Error bars represent mean±s.d.

state were used, respectively:

$$\frac{D}{A}(T) = \frac{[a_\mathrm{f} + b(T - T_\mathrm{min})] + [a_\mathrm{u} + b(T - T_\mathrm{min})] \cdot K_\mathrm{u}}{1 + K_\mathrm{u}}. \tag{6.8}$$

The standard GIBBS energy of unfolding is given by:

$$\Delta G^0_\mathrm{u} = -RT \ln K_\mathrm{u}. \tag{6.9}$$

Considering the temperature dependence of ΔG^0_u, the GIBBS-HELMHOLTZ equation was used:

$$\Delta G^0_\mathrm{u}(T) = \Delta H^0_\mathrm{u} \left(1 - \frac{T}{T_\mathrm{m}}\right) - \Delta C^0_\mathrm{p} \left[(T_\mathrm{m} - T) + T \ln \left(\frac{T}{T_\mathrm{m}}\right)\right], \tag{6.10}$$

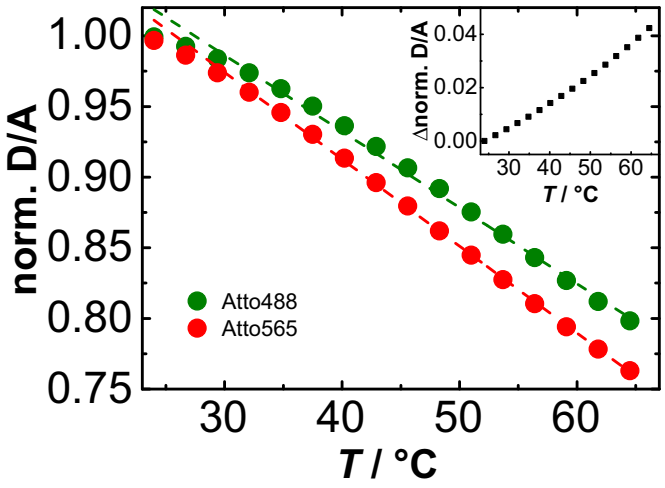

Figure 6.4 | Intrinsic temperature dependence of Atto488 and Atto565. Normalized fluorescence intensities of Atto488 and Atto565 as function of temperature showed a linear trend. The slopes for Atto488 and Atto565 were (-0.005 ± 0.0001)/°C and (-0.006 ± 0.00004)/°C, respectively and thus indicated a higher temperature dependency for Atto565 than Atto488. *Inset*: Calculated intrinsic response of the D/A with increasing temperature.

where T_m is the melting temperature, ΔH^0_u the standard VAN'T HOFF enthalpy change and ΔC^0_p the standard heat capacity change upon unfolding. The difference in heat capacity between the folded and unfolded states was neglected and Eq. 6.10 was simplified as:

$$\Delta G^0_\mathrm{u}(T) \approx -\frac{\Delta H^0_\mathrm{u}}{T_\mathrm{m}} \cdot (T - T_\mathrm{m})\,. \tag{6.11}$$

The standard free energy for unfolding, ΔG^0_u, at T = 310 K (37 °C) was obtained by

$$\Delta G^0_\mathrm{u}(310\ \mathrm{K}) = -\frac{\Delta H^0_\mathrm{u}}{T_\mathrm{m}} \cdot (310\ \mathrm{K} - T_\mathrm{m})\,. \tag{6.12}$$

First, it was verified that the melting temperature measured by FReI was in agreement with that from previous *in vitro* measurements on unlabeled 4U (Tab. 6.1, Fig. 6.6b).[413] This shows that the dyes do not interfere with the thermodynamics of the RNA molecule. In the physiological buffer, Dulbecco's phosphate-buffered saline (DPBS), a melting temperature of T_m = (52.7±1.6) °C was measured. However, such high temperatures required for an accurate thermodynamic analysis would be toxic for cells. As a consequence, the low-melting (G12A-C23U) variant of 4U RNA,[420] which is referred to as lm-4U RNA, was used in the following. In DPBS, lm-4U exhibits a melting temperature of T_m = (47.4±0.6) °C and an unfolding free energy of ΔG^0_u(37 °C) = (5.9±0.8) kJ mol^{-1} (Fig. 6.6b; Tab. 6.1).

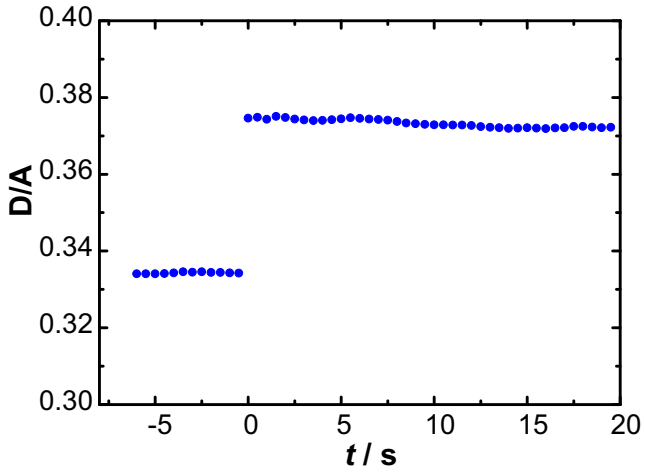

Figure 6.5 | Representative time-resolved response of the D/A FRET-signal to a 2.4 °C temperature jump near to the melting temperature (at $t = 0$ s). The folding kinetics were completely equilibrated within the measured time scale.

In a next step, the thermal unfolding of lm-4U was measured in differently crowded environments. First, the size dependence of the crowding effect was explored, and thereby the commonly used crowding agent polyethylene glycol (PEG) with different degrees of polymerization (molecular weight (MW): 200 Da, 400 Da, 6 kDa, and 20 kDa) and its monomer, ethylene glycol (EG, 62 Da), were used at a concentration of 300 g L^{-1}. The lm-4U hairpin was destabilized in the presence of (P)EG with MW<6 kDa as indicated by the lowered melting temperatures and free energies of unfolding (Tab. 6.1, Fig. 6.7a). Taking into account

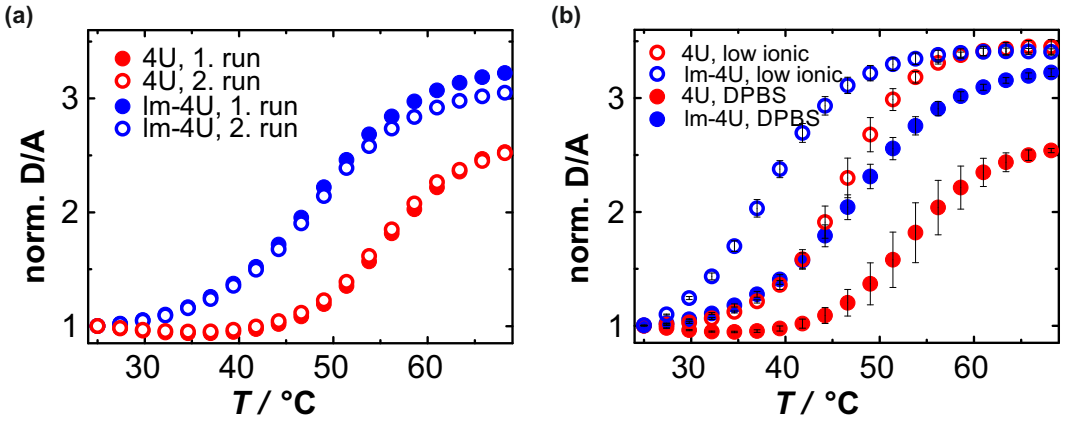

Figure 6.6 | Thermal melting curves of the 4U RNA (4U) and its low-melting variant G12A-C23U variant (lm-4U) *in vitro*. (a) Reversibility of the unfolding transition shown by two consecutive temperature scans. (b) Melting curves of 4U and lm-4U under different buffer conditions. The melting temperature of both hairpins was elevated in DPBS, pH 7.4 (8.1 mM Na_2HPO_4, 1.5 mM KH_2PO_4, 2.7 mM KCl, 136.9 mM NaCl) compared to that in a low ionic buffer, pH 7.4 (15 mM $K_xH_yPO_4$, 25 mM KCl). n=3-4. Error bars represent mean±s.d.

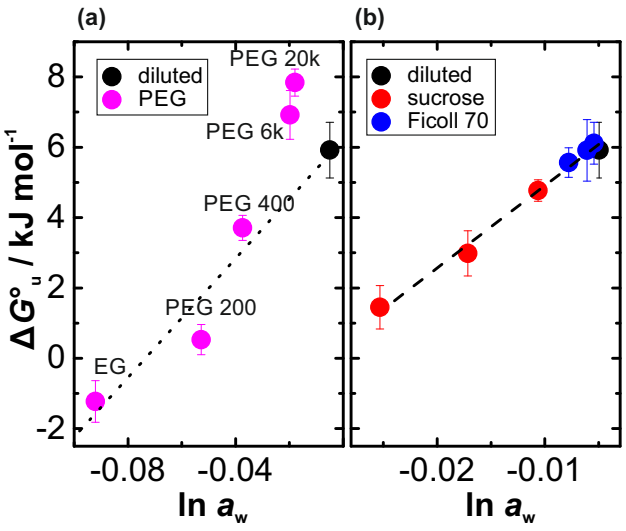

Figure 6.7 | lm-4U RNA folding stability in different crowded solutions *in vitro*. The free energy for unfolding at 37 °C, ΔG^0_u, is plotted against the activity of water, $\ln a_w$. The DPBS buffer is used as diluted reference buffer. (a) Size-dependent effect of PEG (300 g L^{-1}) on the RNA folding stability. The dotted line indicates the dependence of the folding stability on $\ln a_w$ for PEG<6 kDa. (b) Concentration-dependent effect of sucrose and Ficoll 70 (100, 200, and 300 g L^{-1}). The dashed line represents a globally linear fit for sucrose and Ficoll 70, as an analysis of covariance reveals no significant differences for the individual fits. n=4. Error bars represent mean±s.d.

that the water activity of buffers containing water-soluble cosolute is altered, ΔG^0_u at 37 °C was plotted as a function of $\ln a_w$. A monotonic decrease of ΔG^0_u with decreasing water activity caused by EG, PEG 200, and PEG 400 was observed, indicating a relationship between water activity and folding stability. Such water sensitivity was also observed for other nucleic acid secondary structures. That means water uptake and release during base pairing and hairpin formation.[69,161,396,397,408] The base pair stability, which is counteracted by the close proximity of the negatively charged sugar-phosphate backbone, highly depends on the tightness of the hydrogen-bonding network of water surrounding the double strand and thus on the amount of osmotically active water.[396,408] RNA double strands have been reported to be hydrated more than DNA causing increased enthalpic stability.[384] In contrast, the addition of 300 g L^{-1} PEG 6 kDa or 20 kDa caused a significant stabilization of the folded state despite a reduced $\ln a_w$. This stabilization is in line with the excluded volume effect. Upon high volume exclusion, the more compact native state is entropically favored compared to the unfolded state.[8,396,409]

Next, the concentration of Ficoll 70 and its monomeric building block sucrose was varied from 0 to 300 g L^{-1}. In contrast to PEG, Ficoll is a highly branched and approximately globular polysaccharide, but with a comparable particle size with PEG 20 kDa. Here, it was found

that the thermal stability decreased linearly with $\ln a_w$ for sucrose and Ficoll 70 following the same trend, indicating that the folding landscape of 4U is insensitive to the volume exclusion caused by Ficoll 70 (Fig. 6.7b). Furthermore, the different slopes of ΔG_u^0 versus $\ln a_w$ caused by PEG and Ficoll also reveal that chemically different crowding agents act differently on RNA stability. The water activity-dependent destabilization is more pronounced for sucrose/Ficoll compared to PEG. It is very likely that additional interactions between the cosolute and the nucleobases upon unfolding are involved. Thereby, PEG molecules can interact with the nucleobases of the RNA via hydrophobic effects in a size-dependent manner,[411,421] whereas sucrose, featuring more available hydroxyl groups than EG at same mass concentration, can undergo preferential and hydrophilic interactions with the nucleobases, which are exposed to the solvent upon unfolding.[69] Hydrogen-bond interactions between cosolute and nucleic acid base have been demonstrated by MD simulations and experimental data.[69,410] Taken together, the findings presented here show that the stabilizing effect of volume exclusion is counteracted by a reduction of water activity, but also by the attractive interactions between the cosolute and the nucleobases, both with destabilizing contributions.

Inside a cell, the average distance between two biomolecules is about 1-2 nm only and the interfacial water can constitute up to 70% of the total cellular water.[14,422] Those water molecules feature altered physical properties compared to bulk water, ranging from bulk like to bound/frozen (thus osmotically inactive) behavior.[14] Therefore, the thermodynamic activity of cellular water may be decreased compared to the isotonic DPBS buffer.[78] To address this question, the thermal stability of lm-4U was studied in living mammalian cells. To do so, the FRET-labeled lm-4U RNA was delivered into living HeLa cells using microinjection. Those experiments were performed together with David Gnutt (Ruhr-University Bochum, Germany) and revealed that the T_m and ΔG_u^0 values measured in the cell were similar to the results obtained from the dilute DPBS buffer solution (Fig. 6.8). Whereas the different contributions of crowding to RNA folding stability observed *in vitro* revealed significant net effects at a crowding concentration (300 g L^{-1}) similar to the cellular crowding density, the stabilizing contributions from excluded volume effects and the destabilizing contributions from the reduced intracellular water activity and the interaction with nucleobases seem to extinguish each other inside the cell.[75,78,161,410,411] Therefore, only an overall marginal stability modulation was observable inside cells. However, a broad distribution of the melting temperature and the unfolding free energy between different cells was observed

Table 6.1 | Thermodynamic parameters of the helix-to-coil transition in the presence of crowding agents. Melting temperature, T_m, and free energy, ΔG^0_u, for unfolding at 37 °C of the 4U RNA hairpin in DPBS buffer containing different crowding agents. If not otherwise specified, n = 4. Errors indicate mean±s.d.

	T_m / °C	ΔG^0_u(37 °C) / kJ mol^{-1}
wildtype (4U)		
low ionic buffer*	46.2±1.2	7.0±0.4
DPBS, pH 7.4	52.7±1.6	9.9±0.5
G12A-C23U (lm-4U)		
low ionic buffer*	37.9±0.4	0.5±0.2
DPBS, pH 7.4	47.4±0.6	5.9±0.8
+ 100 g/L sucrose	44.8±0.8	4.8±0.3
+ 200 g/L sucrose	42.0±1.0	3.0±0.6
+ 300 g/L sucrose	39.7±1.3	1.4±0.6
+ 100 g/L Ficoll 70	47.1±1.2	6.1±0.6
+ 200 g/L Ficoll 70	46.7±1.7	5.9±0.9
+ 300 g/L Ficoll 70	46.2±0.7	5.6±0.4
+ 300 g/L EG	35.2±0.7	-1.2±0.6
+ 300 g/L PEG 200	37.9±0.7	0.5±0.4
+ 300 g/L PEG 400	42.9±0.5	3.7±0.4
+ 300 g/L PEG 6k	50.0±2.6	6.9±0.7
+ 300 g/L PEG 20k	51.3±0.6	7.8±0.4
HeLa cytosol (n = 9)	50.5±3.2	10.8±4.5
HeLa nucleus (n = 13)	47.9±3.8	7.3±3.8

*In low ionic buffer (15 mM $K_xH_yPO_4$, pH 6.5, 25 mM KCl) the melting temperature of 4U and lm-4U were reported to be 41.1 °C and 35.9 °C, respectively.[420]

(Tab. 6.1, Fig. 6.8). The broadness was determined by two standard deviations corresponding to 95% of the distribution of the unfolding free energies. The free energy at 37 °C spanned a range of 2.9 k_BT (7.6 kJ mol^{-1}) in the nucleus and 3.5 k_BT (9.0 kJ mol^{-1}) in the cytosol. Despite an insignificant thermodynamic difference between cytosol and nucleus, on the single-cell level the results revealed that for certain cells the RNA was more stable in the nucleus than in the cytosol or vice versa (Fig. 6.9). Such broadness and variation of the crowding effect at the subcellular level could arise from a high cell-to-cell variability, which is likely caused by multiple cell physiological processes, for example, the cell cyle or genetic noise.[423,424] For instance, it has been shown that the cell volume and cell dry mass increase at different rates during the cell cycle, thus resulting in different crowding densities.[425,426] This phenomenon has been shown to modulate protein folding stability inside cells.[82] Therefore, temporal changes in the intracellular composition, or rather in

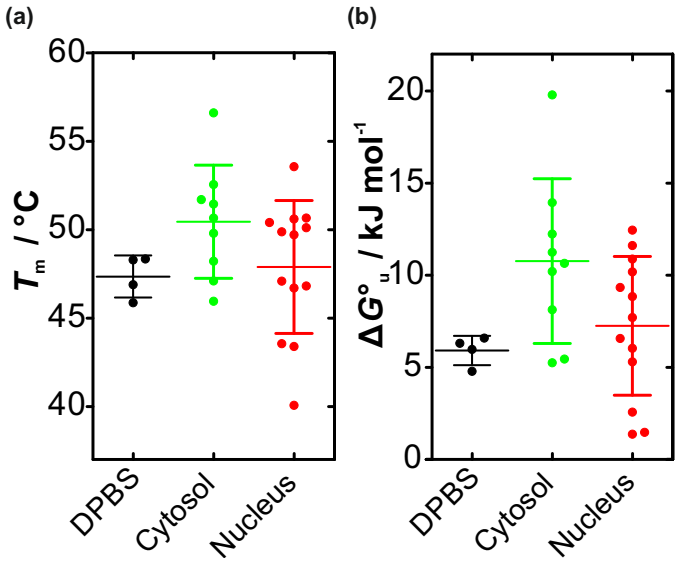

Figure 6.8 | Folding stability of lm-4U in single HeLa cells. Box plots for (a) melting temperature, T_m, and (b) free energy of unfolding at 37 °C, ΔG^0_u. Error bars indicate mean±s.d. and statistical significance was tested by an unpaired t-test.

the physico-chemical properties, of the cytosol as well as the nucleus can finely tune RNA folding stability.

Additionally, cells are not only a crowded but also a very complex environment. The interior of a cell is heterogeneous, highly structured and compartmentalized on many length scales.[427] A pixel-based evaluation of the thermodynamic traces provided further thermodynamic information for distinct areas within single cells. Subcellular heterogeneities within the cytosol and nucleus caused variations of ΔG^0_u by ca. 1.7 to 2.9 k_BT (4.4 and 7.6 kJ mol^{-1} compared to 0.4 kJ mol^{-1} for comparative *in vitro* experiments).[25] This broadness can be explained by locally distinctively crowded regions within the cell.

In summary, the results presented here provide the first thermodynamic insights into the thermal stability of an RNA hairpin in living cells with subcellular resolution. *In vitro* experiments revealed that volume exclusion, water activity as well as nonspecific interactions with nucleobases play a crucial role in the modulation of the folding landscape of RNA secondary structures. Inside cells, the 4U hairpin has, on average, a similar thermal stability as in the physiological buffer that is due to the neutralization of the counteracting contributions from excluded volume versus nonspecific interactions and changes in water activity. However, the observed cell-to-cell variability and subcellular differences may be caused by spatial and temporal fluctuation of the cellular composition and thus of all three factors.[79,80,275] In ad-

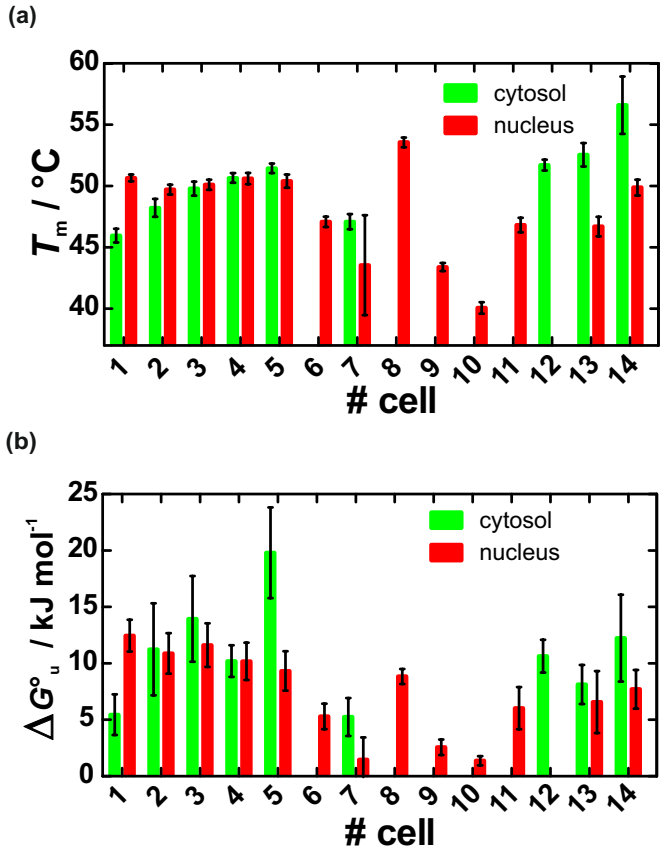

Figure 6.9 | Folding stability of lm-4U in different HeLa cells. (a) Melting temperature (T_m) and (b) free energy change of unfolding at 37 °C (ΔG^0_u) of lm-4U RNA averaged for different single cells over the nucleic and cytosolic regions. Error bars represent the fitting errors for the respective variables.

dition, this study has revealed that synthetic polymers are not appropriate crowding agents to mimic the cellular crowding in its entirety. They might be able to unveil the important contributions of crowding in determining the folding landscape of RNA secondary structures, but they cannot fully reflect their specific interplay to cause the cellular crowding effect.

6.4.2 Modulation of the Thermodynamic Signatures of an RNA Thermometer by Osmolytes and Salts

To study the helix-to-coil transition of 4U in the presence of the osmolytes, again the effect of FRET was used. This time, the 4U RNA was functionalized by end-group labeling using Atto488 and Atto594 (Fig. 6.10a). The fluorescence characteristics of both dyes is only marginally responsive to temperature and pressure (Fig. 6.11). Temperature-induced unfolding of the hairpin structure leads to a rise in the distance between the two dyes, resulting in a fluorescence increase of the donor (D, Atto488) and accordingly a fluorescence decrease of

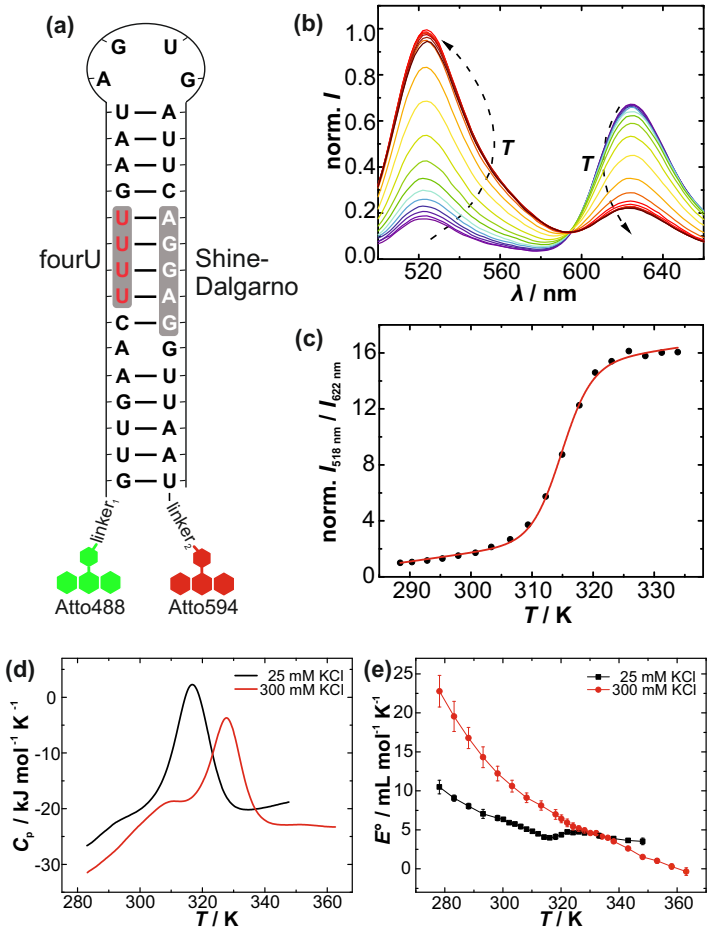

Figure 6.10 | Thermal unfolding of 4U. (a) 4U sequence and secondary structure with Atto488 (donor) and Atto594 (acceptor) as FRET probes. (b) Normalized fluorescence emission spectra of 4U upon thermal unfolding when the donor is excited. (c) The FRET-based melting curve of 4U was fitted to a two-state model (red line). Calorimetric characterization of 4U at various KCl concentrations: (d) DSC thermograms, (e) partial expansibility, E^0, as a function of temperature measured by PPC. The calorimetric experiments were performed by Loana Arns (TU Dortmund).

the acceptor (A, Atto594) (Fig. 6.10b). The fluorescence intensities at 518 and 622 nm were taken to calculate the D/A ratio reflecting the FRET signal. The temperature-dependent D/A ratios were fitted to a two-state unfolding model (Fig. 6.10c). The melting curves were fitted to the final equation:

$$\frac{D}{A}(T) = \frac{[a_\mathrm{f} + b(T - T_\mathrm{min})] - [a_\mathrm{u} + b(T - T_\mathrm{min})]}{1 + \exp\left[-\left(\frac{1}{T} - \frac{1}{T_\mathrm{m}}\right) \cdot \left(\frac{\Delta H^0_\mathrm{u}}{R}\right)\right]} + [a_\mathrm{u} + b(T - T_\mathrm{min})]. \tag{6.13}$$

As K^+ is the predominant intracellular cation and RNA folding is strongly affected by the ionic environment,[390,428] the standard VAN'T HOFF unfolding enthalpy, ΔH^0_u, and the melting temperature, T_m, of the 4U hairpin were determined at three different KCl con-

centrations. The T_m increases by (10.2±0.7) °C linearly with the logarithm of the KCl concentration. Corresponding DSC measurements of unlabeled 4U RNA were performed by Loana Arns (TU Dortmund). Those experiments revealed very similar results, indicating that the dye labeling does not interfere with the thermodynamic signatures of 4U (Fig. 6.10d; Tab. 6.2). However, the DSC thermograms indicate that thermal unfolding of 4U is not strictly two-state, but rather exhibits some kind of pretransitional behavior, which is not detected by FRET, leading to fractional differences in the enthalpy values determined. For the calculation of the calorimetric standard-state enthalpy change of unfolding, $\Delta_{cal} H_u^0$, the pretransitional shoulder in the DSC thermograms was not considered. Such shoulders might correspond to the formation of an intermediate state that features a more flexible AGUG loop with an unchanged duplex stem or a hairpin with pre-molten hydration shell.[429,430]

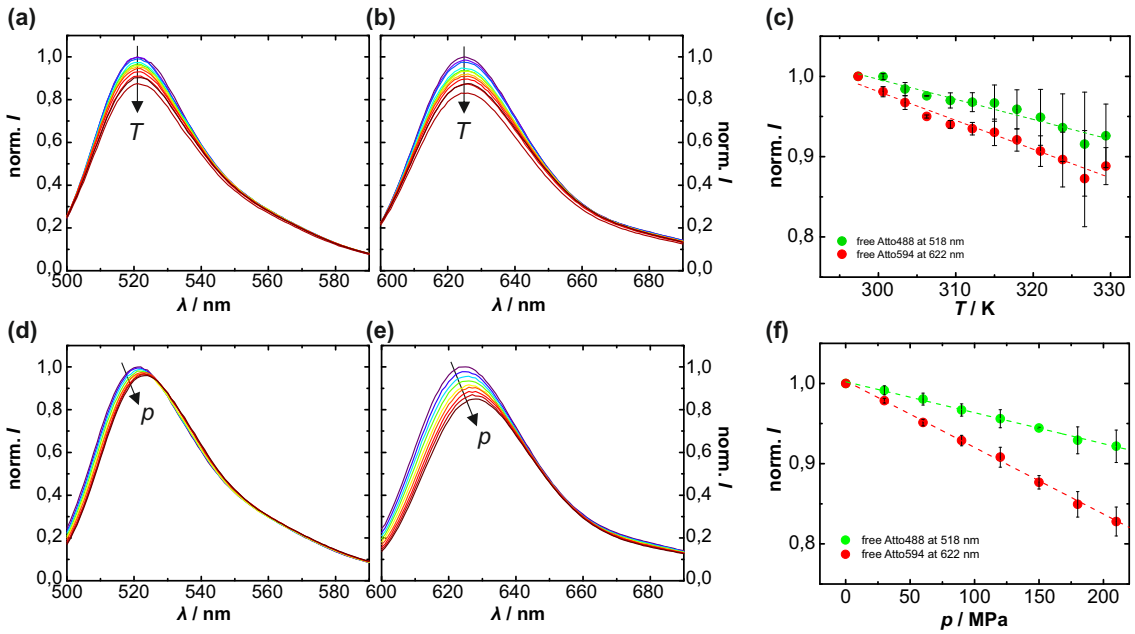

Figure 6.11 | Intrinsic fluorescence response of free Atto488 and Atto594 to temperature and pressure. (a-c) Intrinsic fluorescence response of free Atto488 and Atto594 to temperature. Temperature-dependent fluorescence emission spectra of (a) Atto488 (excitation at 488 nm) and (b) Atto594 (excitation at 590 nm) in 15 mM Tris-HCl buffer (pH 7.4). The fluorescence intensities decrease slightly with increasing temperature. (c) Normalized fluorescence intensities of Atto488 (518 nm) and Atto594 (622 nm) as a function of temperature exhibit a linear decrease. The slopes for Atto488 and Atto594 are (-0.0025±0.0002)/K and (-0.0036±0.0002)/K, respectively. Data points are mean values of three experiments. (d-f) Intrinsic fluorescence response of free Atto488 and Atto594 to hydrostatic pressure. Pressure-dependent fluorescence emission spectra of (d) Atto488 and (e) Atto594 in 15 mM Tris-HCl buffer (pH 7.4). Pressure causes in both cases a slight intensity decrease and red shift of the fluorescence emission. (f) Normalized fluorescence intensities of Atto488 (518 nm) and Atto594 (622 nm) as a function of pressure show a linear trend. The slopes for Atto488 and Atto594 were (-0.00039±0.00001)/MPa and (-0.00083±0.00002)/MPa, respectively. Data points are mean values of three experiments.

The broadness of the DSC peaks indicates a low cooperativity, caused by the G·A mismatch of the 4U RNA.[413] Rescans of the samples showed that the unfolding process is fully reversible. Further, the partial expansibility, $E^0(T)$, of the 4U RNA was measured at two KCl concentrations by pressure perturbation calorimetry (PPC). Those experiments were performed by Loana Arns (TU Dortmund). Figure 6.10e shows that the increase in KCl concentration causes a drastic increase in the level of hydration of the folded 4U RNA, indicated by the more positive E^0 values at 300 mM KCl.[431] This is in agreement with the finding that the ions remain hydrated upon association with the RNA.[390,428] The thermally induced decrease of E^0 for the folded RNA is caused by partial dehydration of the RNA surface and the vanishing difference between the water structure at the RNA surface and the bulk.[431] By integrating $E^0(T)$ over the transition region, the standard molar volume change of the heat-induced hairpin-to-coil transition, $\Delta V_u^0(T_m)$ was obtained (Tab. 6.2). ΔV_u^0 becomes more positive with increasing melting temperature, indicating a positive expansibility change, ΔE_u^0, upon unfolding. With increasing temperature, hydrogen bonds become less favorable and the nucleobases less stacked. Such effects lead to an increase in hydration and the thermal volume of the unfolded state, resulting in an increased expansibility and volume change for the hairpin-to-coil transition.[432,433]

Next, the effect of TMAO and urea on the thermal stability of the 4U RNA at various KCl concentrations was studied and described by the excess standard free energy for unfolding, $\Delta\Delta G_u^0$, at the melting temperature measured in the corresponding buffer containing KCl but

Table 6.2 | Thermodynamic parameters of the helix-to-coil transition. Comparison of the atmospheric pressure transition temperature (T_m), the standard enthalpy change for unfolding (ΔH_u^0), and the molar volume change of the transition (ΔV_u^0) for 4U from calorimetric (DSC and PPC) and spectroscopic (FRET) measurements.

DSC and PPC			
[K$^+$] (mM)	T_m (K)	$\Delta_{cal} H_u^0$ (kJ mol^{-1})	ΔV_u^0 (mL mol^{-1})
25	316.5±0.4	282±11	-12.4±0.2
300	327.8±0.1	189±19	7.5±0.5
FRET-based			
[K$^+$] (mM)	T_m (K)	$\Delta_{vH} H_u^0$ (kJ mol^{-1})	ΔV_u^0 (mL mol^{-1})
25	316.0±0.1	326±1	-7.2±1.1
150	323.4±0.6	315±2	10.6±2.4
300	327.2±0.2	290±16	13.7±0.8

not osmolyte, $T_{m,0}$, using:

$$\Delta\Delta G_u^0(T_{m,0}) = \Delta H_u^0 \left(1 - \frac{T_{m,0}}{T_m}\right). \tag{6.14}$$

Thereby, ΔH_u^0 is assumed to be temperature-independent in the range between $T_{m,0}$ and T_m.

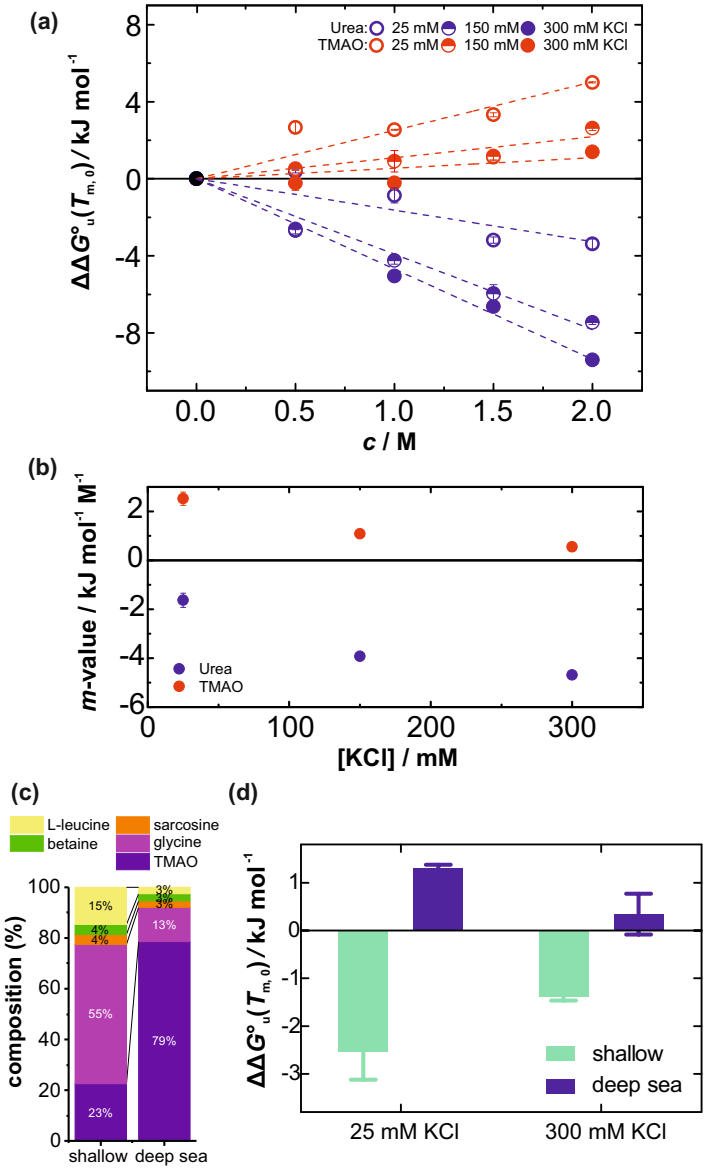

Figure 6.12 | Thermal stability of 4U in the presence of urea and TMAO. (a) The excess standard free energy for unfolding, $\Delta\Delta G_u^0(T_{m,0})$, is plotted as a function of osmolyte concentration, c. $T_{m,0}$ refers to the melting temperature of 4U obtained in the reference buffer solution without osmolyte (black circle). Dashed lines are least-square fits to the data and indicate the dependence of the free energy of unfolding of 4U on the osmolyte concentration. The slopes describe the concentration-dependent free energy constant termed the m-value, ($\Delta\Delta G_u^0(T_{m,0}) = m \cdot c$). (b) Salt concentration-dependent m-values. (c) Typical osmolyte compositions found in shallow and deep sea shrimps.[94] The total concentration of osmolytes in both mixtures is 750 mM. (d) $\Delta\Delta G_u^0(T_{m,0})$ values for 4U at two different KCl concentrations. Error bars represent mean±s.d.

The most pronounced effect of these two common osmolytes is that TMAO causes elevated melting temperatures, whereas urea induces a shift of the melting temperature to lower values (Fig. 6.13). Accordingly, TMAO increases the excess standard free energy of unfolding, $\Delta\Delta G^0_{\mathrm{u}}(T_{\mathrm{m},0})$, and thus stabilizes the 4U hairpin, following linear trends as a function of TMAO concentration. In contrast, urea destabilizes the hairpin structure and caused a concentration-dependent decrease of the $\Delta\Delta G^0_{\mathrm{u}}(T_{\mathrm{m},0})$ (Fig. 6.12a; Fig. 6.13; Fig. 6.14). Interestingly, the concentration dependence of the $\Delta\Delta G^0_{\mathrm{u}}(T_{\mathrm{m},0})$, the so-called m-value, varies markedly with the ionic strength. In both cases, the osmolyte causes a decrease of the m-value with increasing KCl concentration (Fig. 6.12b). Further, the presence of the osmolyte decreases the KCl concentration dependence of the stability of 4U (Fig. 6.15). KCl has been shown to interact only weakly, if at all, with TMAO and urea. Therefore, its effective concentration is probably not markedly affected by the osmolytes.[113,139]

The urea-induced destabilization can be explained by the preferential interaction of urea with all RNA surfaces, in particular with nucleobases that are exposed to the solvent upon

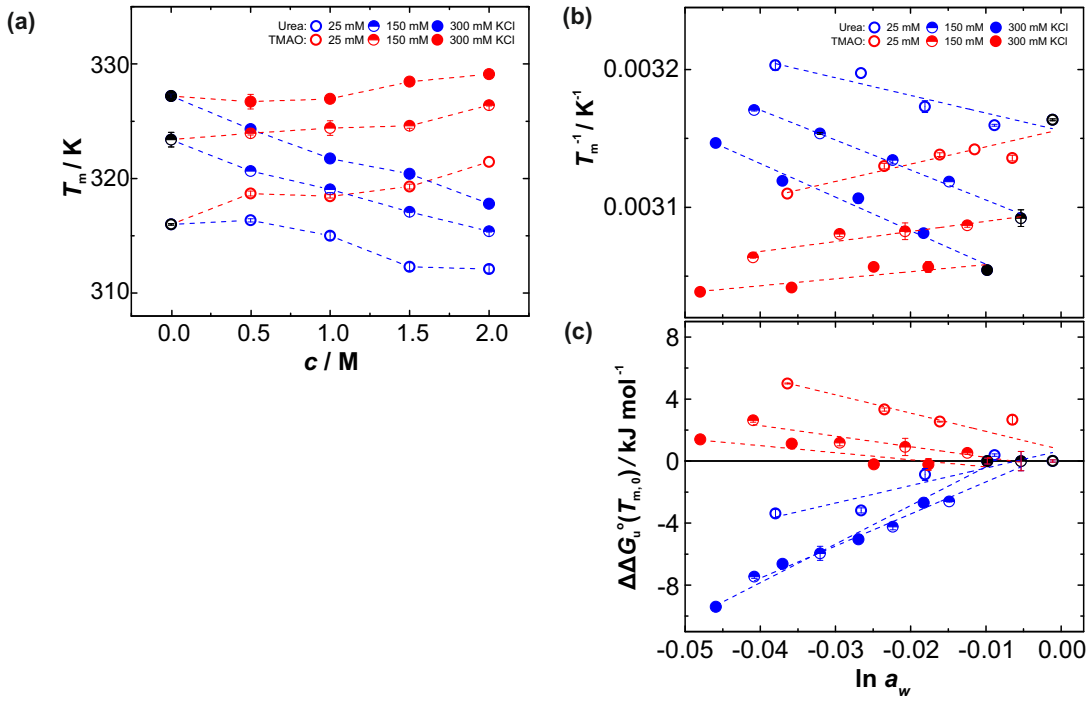

Figure 6.13 | Thermal stability of the 4U RNA hairpin as a function of the water activity. (a) Melting temperature, T_{m}, values for 4U as a function of osmolyte concentration and at various KCl concentrations. Dashed lines connect data points to guide the eye. (b) The inverse melting temperature or (c) the excess standard free energy for unfolding, $\Delta\Delta G^0_{\mathrm{u}}(T_{\mathrm{m},0})$, is plotted against $\ln a_{\mathrm{w}}$. $T_{\mathrm{m},0}$ refers to the melting temperature of 4U obtained in the reference buffer solution without osmolyte (black circles). Error bars represent mean±s.d. Dashed lines represent linear fits.

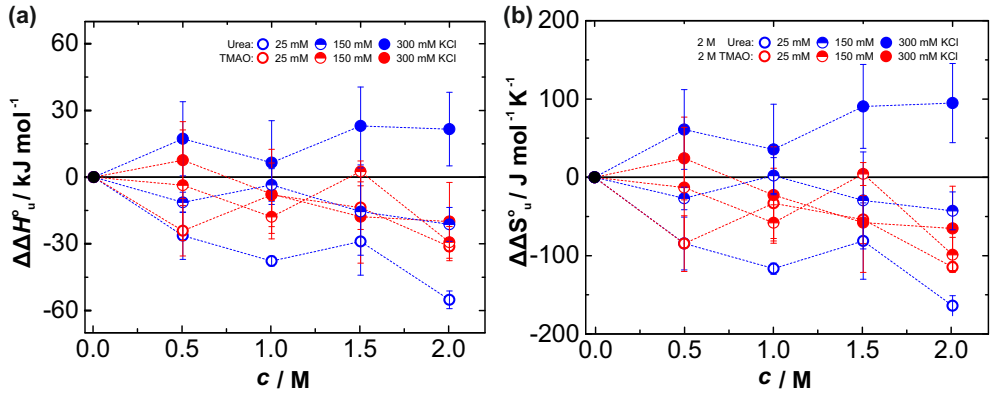

Figure 6.14 | Enthalpy and entropy change for the unfolding event of 4U RNA in the presence of osmolytes. (a) Excess VAN'T HOFF standard enthalpy change and (b) excess standard entropy change of 4U RNA unfolding ($\Delta\Delta X^0_u = \Delta X^0_{u,osmo} - \Delta X^0_{u,0}$) as a function of concentration for the osmolytes urea and TMAO. Error bars represent mean±s.d. Dashed lines connect data points to guide the eye.

unfolding of the hairpin.[110,113] MD simulations report on multiple and very dynamic hydrogen bonds and stacking interactions between urea and the nucleobases.[111,112] In general, the event of RNA unfolding is thought to lead to a release of counterions as the charge density of the unfolded RNA diminishes.[390,428] Hence, an increase of the KCl concentration is expected to shift the folding equilibrium towards the folded state. Differently, the KCl-dependent decrease of the m-value observed here may be explained by increased K^+-binding sites on the RNA surface as the SASA of the unfolded RNA is maximally extended in the presence of urea. Those favorable interactions between K^+ and the RNA surface would reduce the extent of ion release upon unfolding and cause a cooperative effect of urea and KCl on the stabilization of the unfolded state of 4U. In contrast, the stabilizing effect of TMAO on 4U can be explained by the strong interaction of TMAO with water and the unfavorable interactions between solute and co-solute.[116,129,138,141] A more ordered and extensive hydration shell around the 4U RNA hairpin could possibly also counteract the destabilizing neighboring effect of the G·A mismatch, leading to a free energy decrease of the folded state which might then be closer to that of a perfectly matched 4U mutant.[413] This is consistent with literature reporting on marginal effects of TMAO on the stability of perfectly matched RNA secondary structures.[139,161] Further, the attenuating effect of KCl on TMAO-induced stabilization of the 4U RNA hairpin suggests a salt-induced limitation and even counteraction of the preferential hydration effect. This may be explained by the chaotropic nature of KCl.[434] Owing to its low charge density and slightly hydrophobic nature, KCl may impair the structure of the hydration layer, causing attenuation of the preferential hydration effect

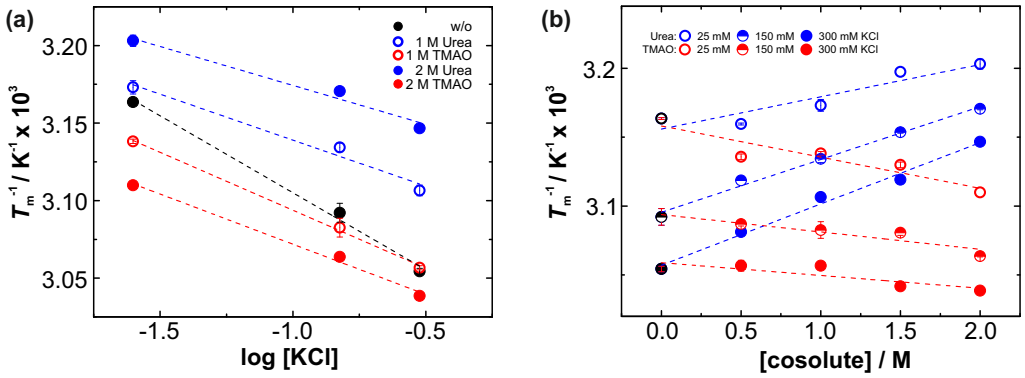

Figure 6.15 | Interplay between KCl and osmolytes. (a) KCl concentration dependence of the thermal stability of 4U in the presence and absence of urea and TMAO, respectively. (b) KCl concentration dependence of m-values. Black circles correspond to the reference buffer solutions without osmolyte. Error bars represent mean$\pm$s.d. Dashed lines represent linear fits.

induced by TMAO.

Further, the effect of TMAO in typical osmolyte mixtures found in shallow and deep sea living shrimps was investigated (Fig. 6.12c). Those mixtures amount to approximately 600 mOsm in cells to balance the high osmolality of the seawater.[94] Thereby, the content of TMAO in such mixtures has been found to increase linearly with the depth of the ocean to counteract the impact of high hydrostatic pressure.[94] The shallow and deep sea osmolyte compositions at two different KCl concentrations were tested (Fig. 6.12d). The deep sea mixture contains 590 mM TMAO and its stabilizing effect follows the m-values measured for TMAO alone. However, for the shallow mixture the other components are likely to destabilize the 4U hairpin structure and thus counteract the stabilizing effect of 170 mM TMAO. In contrast to urea, the destabilizing effect of the shallow mixture is attenuated at the higher KCl concentration, suggesting some type of water-mediated mechanism of destabilization.[20,398] The hydration level of the helix and the coil conformation differs significantly and the folding equilibrium has been shown to highly depend on the water activity modulated by adding osmolytes.[20] A recent MD simulation shows that the presence of such osmolytes increases the free energy of the hydration shell around base pairs and thus decreases the thermal stability of secondary structures of nucleic acids.[398]

To gain further mechanistic insights into the osmolyte effects on the structural dynamics and stability of the 4U RNA, the pressure perturbation approach allowing a volumetric characterization of the helix-to-coil transition of 4U was used. In order to calculate the standard

molar volume change of the heat-induced hairpin-to-coil transition, $\Delta V_{\mathrm{u}}^{0}$, using:

$$\Delta G_{\mathrm{u}}^{0} = \Delta V_{\mathrm{u}}^{0}\mathrm{d}p - \Delta S_{\mathrm{u}}^{0}\mathrm{d}T, \tag{6.15}$$

the CLAPEYRON equation is obtained at equilibrium:

$$\frac{\mathrm{d}T}{\mathrm{d}p} = \frac{\Delta V_{\mathrm{u}}^{0}}{\Delta S_{\mathrm{u}}^{0}}. \tag{6.16}$$

Assuming pressure independence of $\Delta S_{\mathrm{u}}^{0}$ and substituting $\Delta S_{\mathrm{u}}^{0} = \frac{\Delta H_{\mathrm{u,\,1bar}}^{0}}{T_{\mathrm{m,\,1bar}}}$, the following equation is obtained:

$$\frac{\mathrm{d}T_{\mathrm{m}}}{\mathrm{d}p} = \frac{\Delta V_{\mathrm{u}}^{0}}{\Delta H_{\mathrm{u,\,1bar}}^{0}} \cdot T_{\mathrm{m,\,1bar}}, \tag{6.17}$$

where $\Delta H_{\mathrm{u,\,1bar}}^{0}$ can be either the calorimetric or VAN'T HOFF enthalpy change for unfolding.

According to LE CHÂTELIER's principle, an increase of pressure shifts a chemical equilibrium towards conformations occupying smaller volumes, and accelerates processes for which the transition state has a smaller volume than the ground state.[164] For the 4U RNA, its melting temperature was measured as a function of pressure in the absence and presence of TMAO and urea, respectively (Fig. 6.16a). The shape of the temperature-dependent melting curves is not affected by pressure. Also, $\Delta H_{\mathrm{u}}^{0}$ was found to be only weakly pressure-dependent (Fig. 6.17). The standard molar volume change of the heat-induced hairpin-to-coil transition, $\Delta V_{\mathrm{u}}^{0}$, was calculated from the slopes, $\Delta T_{\mathrm{m}}/\Delta p$, and plotted as a function of the corresponding T_{m} at 1 bar (Fig. 6.16b). In the absence of any osmolyte, the temperature dependence of the $\Delta V_{\mathrm{u}}^{0}$, that is, the expansibility change at the transition, $\Delta E_{\mathrm{u}}^{0}$, determined by the FRET-based and the PPC measurements are comparable, only a small intrinsic shift to more positive volumes was obtained by the FRET-based method compared to the PPC data (Fig. 6.16b) which is due to the different approximations applied.[435] At temperatures below around 319 K, the 4U RNA was found to be unstable against pressurization, but becomes resistant to pressure stress at higher temperatures. In the presence of TMAO, the slope of $\Delta V_{\mathrm{u}}^{0}(T)$, that is, $\Delta E_{\mathrm{u}}^{0}$, is unchanged, but more positive $\Delta V_{\mathrm{u}}^{0}$ values are observed. In contrast, the addition of 2 M urea leads to an increase of $\Delta E_{\mathrm{u}}^{0}$, most likely due to a larger partial expansibility of the unfolded state.

Generally, the transition volume change, $\Delta V_{\mathrm{u}}^{0}$, can be considered as the sum of an intrinsic,

thermal, and hydration contribution,[436] that is, $\Delta V_u^0 = \Delta V^M + \Delta V^T + \Delta V^h$. The intrinsic volume change for the helix-to-coil transition of perfectly matched nucleic acids has been assumed to be negligible due to the absence of internal voids.[178] The thermal volume change describes the change of the void space surrounding the SASA of the RNA and is

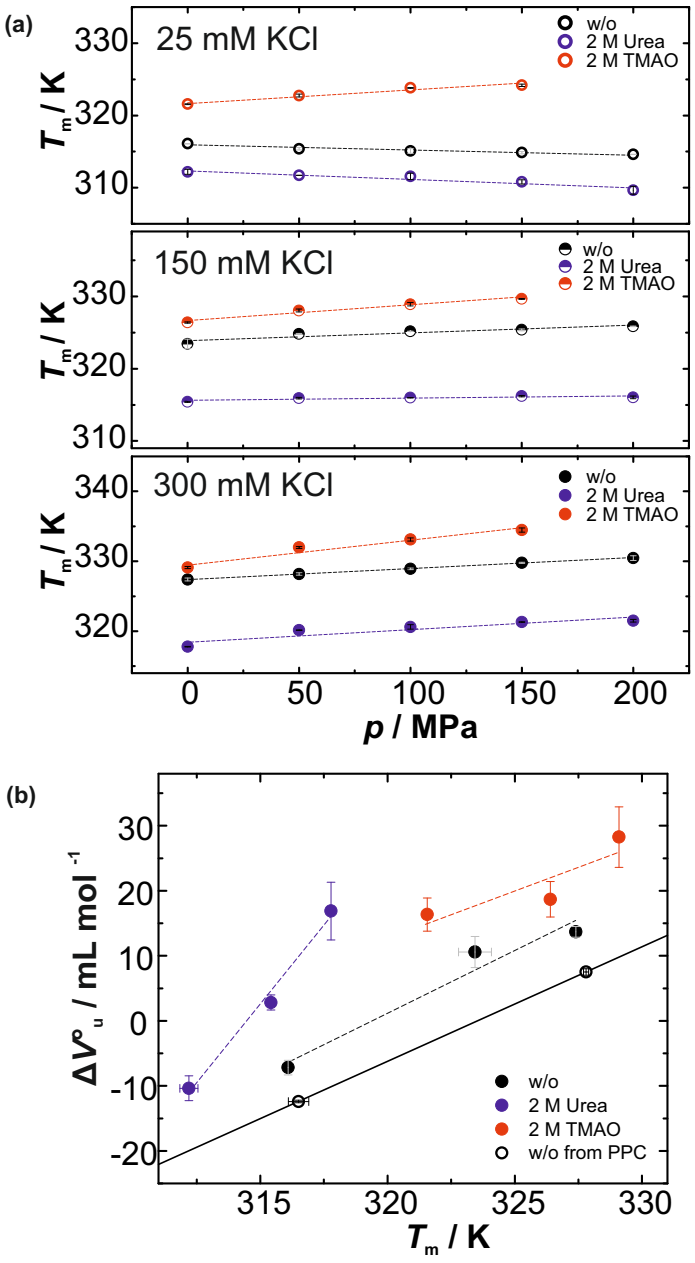

Figure 6.16 | Thermal stability of 4U and its modulation by urea and TMAO under high hydrostatic pressure conditions. (a) T_m values as a function of pressure at three KCl concentrations and in the presence of urea or TMAO. The dashed lines are least-squares fits to the data. (b) Standard molar volume change of the heat-induced hairpin-to-coil transition, ΔV_u^0, as a function of the corresponding melting temperature at atmospheric pressure. The dashed lines are least-square fits to the data and describe the expansibility change at the transition, ΔE_u^0. Error bars represent mean±s.d.

always positive for the helix-to-coil transition as the transition is accompanied by an approximately 25% increase in SASA.[168,399] A change in hydration volume results from the around 10% decrease of the partial molar volume of hydration water compared to bulk water.[168,399] Hence, an increased hydration would lead to a negative hydration volume change. Overall, these different volume contributions cancel each other largely, resulting in very small values that correspond to the volume of very few water molecules, only.[432,437] The preferential interactions between urea and nucleobases are likely to affect the thermal and hydration contributions of $\Delta V_{\mathrm{u}}^{0}$ significantly owing to a marked increase of the partial volume of the unfolded state by the greater hydrated SASA of more extended unfolded conformations and the (transient) adsorption by urea, that is, by $\Delta V_{\mathrm{T/h,\,urea}} = V_{\mathrm{T/h,\,urea}} - V_{\mathrm{T/h;\,0}} > 0$ (Fig. 6.18).[111,112] Thus, overall, the nucleobase-urea interaction, which is supposed to be highly dynamic, causes an increased partial expansibility of the unfolded state.[111]

Conversely, the unfavorable interactions between TMAO and RNA probably affect all three contributions. Both states, the folded and the coil state are expected to be more strongly hydrated in the presence of TMAO. Furthermore, the preferential hydration effect generally

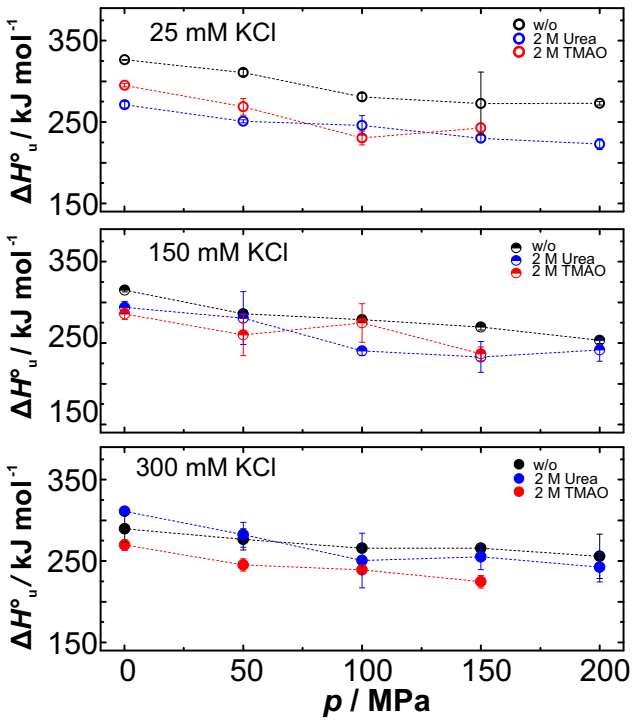

Figure 6.17 | VAN'T HOFF standard enthalpy change of the 4U hairpin-to-coil transition as a function of pressure measured in different osmolyte-containing buffers and in the presence of 25 mM (upper panel), 150 mM (middle panel) and 300 mM KCl (lower panel). Error bars represent mean±s.d. Dashed lines connect data points to guide the eye.

also leads to a compaction of all structures. In particular, it has been shown that due to the unfavorable interaction with all RNA surfaces, TMAO causes less extended conformations of the unfolded state, featuring less SASA.[139] For example, a molten globule-like unfolded 4U would diminish the SASA and result in a smaller hydration contribution, but might cause a larger number of packing defects in the unfolded state, rendering $\Delta V_{\mathrm{M,\,TMAO}} > 0$, but $\Delta V_{\mathrm{T/h,\,TMAO}}$ less negative,[139,438] which would lead to an increased partial volume of the unfolded state, as possibly observed here (Fig. 6.18).

In conclusion, this study has shown that the abundant osmolytes TMAO and urea significantly modulate the folding equilibrium and conformational landscape of a naturally occurring and functional RNA secondary structure element, and the modulation by these osmolytes depends strongly on the KCl concentration. TMAO stabilizes the 4U RNA and causes a more positive transition volume change, whereas urea destabilizes the secondary structure interactions and induces an increased partial molar volume and expansibility of the unfolded state. KCl enhances the concentration-dependent effect of urea, but attenuates that of TMAO. The stabilizing effect of TMAO can be rationalized by the preferential hydration effect and consequentially a stronger hydration shell around the RNA and a compaction of conformations. The destabilizing effect of urea is a result of its favorable interactions with nucleobases which are exposed to the solvent upon unfolding, leading to more extended unfolded conformations. Finally, this study supports a similar working mechanism of TMAO and urea to (de)stabilize folded proteins and RNAs of the type considered here. However, future systematic and detailed experimental and theoretical studies are needed to elucidate the microscopic mechanisms of osmolytes and their mixtures in shaping the conformational dynamics and free energy landscape of RNAs, as the basic building blocks of nucleic acids and proteins are completely different.

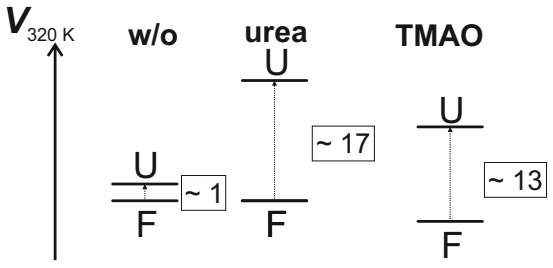

Figure 6.18 | Schematic volume profiles for the helix-to-coil transition of 4U at approximately 320 K, based on the results in Fig. 6.16b. $\Delta V_{\mathrm{u}}^{0}$ data are given in mL mol^{-1} (F=folded, U=unfolded).

6.5 Conclusions

Nucleic acids do not only store the genetic information inside cells, but they are also vitally involved in translating the information into functionality. Therefore, understanding their *in situ* conformational stabilities and dynamics is essentially important. The results presented in this chapter demonstrate the importance of considering the cellular environment as a solvent. It could be shown that both, the effect of macromolecular crowding and osmolytes, can significantly modulate the folding landscape of a functional RNA hairpin. In the case of crowding, thermodynamic insight into the folding stability of the 4U RNA in living cells with subcellular resolution could be provided for the first time. On average, it was found that the stability of the hairpin in cells is similar to that in a physiological buffer due to neutralization of the counteracting contributions from excluded volume versus nonspecific interactions and changes in water activity. Local and temporal fluctuations of all three factors can cause significant folding heterogeneities inside cells. In the case of osmolytes, using pressure perturbation, novel thermodynamic and volumetric insights into their modulation mechanism could be obtained. The presence of TMAO causes an increased thermal stability and a more positive volume change for the helix-to-coil transition, affecting the RNA hairpin to be more pressure resistant as well. In contrast, urea destabilizes the hairpin and leads to an increased expansibility of the unfolded state indicating significant nucleobase-urea interactions. Further, a strong interplay between water, salt, and osmolyte in driving the thermodynamics and defining the temperature and pressure stability limit of the RNA was found. Taken together, these findings point out that the power of background molecules inside cells cannot be easily neglected when studying the dynamics and folding landscapes of biomolecules. Hence, next to binding partners, the crowding density and the presence of different cosolutes are also able to finetune the structure, stability and thus the function of biomolecules.

CHAPTER 7

TEMPERATURE AND PRESSURE LIMITS OF GUANOSINE MONOPHOSPHATE SELF-ASSEMBLIES*

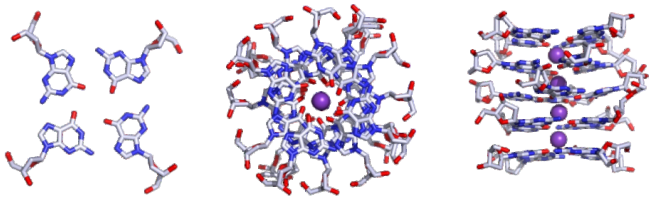

Abstract

Guanosine monophosphate (GMP) is the only nucleotide featuring the property to self-associate and to form nanoscale cylinders consisting of hydrogen-bonded G-quartet disks, which are stacked on top of one another. Such self-assemblies describe not only the basic structural motif of G-quadruplexes formed by, e.g., telomeric DNA sequences, but are also interesting targets for supramolecular chemistry and nanotechnology. The G-quartet stacks serve as an excellent model to understand the fundamentals of their molecular self-association and to unveil their application spectrum. However, the thermodynamic stability of such self-assemblies over an extended temperature and pressure range is largely unexplored. In this study, the temperature and pressure stability of G-quartet stacks formed by disodium guanosine 5'-monophosphate ($Na_2$5'-GMP) are characterized. Both, temperature and pressure tend to disfavor the self-assembly of GMP. In the presence of the alkali cations K^+ and Rb^+, the temperature and pressure resistance of the GMP supramolecular structure is significantly enhanced. Among the tested alkali cations, K^+ is the most efficient one to elevate the temperature as well as the pressure limits of GMP self-assembly.

The images were prepared and modified with PyMol using pdb:4R44.

* The work herein described has been published in the following peer-reviewed research article and subsequently reprinted in parts with the permission of the journal. Contributions of co-authors are either dinstinctly marked or not shown as results of this thesis.

1. M. Gao, B. Harish, M. Berghaus, R. Seymen, L. Arns, S. A. McCallum, C. A. Royer, and R. Winter. Temperature and Pressure Limits of Guanosine Monophosphate Self-Assemblies *Sci. Rep.* **7** (2017) 9864.

   was published online on August 29th, 2017 and the DOI is 10.1038/s41598-017-10689-0. In this chapter, the publication is partially reproduced. The original publication was reformatted to the format of the thesis (e.g. text font, reference numbering, figure numbering). Some phrases in active voice were changed to those in passive voice. In addition, supplementary figures and tables as well as important equations used for fitting were moved to the main text to improve the quality of reading. Further, some rearrangements of have been performed for this thesis and two explaining figures have been added to the introduction.

   Author contribution: M.G. and R.W. designed the research, M.G., B.H., M.B., R.S. and L.A. performed research, M.G. and B.H. analyzed data, S.A.M. assisted with NMR experiments, C.A.R. contributed analytic tools, M.G. and R.W. wrote the paper. All authors discussed the results and commented on the manuscript.

7.1 Introduction

The discovery in 1953 of the right-handed double helical structure and the WATSON-CRICK base pairs of deoxyribonucleic acid (DNA) gave birth to modern molecular biology (Fig. 7.1a).[439–441] However, in recent years it has become evident that DNA can also adopt a variety of non-canonical conformations *in vivo* including G-quadruplex structures,[442] which are thought to be functionally crucial for genome integrity and stability (Fig. 7.1b). G-quadruplex structures have emerged to be substantial nucleic acid based control elements involved in regulating and altering transcription, replication, translation and genome stability (Fig. 7.1e).[443–447] Targeting G-quadruplexes in gene promotors has also drawn attention in anticancer strategies.[445,448] Potential G-quadruplex sequences are highly conserved and have been demonstrated to exist throughout the functional parts of prokaryotic and eukaryotic genomes suggesting importance in biological evolution.[443,445] They are formed in G-rich regions of DNA or RNA sequences. However, there are fundamental differences between RNA and DNA G-quadruplexes. The additional 2'-hydroxyl-group in the ribose sugar causes greater hydration and enhanced stability of the RNA variant.[444,449] However, a very recent study pointed out that the formation of RNA G-quadruplexes is overwhelmingly prevented in eukaryotic cells, whereas the same sequences ectopically expressed in *Escherichia coli* fold into the G-quadruplex conformation, suggesting the presence of a very effective molecular machinery in eukaryotes to maintain such structures in the unfolded state.[450] Similarly, the formation of DNA G-quadruplexes in heterochromatin is also suppressed, whereas G-quadruplexes can be found in nucleosome-depleted regions and their formation is associated with increased transcriptional activity.[451] The structural topology of G-quadruplexes is highly polymorphic and depends on the number, orientation and loop structure of the G-rich chains during G-quadruplex folding (Fig. 7.1c).[452] Despite their structural polymorphism, they share the common feature of forming cyclic, planar and hydrogen-bonded guanine tetramers known as the G-quartets which are stacked on top of one another forming a right-handed four-stranded helical structure (Fig. 7.1d). In the helix, adjacent G-quartets are twisted by 30° and separated by 3.4 Å.[453–455] The G-quadruplex structure is stabilized by monovalent cations which are sandwiched between the G-quartets in the central cavity coordinating the eight guanine O6 atoms.[456–461] However, in case of the smallest alkali cation Na^+, it can exist in- or out-of-plane and move in and out of the

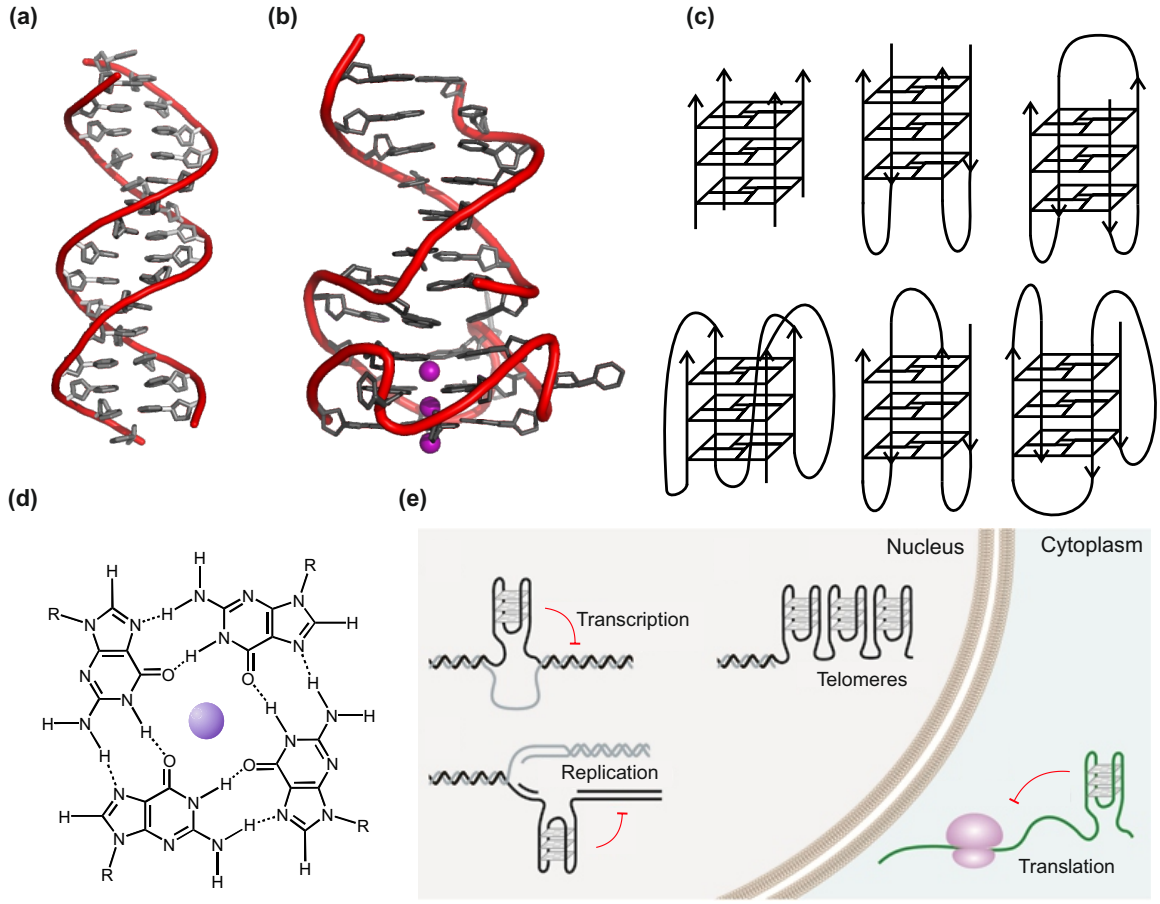

Figure 7.1 | Structural diversity of nucleic acids and their function. (a) Crystal structure of a double helical DNA in the cartoon representation. The image was prepared and modified with PyMol using pdb:4YEX. (b) Crystal structure of a quadruplex-duplex construct as found at the telomeres. The image was prepared and modified with PyMol using pdb:5DWW. (c) Structural polymorphism of G-quadruplexes: The stucture can inter- or intramolecular folded, and the orientation of the strands can be parallel or antiparallel. (d) Chemical structure of the G-quartet. Of note, the monovalent cation (shown in purple) is not in the same plane as the G-quartet. For clarity, only the chemical structure of the guanine base is shown. (e) G-quadruplex structures as regulatory control elements inside the cell during transcription, replication and translation. Taken from [D. Rhodes, H. Lipps (2015) Survey and Summary G-quadruplexes and Their Regulatory Roles in Biology, Nucleic Acids Res., 43, 8627-8637, DOI: 10.1093/nar/gkv862]. Copyright ©2015, Oxford University Press

octamer up to 108 times per second.[458,461–463] Those cation-dipole interactions stabilize the self-complementary hydrogen bonds of guanine and the base stacking interactions along the helix. The cation not only defines the stability of G-quadruplex structures, but also plays an important role in modulating their structural polymorphism.[464,465]

Interestingly, since the early 1960s, long before the existence of telomeres and their G-quadruplex structures had been shown,[455,466] the unique ability of guanosine 5'-monophosphate (5'-GMP) to undergo self-association, thereby forming right-handed helices with G-quartets stacking along the helix axis, was already known.[453,463,467] The propensity of self-

assembly and the size of aggregates depend on the sample concentration, solution acidity and presence of alkali cations.[463,467–470] At acidic pH, the self-association of 5'-GMP can even lead to the formation of anisotropic gels.[471] A recent NMR study revealed that three types of stacked 5'-GMP aggregates can generally coexist upon self-assembly using monomers, dimers and G-quartets as building blocks (Fig. 7.2a).[472] The monomeric and dimeric species undergo exchange on the ms time scale, whereas the tetrameric species are rather kinetically stable.[468,472] The size of the self-aggregates has been shown to be on the nanometer scale corresponding to tens of quartets per stack.[469,470,473] The 5'-GMP quartets are stacked in a head-to-tail manner with alternating C2'-*endo* and C3'-*endo* sugar puckers along the helical strand forming a chiral cylinder.[472] The alternating sugar conformations allow further stabilization of the helix via P-$O^{-}\cdots$H-$O_{2/3}$' hydrogen bonds along the helical strand which are reminiscent of the phosphodiester bonds in DNA or RNA (Fig. 7.2b,c).[472] Self-assembly of 5'-GMP is not only determined by HOOGSTEEN-like base pairing, π-π interaction, the hydrophobic effect and thus release of water, but also by cation binding.[474] The cation-templated self-association requires two different cation binding sites, namely the surface and channel site (Fig. 7.2d).[475,476] The adjacent peripheral phosphate groups are separated by 6.7 Å allowing true ionic binding of a sodium cation to bridge and to partially neutralize the electrostatic repulsion of the two doubly negatively charged groups.[472,475] In contrast, due to steric reasons, potassium and rubidium cations have been shown to undergo only counterion condensation to screen the charge density of the phosphate groups.[475] Consistently, the order of cation binding affinity for the surface site has been found to be $Na^+ > Rb^+ > K^+$.[476] However, the stability of the G-quartet stacks is predominantly determined by the cation type located in the central channel of the helix. The eight inwardly pointing guanine O6 atoms of two adjacent G-quartets span a volume of ca. 40 $Å^3$ serving as the channel binding site which has an affinity order of $K^+ > Rb^+ > Na^+$.[457,475,477–479] *Ab initio* calculations showed that the cation-dipole interaction provides more stabilization than either hydrogen bonding or stacking interaction and diminishes the electrostatic repulsion between the tightly packed cations.[480,481] For a long time, the cation selectivity of the channel site was explained by the concept of optimal fit.[456,482] Compared to the smaller Na^+ and the larger Rb^+, K^+ ions were thought to have the optimal size to fit into the central cavity of the G-quartet helix. However, the mechanism of size-selective coordination does not consider the dehydration process of the cation before entering the cavity and the associated

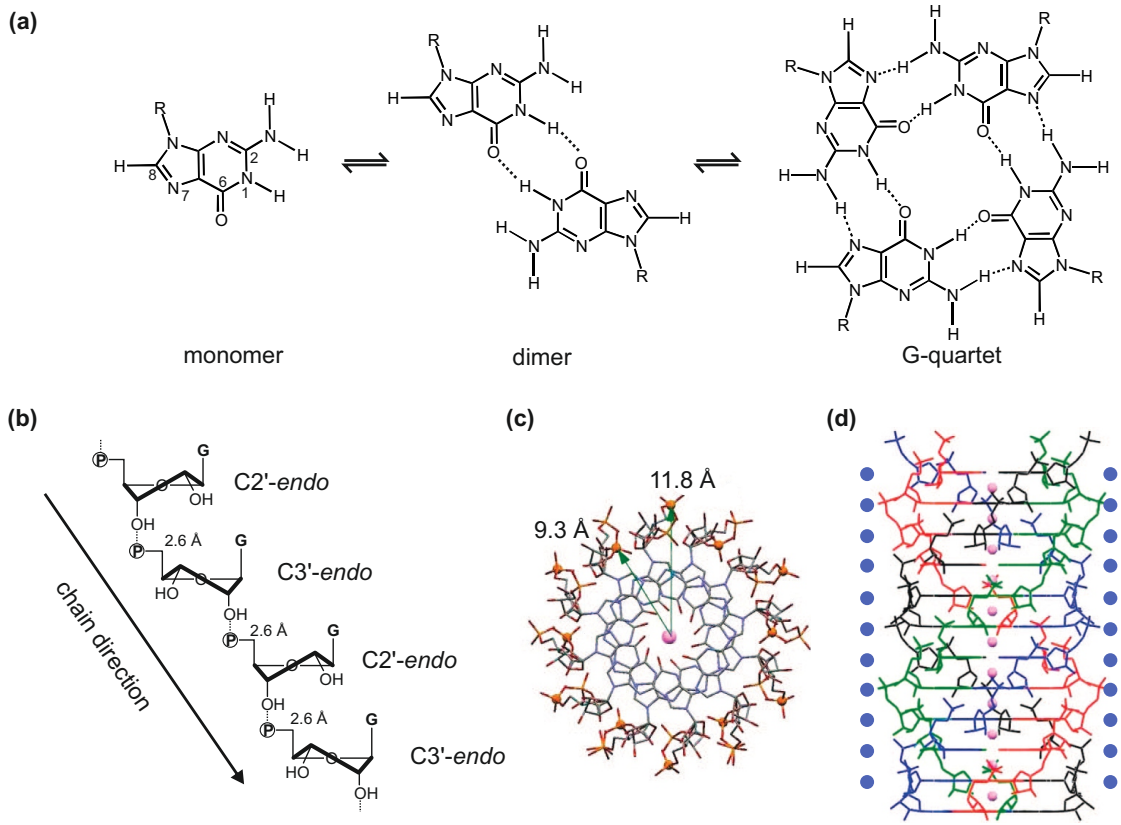

Figure 7.2 | Structural details of 5'-GMP self-assemblies. (a) Schematic structure of 5'-GMP monomer, dimer and G-quartet. For clarity, only the chemical structure of the guanine base is shown. The distance between the diagonal oxygen atoms in the G-quartet is ~ 5 Å. (b) Hydrogen bond formation between adjacent phosphate groups and OH along the helix which is reminiscent of the phosphodiester bond in DNA/RNA. Distances are given for O$\cdots$O. (c) Top view of the 5'-GMP quartet helix showing the 30°-twist of adjacent G-quartets and the position of the two different phosphorus atoms (shown as gold balls) which is caused by the alternating C2'-*endo* and C3'-*endo* conformations of the sugar pucker. Reprinted with permission from [G. Wu, I. Kwan (2009) Helical Structure of Disodium 5'-Guanosine Monophosphate Self-Assembly in Neutral Solution, J. Am. Chem. Soc., 131, 3180-3182, DOI: 10.1021/ja809258y] Copyright ©2009, American Chemical Society. (d) Structure of a full turn of the 5'-GMP quartet helix. The central channel is occupied by Na^+ ions (shown as pink balls). The cations bound to the peripheral phosphate groups (surface site) are indicated by blue balls. Adjacent G-quartets are separated by 3.4 Å. Reprinted and adapted with permission from [G. Wu, I. Kwan (2009) Helical Structure of Disodium 5'-Guanosine Monophosphate Self-Assembly in Neutral Solution, J. Am. Chem. Soc., 131, 3180-3182, DOI: 10.1021/ja809258y] Copyright ©2009, American Chemical Society.

free energy cost which has to be balanced by the free energy of the cation-guanine interaction.[483–485] NMR studies and *ab initio* calculations have revealed that the free energy of the cation-guanine interaction follows the trend in charge density of the alkali cations, but the preferred coordination of K^+ over Na^+ originates from their relative free energies of hydration.[476,484,485] Therefore, the cation affinity for the channel site is controlled by the balance of the free energy cost and gain of cation dehydration and binding, respectively.

Due to its simplicity, the non-covalent self-association of 5'-GMP has drawn unabated attention since its discovery and has become an essential model in many areas including structural biology, medicinal chemistry, supramolecular chemistry and nanotechnology.[463] The G-quartet structures show promise as a scaffold for synthetic ion channels, but also as components in nanotechnology including nanowires, nanomachines, biosensors, and molecular electronic devices.[463] Moreover, in origin-of-life studies, particularly in those where a protein-free RNA world scenario is assumed,[486,487], the self-assembly of GMP could have served as a platform for prebiotic coalescence of nucleotides.[475,488,489] Interestingly, today densely packed guanine crystals can be found in the retinal pigment epithelium of deep sea fishes focusing light to the photoreceptors.[490]

7.2 Aim

As a popular model for numerous disciplines, the thermodynamic stability of GMP self-assemblies is still largely unexplored, however. Hence, the aim of the study presented in this chapter is to reveal the temperature- and pressure-dependent stability of G-quartet stacks formed by 5'-GMP, also in the presence of the alkali cations Na^+, K^+ and Rb^+. A series of scattering and spectroscopic methods was used to unravel the role of hydration, stacking interaction and packing defects in determining the stability of such supramolecular structures.

7.3 Materials and Methods

7.3.1 Sample Preparation

Disodium guanosine 5'-monophosphate salt hydrate ($Na_2$5'-GMP, > 99% purity) from yeast was purchased from Sigma-Aldrich. Stock solutions of $Na_2$5'-GMP (35 wt%) and the alkali salts (1 M) were prepared in doubly distilled water or D_2O and filtered (0.2 μm PVDF membrane). $Na_2$5'-GMP samples were dissolved overnight to ensure homogeneity. The concentration of the stock solution was determined from UV-absorption measurements at a wavelength of 260 nm (20,000-fold dilution, ϵ_{260} =10674 $M^{-1}cm^{-1}$) and adjusted to the appropriate concentration.[469] For FTIR measurements, stock solutions of $Na_2$5'-GMP in D_2O are lyophilized twice before filtration in order to remove H_2O from the crystal water.

7.3.2 Dynamic Light Scattering

Temperature-dependent DLS experiments were performed using a Malvern Zetasizer Nano S. Scattered light of a 632.8 nm helium-neon laser was analyzed at an angle of 173°. The sample was equilibrated for 5 min at each temperature. A total of 3 scans were collected for the sample at each temperature. All samples were analyzed in triplicate. For the polydisperse samples, the method of cumulants and a symmetric spherical model were used. The translational diffusion coefficient, D_t, values were obtained from the acquired correlograms using the software Zetasizer (Malvern). The D_t values were further used to calculate the apparent hydrodynamic diameter, $d_{app,\,h}$, considering the STOKES-EINSTEIN equation. The temperature dependence of the dispersant viscosity (H_2O) was taken into consideration. We used the following relationship $\log \eta(\mathrm{H2O}) = 8.128 - 0.0447 \cdot T + 0.0000579 \cdot T^2$, where the unit for η is centipoise (cP, 1 cP = 0.001 kg m^{-1} s^{-1}).

7.3.3 Temperature- and Pressure-dependent FTIR Spectroscopy

Temperature-dependent FTIR measurements were performed using a Nicolet 5700 (Thermo Fisher Scientific, USA) equipped with a liquid-nitrogen-cooled MCT detector (HgCdTe) in the wavenumber range of 4000-1100 cm^{-1} and in the temperature range of 1-70 °C. The sample was placed between two CaF_2 windows separated by a mylar spacer (thickness, 50 μm) and assembled in a temperature cell which is connected to an external water bath. The temperature was measured with a digital thermometer placed in the sample cell (accuracy: $\pm$ 0.5 °C). The sample was equilibrated for 5 min at each temperature before spectra were collected. Pressure-dependent FTIR spectra were collected using a Nicolet 6700 (Thermo Fisher Scientific, USA) equipped with a liquid-nitrogen-cooled MCT detector (HgCdTe) in the wavenumber range of 4000-650 cm^{-1}. Pressure up to 1200 MPa was applied using a P-series diamond anvil cell (DAC) with type IIa diamonds (High Pressure Diamond Optics Inc., Tucson, USA). A 20 μm thick gasket of CrNi steel with a 0.3 mm drilling was placed between the two diamonds holding 2.5 μL of the sample. The temperature of the DAC was controlled by an external water bath and the internal temperature was measured with a digital thermometer. BaSO4 was used as an internal pressure gauge. The stretching vibration of SO_4^{2-} ($\sim$983 cm^{-1}) is pressure-dependent.[365] For each temperature or pressure, 128 scans were collected with a spectral resolution of 2 cm^{-1} and averaged. Data analysis

was carried out using the GRAMS software (Thermo Electron). After buffer subtraction and baseline correction in the range of 1710-1630 cm^{-1} (band for the C=O stretch vibration) and 1610-1518 cm^{-1} (band for the C=N ring vibration), those bands were area normalized and smoothed. All measurements were performed at least in duplicate.

7.4 Results and Discussion

7.4.1 Concentration-dependent Self-Assembly

In the planar G-quartets, hydrogen bonds are formed between N1-H and N2-H as H-donors and O6 and N7 as H-acceptors, whereas dimer formation is based on hydrogen bonds between N1 and O6 (Fig. 7.3a). Hence, significant shifts and absorbance changes of infrared (IR) bands in the region of 1700-1500 cm^{-1} characteristic of the guanine base can be observed upon 5'-GMP self-assembly.[491] Figure 7.3b displays concentration-dependent FOURIER-transform infrared (FTIR) spectra of $Na_2$5'-GMP at pH 8. The band at $\hat{\nu}_{max}$ = 1657 cm^{-1} has been assigned to the C6=O6 stretch vibration of guanine. Upon 5'-GMP self-association, the carbonyl band is blue shifted to $\hat{\nu}_{max}$ = 1673 cm^{-1} and becomes sharper. Simultaneously, the ring vibrations of guanine including C=C and C=N stretch vibration are also affected by base pairing and stacking of 5'-GMP, i.e., an intensity increase of the bands at $\hat{\nu}_{max}$ = 1592 cm^{-1} and 1537 cm^{-1} as well as an intensity decrease of the bands at $\hat{\nu}_{max}$ = 1582 cm^{-1} and 1568 cm^{-1}. Further, the self-assembly of $Na_2$5'-GMP was followed via dynamic light scattering (DLS) and qualitative information about the size distribution of 5'-GMP aggregates was obtained (Fig. 7.3c). The cylinder diameter of monomeric and tetrameric 5'-GMP aggregates are approximately 1 and 2.6 nm, respectively.[470] The length of the cylinder is defined by (n - 1) x 0.34 nm, where n is the number of quartets in the stack. At a concentration of 0.12 M and pH 8, the FTIR and DLS data indicate that $Na_2$5'-GMP does not form stacks of dimers or quartets, but non-hydrogen-bonded aggregates, thus very likely monomeric stacks are present only. These findings are in agreement with literature data.[470] Starting from 0.24 M, initial formation of larger hydrogen-bonded 5'-GMP assembled species can be observed. They coexist with the monomeric stacks and their presence increases with the concentration of $Na_2$5'-GMP (Fig. 7.3b,c). To further characterize those assemblies, ^{1}H nuclear magnetic resonance (NMR) spectroscopy was applied in collaboration with Prof. Catherine

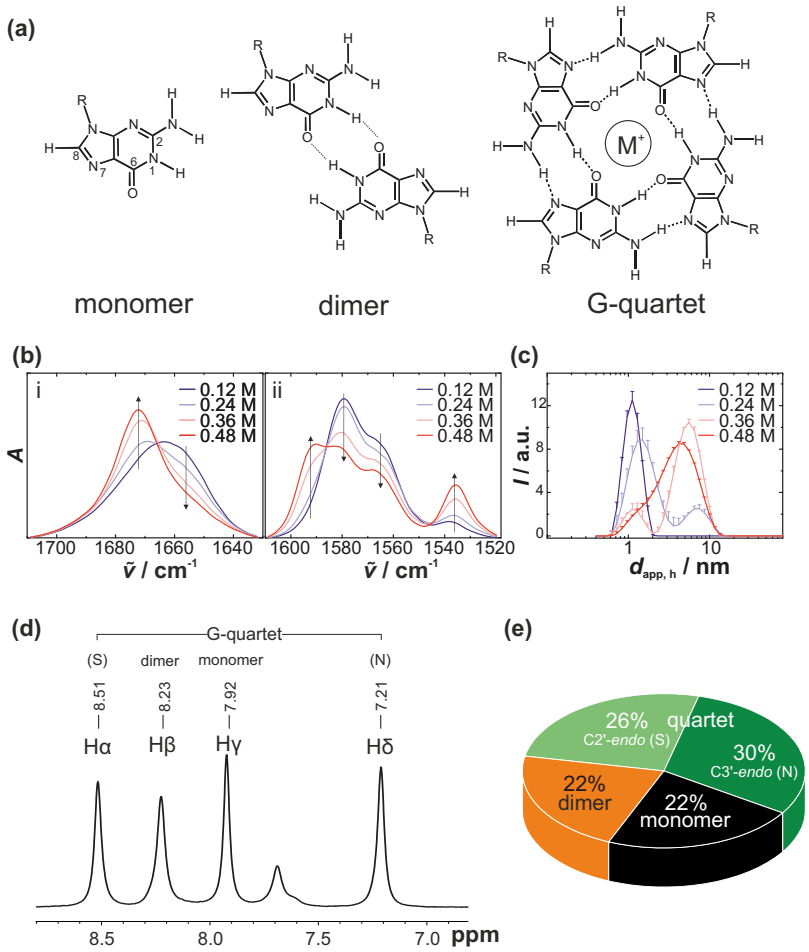

Figure 7.3 | Concentration-dependent self-assembly of disodium 5'-guanosine monophosphate ($Na_2$5'-GMP) at pH 8. (a) Schematic structure of 5'-GMP monomer, dimer and G-quartets. For clarity, only the chemical structure of the guanine base is shown. The cation M^+ can be in-plane or out-of-plane of the G-quartet. (b) Area normalized FTIR spectra of $Na_2$5'-GMP in D_2O at different concentrations: i) in the range of 1700-1640 cm^{-1} (C=O stretch vibration), and ii) in the range of 1600-1520 cm^{-1} at 282 K (C=N and C=C ring vibration). Arrows indicate the absorbance change upon self-assembly. The FTIR spectra were collected together with bachelor student Rana Seymen. (c) DLS diagrams of $Na_2$5'-GMP in H_2O at different concentrations an 282 K. Hydrodynamic diameters calculated based on spherical symmetric particles and using the method of cumulants. Error bars indicate mean±s.d. of three scans. (d) ^{1}H NMR spectrum of the H8 region and (e) the corresponding population distribution for 0.48 M $Na_2$5'-GMP at 283 K. NMR experiments were performed by Dr. Balasubramanian Harish (Rensselaer Polytechnic Institute, Troy, USA).

A. Royer from Rensselaer Polytechnic Institute (Troy, USA). NMR data was collected and primarily analyzed by Dr. Balasubramanian Harish. Upon self-association of 5'-GMP, ring-current and electrostatic effects induce upfield and downfield shifts of the H8 signal.[468] The four peaks of the H8 region located between 7.1 and 8.6 ppm of the ^{1}H NMR spectrum have been assigned to monomeric, dimeric and tetrameric species of 5'-GMP (Fig. 7.3d).[472,492] The "outer" peaks at 8.5 and 7.2 ppm (H_α and H_δ) with equal intensities are attributed to tetrameric 5'-GMP with either a C2'-*endo* or a C3'-*endo* sugar pucker conformation. The

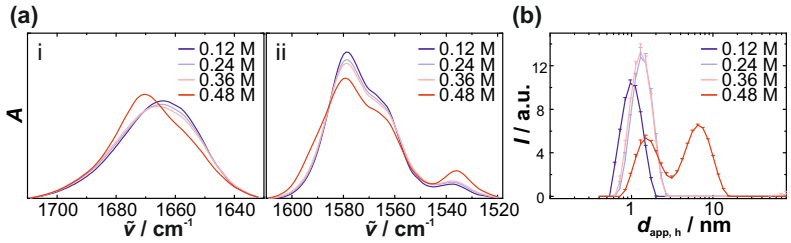

Figure 7.4 | Concentration-dependent self-assembly of $Na_2$5'-GMP at pH 8 and 296 K. (a) Area normalized FTIR spectra of $Na_2$5'-GMP in D_2O at different concentrations: i) in the range of 1700-1640 cm^{-1} at 296 K (C=O stretch vibration), and ii) in the range of 1600-1520 cm^{-1} at 296 K (C=N and C=C ring vibration). The FTIR spectra were collected together with bachelor student Rana Seymen. (b) DLS diagrams of $Na_2$5'-GMP in H_2O at different concentrations and 296 K. Hydrodynamic diameters calculated based on spherical symmetric particles and using the method of cumulants. Error bars indicate mean±s.d. of three scans.

H_γ peak at 7.9 ppm indicates monomeric 5'-GMP, whereas the H_β peak at 8.2 ppm corresponds to dimeric 5'-GMP. By integrating the H8 signals, the population distribution for the self-assembly of $Na_2$5'-GMP could be quantified (Fig. 7.3e). At a concentration of 0.48 M, more than 50% of the 5'-GMP molecules participate in forming G-quartet stacks. Only about 22% of the nucleotides are in the short-lived dimeric state.[472] Previous NMR diffusion experiments have revealed that the number of stacks increases with the nucleotide concentration.[470] Thereby, Wong et al. found the mechanism of stacking to be the same for monomers and G-quartets.[470] Hence, the channel cation in G-quartet stacks might be less needed for stacking, but rather to neutralize the electrostatic repulsion of the O6 atoms of the G-quartets. Furthermore, the concentration dependence of the $Na_2$5'-GMP self-assembly was found to be affected by temperature (Fig. 7.4), in good agreement with literature data.[470] While initial hydrogen-bonded self-assembly is observable at 0.24 M $Na_2$5'-GMP and 282 K, the critical concentration is increased to 0.48 M at 296 K, indicating high entropic costs for the self-association.

7.4.2 Thermal Stability of 5'-GMP Self-Assemblies

Previous NMR diffusion experiments have demonstrated that the stacking behavior of G-quartets and thus the length of the stacks are not modulated by temperature in the range between 278 and 298 K.[470] To yield information about the thermal stability of the hydrogen bonds formed in dimers and G-quartets of 5'-GMP, temperature-dependent FTIR measurements for 0.48 K $Na_2$5'-GMP at pH 8 were performed (Fig. 7.5a,b). IR spectra of both the carbonyl band and the ring vibrations change markedly with increasing temperature, indi-

cating dissociation of the dimers and G-quartets (Fig. 7.5a). Upon temperature increase, the carbonyl band shifts from 1673 to 1657 cm^{-1} and broadens. In the case of the ring vibrations, the band intensities at 1592 and 1537 cm^{-1} decrease at elevated temperatures, whereas the bands at 1582 and 1568 cm^{-1} show increased intensities and slight red shifts. To better describe the "melting" behavior, the band intensities at 1673, 1592, 1568 and 1537 cm^{-1} were plotted as a function of temperature (Fig. 7.5b). The "melting" curves follow the same course, indicating that any of those bands can be used to follow the self-association of 5'-GMP. Assuming an apparent thermodynamic equilibrium between all the hydrogen-bonded

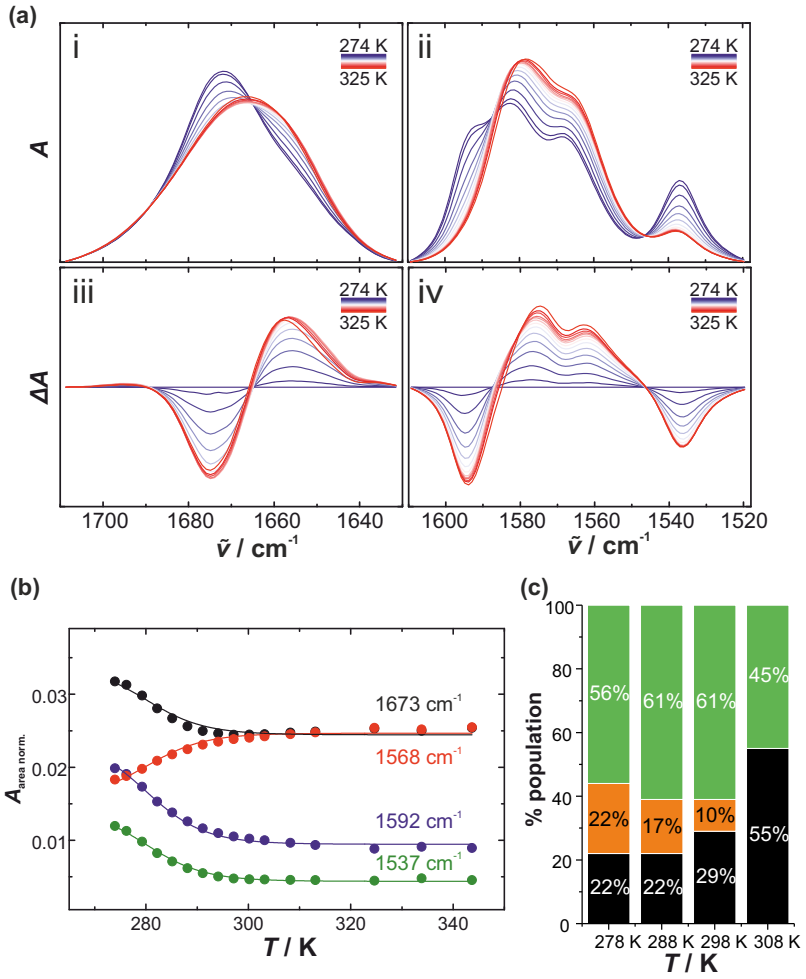

Figure 7.5 | Temperature dependence of 5'-GMP self-assembly. (a) Area normalized FTIR spectra of 0.48 M $Na_2$5'-GMP in D_2O as a function of temperature for i) the C=O stretch vibration, and ii) the ring vibrations (C=C, C=N), with iii-iv) the corresponding difference spectra. The absorption spectrum at 274 K was subtracted for the spectra at high temperatures. (b) Absorbance intensities at the given wavenumbers as a function of temperature. The lines indicate a global BOLTZMANN fit to the experimental data. (c) Population distribution of 0.48 M $Na_2$5'-GMP at different temperatures obtained from ^{1}H NMR. Green: G-quartet, orange: dimer, black: monomer. NMR experiments were performed by Dr. Balasubramanian Harish (Rensselaer Polytechnic Institute, Troy, USA).

and the monomer stacks, a global BOLTZMANN fit of the IR data was performed using:

$$I(T) = \frac{I_1 - I_2}{1 + \exp[-(\frac{1}{T_m} - \frac{1}{T}) \cdot \frac{\Delta H^0_{vH}}{R}]} + I_2, \quad (7.1)$$

where I_1 and I_2 are the plateau values of the IR band intensities of the monomeric and hydrogen-bonded state, respectively. T_m is the melting temperature and ΔH^0_{vH} the standard VAN'T HOFF enthalpy for the dissociation reaction. A melting temperature of T_m=(281±2) K and a standard-state VAN'T HOFF enthalpy change of ΔH^0_{vH}=(124±8) kJ mol^{-1} for the dissociation reaction of $Na_2$5'-GMP were obtained. In this thermodynamic model, the contribution of 5'-GMP monomers not participating in the self-association reaction, are not considered in the initial plateau values. Using ^{1}H NMR, comparable trends were obtained by analyzing the temperature-dependent population distribution of the monomer, dimer and G-quartet species (Fig. 7.5c). Although *ab initio* calculations have assigned the WATSON-CRICK faced guanine dimer (GG3^2) to be the most stable homo base pair,[493] it is less thermally stable compared to the cation-templated G-quartet. Furthermore, the temperature-dependent DLS measurements suggest that temperatures up to 348 K induce only the dissociation of hydrogen bonds and do not affect the stacking behavior (Fig. 7.6). The hydrodynamic size of the monomer stacks is hardly changed by the temperature.

Taken together, the data presented here reveal that the stacking interaction involved in 5'-GMP self-assembly can withstand a wide range of temperatures, whereas the base pairs are only stable at low temperatures. In an entropy-centered view, the favorable stacking interactions at high temperature can be explained by the hydrophobic effect and thus an entropy gain due to water release, whereas the G-quartet formation is accompanied by conformational entropy loss and thus becomes unfavorable with increasing temperature.

7.4.3 Effect of Pressure on 5'-GMP Self-Assembly

Pressure acts on molecular systems through changes in specific volume that are due to changes in hydration and packing efficiency.[172] According to LE CHÂTELIER's principle, conformations occupying smaller volumes and processes for which the transition state has a smaller volume than the ground state are favored under high pressure conditions.[164] In the case of proteins, pressure favors conformations that minimize solvent-excluded void

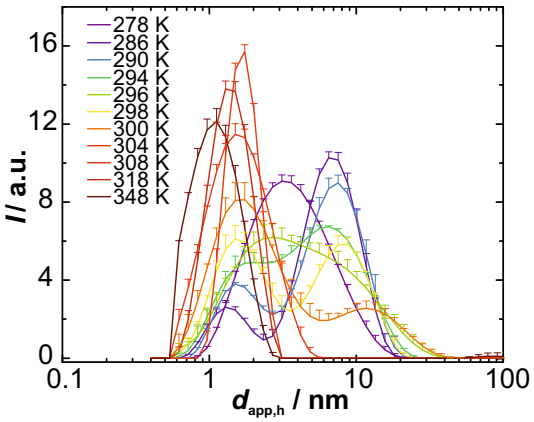

Figure 7.6 | DLS diagrams of 0.48 M $Na_2$5'-GMP in H_2O as a function of temperature. Hydrodynamic radii calculated based on spherical symmetric particles and using the method of cumulants. Error bars indicate mean±s.d. of three scans.

volume and causes water filling of hydrophobic cavities/voids. Furthermore, pressure leads to greater hydration of polar/charged amino acids, resulting in attenuation of ionic interactions.[164] Therefore, pressure is particularly sensitive to changes in hydration as the density of hydration water around charged residues is higher than that of bulk water.[168] Interestingly, conformations and configurations of DNA duplexes have been demonstrated to be relatively unaffected by pressure perturbation,[177,178,432,433] whereas an intramolecular, antiparallel DNA G-quadruplex structure has been reported to be more pressure-sensitive.[181] To study the pressure effect on the self-assembly of 5'-GMP, first pressure-dependent FTIR measurements at various temperatures were applied (Fig. 7.7). Upon pressurization, a blue shift of the IR bands is observable and can be explained by the pressure-induced compression of the bond lengths (Fig. 7.7a).[369] Due to this intrinsic elastic pressure effect on the vibrational frequency, the IR band at ∼1537 cm^{-1} was only considered for further analysis and the absorbance intensity of the band maximum was plotted as a function of pressure (Fig. 7.7b). Again, an intensity decrease was obtained suggesting pressure-induced dissociation of the hydrogen-bonded species. However, the pressure-induced disassembly is less pronounced compared to the thermal-induced dissociation. At 278 K, dissociation could not be completed upon pressurization up to 1200 MPa. When the thermal disassembly is nearly complete at 308 K, no further pressure-induced assembly or disassembly of G-quartets is observable.

Complementary high pressure ^{1}H NMR measurements confirm that pressure populates the monomeric state (Fig. 7.8). Upon pressurization up to 240 MPa, the tetrameric fraction is

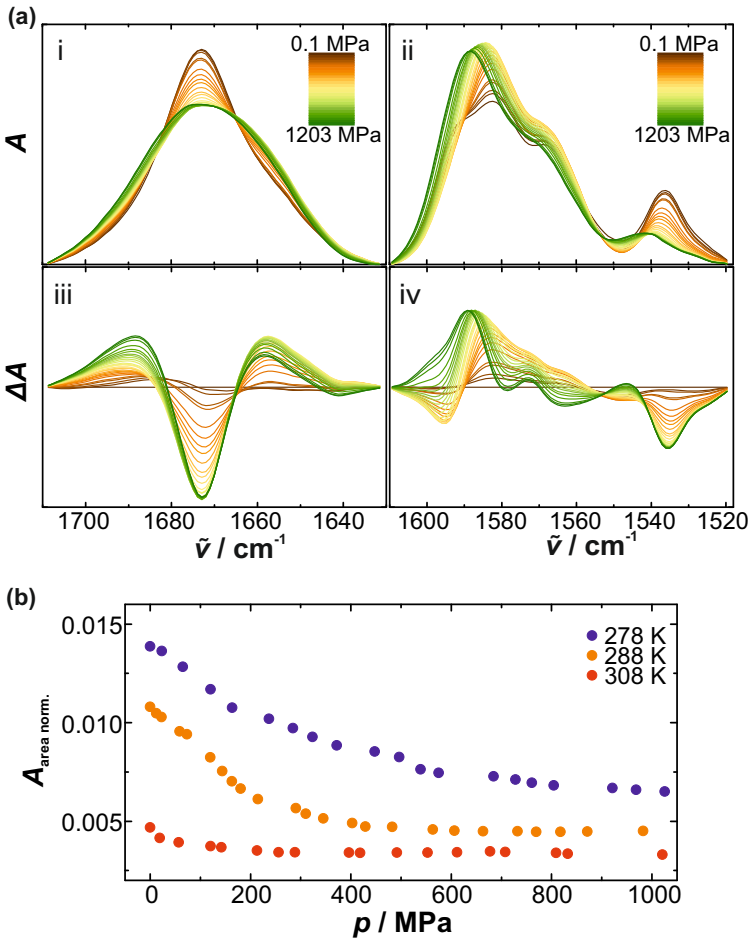

Figure 7.7 | Pressure dependence of 5'-GMP self-assembly. (a) Area normalized FTIR spectra of 0.48 M $Na_2$5'-GMP in D_2O and at 288 K as a function of pressure for i) the C=O stretch vibration, and ii) the ring vibrations (C=C, C=N), with iii-iv) the corresponding difference spectra. The absorption spectrum at 0.1 MPa was subtracted for the spectra at high pressure values. (b) Absorbance intensities of the IR band at ∼1537 cm^{-1} as a function of pressure upon area normalization.

reduced from 56% to 26%, whereas the dimeric fraction diminishes from 22% to 11%, indicating that the G-quartets and the rather thermally unstable dimers feature similar pressure stabilities (Fig. 7.8b). The standard-state free energy change for the disassembly process of 5'-GMP, ΔG^0_D, was calculated from the mole fractions of monomeric and hydrogen-bonded species and plotted as a function of pressure (Fig. 7.8c). The standard-state free energy of dissociation, ΔG^0_D, was determined by:

$$\Delta G^0_D(p) = -RT \ln K_{app} = -RT \ln \frac{f_m}{f_{hb}}, \tag{7.2}$$

where the apparent equilibrium constant, K_{app}, for the disassembly reaction is given by the ratio of the mole fractions of monomer and hydrogen-bonded 5'-GMP assemblies (dimers

and G-quartets), f_{m} and f_{hb}. The pressure-dependence of ΔG^0_{D} describes the standard molar volume change for the disassembly process of 5'-GMP, ΔV^0_{D}:

$$\left(\frac{\partial \Delta G^0_{\mathrm{D}}}{\partial p}\right)_T = \Delta V^0_{\mathrm{D}}. \tag{7.3}$$

ΔV^0_{D} = -18 mL mol^{-1} at 278 K was obtained. The corresponding transition pressure value, p_{m}, is 164 MPa (at $\Delta G^0_{\mathrm{D}}(p_{\mathrm{m}}) = 0$). ΔV^0_{D} increases, whereas p_{m} decreases with elevated temperature (Fig. 7.9). To address the question whether the length of the stacks and thus the stacking interaction is affected by pressure, pressure-dependent small-angle X-ray scattering (SAXS) and diffusion-ordered NMR spectroscopy (DOSY) were performed. The SAXS experiments were performed by Dr. Melanie Berghaus (TU Dortmund) and the DOSY measurements by Dr. Balasubramanian Harish (Rensselaer Polytechnic Institute, Troy, USA). The SAXS data indicate that longitudinal dimension of the monomer stacks is hardly affected by pressure.[494] Complementary ^{1}H DOSY NMR experiments yielded the molecular translational diffusion coefficients, D_{t}, of stacks formed by 5'-GMP monomers and G-quartets as a function of pressure.[494] The D_{t} values reveal that the stacking interaction and thus the longitudinal dimension of the G-quartet stacks are pressure-resistant up to about 240 MPa, independent of temperature. In contrast, at low temperature the number of stacks for 5'-GMP monomers is even increased with pressure, indicating dense packing of such assemblies.[494]

Overall, the results presented here show that pressure increases base stacking and induces lateral dissociation of dimer and G-quartet stacks of 5'-GMP into monomer stacks. In general, high pressure studies on DNA duplexes have revealed that pressure decreases the extent of charge neutralization by cations, reduces the WATSON-CRICK hydrogen-bond distance and favors base stacking, but leads to a very small net effect on the stability and conformation.[177,178,180] The attenuation of electrostatic interactions is explained by greater hydration of the cations and the phosphate groups under high-pressure conditions (electrostrictive effect). Consequently, the electrostatic repulsion between adjacent, negatively charged phosphates is also decreased, favoring stacking of neighboring bases.[180,495] Stacking of aromatic compounds has been shown to be accompanied by a negative volume change and is thus favored at elevated pressures.[496] In case of the 5'-GMP self-assembly, the observed pressure resistance of the longitudinal dimension and thus the stacking interaction can be explained by the same mechanism. In the liquid-crystalline phase, where the 5'-GMP quartet stacks are

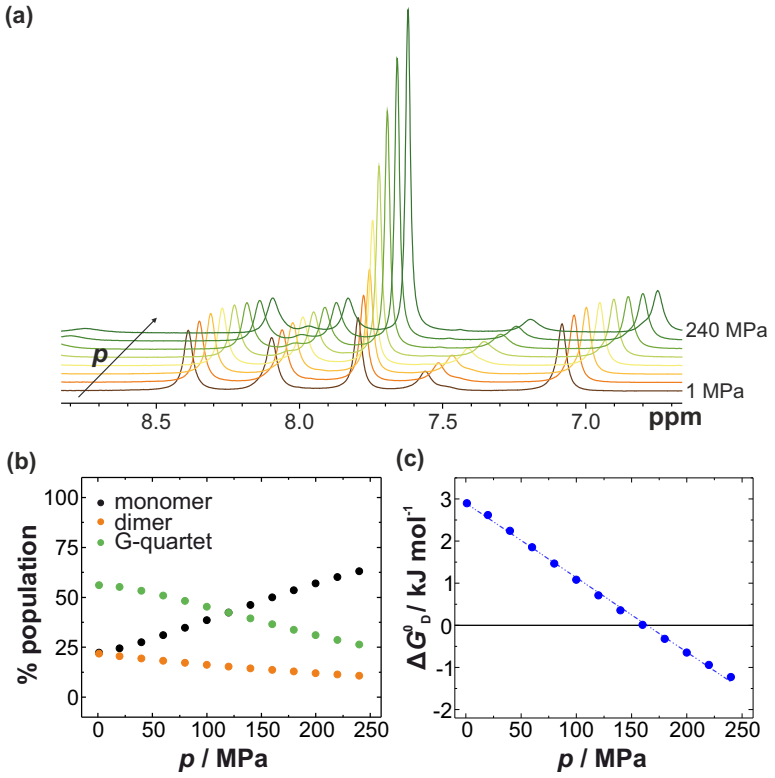

Figure 7.8 | High pressure ^{1}H NMR of 5'-GMP self-assembly at 278 K. (a) Stack plot of the ^{1}H NMR spectra for 0.48 M $Na_2$5'-GMP as a function of pressure. b) Pressure-dependent population distribution of 5'-GMP. (c) Pressure-dependent standard free energy of the 5'-GMP disassembly. The solid line is the least-square fit to the data and describes the standard molar volume change of the dissociation process. NMR experiments were performed by Dr. Balasubramanian Harish (Rensselaer Polytechnic Institute, Troy, USA).

hexagonally arranged, the stacking distance has been shown to be decreased upon compression.[497] Further, an acidic shift of the water pH upon pressurization would lead to partial protonation of the doubly charged phosphate groups, thus reducing the electrostatic repulsion between adjacent guanine bases.[498] In contrast, the typical pressure-induced strengthening of hydrogen bonds does not lead to a stabilization of the G-quartet structure, but rather a dissociation at elevated pressures. This finding suggests a volume increase upon G-quartet formation, which is unfavorable under high pressure conditions. The distance between the diagonal O6 atoms in the G-quartet is approximately 5 Å and eight inwardly pointing guanine O6 atoms of two adjacent G-quartets span a volume of 40 Å^3.[476] The Na^+ ion has a diameter of 1.9 Å and a volume of 3.6 Å^3. As the central channel formed by G-quartet stacks is only occupied by dehydrated cations and very few water molecules (diameter d = 2.75 Å),[499] it is reasonable to assume that a significant amount of water-inaccessible voids is present in the G-quartet stacks. Those voids will disappear upon dissociation of the G-quartet structure. Further volume reduction can be obtained from rehydration of the Na^+

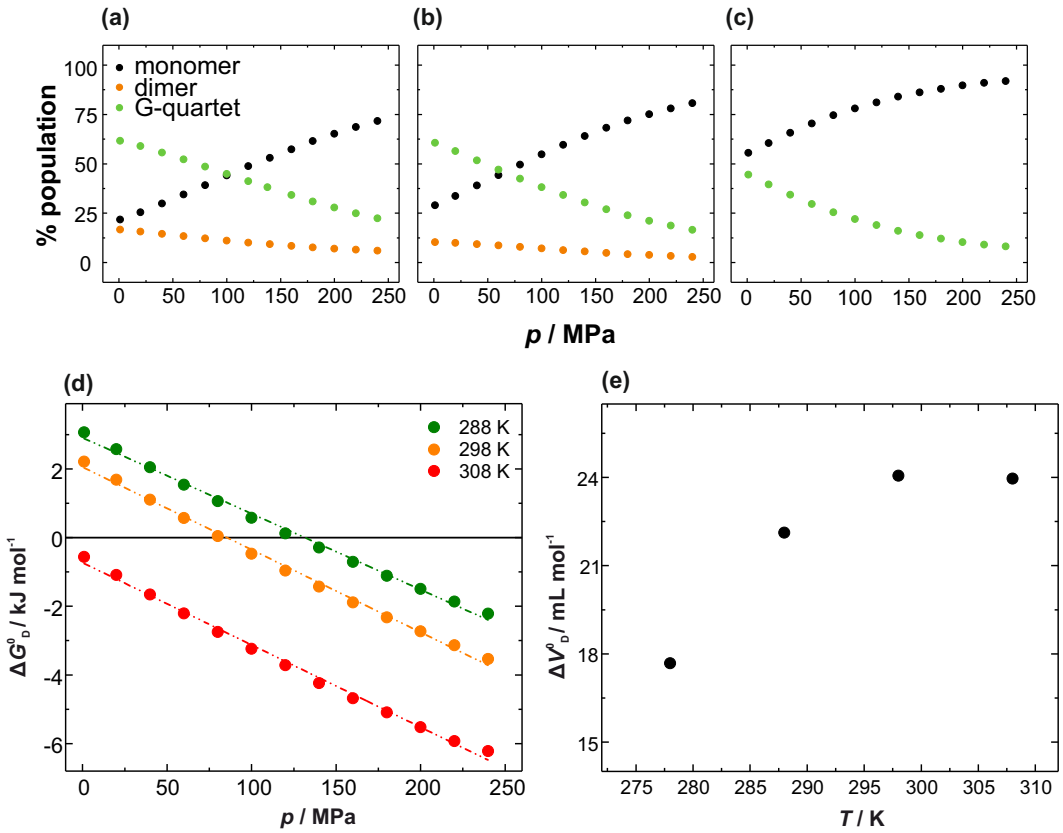

Figure 7.9 | Pressure-dependent population distribution of $Na_2$5'-GMP as a function of temperature obtained from ^{1}H NMR measurements: (a) at 288 K, (b) 298 K, and (c) 308 K. (d) Pressure-dependent standard free energy, G^0_D, of the 5'-GMP disassembly at various temperatures. The dashed lines are the least-square fit to the data and describe the standard molar volume changes, ΔV^0_D, of the dissociation process as shown in (e). NMR data were collected by Dr. Balasubramanian Harish (Rensselaer Polytechnic Institute, Troy, USA).

ions and the nucleobases after release from the channel, as the density of the hydration water is higher compared to that of bulk water.[168,399,500] Elimination of void volume, though of much lesser extent, in the dimer stacks upon pressure-induced formation of monomer stacks explains their pressure sensitivity as well.

7.4.4 Effect of Alkali Salt on the Thermal and Pressure Stability of 5'-GMP Self-Assemblies

In a very elegant approach, using NMR titration experiments Wong and Wu have shown that the channel Na^+ ions bound to the G-quartet stacks are replaced by K^+ and Rb^+ ions in a competitive equilibrium, whereas the Na^+ ions bound to the peripheral phosphates remain unaffected.[476] This allows one to explore the thermal and pressure stability of 5'-GMP

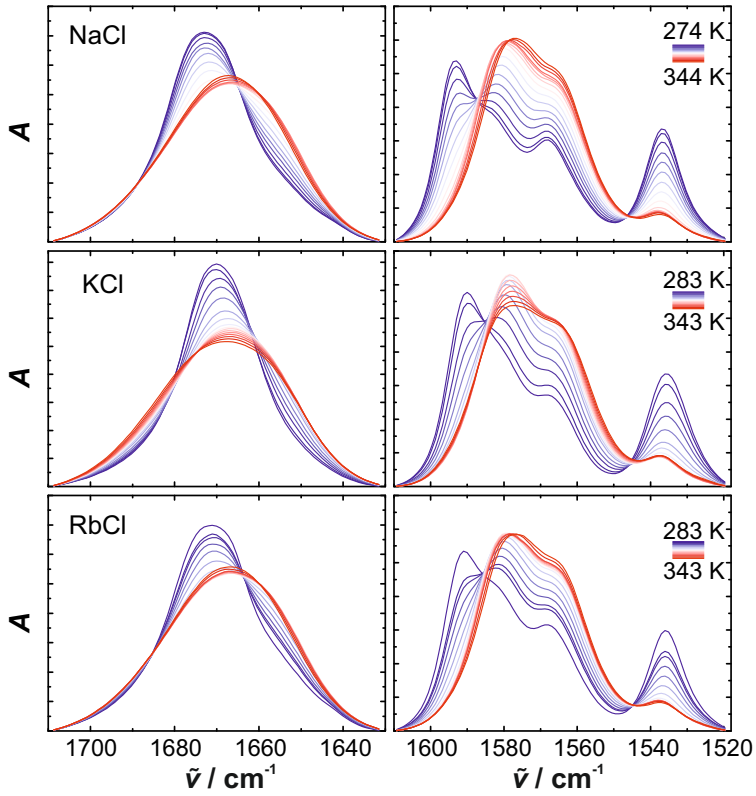

Figure 7.10 | Temperature-dependent area normalized FTIR spectra of 0.48 M $Na_2$5'-GMP in D_2O and in the presence of 0.2 M additional alkali salt. The spectra were taken at 0.1 MPa. *Left* C=O stretch vibration, *right* ring vibrations.

quartet stacks when the channel Na^+ ions are gradually replaced by K^+ and Rb^+, respectively. Hence, increasing amounts of additional MCl was added to 0.48 M $Na_2$5'-GMP. First, temperature-dependent FTIR experiments were performed and the thermal stability of the hydrogen-bonded 5'-GMP self-assemblies in the presence of the alkali salts were studied, MCl = NaCl, KCl and RbCl (Fig. 7.10). The IR bands assigned for guanine are not affected by the alkali salts, indicating that additional structures are not formed. The "melting" curves reveal that all three alkali salts are able to increase the thermal stability of the hydrogen-bonded 5'-GMP self-assemblies (Fig. 7.12a). While the melting temperature, T_m, in the presence of additional NaCl is only slightly increased, additional KCl causes a concentration-dependent stabilization of G-quartets against temperature, indicating gradual replacement of the channel Na^+ by K^+ (Fig. 7.12b). In contrast, the addition of RbCl induces a moderate stabilization, which seems to be concentration-independent. RbCl could be tested only up to 0.2 M due to precipitation of 5'-GMP at higher concentrations of RbCl. The stabilization effect of these alkali cations follows the affinity order $K^+ > Rb^+ > Na^+$

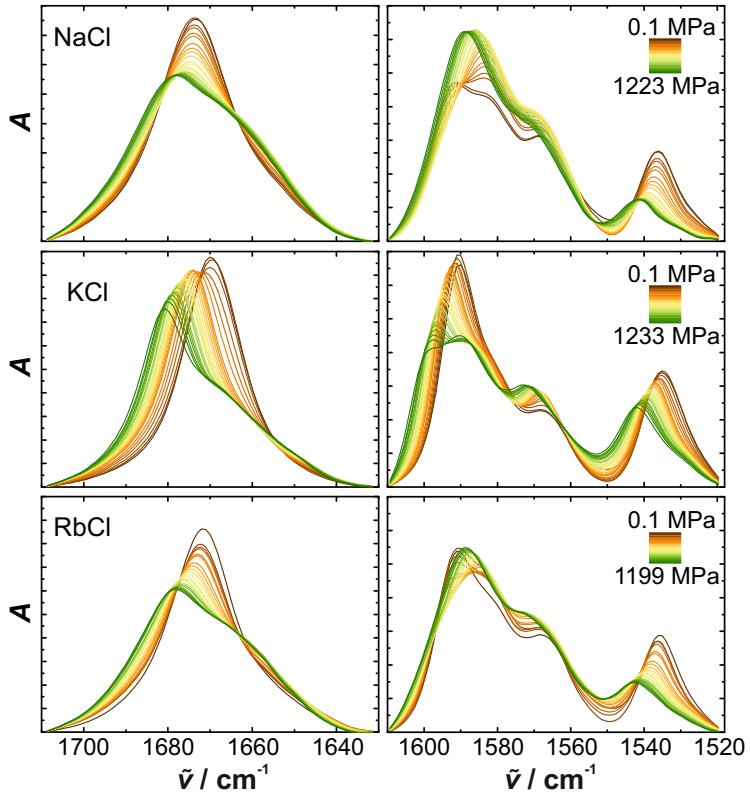

Figure 7.11 | Pressure-dependent area normalized FTIR spectra of 0.48 M $Na_2$5'-GMP in D_2O and in the presence of 0.2 M additional alkali salt. The spectra were taken at 288 K. *Left* C=O stretch vibration, *right* ring vibrations.

found for the channel site,[476] confirming the hypothesis that the channel cation determines the thermal stability of the G-quartet structure.[476] To examine the effect of the alkali salts on the pressure stability of the G-quartets, pressure-dependent FTIR and ^{1}H NMR experiments were performed in the presence of 0.2 M additional MCl (Fig. 7.11; Fig. 7.12). KCl was found to be most effective against pressure-induced dissociation of G-quartets. At 240 MPa and 278 K, the population distribution is 40% G-quartets, 16% dimers, and 44% monomers (Fig. 7.12c). This is consistent with the complementary FTIR results revealing a stabilization trend of $K^+ > Rb^+ > Na^+$ (Fig. 7.12d). This stabilization sequence against pressure can be explained by the concept of optimal packing. The K^+ ion has a diameter of 2.66 Å and occupies consequently a larger volume of the channel cavity leading to reduced voids. Furthermore, owing to its low charge density and slightly hydrophobic nature,[434] K^+ is very likely less densely hydrated and thus the volume reduction upon rehydration would be less compared to Na^+. Both contributions result in a reduced ΔV_D^0 and an improved pressure resistance. In the case of Rb^+, the same argumentation should be valid, causing even

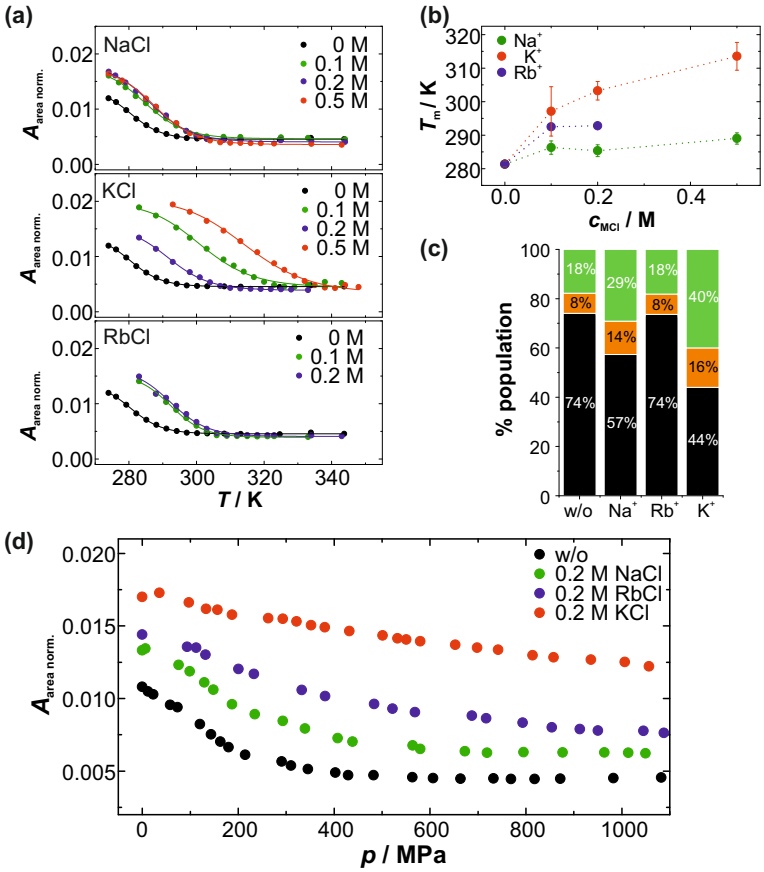

Figure 7.12 | Effect of alkali salts on 5'-GMP self-assembly. (a) Area normalized absorbance intensities of the IR band at ∼1537 cm^{-1} as a function of temperature. Various concentrations of additional alkali salts were added to 0.48 M $Na_2$5'-GMP. (b) Melting temperature, T_m, as a function of the alkali salt concentration. n = 2-3, error bars indicate mean±s.d. The pointed lines are drawn to guide the eyes. (c) Population distribution of 0.48 M $Na_2$5'-GMP in the presence of 0.2 M additional alkali salt at 278 K and 240 MPa obtained from ^{1}H NMR. Green: G-quartet, orange: dimer, black: monomer. NMR data were collected by Dr. Balasubramanian Harish (Rensselaer Polytechnic Institute, Troy, USA). (d) Pressure-dependent absorbance intensities of the IR band at ∼1537 cm^{-1} and at 288 K upon area normalization.

more increased pressure stability. However, it is very likely that the channel Na^+ ions are not completely replaced by Rb^+, as the constant for the competition equilibrium has been found to be 1.8.[476] Thus, the observed stabilizing effect is achieved by both cations, Na^+ and Rb^+, in the channel cavity.

7.5 Conclusions

In summary, the study presented here is the first comprehensive thermodynamic study on the molecular self-assembly of 5'-GMP. Using a combination of scattering and spectroscopic methods, the stability of supramolecular self-assemblies of 5'-GMP and the stabilization ef-

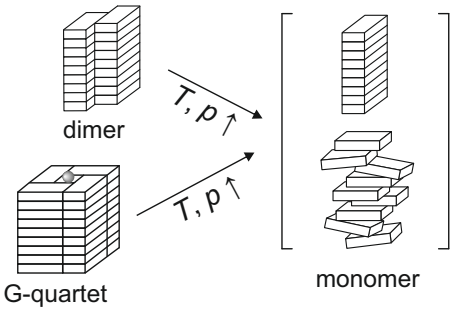

Figure 7.13 | Tentative illustration of the dissociation process of 5'-GMP self-assemblies induced by temperature and pressure. Of note, the morphology of the monomeric stacks/aggregates is not known.

fect of alkali salts over a wide range of temperatures and pressures have been studied. Under abyssal conditions, where temperatures as low as 5 °C and pressures up to 1 kbar are reached, the G-quartet structure of $Na_2$5'-GMP was found to be stable. Beyond those conditions, the G-quartet stacks dissociate laterally into monomer stacks without changing the longitudinal dimension (Fig. 7.13). Hydration, stacking interactions and packing defects play important roles in determining the stability of such supramolecular structures. In the presence of the alkali cations K^+ and Rb^+, which bind and replace the Na^+ cation from the channel cavity of the G-quartet stacks, the temperature and pressure stability of the 5'-GMP quartets is significantly increased. As the G-quartets serve as building blocks of G-quadruplexes, the results provide also insights into how different forces determining the folding of G-quadruplexes are modulated by temperature and pressure. Especially, the pressure effect on the G-quartets can be extrapolated to their oligomeric analogues and help to explain the pressure sensitivity of G-quadruplexes in general.[181,500]

CHAPTER 8

GENERAL CONCLUSIONS

Accurate folding and dynamics of biomolecules are substantially important for the functionality of living systems. As life can also be found in the realm of environmental extremes, biomolecules as well as their homo- and heterotypic interactions must withstand different environmental stresses inlcuding a wide range of temperature, pressure and salinity. For example, extreme conditions including high temperature (up to 400 °C), high hydrostatic pressure (up to 100 MPa) and high salinity (up to 600 mM) can be found close to marine hydrothermal vents. Hence, adaptation strategies, both intrinsic and extrinsic, must exist to ensure life of extremophiles. Notably, globular proteins and double-stranded nucleic acids have been reported to be very pressure stable. In contrast, initial studies have shown that quaternary interactions of proteins and non-canonical structures of nucleic acids, being essential components of cellular entities, are rather pressure-sensitive. In particular, non-covalent self-assemblies of proteins such as filamentous components of the cytoskeleton, responsible for mechanical integrity and functional architecture of the cell, have been demonstrated to be one of the most pressure-sensitive structures. However, those early and initial studies do not provide any insight into the origin of the high pressure sensitivity.

This work shed light on the origin of the pressure sensitivity of the eukaryotic cytoskeleton by focusing on the components actin filaments and microtubules. More importantly, it addressed the issue of molecular strategies for pressure resistance. In particular, it answered (1) if and how accessory proteins of the cytoskeleton can assist to improve and guarantee the mechanical strength of the cell under high pressure conditions, (2) if the cellular effect of crowding is an active contributor to counteract the pressure sensitivity, and (3) how small organic cosolutes can act as piezolytes to improve the pressure resistance. Further, the later two aspects were also investigated for a functional and temperature-sensitive ribonucleic acid molecule known to regulate the gene expression in bacteria. To fundamentally understand

the pressure effect on nucleic acids, the self-assembly reaction of guanosine-monophosphate as a single nucleotide was focus of this work as well.
Using a high hydrostatic pressure measuring platform based on spectroscopic, scattering and microscopic techniques, the following observations and conclusions have been drawn for the high pressure behavior of the eukaryotic cytoskeleton:

- At every structural level, microtubules are less pressure stabile compared to actin filaments. At 150 MPa, the upper limit of the physiologically relevant pressure range, when the microtubules and their bundles are completely disintegrated, actin filaments have previously been shown to start to deform, and their dissociation is completed beyond 400 MPa.

- The pressure-induced disorganizations of microtubules and actin filaments exhibit distinct molecular mechanisms. While the morphology and stability of actin filaments have previously been reported to be determined by the pressure stability limit of their monomeric building blocks, lateral and longitudinal contacts of microtubules are found to feature different pressure stabilities and arise mainly from internal voids and packing defects at the interfaces of the self-assemblies. High hydrostatic pressure causes first lateral dissociation of the microtubules into protofilaments, which disintegrate in a second step upon further pressurization. However, the intactness of both contact types is necessary for the functionality of microtubules *in vivo*.

- Binding partners, known to modulate the dynamics of microtubules, are found to decrease the pressure stability of microtubule protofilaments, most likely caused by forming additional packing defects in the proteins and at the longitudinal interfaces.

- In contrast, a protein crosslinker of actin filaments is found to enable the formation of pressure-resistant bundles of actin filaments, whereby their packing geometry and tightness are not affected by pressure values up to 100 MPa, which cover the physiologically relevant range encountered in the deep sea. A comparison to purely electrostatically induced actin bundles suggests that a chemically heterogeneous contact interface between actin and the crosslinker is the reason for the improved pressure resistance.

- Further, the effect of macromolecular crowding, a typical generic phenomenon of the

cellular environment, is found to increase the pressure stability of both cytoskeletal components.

- Distinct steps during the formation of both biopolymers are found to be differently modulated by high hydrostatic pressure. While the initial nucleation step is very pressure-sensitive and largely retarded under high pressure conditions, the elongation kinetics is hardly affected by pressure. This highlights the importance and need of protein nucleators to bypass the otherwise highly pressure-sensitive *de novo* formation of actin filaments and microtubules, a reaction, in which large packing defects are formed.

Using the example of a naturally occuring and functional RNA hairpin, it was found that studying biomolecules in isolation and dilute solution does not unveil the *in vivo* scenario because background molecules inside cells can actively modulate their dynamics and folding landscapes. Effects of macromolecular crowding, osmolytes, and high hydrostatic pressure were considered:

- Contributions from volume exclusion, nonspecific interactions and water activity change may modulate the folding stability of the RNA hairpin spatially and temporally causing even folding heterogeneities inside cells.

- Further, a strong interplay between water, salt, and osmolyte is found to drive the thermodynamics and to define the temperature and pressure stability limit of the RNA hairpin. With increasing concentration of KCl, the stabilizing effect of TMAO on the RNA hairpin is attenuated, whereas the destabilizing effect of urea is increased. High pressure application reveals that TMAO causes a more positive volume change for the helix-to-coil transition, whereas urea leads to an increased expansibility of the unfolded state.

Finally, studying the self-assembly reaction of guanosine-monophosphate as a single nucleotide could shed light on the origin of the high pressure sensitivity of non-canonical nucleic acid structures such as G-quadruplexes. Hydration, stacking interactions and packing defects play an important role in determining the pressure stability.

REFERENCES

[1] I. Daniel, P. Oger, R. Winter, *Chem. Soc. Rev.* **2006**, *35*(10), 858–875.
[2] T. Ikkai, T. Ooi, *Biochemistry* **1966**, *5*(5), 1551–1560.
[3] E. D. Salmon, *Science* **1975**, *189*(4206), 884–886.
[4] S. B. Zimmerman, S. O. Trach, *J. Mol. Biol.* **1991**, *222*(3), 599–620.
[5] R. J. Ellis, A. P. Minton, *Nature* **2003**, *425*(6953), 27–28.
[6] M. Gao, C. Held, S. Patra, L. Arns, G. Sadowski, R. Winter, *ChemPhysChem* **2017**, DOI: 10.1002/cphc.201700762.
[7] P. H. Yancey, M. E. Clark, S. C. Hand, R. D. Bowlus, G. N. Somero, *Science* **1982**, *217*, 1214–1222.
[8] H.-X. Zhou, G. Rivas, A. P. Minton, *Annu. Rev. Biophys.* **2008**, *37*, 375–397.
[9] D. R. Canchi, A. E. García, *Annu. Rev. Phys. Chem.* **2013**, *64*, 273–293.
[10] A. G. Ogston, *Trans. Faraday Soc.* **1958**, *54*, 1754–1757.
[11] T. C. Laurent, *Biochem. J.* **1963**, *89*, 253–257.
[12] A. P. Minton, *Biopolymers* **1981**, *20*, 2093–2120.
[13] E. H. McConkey, *Proc. Natl. Acad. Sci. U. S. A.* **1982**, *79*(10), 3236–3240.
[14] P. Ball, *Chem. Rev.* **2008**, *108*, 74–108.
[15] G. Rivas, A. P. Minton, *Trends Biochem. Sci.* **2016**, *41*(11), 970–981.
[16] J. A. Dix, A. Verkman, *Annu. Rev. Biophys.* **2008**, *37*(1), 247–263.
[17] I. Kuznetsova, B. Zaslavsky, L. Breydo, K. Turoverov, V. Uversky, *Molecules* **2015**, *20*(1), 1377–1409.
[18] D. Gnutt, S. Ebbinghaus, *Biol. Chem.* **2016**, *397*(1), 37–44.
[19] M. Gruebele, K. Dave, S. Sukenik, *Annu. Rev. Biophys.* **2016**, *45*(1), 233–251.
[20] S. I. Nakano, D. Miyoshi, N. Sugimoto, *Chem. Rev.* **2014**, *114*(5), 2733–2758.
[21] S. Ghaemmaghami, T. G. Oas, *Nat. Struct. Biol.* **2001**, *8*(10), 879–882.
[22] W. B. Monteith, G. J. Pielak, *Proc. Natl. Acad. Sci. U. S. A.* **2014**, *111*(31), 11335–11340.
[23] A. E. Smith, L. Z. Zhou, A. H. Gorensek, M. Senske, G. J. Pielak, *Proc. Natl. Acad. Sci. U. S. A.* **2016**, *113*(7), 1725–1730.
[24] R. D. Cohen, G. J. Pielak, *J. Am. Chem. Soc.* **2016**, *138*(40), 13139–13142.
[25] M. Gao, D. Gnutt, A. Orban, B. Appel, F. Righetti, R. Winter, F. Narberhaus, S. Müller, S. Ebbinghaus, *Angew. Chemie Int. Ed.* **2016**, *55*(9), 3224–3228.
[26] I. Guzman, H. Gelman, J. Tai, M. Gruebele, *J. Mol. Biol.* **2014**, *426*(1), 11–20.
[27] A. P. Schlesinger, Y. Wang, X. Tadeo, O. Millet, G. J. Pielak, *J. Am. Chem. Soc.* **2011**, *133*(21), 8082–8085.
[28] Z. Ignatova, L. M. Gierasch, *Proc. Natl. Acad. Sci. U. S. A.* **2004**, *101*(2), 523–528.
[29] Z. Ignatova, B. Krishnan, J. P. Bombardier, A. M. C. Marcelino, J. Hong, L. M. Gierasch, *Pept. Sci.* **2007**, *88*(80), 157–163.
[30] K. Inomata, A. Ohno, H. Tochio, S. Isogai, T. Tenno, I. Nakase, T. Takeuchi, S. Futaki, Y. Ito, H. Hiroaki, M. Shirakawa, *Nature* **2009**, *458*(7234), 106–109.
[31] S. R. McGuffee, A. H. Elcock, *PLoS Comput. Biol.* **2010**, *6*(3), e1000694.
[32] L. Sapir, D. Harries, *Curr. Opin. Colloid Interface Sci.* **2015**, *20*(1), 3–10.
[33] J. L. Lebowitz, E. Helfand, E. Praestgaard, *J. Chem. Phys.* **1965**, *43*(3), 774–779.
[34] R. J. Ellis, *Curr. Opin. Struct. Biol.* **2001**, *11*(1), 114–119.
[35] K. A. Sharp, *Proc. Natl. Acad. Sci. U. S. A.* **2015**, *112*(26), 7990–7995.
[36] M. Erlkamp, S. Grobelny, R. Winter, *Phys. Chem. Chem. Phys.* **2014**, *16*(13), 5965–5976.
[37] A. Dhar, A. Samiotakis, S. Ebbinghaus, L. Nienhaus, D. Homouz, M. Gruebele, M. S. Cheung, *Proc. Natl. Acad. Sci. U. S. A.* **2010**, *107*(41), 17586–17591.
[38] K. Sasahara, P. McPhie, A. P. Minton, *J. Mol. Biol.* **2003**, *326*(4), 1227–1237.
[39] D. Kilburn, J. H. Roh, L. Guo, R. M. Briber, S. A. Woodson, *J. Am. Chem. Soc.* **2010**, *132*(25),

8690–8696.
[40] H. T. Lee, D. Kilburn, R. Behrouzi, R. M. Briber, S. A. Woodson, *Nucleic Acids Res.* **2015**, *43*(2), 1170–1176.
[41] R. Desai, D. Kilburn, H. T. Lee, S. A. Woodson, *J. Biol. Chem.* **2014**, *289*(5), 2972–2977.
[42] S.-I. Nakano, H. T. Karimata, Y. Kitagawa, *J. Am. Chem. Soc.* **2009**, *131*(46), 16881–16888.
[43] J. Batra, K. Xu, S. Qin, H. X. Zhou, *Biophys. J.* **2009**, *97*(3), 906–911.
[44] D. M. Hatters, A. P. Minton, G. J. Howlett, *J. Biol. Chem.* **2002**, *277*(10), 7824–7830.
[45] D. A. White, A. K. Buell, T. P. J. Knowles, M. E. Welland, C. M. Dobson, *J. Am. Chem. Soc.* **2010**, *132*(14), 5170–5175.
[46] L. A. Munishkina, A. Ahmad, A. L. Fink, V. N. Uversky, *Biochemistry* **2008**, *47*(34), 8993–9006.
[47] H.-X. Zhou, *FEBS Lett.* **2013**, *587*(8), 1053–1061.
[48] C. Rosin, P. H. Schummel, R. Winter, *Phys. Chem. Chem. Phys.* **2015**, *17*(13), 8330–8337.
[49] M. Gao, K. Estel, J. Seeliger, R. P. Friedrich, S. Dogan, E. E. Wanker, R. Winter, S. Ebbinghaus, *Phys. Chem. Chem. Phys.* **2015**, *17*(13), 8338–8348.
[50] M. Wieczorek, S. Chaaban, G. J. Brouhard, *Cell. Mol. Bioeng.* **2013**, *6*(4), 383–392.
[51] P. H. Schummel, M. Gao, R. Winter, *ChemPhysChem* **2017**, *18*(2), 189–197.
[52] J. Batra, K. Xu, H.-X. Zhou, *Proteins* **2009**, *77*(1), 133–138.
[53] T. Ando, I. Yu, M. Feig, Y. Sugita, *J. Phys. Chem. B* **2016**, *120*(46), 11856–11865.
[54] K. Luby-Phelps, P. E. Castles, D. L. Taylort, F. Lannit, *Proc. Natl. Acad. Sci. U. S. A.* **1987**, *84*(14), 4910–4913.
[55] J. Seeliger, A. Werkmüller, R. Winter, *PLoS One* **2013**, *8*(7), e69652.
[56] S. Mukherjee, M. M. Waegele, P. Chowdhury, L. Guo, F. Gai, *J. Mol. Biol.* **2009**, *393*(1), 227–236.
[57] J. Jung, A. Van Orden, *J. Am. Chem. Soc.* **2006**, *128*(4), 1240–1249.
[58] A. Christiansen, Q. Wang, M. S. Cheung, P. Wittung-Stafshede, *Biophys. Rev.* **2013**, *5*(2), 137–145.
[59] M. S. Cheung, D. Klimov, D. Thirumalai, *Proc. Natl. Acad. Sci. U. S. A.* **2005**, *102*(13), 4753–4758.
[60] D. Lavalette, M. A. Hink, M. Tourbez, C. Tétreau, A. J. Visser, *Eur. Biophys. J.* **2006**, *35*(6), 517–522.
[61] M. Senske, L. Törk, B. Born, M. Havenith, C. Herrmann, S. Ebbinghaus, *J. Am. Chem. Soc.* **2014**, *136*(25), 9036–9041.
[62] M. Jiao, H. T. Li, J. Chen, A. P. Minton, Y. Liang, *Biophys. J.* **2010**, *99*(3), 914–923.
[63] Y. Wang, M. Sarkar, A. E. Smith, A. S. Krois, G. J. Pielak, *J. Am. Chem. Soc.* **2012**, *134*(40), 16614–16618.
[64] M. Sarkar, J. Lu, G. J. Pielak, *Biochemistry* **2014**, *53*(10), 1601–1606.
[65] M. Feig, Y. Sugita, *J. Phys. Chem. B* **2012**, *116*(1), 599–605.
[66] M. Sarkar, C. Li, G. J. Pielak, *Biophys. Rev.* **2013**, *5*(2), 187–194.
[67] Y. Wang, C. Li, G. J. Pielak, *J. Am. Chem. Soc.* **2010**, *132*(16), 9392–9397.
[68] A. C. Miklos, M. Sarkar, Y. Wang, G. J. Pielak, *J. Am. Chem. Soc.* **2011**, *133*(18), 7116–7120.
[69] S. I. Nakano, H. Karimata, T. Ohmichi, J. Kawakami, N. Sugimoto, *J. Am. Chem. Soc.* **2004**, *126*(44), 14330–14331.
[70] R. Gilman-Politi, D. Harries, *J. Chem. Theory Comput.* **2011**, *7*(11), 3816–3828.
[71] A. P. Minton, *Biopolymers* **2013**, *99*(4), 239–244.
[72] M. Sarkar, A. E. Smith, G. J. Pielak, *Proc. Natl. Acad. Sci. U. S. A.* **2013**, *110*(48), 19342–19347.
[73] L. A. Benton, A. E. Smith, G. B. Young, G. J. Pielak, *Biochemistry* **2012**, *51*(49), 9773–9775.
[74] P. Wang, I. Yu, M. Feig, Y. Sugita, *Chem. Phys. Lett.* **2017**, *671*, 63–70.
[75] R. Harada, Y. Sugita, M. Feig, *J. Am. Chem. Soc.* **2012**, *134*(10), 4842–4849.
[76] J. T. King, E. J. Arthur, C. L. Brooks, K. J. Kubarych, *J. Am. Chem. Soc.* **2014**, *136*(1), 188–194.
[77] K. Y. Huang, C. N. Kingsley, R. Sheil, C. Y. Cheng, J. C. Bierma, K. W. Roskamp, D. Khago,

R. W. Martin, S. Han, *J. Am. Chem. Soc.* **2016**, *138*(16), 5392–5402.
[78] K. D. Garlid, *Int. Rev. Cytol.* **2000**, *192*, 281–302.
[79] A. Dhar, K. Girdhar, D. Singh, H. Gelman, S. Ebbinghaus, M. Gruebele, *Biophys. J.* **2011**, *101*(2), 421–430.
[80] S. Ebbinghaus, M. Gruebele, *J. Phys. Chem. Lett.* **2011**, *2*(4), 314–319.
[81] I. Schoen, H. Krammer, D. Braun, *Proc. Natl. Acad. Sci. U. S. A.* **2009**, *106*(51), 21649–21654.
[82] A. J. Wirth, M. Platkov, M. Gruebele, *J. Am. Chem. Soc.* **2013**, *135*(51), 19215–19221.
[83] A. Minton, *Biophys. J.* **1992**, *63*(4), 1090–1100.
[84] A. P. Minton, *Biophys. J.* **1995**, *68*(4), 1311–1322.
[85] C. D. Keating, *Acc. Chem. Res.* **2012**, *45*(12), 2114–2124.
[86] D. I. Freedberg, P. Selenko, *Annu. Rev. Biophys.* **2014**, *43*(1), 171–192.
[87] S. Ebbinghaus, A. Dhar, J. D. McDonald, M. Gruebele, *Nat. Methods* **2010**, *7*(4), 319–323.
[88] I. Yu, T. Mori, T. Ando, R. Harada, J. Jung, Y. Sugita, M. Feig, *Elife* **2016**, *5*, e19274.
[89] X. Mu, S. Choi, L. Lang, D. Mowray, N. V. Dokholyan, J. Danielsson, M. Oliveberg, *Proc. Natl. Acad. Sci. U. S. A.* **2017**, *114*(23), E4556–E4563.
[90] W. B. Monteith, R. D. Cohen, A. E. Smith, E. Guzman-Cisneros, G. J. Pielak, *Proc. Natl. Acad. Sci.* **2015**, *112*(6), 1739–1742.
[91] R. D. Cohen, G. J. Pielak, *Protein Sci.* **2017**, *26*(3), 403–413.
[92] G. N. Somero, *Am. J. Physiol.* **1986**, *251*(2), 197–213.
[93] K. Lippert, E. Galinski, *Appl. Microbiol. Biotechnol.* **1992**, *37*, 61–65.
[94] R. H. Kelly, P. H. Yancey, *Biol. Bull.* **1999**, *196*(1), 18–25.
[95] P. H. Yancey, W. R. Blake, J. Conley, *Comp. Biochem. Physiol. A Mol. Integr. Physiol.* **2002**, *133*(3), 667–676.
[96] A. D. Brown, *Bacteriol. Rev.* **1976**, *40*(4), 803–846.
[97] W. J. Welch, C. R. Brown, *Cell Stress Chaperones* **1996**, *1*(2), 109–115.
[98] M. B. Burg, J. D. Ferraris, *J. Biol. Chem.* **2008**, *283*(12), 7309–7313.
[99] S. S. Stadmiller, A. H. Gorensek-Benitez, A. J. Guseman, G. J. Pielak, *J. Mol. Biol.* **2017**, *429*(8), 1155–1161.
[100] P. H. Yancey, G. N. Somero, *Biochem. J.* **1979**, *183*(2), 317–323.
[101] A. K. Soper, E. W. Castner, A. Luzar, *Biophys. Chem.* **2003**, *105*(2-3), 649–666.
[102] Y. L. A. Rezus, H. J. Bakker, *Proc. Natl. Acad. Sci. U. S. A.* **2006**, *103*(49), 18417–18420.
[103] V. Agieienko, R. Buchner, *Phys. Chem. Chem. Phys.* **2016**, *18*(4), 2597–2607.
[104] M. C. Stumpe, H. Grubmüller, *J. Phys. Chem. B* **2007**, *111*(22), 6220–6228.
[105] Y. M. Jung, *Bull. Korean Chem. Soc.* **2003**, *24*(9), 1243–1244.
[106] M. Auton, D. W. Bolen, *Proc. Natl. Acad. Sci. U. S. A.* **2005**, *102*(42), 15065–15068.
[107] M. C. Stumpe, H. Grubmüller, *J. Am. Chem. Soc.* **2007**, *129*(51), 16126–16131.
[108] S. Lee, Y. L. Shek, T. V. Chalikian, *Biopolymers* **2010**, *93*(10), 866–879.
[109] E. J. Guinn, L. M. Pegram, M. W. Capp, M. N. Pollock, M. T. Record, *Proc. Natl. Acad. Sci. U. S. A.* **2011**, *108*(41), 16932–16937.
[110] E. J. Guinn, J. Schwinefus, H. K. Cha, J. L. Mcdevitt, W. E. Merker, R. Ritzer, G. W. Muth, S. W. Engelsgjerd, K. E. Mangold, P. J. Thompson, M. J. Kerins, M. T. Record, *J. Am. Chem. Soc.* **2013**, *135*(15), 5828–5838.
[111] J. Yoon, D. Thirumalai, C. Hyeon, *J. Am. Chem. Soc.* **2013**, *135*(32), 12112–12121.
[112] U. D. Priyakumar, C. Hyeon, D. Thirumalai, A. D. MacKerell, *J. Am. Chem. Soc.* **2009**, *131*(49), 17759–17761.
[113] D. Lambert, D. E. Draper, *Biochemistry* **2012**, *51*(44), 9014–9026.
[114] P. J. Rossky, *Proc. Natl. Acad. Sci. U. S. A.* **2008**, *105*(44), 16825–16826.
[115] L. B. Sagle, Y. Zhang, V. A. Litosh, X. Chen, Y. Cho, P. S. Cremer, *J. Am. Chem. Soc.* **2009**, *131*(26), 9304–9310.
[116] F. Meersman, D. Bowron, A. K. Soper, M. H. J. Koch, *Biophys. J.* **2009**, *97*(9), 2559–2566.
[117] L. Knake, G. Schwaab, K. Kartaschew, M. Havenith, *J. Phys. Chem. B* **2015**, *119*(43), 13842–13851.
[118] A. Panuszko, P. Bruździak, J. Zielkiewicz, D. Wyrzykowski, J. Stangret, *J. Phys. Chem. B*

2009, *113*(44), 14797–14809.
[119] A. Kuffel, J. Zielkiewicz, *J. Chem. Phys.* **2010**, *133*(3), 035102.
[120] Y. L. A. Rezus, H. J. Bakker, *J. Phys. Chem. B* **2009**, *113*(13), 4038–4044.
[121] H. Wei, Y. Fan, Y. Q. Gao, *J. Phys. Chem. B* **2010**, *114*(1), 557–568.
[122] S. Paul, G. N. Patey, *J. Phys. Chem. B* **2007**, *111*(28), 7932–7933.
[123] B. J. Bennion, V. Daggett, *Proc. Natl. Acad. Sci. U. S. A.* **2004**, *101*(17), 6433–6438.
[124] A. Di Michele, M. Freda, G. Onori, M. Paolantoni, A. Santucci, P. Sassi, *J. Phys. Chem. B* **2006**, *110*(42), 21077–85.
[125] J. Qvist, B. Halle, *J. Am. Chem. Soc.* **2008**, *130*(31), 10345–10353.
[126] M. Freda, G. Onori, A. Santucci, *J. Phys. Chem. B* **2001**, *105*(51), 12714–12718.
[127] T. Shikata, S. Itatani, *J. Solution Chem.* **2002**, *31*(10), 823–844.
[128] J. D. Batchelor, A. Olteanu, A. Tripathy, G. J. Pielak, *J. Am. Chem. Soc.* **2004**, *126*(7), 1958–1961.
[129] Q. Zou, B. J. Bennion, V. Daggett, K. P. Murphy, *J. Am. Chem. Soc.* **2002**, *124*(7), 1192–1202.
[130] Y. L. A. Rezus, H. J. Bakker, *Phys. Rev. Lett.* **2007**, *99*(14), 148301.
[131] D. Laage, G. Stirnemann, J. T. Hynes, *J. Phys. Chem. B* **2009**, *113*(8), 2428–2435.
[132] G. Stirnemann, J. T. Hynes, D. Laage, *J. Phys. Chem. B* **2010**, *114*(8), 3052–3059.
[133] K. L. Munroe, D. H. Magers, N. I. Hammer, *J. Phys. Chem. B* **2011**, *115*(23), 7699–7707.
[134] J. Hunger, K. J. Tielrooij, R. Buchner, M. Bonn, H. J. Bakker, *J. Phys. Chem. B* **2012**, *116*(16), 4783–4795.
[135] K. Usui, J. Hunger, M. Sulpizi, T. Ohto, M. Bonn, Y. Nagata, *J. Phys. Chem. B* **2015**, *119*(33), 10597–10606.
[136] T. Arakawa, S. N. Timasheff, *Biophys. J.* **1985**, *47*(3), 411–414.
[137] T.-Y. Lin, S. N. Timasheff, *Biochemistry* **1994**, *33*(42), 12695–12701.
[138] D. W. Bolen, I. V. Baskakov, *J. Mol. Biol.* **2001**, *310*(5), 955–963.
[139] D. Lambert, D. Leipply, D. E. Draper, *J. Mol. Biol.* **2010**, *404*(1), 138–157.
[140] D. W. Bolen, G. D. Rose, *Annu. Rev. Biochem.* **2008**, *77*(1), 339–362.
[141] J. Ma, I. M. Pazos, F. Gai, *Proc. Natl. Acad. Sci. U. S. A.* **2014**, *111*(23), 8476–8481.
[142] S. S. Cho, G. Reddy, J. E. Straub, D. Thirumalai, *J. Phys. Chem. B* **2011**, *115*(45), 13401–13407.
[143] J. Rösgen, R. Jackson-Atogi, *J. Am. Chem. Soc.* **2012**, *134*(7), 3590–3597.
[144] A. Wang, D. W. Bolen, *Biochemistry* **1997**, *36*(30), 9101–9108.
[145] F. Meersman, D. Bowron, A. K. Soper, M. H. J. Koch, *Phys. Chem. Chem. Phys.* **2011**, *13*(30), 13765–13771.
[146] J. Hunger, N. Ottosson, K. Mazur, M. Bonn, H. J. Bakker, *Phys. Chem. Chem. Phys.* **2015**, *17*(1), 298–306.
[147] C. J. Sahle, M. A. Schroer, I. Juurinen, J. Niskanen, *Phys. Chem. Chem. Phys.* **2016**, *18*(24), 16518–16526.
[148] D. R. Canchi, P. Jayasimha, D. C. Rao, G. I. Makhatadze, A. E. Garcia, *J. Phys. Chem. B* **2012**, *116*(2), 12095–12104.
[149] P. Ganguly, T. Hajari, J. E. Shea, N. F. A. Van Der Vegt, *J. Phys. Chem. Lett.* **2015**, *6*(4), 581–585.
[150] G. Borgohain, S. Paul, *J. Phys. Chem. B* **2016**, *120*(9), 2352–2361.
[151] S. N. Timasheff, *Proc. Natl. Acad. Sci. U. S. A.* **2002**, *99*(15), 9721–9726.
[152] S. N. Timasheff, *Annu. Rev. Biophys. Biomol. Struct.* **1993**, *22*, 67–97.
[153] M. Record, C. Anderson, *Biophys. J.* **1995**, *68*(3), 786–794.
[154] V. A. Parsegian, R. P. Rand, D. C. Rau, *Proc. Natl. Acad. Sci. U. S. A.* **2000**, *97*(8), 3987–3992.
[155] C. Tanford, *J. Am. Chem. Soc.* **1964**, *86*(10), 2050–2059.
[156] X. Cheng, I. A. Shkel, K. O. Connor, J. Henrich, C. Molzahn, D. Lambert, M. T. Record, *J. Am. Chem. Soc.* **2017**, *139*(29), 9885–9894.
[157] C. N. Pace, *Methods Enzym.* **1986**, *131*, 266–279.
[158] J. K. Myers, C. N. Pace, J. M. Scholtz, *Protein Sci.* **1995**, *4*(10), 2138–2148.
[159] E. Courtenay, M. W. Capp, R. M. Saecker, M. Record, *Proteins* **2000**, *Suppl 4*, 72–85.

[160] S. Patra, C. Anders, N. Erwin, R. Winter, *Angew. Chemie Int. Ed.* **2017**, *56*(18), 5045–5049.
[161] D. Lambert, D. E. Draper, *J. Mol. Biol.* **2007**, *370*(5), 993–1005.
[162] M. Gao, L. Arns, R. Winter, *Angew. Chemie Int. Ed.* **2017**, *56*(9), 2302–2306.
[163] V. M. Shelton, T. R. Sosnick, T. Pan, *Biochemistry* **1999**, *38*(51), 16831–16839.
[164] T. Q. Luong, S. Kapoor, R. Winter, *ChemPhysChem* **2015**, *16*(17), 3555–3571.
[165] P. W. Bridgman, *J. Biol. Chem.* **1914**, *19*, 511–512.
[166] J. Roche, J. A. Caro, D. R. Norberto, P. Barthe, C. Roumestand, J. L. Schlessman, A. E. Garcia, B. Garcia-Moreno E., C. A. Royer, *Proc. Natl. Acad. Sci.* **2012**, *109*(18), 6945–6950.
[167] C. R. Chen, G. I. Makhatadze, *Nat. Commun.* **2017**, *8*, 14561.
[168] T. V. Chalikian, *J. Phys. Chem. B* **2001**, *105*(50), 12566–12578.
[169] T. V. Chalikian, *Annu. Rev. Biophys. Biomol. Struct.* **2003**, *32*, 207–235.
[170] M. D. Collins, G. Hummer, M. L. Quillin, B. W. Matthews, S. M. Gruner, *Proc. Natl. Acad. Sci.* **2005**, *103*(12).
[171] B. B. Boonyaratanakornkit, C. B. Park, D. S. Clark, *Biochim. Biophys. Acta* **2002**, *1595*(1-2), 235–249.
[172] F. Meersman, I. Daniel, D. H. Bartlett, R. Winter, R. Hazael, P. F. McMillan, *Rev. Miner. Geochem.* **2013**, *75*(1), 607–648.
[173] P. Atkins, J. de Paula, *Physical Chemistry*, 9. Aufl., Oxford University Press, **2009**, S. 1008.
[174] F. Abe, C. Kato, K. Horikoshi, *Trends Microbiol.* **1999**, *7*(11), 447–453.
[175] W. Kauzmann, *Nature* **1987**, *325*(6107), 763–764.
[176] C. A. Royer, *Biochim. Biophys. Acta - Protein Struct. Mol. Enzymol.* **2002**, *1595*(1-2), 201–209.
[177] E. Girard, T. Prangé, A. C. Dhaussy, E. Migianu-Griffoni, M. Lecouvey, J. C. Chervin, M. Mezouar, R. Kahn, R. Fourme, *Nucleic Acids Res.* **2007**, *35*(14), 4800–4808.
[178] D. J. Wilton, M. Ghosh, K. V. A. Chary, K. Akasaka, M. P. Williamson, *Nucleic Acids Res.* **2008**, *36*(12), 4032–4037.
[179] C. Schuabb, M. Berghaus, C. Rosin, R. Winter, *ChemPhysChem* **2015**, *16*(1), 138–146.
[180] M. C. Lin, P. Eid, P. T. T. Wong, R. B. MacGregor, *Biophys. Chem.* **1999**, *76*(2), 87–94.
[181] S. Takahashi, N. Sugimoto, *Angew. Chemie Int. Ed.* **2013**, *52*(51), 13774–13778.
[182] D. M. Korzhnev, I. Bezsonova, F. Evanics, N. Taulier, Z. Zhou, Y. Bai, T. V. Chalikian, R. S. Prosser, L. E. Kay, *J. Am. Chem. Soc.* **2006**, *128*(15), 5262–9.
[183] G. Panick, R. Malessa, R. Winter, G. Rapp, K. J. Frye, C. A. Royer, *J. Mol. Biol.* **1998**, *275*(2), 389–402.
[184] G. Pappenberger, C. Saudan, M. Becker, a. E. Merbach, T. Kiefhaber, *Proc. Natl. Acad. Sci.* **2000**, *97*(1), 17–22.
[185] T. Q. Luong, N. Erwin, M. Neumann, A. Schmidt, C. Loos, V. Schmidt, M. F??ndrich, R. Winter, *Angew. Chemie - Int. Ed.* **2016**, *55*(40), 12412–12416.
[186] S. Kapoor, G. Triola, I. R. Vetter, M. Erlkamp, H. Waldmann, R. Winter, *Proc. Natl. Acad. Sci. U. S. A.* **2011**, *109*(2), 460–465.
[187] H. R. Kalbitzer, M. Spoerner, P. Ganser, C. Hozsa, W. Kremer, *J. Am. Chem. Soc.* **2009**, *131*(46), 16714–16719.
[188] J. L. Silva, D. Foguel, C. A. Royer, *Trends Biochem. Sci.* **2001**, *26*(10), 612–618.
[189] D. Vanlint, R. Mitchell, E. Bailey, *MBio* **2011**, *2*(1), e00130–10.
[190] R. Ellis, *Deep Atlantic: Life, Death, and Exploration in the Abyss*, Lyons Press, Guilford, **1998**.
[191] N. Rivalain, J. Roquain, G. Demazeau, *Biotechnol. Adv.* **2010**, *28*(6), 659–672.
[192] H.-W. Huang, S.-J. Wu, J.-K. Lu, Y.-T. Shyu, C.-Y. Wang, *Food Control* **2017**, *72*(A), 1–8.
[193] J. L. Silva, A. C. Oliveira, T. C. R. G. Vieira, G. A. P. de Oliveira, M. C. Suarez, D. Foguel, *Chem. Rev.* **2014**, *114*(14), 7239–7267.
[194] P. Masson, C. Tonello, C. Balny, *J. Biomed. Biotechnol.* **2001**, *2001*(2), 85–88.
[195] V. B. Balasubramaniam, S. I. Martínez-Monteagudo, R. Gupta, *Annu. Rev. Food Sci. Technol.* **2015**, *6*(1), 435–462.
[196] S. Suladze, S. Cinar, B. Sperlich, R. Winter, *J. Am. Chem. Soc.* **2015**, *137*(39), 12588–12596.

[197] R. Mishra, R. Winter, *Angew. Chemie Int. Ed.* **2008**, *47*(35), 6518–6521.
[198] R. L. Crisman, T. W. Randolph, *Biotechnol. Bioeng.* **2009**, *102*(2), 483–92.
[199] F. Meersman, C. M. Dobson, K. Heremans, *Chem. Soc. Rev.* **2006**, *35*(10), 908–917.
[200] V. P. Voloshin, N. N. Medvedev, N. Smolin, A. Geiger, R. Winter, *J. Phys. Chem. A* **2015**, *119*(5), 1881–1890.
[201] R. Winter, F. Noll, C. Czeslik, *Methoden der Biophysikalischen Chemie*, 2. Aufl., Vieweg+Teubner, Wiesbaden, **2011**.
[202] J. R. Lakowicz, *Principles of Fluorescence Spectroscopy*, 3. Aufl., Springer, New York, **2006**.
[203] G. Bains, A. B. Patel, V. Narayanaswami, *Molecules* **2011**, *16*(9), 7909–7935.
[204] T. Foerster, *Ann. Phys.* **1948**, *437*(1-2), 55–75.
[205] T. Wilson, *J. Microsc.* **2011**, *244*(2), 113–121.
[206] M. Minsky, *Scanning* **1988**, *10*(4), 128–138.
[207] D. Semwogerere, E. R. Weeks, *Encycl. Biomater. Biomed. Eng.* **2005**, 1–10.
[208] M. Eigen, *Discuss. Faraday Soc.* **1954**, *17*, 194–203.
[209] J. Hofrichter, „Laser Temperature-Jump Methods for Studying Folding Dynamics“ in *Protein Struct. Stability, Fold.*, , *Bd. 168 von* Methods in Molecular BiologyHumana Press, **2001**, S. 159–191.
[210] C. Czeslik, H. Seemann, R. Winter, *Basiswissen Physikalische Chemie*, 3. Aufl., Vieweg+Teubner, Wiesbaden, **2009**, S. 372.
[211] J. L. Arrondo, a. Muga, J. Castresana, F. M. Goñi, *Prog. Biophys. Mol. Biol.* **1993**, *59*(1), 23–56.
[212] R. Bretzlaff, T. Bahder, *Rev. Phys. Appliquée* **1986**, *21*(12), 833–844.
[213] M. Banyay, M. Sarkar, A. Gräslund, *Biophys. Chem.* **2003**, *105*(2-3), 411–420.
[214] J. Kong, S. Yu, *Acta Biochim. Biophys. Sin. (Shanghai).* **2007**, *39*, 549–559.
[215] D. M. Byler, H. Susi, *Biopolymers* **1986**, *25*(3), 469–487.
[216] H. H. Mantsch, D. J. Moffatt, H. L. Casal, *J. Mol. Struct.* **1988**, *173*(C), 285–298.
[217] J. K. Kauppinen, D. J. Moffatt, H. H. Mantsch, D. G. Camero, *Appl. Spectrosc.* **1981**, *35*, 271–276.
[218] P. B. Tooke, *Trends Anal. Chem.* **1988**, *7*(4), 130–136.
[219] J. Stetefeld, S. A. McKenna, T. R. Patel, *Biophys. Rev.* **2016**, *8*(4), 409–427.
[220] T. Narayanan, *Synchrotron Small-Angle X-Ray Scattering*, S. 899–952, Springer, Dordrecht, **2008**.
[221] J. Kohlbrecher, „User guide for the SASfit software package SASfit“, **2010**.
[222] M. H. J. Koch, P. Vachette, D. I. Svergun, *Q. Rev. Biophys.* **2003**, *36*(2), 147–227.
[223] C. D. Putnam, M. Hammel, G. L. Hura, J. A. Tainer, *Q. Rev. Biophys.* **2007**, *40*(3), 191–285.
[224] „Vapor pressure osmometer model 5520 - user's manual“.
[225] E. F. Pettersen, T. D. Goddard, C. C. Huang, G. S. Couch, D. M. Greenblatt, E. C. Meng, T. E. Ferrin, *J. Comput. Chem.* **2004**, *25*(13), 1605–1612.
[226] D. A. Fletcher, R. D. Mullins, *Nature* **2010**, *463*(7280), 485–492.
[227] A. G. Szent-Györgyi, *J. Gen. Physiol.* **2004**, *123*(6), 631–41.
[228] T. D. Pollard, J. A. Cooper, *Science* **2009**, *326*(5957), 1208–1212.
[229] T. D. Pollard, G. G. Borisy, N. Haven, *Cell* **2003**, *112*(4), 453–465.
[230] T. D. Pollard, *Annu. Rev. Biophys. Biomol. Struct.* **2007**, *36*, 451–77.
[231] J. A. Spudich, H. E. Huxley, J. T. Finch, *J. Mol. Biol.* **1972**, *72*(3), 619–632.
[232] F. Wang, R. V. Sampogna, B. R. Ware, *Biophys. J.* **1989**, *55*(February), 293–298.
[233] A. Bertazzon, G. H. Tian, A. Lamblin, T. Y. Tsong, *Biochemistry* **1990**, *29*(1), 291–298.
[234] A. Orlova, E. H. Egelman, *J. Mol. Biol.* **1992**, *227*(4), 1043–1053.
[235] R. Cooke, *Biochemistry* **1975**, *14*(14), 3250–3256.
[236] C. G. dos Remedios, D. Chhabra, M. Kekic, I. V. Dedova, M. Tsubakihara, D. A. Berry, N. J. Nosworthy, *Physiol. Rev.* **2003**, *83*(2), 433–473.
[237] S. J. Winder, *J. Cell Sci.* **2005**, *118*(4), 651–654.
[238] R. Dominguez, K. C. Holmes, *Annu. Rev. Biophys.* **2011**, *40*, 169–86.
[239] A. Wegner, *J. Mol. Biol.* **1976**, *108*(1), 139–150.

[240] T. Fujii, A. H. Iwane, T. Yanagida, K. Namba, *Nature* **2010**, *467*(7316), 724–728.
[241] J. von der Ecken, M. Müller, W. Lehman, D. J. Manstein, P. A. Penczek, S. Raunser, *Nature* **2014**, *519*(7541), 114–117.
[242] M. D. Welch, R. D. Mullins, *Annu. Rev. Cell Dev. Biol.* **2002**, *18*, 247–88.
[243] L. S. Tobacman, E. D. Korn, *J. Biol. Chem.* **1983**, *258*(5), 3207–3214.
[244] T. D. Pollard, *J. Cell Biol.* **1986**, *103*(6), 2747–2754.
[245] N. Selve, A. Wegner, *Eur. J. Biochem.* **1986**, *160*(2), 379–387.
[246] L. Blanchoin, R. Boujemaa-Paterski, C. Sykes, J. Plastino, *Physiol. Rev.* **2014**, *94*(1), 235–263.
[247] M. M. A. E. Claessens, M. Bathe, E. Frey, A. R. Bausch, *Nat. Mater.* **2006**, *5*(9), 748–753.
[248] J. X. Tang, P. A. Janmey, *J. Biol. Chem.* **1996**, *271*(15), 8556–8563.
[249] M. Hosek, J. X. Tang, *Phys. Rev. E. Stat. Nonlin. Soft Matter Phys.* **2004**, *69*(5 Pt 1), 051907.
[250] S. Khurana, S. P. George, *Cell Adh. Migr.* **2011**, *5*(5), 409–420.
[251] T. E. Angelini, H. Liang, W. Wriggers, G. C. L. Wong, *Proc. Natl. Acad. Sci. U. S. A.* **2003**, *100*(15), 8634–8637.
[252] P. K. Mattila, P. Lappalainen, *Nat. Rev. Mol. Cell Biol.* **2008**, *9*(6), 446–454.
[253] N. Kureishy, V. Sapountzi, S. Prag, N. Anilkumar, J. C. Adams, *BioEssays* **2002**, *24*(4), 350–361.
[254] S. Jansen, A. Collins, C. Yang, G. Rebowski, T. Svitkina, R. Dominguez, *J. Biol. Chem.* **2011**, *286*(34), 300873–300896.
[255] S. Yang, F. K. Huang, J. Huang, S. Chen, J. Jakoncic, A. Leo-Macias, R. Diaz-Avalos, L. Chen, J. J. Zhang, X. Y. Huang, *J. Biol. Chem.* **2013**, *288*(1), 274–284.
[256] M. M. A. E. Claessens, C. Semmrich, L. Ramos, A. R. Bausch, *Proc. Natl. Acad. Sci. U. S. A.* **2008**, *105*(26), 8819–8822.
[257] H. Shin, K. R. P. Drew, J. R. Bartles, G. C. L. Wong, G. M. Grason, *Phys. Rev. Lett.* **2009**, *103*(23), 238102.
[258] J. N. Israelachvili, *Intermolecular and Surface Forces*, Elsevier, **2011**.
[259] T. E. Angelini, H. Liang, W. Wriggers, G. C. L. Wong, *Eur. Phys. J. E* **2005**, *16*(4), 389–400.
[260] D. Nicholls, S. Ferguson, *Bioenergetics 3rd Edition*, Elsevier, **2002**, S. 288.
[261] R. Tharmann, M. M. A. E. Claessens, A. R. Bausch, *Biophys. J.* **2006**, *90*(7), 2622–2627.
[262] E. D. Salmon, *J. Cell Biol.* **1975**, *65*(3), 603–614.
[263] R. R. Swezey, G. N. Somero, *Biochemistry* **1985**, *24*(1985), 852–860.
[264] C. R. S. Garcia, J. A. Amaral Jr, P. Abrahamsohn, S. Vekjovski-Almeida, *Eur. J. Biochem.* **1992**, *209*, 1005–1011.
[265] H. Bombardier, P. Wong, C. Gicquaud, *Biochem. Biophys. Res. Commun.* **1997**, *236*(3), 798–803.
[266] T. Kawarai, S. Arai, S. Furukawa, H. Ogihara, M. Yamasaki, *J. Biosci. Bioeng.* **2006**, *101*(6), 515–8.
[267] Y. Ikeuchi, A. Suzuki, T. Oota, K. Hagiwara, R. Tatsumi, T. Ito, C. Balny, *Eur. J. Biochem.* **2002**, *269*(1), 364–371.
[268] J. N. A. Matthews, P. B. Yim, D. T. Jacobs, J. G. Forbes, N. D. Peters, S. C. Greer, *J. Chem. Phys.* **2005**, *123*(7), 074904.
[269] T. Morita, *J. Biol. Chem.* **2003**, *278*(30), 28060–28066.
[270] C. Rosin, M. Erlkamp, J. von der Ecken, S. Raunser, R. Winter, *Biophys. J.* **2014**, *107*(12), 2982–2992.
[271] T. A. Binkowski, S. Naghibzadeh, J. Liang, *Nucleic Acids Res.* **2003**, *31*(13), 3352–3355.
[272] R. J. Ellis, A. P. Minton, *Biol. Chem.* **2006**, *387*(5), 485–497.
[273] D. S. Banks, C. Fradin, *Biophys. J.* **2005**, *89*(5), 2960–2971.
[274] R. Harada, N. Tochio, T. Kigawa, Y. Sugita, M. Feig, *J. Am. Chem. Soc.* **2013**, *135*(9), 3696–3701.
[275] D. Gnutt, M. Gao, O. Brylski, M. Heyden, S. Ebbinghaus, *Angew. Chemie Int. Ed.* **2015**, *54*(8), 2548–2551.
[276] K. B. Frederick, D. Sept, E. M. De La Cruz, *J. Mol. Biol.* **2008**, *378*(3), 540–50.
[277] C. Rosin, K. Estel, J. Hälker, R. Winter, *ChemPhysChem* **2015**, *16*(7), 1379–1385.

[278] H. L. Yin, T. P. Stossel, *Nature* **1979**, *281*(5732), 583–586.
[279] L. D. Burtnick, E. K. Koepf, J. Grimes, E. Jones, D. I. Stuart, P. J. McLaughlin, R. C. Robinson, *Cell* **1997**, *90*(4), 661–670.
[280] H. Q. Sun, M. Yamamoto, M. Mejillano, H. L. Yin, *J. Biol. Chem.* **1999**, *274*(47), 33179–33182.
[281] A. Ditsch, A. Wegner, *Eur. J. Biochem.* **1994**, *224*(1), 223–227.
[282] A. A. Lal, S. L. Brenner, E. D. Korn, *J. Biol. Chem.* **1984**, *259*(21), 13061–13065.
[283] N. Selve, A. Wegner, *Eur. J. Biochem.* **1987**, *168*(1), 111–115.
[284] B. Schoepper, A. Wegner, *Eur. J. Biochem.* **1991**, *202*(3), 1127–1131.
[285] P. A. Janmey, C. Chaponnier, S. E. Lind, K. S. Zaner, T. P. Stossel, H. L. Yin, *Biochemistry* **1985**, *24*(14), 3714–3723.
[286] A. Wegner, *Nature* **1982**, *296*(5854), 266–267.
[287] H. P. Erickson, *J. Mol. Biol.* **1989**, *206*(3), 465–474.
[288] T. I. Lin, R. M. Dowben, *Biophys. Chem.* **1982**, *15*(4), 289–298.
[289] A. Wegner, P. Savko, *Biochemistry* **1982**, *21*(8), 1909–1913.
[290] J. F. Swindells, C. F. Snyder, R. C. Hardy, P. E. Golden, „Viscosities of sucrose solutions at various temperatures: tables of recalculated values“, **1958**.
[291] J. Kestin, M. Sokolov, W. A. Wakeham, *J. Phys. Chem.* **1978**, *7*(3), 941–948.
[292] R. Politi, D. Harries, *Chem. Commun.* **2010**, *46*(35), 6449–6451.
[293] E. Nishida, H. Sakai, *J. Biochem.* **1983**, *93*(4), 1011–1020.
[294] D. Drenckhahn, T. D. Pollard, *J. Biol. Chem.* **1986**, *261*(27), 12754–12758.
[295] S. Yadav, S. J. Shire, D. S. Kalonia, *Pharm. Res.* **2011**, *28*(8), 1973–1983.
[296] C. Kuckel, P. Lambooy, P. Farnsworth, *Biochem. Cell Biol.* **1993**, *71*(1-2), 65–72.
[297] Y. Kusumoto, a. Lomakin, D. B. Teplow, G. B. Benedek, *Proc. Natl. Acad. Sci. U. S. A.* **1998**, *95*(21), 12277–12282.
[298] N. V. Nucci, B. Fuglestad, E. A. Athanasoula, A. J. Wand, *Proc. Natl. Acad. Sci.* **2014**, *111*(38), 13846–13851.
[299] P. W. Bridgman, *Proc. Natl. Acad. Sci. U. S. A.* **1925**, *11*(10), 603–606.
[300] M. Gao, M. Berghaus, J. von der Ecken, S. Raunser, R. Winter, *Angew. Chemie Int. Ed.* **2015**, *54*(38), 11088–11092.
[301] K. Akasaka, *Chem. Rev.* **2006**, *106*(5), 1814–1835.
[302] P. W. Gunning, U. Ghoshdastider, S. Whitaker, D. Popp, R. C. Robinson, *J. Cell Sci.* **2015**, *128*(11), 2009–2019.
[303] R. S. Sedeh, A. A. Fedorov, E. V. Fedorov, S. Ono, F. Matsumura, S. C. Almo, M. Bathe, *J. Mol. Biol.* **2010**, *400*(3), 589–604.
[304] N. Wakai, K. Takemura, T. Morita, A. Kitao, *PLoS One* **2014**, *9*(1), e85852.
[305] A. Akhmanova, M. O. Steinmetz, *Nat. Rev. Mol. Cell Biol.* **2015**, *16*(12), 711–726.
[306] A. Desai, T. J. Mitchison, *Annu. Rev. Cell Dev. Biol.* **1997**, *13*, 83–117.
[307] L. Amos, A. Klug, *J. Cell Sci.* **1974**, *14*(3), 523–549.
[308] D. Chretien, F. Metoz, F. Verde, E. Karsenti, R. H. Wade, *J. Cell Biol.* **1992**, *117*(5), 1031–1040.
[309] R. G. Burns, *Cell Motil. Cytoskeleton* **1991**, *20*(3), 181–189.
[310] R. C. Weisenberg, G. G. Borisy, E. W. Taylor, *Biochemistry* **1968**, *7*(12), 4466–4479.
[311] E. Nogales, S. G. Wolf, K. H. Downing, *Nature* **1998**, *391*(6663), 199–203.
[312] M. F. Carlier, D. Pantaloni, *Biochemistry* **1981**, *20*(7), 1918–1924.
[313] E. Nogales, M. Whittaker, R. A. Milligan, K. H. Downing, *Cell* **1999**, *96*(1), 79–88.
[314] C. Allen, G. G. Borisy, *J. Mol. Biol.* **1974**, *90*(2), 381–402.
[315] T. J. Mitchison, *Science* **1993**, *261*(5124), 1044–1047.
[316] J. M. Kollman, A. Merdes, L. Mourey, D. A. Agard, *Nat. Rev. Mol. Cell Biol.* **2011**, *12*(11), 709–721.
[317] E. M. Mandelkow, R. Schultheiss, R. Rapp, M. Müller, E. Mandelkow, *J. Cell Biol.* **1986**, *102*(3), 1067–1073.
[318] R. Zhang, G. M. Alushin, A. Brown, E. Nogales, *Cell* **2015**, *162*(4), 849–859.

[319] T. Mitchison, M. Kirschner, *Nature* **1984**, *312*(5991), 232–237.
[320] D. Job, O. Valiron, B. Oakley, *Curr. Opin. Cell Biol.* **2003**, *15*(1), 111–117.
[321] N. Caudron, I. Arnal, E. Buhler, D. Job, O. Valiron, *J. Biol. Chem.* **2002**, *277*(52), 50973–50979.
[322] J. Mozziconacci, L. Sandblad, M. Wachsmuth, D. Brunner, E. Karsenti, *PLoS One* **2008**, *3*(11), e3821.
[323] J. W. J. Kerssemakers, E. L. Munteanu, L. Laan, T. L. Noetzel, M. E. Janson, M. Dogterom, *Nature* **2006**, *442*(7103), 709–712.
[324] R. A. Walker, E. T. O'Brien, N. K. Pryer, M. F. Soboeiro, W. A. Voter, H. P. Erickson, E. D. Salmon, *J. Cell Biol.* **1988**, *107*(4), 1437–1448.
[325] D. Chrétien, S. D. Fuller, E. Karsenti, *J. Cell Biol.* **1995**, *129*(5), 1311–1328.
[326] L. A. Amos, *Trends Cell Biol.* **1995**, *5*(2), 48–51.
[327] T. Mitchison, M. Kirschner, *Nature* **1984**, *312*(5991), 237–242.
[328] R. B. G. Ravelli, B. Gigant, P. A. Curmi, I. Jourdain, S. Lachkar, A. Sobel, M. Knossow, *Nature* **2004**, *428*(6979), 198–202.
[329] E. Nogales, H.-W. Wang, *Curr. Opin. Struct. Biol.* **2006**, *16*(2), 221–229.
[330] E. M. Mandelkow, *J. Cell Biol.* **1991**, *114*(5), 977–991.
[331] G. M. Alushin, G. C. Lander, E. H. Kellogg, R. Zhang, D. Baker, E. Nogales, *Cell* **2014**, *157*(5), 1117–1129.
[332] E. H. Kellogg, N. M. A. Hejab, S. Howes, P. Northcote, J. H. Miller, J. F. Díaz, K. H. Downing, E. Nogales, *J. Mol. Biol.* **2017**, *429*(5), 633–646.
[333] M. A. Jordan, L. Wilson, *Nat. Rev. Cancer* **2004**, *4*(4), 253–265.
[334] J. Howard, A. A. Hyman, *Curr. Opin. Cell Biol.* **2007**, *19*(1), 31–35.
[335] D. Panda, J. E. Daijo, M. A. Jordan, L. Wilson, *Biochemistry* **1995**, *34*(31), 9921–9929.
[336] J. M. Bunker, L. Wilson, M. A. Jordan, S. C. Feinstein, *Mol. Biol. Cell* **2004**, *15*(6), 2720–2728.
[337] J. Chen, Y. Kanai, N. J. Cowan, N. Hirokawa, *Nature* **1992**, *360*(6405), 674–677.
[338] H. Kim, L. I. Binder, J. L. Rosenbaum, *J. Cell Biol.* **1979**, *80*(2), 266–276.
[339] T. H. MacRae, *Biochim. Biophys. Acta* **1992**, *1160*(2), 145–155.
[340] J. Iida, T. J. Itoh, H. Hotani, K. I. Nishiyama, H. Murofushi, J. C. Bulinski, S. I. Hisanaga, *J. Mol. Biol.* **2002**, *320*(1), 97–106.
[341] P. J. Chung, C. Song, J. Deek, H. P. Miller, Y. Li, M. C. Choi, L. Wilson, S. C. Feinstein, C. R. Safinya, *Nat. Commun.* **2016**, *7*, 12278.
[342] C. Conde, A. Cáceres, *Nat. Rev. Neurosci.* **2009**, *10*(5), 319–332.
[343] R. Mukhopadhyay, J. H. Hoh, *FEBS Lett.* **2001**, *505*(3), 374–378.
[344] L. Dehmelt, S. Halpain, *Genome Biol.* **2004**, *6*(204), 1–9.
[345] S. A. Lewis, D. H. Wang, N. J. Cowan, *Science* **1988**, *242*(4880), 936–939.
[346] A. Himmler, D. Drechsel, M. W. Kirschner, D. W. Martin, *Mol. Cell. Biol.* **1989**, *9*(4), 1381–1388.
[347] J. Al-Bassam, R. S. Ozer, D. Safer, S. Halpain, R. A. Milligan, *J. Cell Biol.* **2002**, *157*(7), 1187–1196.
[348] R. B. Dye, S. P. Fink, R. C. Williams, *J. Biol. Chem.* **1993**, *268*(10), 6847–6850.
[349] D. W. Cleveland, S. Y. Hwo, M. W. Kirschner, *J. Mol. Biol.* **1977**, *116*(2), 227–247.
[350] D. N. Drechsel, A. A. Hyman, M. H. Cobb, M. W. Kirschner, *Mol. Biol. Cell* **1992**, *3*(10), 1141–1154.
[351] J. Wolff, L. Knipling, D. L. Sackett, *Biochemistry* **1996**, *35*(95), 5910–5920.
[352] D. J. Needleman, M. a. Ojeda-Lopez, U. Raviv, H. P. Miller, L. Wilson, C. R. Safinya, *Proc. Natl. Acad. Sci. U. S. A.* **2004**, *101*(46), 16099–16103.
[353] D. J. Needleman, M. A. Ojeda-Lopez, U. Raviv, K. Ewert, J. B. Jones, H. P. Miller, L. Wilson, C. R. Safinya, *Phys. Rev. Lett.* **2004**, *93*(19), 198104.
[354] S. Asakura, F. Oosawa, *J. Polym. Sci.* **1958**, *33*(126), 183–192.
[355] A. M. Zimmerman, D. Marsland, *Exp. Cell Res.* **1964**, *35*, 293–302.
[356] B. Bourns, S. Franklin, L. Cassimeris, E. D. Salmon, *Cell Motil. Cytoskeleton* **1988**, *10*(3),

380–390.
[357] Y. Engelborghs, K. A. H. Heremans, L. C. M. Maeyer, J. Hoebeke, *Nature* **1976**, *259*(5545), 686–689.
[358] T. C. Gamblin, K. Nachmanoff, S. Halpain, R. C. Williams, *Biochemistry* **1996**, *35*(38), 12576–12586.
[359] T. Doll, A. Papandrikopoulou, A. Matus, *Nucleic Acids Res.* **1990**, *18*(2), 361.
[360] C. Krywka, C. Sternemann, M. Paulus, N. Javid, R. Winter, A. Al-Sawalmih, S. Yi, D. Raabe, M. Tolan, *J. Synchrotron Radiat.* **2007**, *14*(3), 244–251.
[361] N. J. Brooks, B. L. L. E. Gauthe, N. J. Terrill, S. E. Rogers, R. H. Templer, O. Ces, J. M. Seddon, *Rev. Sci. Instrum.* **2010**, *81*(6), 064103.
[362] M. Sztucki, T. Narayanan, *J. Appl. Crystallogr.* **2006**, *40*, 459–462.
[363] I. Breßler, J. Kohlbrecher, A. F. Thünemann, *J. Appl. Crystallogr.* **2015**, *48*(Pt 5), 1587–1598.
[364] D. Franke, M. V. Petoukhov, P. V. Konarev, A. Panjkovich, A. Tuukkanen, H. D. T. Mertens, A. G. Kikhney, N. R. Hajizadeh, J. M. Franklin, C. M. Jeffries, D. I. Svergun, R. M., S. D. I., *J. Appl. Crystallogr.* **2017**, *50*(4), 1151–1158.
[365] P. T. T. Wong, D. J. Moffatt, *Appl. Spectrosc.* **1989**, *43*(7), 1279–1281.
[366] J. M. De Pereda, D. Leynadier, J. A. Evangelio, P. Chacón, J. M. Andreu, *Biochemistry* **1996**, *35*(45), 14203–14215.
[367] M. B. Prigozhin, Y. Liu, A. J. Wirth, S. Kapoor, R. Winter, K. Schulten, M. Gruebele, *Proc. Natl. Acad. Sci. U. S. A.* **2013**, *110*(20), 8087–8092.
[368] J. R. Parrish, E. R. Blout, *Biopolymers* **1972**, *11*(5), 1001–1020.
[369] L. Smeller, F. Meersman, J. Fidy, K. Heremans, *Biochemistry* **2003**, *42*(2), 553–561.
[370] G. Zandomeneghi, M. R. H. Krebs, M. G. McCammon, M. Fändrich, *Protein Sci.* **2004**, *13*(12), 3314–3321.
[371] U. Raviv, T. Nguyen, R. Ghafouri, D. J. Needleman, Y. Li, H. P. Miller, L. Wilson, R. F. Bruinsma, C. R. Safinya, *Biophys. J.* **2007**, *92*(1), 278–287.
[372] J. F. Díaz, J. M. Valpuesta, P. Chacón, G. Diakun, J. M. Andreu, *J. Biol. Chem.* **1998**, *273*(50), 33803–33810.
[373] M. C. Choi, U. Raviv, H. P. Miller, M. R. Gaylord, E. Kiris, D. Ventimiglia, D. J. Needleman, M. W. Kim, L. Wilson, S. C. Feinstein, C. R. Safinya, *Biophys. J.* **2009**, *97*(2), 519–527.
[374] D. Marenduzzo, K. Finan, P. R. Cook, *J. Cell Biol.* **2006**, *175*(5), 681–686.
[375] D. Popp, A. Narita, T. Oda, T. Fujisawa, H. Matsuo, Y. Nitanai, M. Iwasa, K. Maeda, H. Onishi, Y. Maéda, *EMBO J.* **2008**, *27*(3), 570–579.
[376] M. Gao, R. Winter, *ChemPhysChem* **2015**, *16*(17), 3681–3686.
[377] B. Albers, A. Johnson, J. Lewis, D. Morgan, M. Raff, K. Roberts, P. Walter, *Molecular biology of the cell, 6th edition*, Garland Science, New York, **2014**, S. 1464.
[378] M. J. Fedor, J. R. Williamson, *Nat. Rev. Mol. Cell Biol.* **2005**, *6*(5), 399–412.
[379] M. V. Rodnina, „Peptidyl Transferase Mechanism : The Ribosome as a Ribozyme“ in *Ribozymes RNA Catal.* (Hrsg.: D. M. J. Lilley, F. Eckstein), Roy. Soc. Chem., Cambridge, **2008**, S. 270–294.
[380] J. Kortmann, F. Narberhaus, *Nat. Rev. Microbiol.* **2012**, *10*(4), 255–265.
[381] A. Serganov, D. J. Patel, *Nat. Rev. Genet.* **2007**, *8*(10), 776–90.
[382] H. Lodish, A. Berk, S. L. Zikursky, P. Matsudaira, D. Baltimore, J. Darnell, *Molecular cell biology. 4th edition*, W. H. Freeman, New York, **2000**.
[383] J. M. Berg, J. L. Tymoczko, L. Stryer, *Biochemistry, 5th edition*, W H Freeman, New York, **2002**.
[384] M. Egli, *Angew. Chemie Int. Ed. English* **1996**, *35*(17), 1894–1909.
[385] S.-J. Chen, *Annu. Rev. Biophys.* **2008**, *37*, 197–214.
[386] G. M. Giambasu, T. Luchko, D. Herschlag, D. M. York, D. A. Case, *Biophys. J.* **2014**, *106*(4), 883–894.
[387] D. R. Jacobson, O. A. Saleh, *Nucleic Acids Res.* **2016**, *45*(4), 1596–1605.
[388] J. Lipfert, S. Doniach, R. Das, D. Herschlag, *Annu. Rev. Biochem.* **2014**, *83*, 813–841.
[389] D. E. Draper, D. Grilley, A. M. Soto, *Annu. Rev. Biophys. Biomol. Struct.* **2005**, *34*(1), 221–

243.
[390] D. E. Draper, *RNA* **2004**, *10*(3), 335–343.
[391] M. Gebala, G. M. Giambasu, J. Lipfert, N. Bisaria, S. Bonilla, G. Li, D. M. York, D. Herschlag, *J. Am. Chem. Soc.* **2015**, *137*(46), 14705–14715.
[392] Y. Bai, M. Greenfeld, K. J. Travers, V. B. Chu, J. Lipfert, S. Doniach, D. Herschlag, *J. Am. Chem. Soc.* **2007**, *129*(48), 14981–14988.
[393] G. S. Manning, *J. Chem. Phys.* **1969**, *51*(3), 924–933.
[394] V. Parsegian, R. Rand, D. C. Rau, *Methods Enzymol.* **1995**, *259*, 43–94.
[395] J. Wyman, *Adv. Protein Chem.* **1964**, *19*, 223–286.
[396] C. H. Spink, J. B. Chaires, *Biochemistry* **1999**, *38*(1), 496–508.
[397] E. Rozners, J. Moulder, *Nucleic Acids Res.* **2004**, *32*(1), 248–254.
[398] M. Nakano, H. Tateishi-Karimata, S. Tanaka, F. Tama, O. Miyashita, S.-I. Nakano, N. Sugimoto, *Nucleic Acids Res.* **2015**, *43*(21), 10114–10125.
[399] I. Son, Y. L. Shek, D. N. Dubins, T. V. Chalikian, *J. Am. Chem. Soc.* **2014**, *136*(10), 4040–4047.
[400] T. C. Gluick, S. Yadav, *J. Am. Chem. Soc.* **2003**, *125*(15), 4418–4419.
[401] E. D. Holmstrom, N. F. Dupuis, D. J. Nesbitt, *J. Phys. Chem. B* **2015**, *119*(9), 3687–3696.
[402] J. J. Schwinefus, M. J. Kuprian, J. W. Lamppa, W. E. Merker, K. N. Dorn, G. W. Muth, *Biochemistry* **2007**, *46*(31), 9068–9079.
[403] A. R. Davis, C. C. Kirkpatrick, B. M. Znosko, *Nucleic Acids Res.* **2011**, *39*(3), 1081–1094.
[404] P. Auffinger, E. Westhof, *J. Biomol. Struct. Dyn.* **1998**, *16*(3), 693–707.
[405] R. J. Carter, K. J. Baeyens, J. SantaLucia, D. H. Turner, S. R. Holbrook, *Nucleic Acids Res* **1997**, *25*(20), 4117–4122.
[406] S. B. Zimmerman, S. O. Trach, *Nucleic Acids Res.* **1988**, *16*(14), 6309–6326.
[407] N. F. Dupuis, E. D. Holmstrom, D. J. Nesbitt, *Proc. Natl. Acad. Sci. U. S. A.* **2014**, *111*(23), 8464–8469.
[408] S.-I. Nakano, D. Yamaguchi, H. Tateishi-Karimata, D. Miyoshi, N. Sugimoto, *Biophys. J.* **2012**, *102*(12), 2808–17.
[409] D. Kilburn, J. H. Roh, R. Behrouzi, R. M. Briber, S. A. Woodson, *J. Am. Chem. Soc.* **2013**, *135*(27), 10055–10063.
[410] D. L. Pincus, C. Hyeon, D. Thirumalai, *J. Am. Chem. Soc.* **2008**, *130*(23), 7364–7372.
[411] D. B. Knowles, A. S. Lacroix, N. F. Deines, I. Shkel, M. T. Record, *Proc. Natl. Acad. Sci. U. S. A.* **2011**, *108*(31), 12699–12704.
[412] T. Waldminghaus, N. Heidrich, S. Brantl, F. Narberhaus, *Mol. Microbiol.* **2007**, *65*(2), 413–424.
[413] J. Rinnenthal, B. Klinkert, F. Narberhaus, H. Schwalbe, *Nucleic Acids Res.* **2010**, *38*(11), 3834–3847.
[414] W. Zhang, M. W. Capp, J. P. Bond, C. F. Anderson, M. T. Record, *Biochemistry* **1996**, *35*(32), 10506–10516.
[415] J. Tyrrell, J. L. McGinnis, K. M. Weeks, G. J. Pielak, *Biochemistry* **2013**, *52*(48), 8777–8785.
[416] J. Tyrrell, K. M. Weeks, G. J. Pielak, *Biochemistry* **2015**, *54*(42), 6447–6453.
[417] R. Hänsel, F. Löhr, S. Foldynová-Trantírková, E. Bamberg, L. Trantírek, V. Dötsch, *Nucleic Acids Res.* **2011**, *39*(13), 5768–75.
[418] J. Danielsson, X. Mu, L. Lang, H. Wang, A. Binolfi, F.-x. Theillet, B. Bekei, D. T. Logan, P. Selenko, H. Wennerström, M. Oliveberg, *Proc. Natl. Acad. Sci. U. S. A.* **2015**, *112*(40), 12402–12407.
[419] M. Guo, Y. Xu, M. Gruebele, *Proc. Natl. Acad. Sci. U. S. A.* **2012**, *109*(44), 17863–17867.
[420] J. Rinnenthal, B. Klinkert, F. Narberhaus, H. Schwalbe, *Nucleic Acids Res.* **2011**, *39*(18), 8258–8270.
[421] R. Buscaglia, M. C. Miller, W. L. Dean, R. D. Gray, A. N. Lane, J. O. Trent, J. B. Chaires, *Nucleic Acids Res.* **2013**, *41*(16), 7934–7946.
[422] F. Despa, D. P. Orgill, R. C. Lee, *Ann. N. Y. Acad. Sci.* **2005**, *1066*, 54–66.
[423] A. Pardee, R. Dubrow, J. Hamlin, R. F. Kletzien, *Annu. Rev. Biochem.* **1978**, *47*, 715–750.
[424] M. B. Elowitz, A. J. Levine, E. D. Siggia, P. S. Swain, *Science* **2002**, *297*(5584), 1183–1186.

[425] A. Tzur, R. Kafri, V. S. Lebleu, G. Lahav, M. W. Kirschner, *Science (80-.).* **2009**, *325*(5937), 167–171.
[426] M. Mir, Z. Wang, Z. Shen, M. Bednarz, R. Bashir, I. Golding, S. G. Prasanth, G. Popescu, *Proc. Natl. Acad. Sci. U. S. A.* **2011**, *108*(32), 13124–13129.
[427] M. Weiss, M. Elsner, F. Kartberg, T. Nilsson, *Biophys. J.* **2004**, *87*(5), 3518–3524.
[428] D. Leipply, D. Lambert, D. E. Draper, *Methods Enzymol.* **2009**, *469*(09), 433–463.
[429] J. Lah, M. Seručnik, G. Vesnaver, *J. Nucleic Acids* **2011**, *2011*, 513910.
[430] P. Auffinger, E. Westhof, *Biophys. Chem.* **2002**, *95*(3), 203–210.
[431] S. Suladze, M. Kahse, N. Erwin, D. Tomazic, R. Winter, *Methods* **2015**, *76*, 67–77.
[432] D. N. Dubins, A. Lee, R. B. Macgregor, T. V. Chalikian, *J. Am. Chem. Soc.* **2001**, *123*(38), 9254–9259.
[433] A. R. Amiri, R. B. Macgregor, *Biophys. Chem.* **2011**, *156*(1), 88–95.
[434] K. D. Collins, *Biophys. J.* **1997**, *72*(1), 65–76.
[435] G. Rayan, A. D. Tsamaloukas, R. B. Macgregor, H. Heerklotz, *J. Phys. Chem. B* **2009**, *113*(6), 1738–1742.
[436] T. V. Chalikian, K. J. Breslauer, *Biopolymers* **1996**, *39*(5), 619–626.
[437] S. Takahashi, N. Sugimoto, *Molecules* **2013**, *18*(11), 13297–13319.
[438] L. M. F. Holthauzen, J. Rösgen, D. W. Bolen, *Biochemistry* **2010**, *49*(6), 1310–1318.
[439] J. D. Watson, F. H. C. Crick, *Nature* **1953**, *171*(4356), 737–738.
[440] J. D. Watson, F. H. Crick, *Nature* **1953**, *171*(4361), 964–967.
[441] R. E. Franklin, R. G. Gosling, *Nature* **1953**, *171*(4356), 740–741.
[442] M. Kaushik, S. Kaushik, K. Roy, A. Singh, S. Mahendru, M. Kumar, S. Chaudhary, S. Ahmed, S. Kukreti, *Biochem. Biophys. Reports* **2016**, *5*, 388–395.
[443] D. Rhodes, H. J. Lipps, *Nucleic Acids Res.* **2015**, *43*(18), 8627–8637.
[444] M. M. Fay, S. M. Lyons, P. Ivanov, *J. Mol. Biol.* **2017**, *429*(14), 2127–2147.
[445] R. Hänsel-Hertsch, M. D. Antonio, S. Balasubramanian, *Nat. Rev. Mol. Cell Biol.* **2017**, *18*(5), 279–284.
[446] A. M. Fleming, Y. Ding, C. J. Burrows, *Proc. Natl. Acad. Sci. U. S. A.* **2017**, *114*(10), 2604–2609.
[447] B. I. Fedeles, *Proc. Natl. Acad. Sci. U. S. A.* **2017**, *114*(11), 2788–2790.
[448] S. Neidle, *Nat. Rev. Chem.* **2017**, *1*(5), 0041.
[449] A. Arora, S. Maiti, *J. Phys. Chem. B* **2009**, *113*(30), 10515–10520.
[450] J. U. Guo, D. P. Bartel, *Science* **2016**, *353*(6306), aaf5371.
[451] R. Hänsel-Hertsch, D. Beraldi, S. V. Lensing, G. Marsico, K. Zyner, A. Parry, M. Di Antonio, J. Pike, H. Kimura, M. Narita, D. Tannahill, S. Balasubramanian, *Nat. Genet.* **2016**, *48*(10), 1267–1272.
[452] S. Burge, G. N. Parkinson, P. Hazel, A. K. Todd, S. Neidle, *Nucleic Acids Res.* **2006**, *34*(19), 5402–5415.
[453] M. Gellert, M. N. Lipsett, D. R. Davies, *Proc. Natl. Acad. Sci. U. S. A.* **1962**, *48*(12), 2013–2018.
[454] S. B. Zimmerman, *J. Mol. Biol.* **1976**, *106*(3), 663–672.
[455] C. Kang, X. Zhang, R. Ratliff, R. Moyzis, A. Rich, *Nature* **1992**, *356*(6365), 126–131.
[456] J. R. Williamson, M. K. Raghuraman, T. R. Cech, *Cell* **1989**, *59*(5), 871–880.
[457] T. J. Pinnavaia, C. L. Marshall, C. M. Mettler, C. L. Fisk, H. T. Miles, E. D. Becker, *J. Am. Chem. Soc.* **1978**, *100*(5), 3625–3627.
[458] G. Laughlan, A. I. H. Murchie, D. G. Norman, M. H. Moore, P. C. E. Moody, D. M. J. Lilley, B. Luisi, *Science* **1994**, *265*(5171), 520–524.
[459] G. N. Parkinson, M. P. H. Lee, S. Neidle, *Nature* **2002**, *417*(6891), 876–80.
[460] S. Haider, G. N. Parkinson, S. Neidle, *J. Mol. Biol.* **2002**, *320*(2), 189–200.
[461] K. Phillips, Z. Dauter, A. I. H. Murchie, D. M. Lilley, B. Luisi, *J. Mol. Biol.* **1997**, *273*(1), 171–182.
[462] A. Delville, C. Detellier, P. Laszlo, *J. Magn. Reson.* **1979**, *34*(2), 301–315.
[463] J. T. Davis, *Angew. Chemie Int. Ed.* **2004**, *43*(6), 668–698.

[464] J. R. Williamson, *Annu. Rev. Biophys. Biomol. Struct.* **1994**, *23*, 703–730.
[465] D. Sen, W. Gilbert, *Nature* **1990**, *344*(6265), 410–414.
[466] E. H. Blackburn, J. G. Gall, *J. Mol. Biol.* **1978**, *120*(1), 33–53.
[467] W. Guschlbauer, J.-F. Chantot, D. Thiele, *J. Biomol. Struct. Dyn.* **1990**, *8*(3), 491–511.
[468] T. J. Pinnavaia, H. T. Miles, E. D. Becker, *J. Am. Chem. Soc.* **1975**, *97*(5), 7198–7200.
[469] H. Jurga-Nowak, E. Banachowicz, A. Dobek, A. Patkowski, *J. Phys. Chem. B* **2004**, *108*(8), 2744–2750.
[470] A. Wong, R. Ida, L. Spindler, G. Wu, *J. Am. Chem. Soc.* **2005**, *127*(19), 6990–6998.
[471] I. Bang, *Biochem. Z.* **1910**, *26*, 293–311.
[472] G. Wu, I. C. M. Kwan, *J. Am. Chem. Soc.* **2009**, *131*(9), 3180–3182.
[473] W. Eimer, T. Dorfmüller, *J. Phys. Chem.* **1992**, *96*(16), 6801–6804.
[474] M. Borzo, C. Detellier, P. Laszlo, A. Paris, *J. Am. Chem. Soc.* **1980**, *102*(3), 1124–1134.
[475] C. Detellier, P. Laszlo, *J. Am. Chem. Soc.* **1980**, *102*(3), 1135–1141.
[476] A. Wong, G. Wu, *J. Am. Chem. Soc.* **2003**, *125*(10), 13895–13905.
[477] G. C. L. Wong, A. Lin, J. X. Tang, Y. Li, P. a. Janmey, C. R. Safinya, *Phys. Rev. Lett.* **2003**, *91*(1), 018103.
[478] A. Wong, J. C. Fettinger, S. L. Forman, J. T. Davis, G. Wu, *J. Am. Chem. Soc.* **2002**, *124*(5), 742–743.
[479] G. Wu, A. Wong, Z. Gan, J. T. Davis, *J. Am. Chem. Soc.* **2003**, *125*(24), 7182–7183.
[480] J. Gu, J. Leszczynski, M. Bansal, *Chem. Phys. Lett.* **1999**, *311*(3-4), 209–214.
[481] M. Meyer, T. Steinke, M. Brandl, J. Sühnel, *J. Comput. Chem.* **2000**, *22*(1), 109–124.
[482] W. I. Sundquist, A. Klug, *Nature* **1989**, *342*(6251), 825–829.
[483] W. S. Ross, C. C. Hardin, *J. Am. Chem. Soc.* **1994**, *116*(14), 6070–6080.
[484] N. V. Hud, F. W. Smith, F. A. L. Anet, J. Feigon, *Biochemistry* **1996**, *35*(48), 15383–15390.
[485] J. Gu, J. Leszczynski, *J. Phys. Chem. A* **2002**, *106*(3), 529–532.
[486] L. Orgel, *J. Mol. Biol.* **1968**, *38*(3), 381–393.
[487] F. Crick, *J. Mol. Biol.* **1968**, *38*(3), 367–379.
[488] L. M. Cassidy, B. T. Burcar, W. Stevens, E. M. Moriarty, L. B. McGown, *Astrobiology* **2014**, *14*(10), 876–886.
[489] M. Callahan, K. Smith, H. Cleaves, J. Ruzicka, J. Stern, D. Glavin, C. House, J. Dworkin, *Proc. Natl. Acad. Sci. U. S. A.* **2011**, *108*(34), 13995–13998.
[490] R. H. Douglas, J. C. Partridge, N. J. Marshall, *Prog. Retin. Eye Res.* **1998**, *17*(4), 597–636.
[491] H. T. Miles, J. Frazier, *Biochem. Biophys. Res. Commun.* **1972**, *49*(1), 199–204.
[492] C. L. Fisk, E. D. Becker, H. Todd, T. J. Pinnavaia, *J. Am. Chem. Soc.* **1982**, *104*(11), 3307–3314.
[493] W. Saenger, *Principles of nucleic acid structure*, **1984**.
[494] M. Gao, B. Harish, M. Berghaus, R. Seymen, L. Arns, S. A. McCallum, C. A. Royer, R. Winter, *Sci. Rep.* **2017**, *7*(1), 9864.
[495] D. Perahia, M. S. Jhon, B. Pullman, *Biochim. Biophys. Acta* **1977**, *474*(3), 349–362.
[496] A. J. W. G. Visser, T. M. Li, H. G. Drickamer, G. Weber, *Biochemistry* **1977**, *16*(22), 4883–4886.
[497] P. Ausili, M. Pisani, S. Finet, H. Amenitsch, C. Ferrero, P. Mariani, *J. Phys. Chem. B* **2004**, *108*(5), 1783–1789.
[498] Y. Kitamura, T. Itoh, *J. Solution Chem.* **1987**, *16*(9), 715–725.
[499] F. Federiconi, P. Ausili, G. Fragneto, C. Ferrero, P. Mariani, *J. Phys. Chem. B* **2005**, *109*(21), 11037–11045.
[500] H. Y. Fan, Y. L. Shek, A. Amiri, D. N. Dubins, H. Heerklotz, R. B. MacGregor, T. V. Chalikian, *J. Am. Chem. Soc.* **2011**, *133*(12), 4518–4526.

Mimi Gao

Curriculum Vitae

Academic Education

since 10/2014 **PhD student**| **Technische Universität Dortmund**
Physical Chemistry I, Prof. Dr. Roland Winter

10/2012- **Master of Science in Biochemistry**| **Ruhr-Universität Bochum**
09/2014 Focal point: Biomolecular Chemistry
Thesis: "Characterization and inhibition of hIAPP aggregation in the native environment - from diluted solutions into living cells" | Advisor: Prof. Dr. Simon Ebbinghaus

10/2009- **Bachelor of Science in Biochemistry**| **Ruhr-Universität Bochum**
09/2012 Thesis: "Structure and folding of polyglutamine in the cellular environment studied with a huntingtin-FRET construct" | Advisor: Prof. Dr. Simon Ebbinghaus

06/2009 **Abitur**| **Heinrich-von-Kleist Schule**, Bochum

Experience

Industrial

08/2014 **Working student**| **Merck KGaA, Darmstadt**|
Lab for Particle Size Distribution

08/2011 **Five-week Internship**| **Bayer Technology Services GmbH**, Leverkusen|
Department for Enzyme and Fermentation

Academic

since 10/2014 **Research assistant**| **Technische Universität Dortmund**, Physical Chemistry I|
Prof. Dr. Roland Winter

Awards and Scholarships

06/2017 **Attendee of the 67th Lindau Nobel Laureate Meeting**

2015-2017 **PhD Fellowship from Stiftung Stipendien-Fonds des Verbandes der Chemischen Industrie e.V.**

07/2015 **Wilke Award**, Best graduated master student in biochemistry at Ruhr University Bochum

12/2014 **Master Award from Society for Biochemistry and Molecular Biology**, Award for outstanding master thesis

2013-2014 **Qualification Scholarship from Cluster of Excellence RESOLV**, funded by German Research Foundation

2012-2014 **Undergraduate Fellowship from the German National Academic Foundation**, Studienstiftung des deutschen Volkes

2011-2012 **Germany Scholarship**, Deutschlandstipendium

12/2012 **Wilke Award**, Best graduated bachelor student in biochemistry at Ruhr University Bochum

since 12/2012 **Fellowship from e-fellow.net-Scholarship-Network**

06/2009 **Abitur Award from the German Physical Society**

Languages

German mother tongue

Chinese mother tongue

English fluent

Additional Qualifications

2017 **Course in Good Manufacturing Practice**

2014 **Course in Basics of Laboratory Animal Science according to FELASA B**, conducted by Bayer Healthcare AG in Wuppertal

2012 **Training in radiation protection according to Section S4.1**, conducted by RUBION in Bochum

2011 **Expertise in Chemical Act (Sachkunde im Chemikalienrecht)**, conducted by Ruhr-Universität Bochum

Conference Contributions

1. 9th International Meeting on Biomolecules under Pressure (20.08-24.08.2017 Kyoto, JP) - **Talk**
2. 116th General Assembly of the German Bunsen Society for Physical Chemistry (25.05-27.05.2017 Kaiserslautern, D) - **Talk**
3. 27th Faltertage on "Protein Folding, Dynamics and Stability" (21.10-23.10.2016 Halle, Germany) - **Talk**
4. 9th International Conference on High Pressure Bioscience and Biotechnology (25.07-29.07.2016 Toronto, Canada) - **Poster**
5. 60th Biophyiscal Society Meeting (28.02-02.03.2016 Los Angeles, USA) - **Poster**
6. 8th International Meeting on Biomolecules under Pressure (15.02-17.02.2016 Dortmund, Germany) - **Talk**
7. Joint AIRAPT-25 & EHPRG-53 (30.08-04.09.2015 Madrid, Spain) - **Poster**
8. 114th General Assembly of the German Bunsen Society for Physical Chemistry (14.-16.05.2015 Bochum, Germany) - **Poster**
9. FASEB Science Research Conferences - Protein Folding in the Cell (20.-25.07.2014 Saxtons River, VT, USA) - **Poster**
10. 65th Mosbacher Kolloquium of the Society for Biochemistry and Molecular Biology - Cellular Protein Quality Control in Health, Aging and Disease (27.-29.03.2014 Mosbach, Germany) - **Poster**

Publications

1. M. Gao, M. Berghaus, S. Möbitz, V. Schuabb, N. Erwin, M. Herzog, K. Julius, C. Sternemann, and R. Winter, "On the Origin of Microtubules' High Pressure Sensitivity", submitted.

2. M. Gao, C. Held, S. Patra, L. Arns, G. Sadowski, and R. Winter, "Crowders and Cosolvents - Major Contributors to the Cellular Milieu and Efficient Means to Counteract Environmental Stresses", *ChemPhysChem* (2017), DOI: 10.1002/cphc.201700762.
3. M. Gao, B. Harish, M. Berghaus, R. Seymen, L. Arns, C. A. Royer, R.Winter, "Temperature and Pressure Limits of Guanosine Monophosphate Self-assemblies", *Sci. Rep.* **7** (2017) 9864.
4. M. Gao, L. Arns, and R. Winter, "Modulation of the Thermodynamic Signatures of an RNA Thermometer by Osmolytes and Salts", *Angew. Chem. Int. Ed.* **56** (2017) 2302-2306.
5. P.H. Schummel, M. Gao, and R. Winter, "Modulation of the Polymerization Kinetics of α/β-Tubulin by Osmolytes and Macromolecular Crowding", *ChemPhysChem* **18** (2017) 189-197.
6. S. Büning, A. Sharma, S. Vachharajani, E. Newcombe, A. Ormsby, M. Gao, D. Gnutt, T. Vöpel, D. M. Hatters, and S. Ebbinghaus, "Conformational Dynamics and Self-Association of Intrinsically Disordered Huntingtin Exon 1 in Cells", *Phys. Chem. Chem. Phys.* **19** (2017) 10738-10747.
7. M. Gao*, D. Gnutt*, A. Orban, B. Appel, F. Righetti, R. Winter, F. Narberhaus, S. Müller, and S. Ebbinghaus, "RNA Hairpin Folding in the Crowded Cell", *Angew. Chem. Int. Ed.* **55** (2016) 3224-3228.
8. M. Gao, and R. Winter, "Kinetic Insights into the Elongation Reaction of Actin Filaments as a Function of Temperature, Pressure and Macromolecular Crowding", *ChemPhysChem* **16** (2015) 3681-3686.
9. M. Gao*, M. Berghaus*, J. von der Ecken, S. Raunser, and R. Winter, "Condensation Agents Determine the Temperature-Pressure Stability of F-actin Bundles", *Angew. Chem. Int. Ed.* **54** (2015) 11088-11092.
10. M. Gao, and R. Winter, "The Effects of Lipid Membranes, Crowding and Osmolytes on the Aggregation and Fibrillation Propensity of Human IAPP", *J. Diabetes Res.* (2015) Article ID 849017, 21 pages.
11. M. Gao, K. Estel, J. Seeliger, R. P. Friedrich, S. Dogan, E. E. Wanker, R. Winter, and S. Ebbinghaus, "Modulation of Human IAPP Fibrillation: Cosolutes, Crowders and Chaperones", *Phys. Chem. Chem. Phys.* **17** (2015) 8338-8348.
12. D. Gnutt, M. Gao, O. Brylski, M. Heyden, and S. Ebbinghaus, "Excluded-volume Effect in Living Cells", *Angew. Chem. Int. Ed.* **54** (2015) 2548-2551.

Eidesstattliche Versicherung (Affidavit)

Gao, Mimi
Name, Vorname
(Surname, first name)

181000
Matrikel-Nr.
(Enrolment number)

Belehrung:

Wer vorsätzlich gegen eine die Täuschung über Prüfungsleistungen betreffende Regelung einer Hochschulprüfungsordnung verstößt, handelt ordnungswidrig. Die Ordnungswidrigkeit kann mit einer Geldbuße von bis zu 50.000,00 € geahndet werden. Zuständige Verwaltungsbehörde für die Verfolgung und Ahndung von Ordnungswidrigkeiten ist der Kanzler/die Kanzlerin der Technischen Universität Dortmund. Im Falle eines mehrfachen oder sonstigen schwerwiegenden Täuschungsversuches kann der Prüfling zudem exmatrikuliert werden, § 63 Abs. 5 Hochschulgesetz NRW.

Die Abgabe einer falschen Versicherung an Eides statt ist strafbar.

Wer vorsätzlich eine falsche Versicherung an Eides statt abgibt, kann mit einer Freiheitsstrafe bis zu drei Jahren oder mit Geldstrafe bestraft werden, § 156 StGB. Die fahrlässige Abgabe einer falschen Versicherung an Eides statt kann mit einer Freiheitsstrafe bis zu einem Jahr oder Geldstrafe bestraft werden, § 161 StGB.

Die oben stehende Belehrung habe ich zur Kenntnis genommen:

Official notification:

Any person who intentionally breaches any regulation of university examination regulations relating to deception in examination performance is acting improperly. This offence can be punished with a fine of up to EUR 50,000.00. The competent administrative authority for the pursuit and prosecution of offences of this type is the chancellor of the TU Dortmund University. In the case of multiple or other serious attempts at deception, the candidate can also be unenrolled, Section 63, paragraph 5 of the Universities Act of North Rhine-Westphalia.

The submission of a false affidavit is punishable.

Any person who intentionally submits a false affidavit can be punished with a prison sentence of up to three years or a fine, Section 156 of the Criminal Code. The negligent submission of a false affidavit can be punished with a prison sentence of up to one year or a fine, Section 161 of the Criminal Code.

I have taken note of the above official notification.

Dortmund,
Ort, Datum
(Place, date)

Unterschrift
(Signature)

Titel der Dissertation:
(Title of the thesis):

Biophysical Insights into the High Pressure Sensitivity of Biomolecules

Ich versichere hiermit an Eides statt, dass ich die vorliegende Dissertation mit dem Titel selbstständig und ohne unzulässige fremde Hilfe angefertigt habe. Ich habe keine anderen als die angegebenen Quellen und Hilfsmittel benutzt sowie wörtliche und sinngemäße Zitate kenntlich gemacht.
Die Arbeit hat in gegenwärtiger oder in einer anderen Fassung weder der TU Dortmund noch einer anderen Hochschule im Zusammenhang mit einer staatlichen oder akademischen Prüfung vorgelegen.

I hereby swear that I have completed the present dissertation independently and without inadmissible external support. I have not used any sources or tools other than those indicated and have identified literal and analogous quotations.

The thesis in its current version or another version has not been presented to the TU Dortmund University or another university in connection with a state or academic examination.*

*Please be aware that solely the German version of the affidavit ("Eidesstattliche Versicherung") for the PhD thesis is the official and legally binding version.

Dortmund,
Ort, Datum
(Place, date)

Unterschrift
(Signature)

Order Date	Article Title	Publication	Type Of Use	Order Status	Order Number
11-Oct-2017	Cell mechanics and the cytoskeleton	Nature	reuse in a dissertation / thesis	Completed	4206041089774
11-Oct-2017	Modulation of the Thermodynamic Signatures of an RNA Thermometer by Osmolytes and Salts	Angewandte Chemie International Edition	Dissertation/Thesis	Completed	4205940438845
11-Oct-2017	Condensation Agents Determine the Temperature–Pressure Stability of F-Actin Bundles	Angewandte Chemie International Edition	Dissertation/Thesis	Completed	4205931441360
11-Oct-2017	Kinetic Insights into the Elongation Reaction of Actin Filaments as a Function of Temperature, Pressure, and Macromolecular Crowding	ChemPhysChem	Dissertation/Thesis	Completed	4205931235549
11-Oct-2017	Exploring the Stability Limits of Actin and Its Suprastructures	Biophysical Journal	reuse in a thesis/dissertation	Completed	4205920958322
11-Oct-2017	Control of microtubule organization and dynamics: two ends in the limelight	Nature Reviews Molecular Cell Biology	reuse in a dissertation / thesis	Completed	4205820484657
11-Oct-2017	Crowders and Cosolvents—Major Contributors to the Cellular Milieu and Efficient Means to Counteract Environmental Stresses	ChemPhysChem	Dissertation/Thesis	Completed	4205810687884

JOHN WILEY AND SONS LICENSE
TERMS AND CONDITIONS

Oct 11, 2017

This Agreement between Mimi Gao ("You") and John Wiley and Sons ("John Wiley and Sons") consists of your license details and the terms and conditions provided by John Wiley and Sons and Copyright Clearance Center.

License Number	4205931441360
License date	Oct 11, 2017
Licensed Content Publisher	John Wiley and Sons
Licensed Content Publication	Angewandte Chemie International Edition
Licensed Content Title	Condensation Agents Determine the Temperature–Pressure Stability of F-Actin Bundles
Licensed Content Author	Mimi Gao,Melanie Berghaus,Julian von der Ecken,Stefan Raunser,Roland Winter
Licensed Content Date	Aug 5, 2015
Licensed Content Pages	5
Type of use	Dissertation/Thesis
Requestor type	Author of this Wiley article
Format	Print and electronic
Portion	Full article
Will you be translating?	No
Title of your thesis / dissertation	Biophysical Insights into the High Pressure Sensitivity of Biomolecules
Expected completion date	Dec 2017
Expected size (number of pages)	200
Requestor Location	Mimi Gao Otto-Hahn-Straßße 6 TU Dortmund Faculty of Chemistry, PC1 Dortmund, 44227 Germany Attn: Mimi Gao
Publisher Tax ID	EU826007151
Billing Type	Invoice
Billing Address	Mimi Gao Otto-Hahn-Straßße 6 TU Dortmund Faculty of Chemistry, PC1 Dortmund, Germany 44227 Attn: Mimi Gao
Total	0.00 EUR
Terms and Conditions	

TERMS AND CONDITIONS

This copyrighted material is owned by or exclusively licensed to John Wiley & Sons, Inc. or one of its group companies (each a"Wiley Company") or handled on behalf of a society with which a Wiley Company has exclusive publishing rights in relation to a particular work (collectively "WILEY"). By clicking "accept" in connection with completing this licensing transaction, you agree that the following terms and conditions apply to this transaction

(along with the billing and payment terms and conditions established by the Copyright Clearance Center Inc., ("CCC's Billing and Payment terms and conditions"), at the time that you opened your RightsLink account (these are available at any time at http://myaccount.copyright.com).

Terms and Conditions

- The materials you have requested permission to reproduce or reuse (the "Wiley Materials") are protected by copyright.

- You are hereby granted a personal, non-exclusive, non-sub licensable (on a stand-alone basis), non-transferable, worldwide, limited license to reproduce the Wiley Materials for the purpose specified in the licensing process. This license, **and any CONTENT (PDF or image file) purchased as part of your order,** is for a one-time use only and limited to any maximum distribution number specified in the license. The first instance of republication or reuse granted by this license must be completed within two years of the date of the grant of this license (although copies prepared before the end date may be distributed thereafter). The Wiley Materials shall not be used in any other manner or for any other purpose, beyond what is granted in the license. Permission is granted subject to an appropriate acknowledgement given to the author, title of the material/book/journal and the publisher. You shall also duplicate the copyright notice that appears in the Wiley publication in your use of the Wiley Material. Permission is also granted on the understanding that nowhere in the text is a previously published source acknowledged for all or part of this Wiley Material. Any third party content is expressly excluded from this permission.

- With respect to the Wiley Materials, all rights are reserved. Except as expressly granted by the terms of the license, no part of the Wiley Materials may be copied, modified, adapted (except for minor reformatting required by the new Publication), translated, reproduced, transferred or distributed, in any form or by any means, and no derivative works may be made based on the Wiley Materials without the prior permission of the respective copyright owner.**For STM Signatory Publishers clearing permission under the terms of the STM Permissions Guidelines only, the terms of the license are extended to include subsequent editions and for editions in other languages, provided such editions are for the work as a whole in situ and does not involve the separate exploitation of the permitted figures or extracts,** You may not alter, remove or suppress in any manner any copyright, trademark or other notices displayed by the Wiley Materials. You may not license, rent, sell, loan, lease, pledge, offer as security, transfer or assign the Wiley Materials on a stand-alone basis, or any of the rights granted to you hereunder to any other person.

- The Wiley Materials and all of the intellectual property rights therein shall at all times remain the exclusive property of John Wiley & Sons Inc, the Wiley Companies, or their respective licensors, and your interest therein is only that of having possession of and the right to reproduce the Wiley Materials pursuant to Section 2 herein during the continuance of this Agreement. You agree that you own no right, title or interest in or to the Wiley Materials or any of the intellectual property rights therein. You shall have no rights hereunder other than the license as provided for above in Section 2. No right, license or interest to any trademark, trade name, service mark or other branding ("Marks") of WILEY or its licensors is granted hereunder, and you agree that you shall not assert any such right, license or interest with respect thereto

- NEITHER WILEY NOR ITS LICENSORS MAKES ANY WARRANTY OR REPRESENTATION OF ANY KIND TO YOU OR ANY THIRD PARTY, EXPRESS, IMPLIED OR STATUTORY, WITH RESPECT TO THE MATERIALS OR THE ACCURACY OF ANY INFORMATION CONTAINED IN THE MATERIALS, INCLUDING, WITHOUT LIMITATION, ANY IMPLIED WARRANTY OF MERCHANTABILITY, ACCURACY, SATISFACTORY

QUALITY, FITNESS FOR A PARTICULAR PURPOSE, USABILITY, INTEGRATION OR NON-INFRINGEMENT AND ALL SUCH WARRANTIES ARE HEREBY EXCLUDED BY WILEY AND ITS LICENSORS AND WAIVED BY YOU.

- WILEY shall have the right to terminate this Agreement immediately upon breach of this Agreement by you.

- You shall indemnify, defend and hold harmless WILEY, its Licensors and their respective directors, officers, agents and employees, from and against any actual or threatened claims, demands, causes of action or proceedings arising from any breach of this Agreement by you.

- IN NO EVENT SHALL WILEY OR ITS LICENSORS BE LIABLE TO YOU OR ANY OTHER PARTY OR ANY OTHER PERSON OR ENTITY FOR ANY SPECIAL, CONSEQUENTIAL, INCIDENTAL, INDIRECT, EXEMPLARY OR PUNITIVE DAMAGES, HOWEVER CAUSED, ARISING OUT OF OR IN CONNECTION WITH THE DOWNLOADING, PROVISIONING, VIEWING OR USE OF THE MATERIALS REGARDLESS OF THE FORM OF ACTION, WHETHER FOR BREACH OF CONTRACT, BREACH OF WARRANTY, TORT, NEGLIGENCE, INFRINGEMENT OR OTHERWISE (INCLUDING, WITHOUT LIMITATION, DAMAGES BASED ON LOSS OF PROFITS, DATA, FILES, USE, BUSINESS OPPORTUNITY OR CLAIMS OF THIRD PARTIES), AND WHETHER OR NOT THE PARTY HAS BEEN ADVISED OF THE POSSIBILITY OF SUCH DAMAGES. THIS LIMITATION SHALL APPLY NOTWITHSTANDING ANY FAILURE OF ESSENTIAL PURPOSE OF ANY LIMITED REMEDY PROVIDED HEREIN.

- Should any provision of this Agreement be held by a court of competent jurisdiction to be illegal, invalid, or unenforceable, that provision shall be deemed amended to achieve as nearly as possible the same economic effect as the original provision, and the legality, validity and enforceability of the remaining provisions of this Agreement shall not be affected or impaired thereby.

- The failure of either party to enforce any term or condition of this Agreement shall not constitute a waiver of either party's right to enforce each and every term and condition of this Agreement. No breach under this agreement shall be deemed waived or excused by either party unless such waiver or consent is in writing signed by the party granting such waiver or consent. The waiver by or consent of a party to a breach of any provision of this Agreement shall not operate or be construed as a waiver of or consent to any other or subsequent breach by such other party.

- This Agreement may not be assigned (including by operation of law or otherwise) by you without WILEY's prior written consent.

- Any fee required for this permission shall be non-refundable after thirty (30) days from receipt by the CCC.

- These terms and conditions together with CCC's Billing and Payment terms and conditions (which are incorporated herein) form the entire agreement between you and WILEY concerning this licensing transaction and (in the absence of fraud) supersedes all prior agreements and representations of the parties, oral or written. This Agreement may not be amended except in writing signed by both parties. This Agreement shall be binding upon and inure to the benefit of the parties' successors, legal representatives, and authorized assigns.

- In the event of any conflict between your obligations established by these terms and conditions and those established by CCC's Billing and Payment terms and conditions,

these terms and conditions shall prevail.

- WILEY expressly reserves all rights not specifically granted in the combination of (i) the license details provided by you and accepted in the course of this licensing transaction, (ii) these terms and conditions and (iii) CCC's Billing and Payment terms and conditions.

- This Agreement will be void if the Type of Use, Format, Circulation, or Requestor Type was misrepresented during the licensing process.

- This Agreement shall be governed by and construed in accordance with the laws of the State of New York, USA, without regards to such state's conflict of law rules. Any legal action, suit or proceeding arising out of or relating to these Terms and Conditions or the breach thereof shall be instituted in a court of competent jurisdiction in New York County in the State of New York in the United States of America and each party hereby consents and submits to the personal jurisdiction of such court, waives any objection to venue in such court and consents to service of process by registered or certified mail, return receipt requested, at the last known address of such party.

WILEY OPEN ACCESS TERMS AND CONDITIONS
Wiley Publishes Open Access Articles in fully Open Access Journals and in Subscription journals offering Online Open. Although most of the fully Open Access journals publish open access articles under the terms of the Creative Commons Attribution (CC BY) License only, the subscription journals and a few of the Open Access Journals offer a choice of Creative Commons Licenses. The license type is clearly identified on the article.
The Creative Commons Attribution License
The Creative Commons Attribution License (CC-BY) allows users to copy, distribute and transmit an article, adapt the article and make commercial use of the article. The CC-BY license permits commercial and non-
Creative Commons Attribution Non-Commercial License
The Creative Commons Attribution Non-Commercial (CC-BY-NC)License permits use, distribution and reproduction in any medium, provided the original work is properly cited and is not used for commercial purposes.(see below)

Creative Commons Attribution-Non-Commercial-NoDerivs License
The Creative Commons Attribution Non-Commercial-NoDerivs License (CC-BY-NC-ND) permits use, distribution and reproduction in any medium, provided the original work is properly cited, is not used for commercial purposes and no modifications or adaptations are made. (see below)
Use by commercial "for-profit" organizations
Use of Wiley Open Access articles for commercial, promotional, or marketing purposes requires further explicit permission from Wiley and will be subject to a fee.
Further details can be found on Wiley Online Library
http://olabout.wiley.com/WileyCDA/Section/id-410895.html

Other Terms and Conditions:

v1.10 Last updated September 2015

Questions? customercare@copyright.com or +1-855-239-3415 (toll free in the US) or +1-978-646-2777.

JOHN WILEY AND SONS LICENSE TERMS AND CONDITIONS

Oct 11, 2017

This Agreement between Mimi Gao ("You") and John Wiley and Sons ("John Wiley and Sons") consists of your license details and the terms and conditions provided by John Wiley and Sons and Copyright Clearance Center.

License Number	4205931235549
License date	Oct 11, 2017
Licensed Content Publisher	John Wiley and Sons
Licensed Content Publication	ChemPhysChem
Licensed Content Title	Kinetic Insights into the Elongation Reaction of Actin Filaments as a Function of Temperature, Pressure, and Macromolecular Crowding
Licensed Content Author	Mimi Gao,Roland Winter
Licensed Content Date	Nov 13, 2015
Licensed Content Pages	6
Type of use	Dissertation/Thesis
Requestor type	Author of this Wiley article
Format	Print and electronic
Portion	Full article
Will you be translating?	No
Title of your thesis / dissertation	Biophysical Insights into the High Pressure Sensitivity of Biomolecules
Expected completion date	Dec 2017
Expected size (number of pages)	200
Requestor Location	Mimi Gao Otto-Hahn-Straßße 6 TU Dortmund Faculty of Chemistry, PC1 Dortmund, 44227 Germany Attn: Mimi Gao
Publisher Tax ID	EU826007151
Billing Type	Invoice
Billing Address	Mimi Gao Otto-Hahn-Straßße 6 TU Dortmund Faculty of Chemistry, PC1 Dortmund, Germany 44227 Attn: Mimi Gao
Total	0.00 EUR
Terms and Conditions	

TERMS AND CONDITIONS

This copyrighted material is owned by or exclusively licensed to John Wiley & Sons, Inc. or one of its group companies (each a"Wiley Company") or handled on behalf of a society with which a Wiley Company has exclusive publishing rights in relation to a particular work (collectively "WILEY"). By clicking "accept" in connection with completing this licensing transaction, you agree that the following terms and conditions apply to this transaction (along with the billing and payment terms and conditions established by the Copyright

Clearance Center Inc., ("CCC's Billing and Payment terms and conditions"), at the time that you opened your RightsLink account (these are available at any time at http://myaccount.copyright.com).

Terms and Conditions

- The materials you have requested permission to reproduce or reuse (the "Wiley Materials") are protected by copyright.

- You are hereby granted a personal, non-exclusive, non-sub licensable (on a stand-alone basis), non-transferable, worldwide, limited license to reproduce the Wiley Materials for the purpose specified in the licensing process. This license, **and any CONTENT (PDF or image file) purchased as part of your order,** is for a one-time use only and limited to any maximum distribution number specified in the license. The first instance of republication or reuse granted by this license must be completed within two years of the date of the grant of this license (although copies prepared before the end date may be distributed thereafter). The Wiley Materials shall not be used in any other manner or for any other purpose, beyond what is granted in the license. Permission is granted subject to an appropriate acknowledgement given to the author, title of the material/book/journal and the publisher. You shall also duplicate the copyright notice that appears in the Wiley publication in your use of the Wiley Material. Permission is also granted on the understanding that nowhere in the text is a previously published source acknowledged for all or part of this Wiley Material. Any third party content is expressly excluded from this permission.

- With respect to the Wiley Materials, all rights are reserved. Except as expressly granted by the terms of the license, no part of the Wiley Materials may be copied, modified, adapted (except for minor reformatting required by the new Publication), translated, reproduced, transferred or distributed, in any form or by any means, and no derivative works may be made based on the Wiley Materials without the prior permission of the respective copyright owner.**For STM Signatory Publishers clearing permission under the terms of the STM Permissions Guidelines only, the terms of the license are extended to include subsequent editions and for editions in other languages, provided such editions are for the work as a whole in situ and does not involve the separate exploitation of the permitted figures or extracts,** You may not alter, remove or suppress in any manner any copyright, trademark or other notices displayed by the Wiley Materials. You may not license, rent, sell, loan, lease, pledge, offer as security, transfer or assign the Wiley Materials on a stand-alone basis, or any of the rights granted to you hereunder to any other person.

- The Wiley Materials and all of the intellectual property rights therein shall at all times remain the exclusive property of John Wiley & Sons Inc, the Wiley Companies, or their respective licensors, and your interest therein is only that of having possession of and the right to reproduce the Wiley Materials pursuant to Section 2 herein during the continuance of this Agreement. You agree that you own no right, title or interest in or to the Wiley Materials or any of the intellectual property rights therein. You shall have no rights hereunder other than the license as provided for above in Section 2. No right, license or interest to any trademark, trade name, service mark or other branding ("Marks") of WILEY or its licensors is granted hereunder, and you agree that you shall not assert any such right, license or interest with respect thereto

- NEITHER WILEY NOR ITS LICENSORS MAKES ANY WARRANTY OR REPRESENTATION OF ANY KIND TO YOU OR ANY THIRD PARTY, EXPRESS, IMPLIED OR STATUTORY, WITH RESPECT TO THE MATERIALS OR THE ACCURACY OF ANY INFORMATION CONTAINED IN THE MATERIALS, INCLUDING, WITHOUT LIMITATION, ANY IMPLIED WARRANTY OF MERCHANTABILITY, ACCURACY, SATISFACTORY QUALITY, FITNESS FOR A PARTICULAR PURPOSE, USABILITY,

INTEGRATION OR NON-INFRINGEMENT AND ALL SUCH WARRANTIES ARE HEREBY EXCLUDED BY WILEY AND ITS LICENSORS AND WAIVED BY YOU.

- WILEY shall have the right to terminate this Agreement immediately upon breach of this Agreement by you.
- You shall indemnify, defend and hold harmless WILEY, its Licensors and their respective directors, officers, agents and employees, from and against any actual or threatened claims, demands, causes of action or proceedings arising from any breach of this Agreement by you.
- IN NO EVENT SHALL WILEY OR ITS LICENSORS BE LIABLE TO YOU OR ANY OTHER PARTY OR ANY OTHER PERSON OR ENTITY FOR ANY SPECIAL, CONSEQUENTIAL, INCIDENTAL, INDIRECT, EXEMPLARY OR PUNITIVE DAMAGES, HOWEVER CAUSED, ARISING OUT OF OR IN CONNECTION WITH THE DOWNLOADING, PROVISIONING, VIEWING OR USE OF THE MATERIALS REGARDLESS OF THE FORM OF ACTION, WHETHER FOR BREACH OF CONTRACT, BREACH OF WARRANTY, TORT, NEGLIGENCE, INFRINGEMENT OR OTHERWISE (INCLUDING, WITHOUT LIMITATION, DAMAGES BASED ON LOSS OF PROFITS, DATA, FILES, USE, BUSINESS OPPORTUNITY OR CLAIMS OF THIRD PARTIES), AND WHETHER OR NOT THE PARTY HAS BEEN ADVISED OF THE POSSIBILITY OF SUCH DAMAGES. THIS LIMITATION SHALL APPLY NOTWITHSTANDING ANY FAILURE OF ESSENTIAL PURPOSE OF ANY LIMITED REMEDY PROVIDED HEREIN.
- Should any provision of this Agreement be held by a court of competent jurisdiction to be illegal, invalid, or unenforceable, that provision shall be deemed amended to achieve as nearly as possible the same economic effect as the original provision, and the legality, validity and enforceability of the remaining provisions of this Agreement shall not be affected or impaired thereby.
- The failure of either party to enforce any term or condition of this Agreement shall not constitute a waiver of either party's right to enforce each and every term and condition of this Agreement. No breach under this agreement shall be deemed waived or excused by either party unless such waiver or consent is in writing signed by the party granting such waiver or consent. The waiver by or consent of a party to a breach of any provision of this Agreement shall not operate or be construed as a waiver of or consent to any other or subsequent breach by such other party.
- This Agreement may not be assigned (including by operation of law or otherwise) by you without WILEY's prior written consent.
- Any fee required for this permission shall be non-refundable after thirty (30) days from receipt by the CCC.
- These terms and conditions together with CCC's Billing and Payment terms and conditions (which are incorporated herein) form the entire agreement between you and WILEY concerning this licensing transaction and (in the absence of fraud) supersedes all prior agreements and representations of the parties, oral or written. This Agreement may not be amended except in writing signed by both parties. This Agreement shall be binding upon and inure to the benefit of the parties' successors, legal representatives, and authorized assigns.
- In the event of any conflict between your obligations established by these terms and conditions and those established by CCC's Billing and Payment terms and conditions,

these terms and conditions shall prevail.

- WILEY expressly reserves all rights not specifically granted in the combination of (i) the license details provided by you and accepted in the course of this licensing transaction, (ii) these terms and conditions and (iii) CCC's Billing and Payment terms and conditions.

- This Agreement will be void if the Type of Use, Format, Circulation, or Requestor Type was misrepresented during the licensing process.

- This Agreement shall be governed by and construed in accordance with the laws of the State of New York, USA, without regards to such state's conflict of law rules. Any legal action, suit or proceeding arising out of or relating to these Terms and Conditions or the breach thereof shall be instituted in a court of competent jurisdiction in New York County in the State of New York in the United States of America and each party hereby consents and submits to the personal jurisdiction of such court, waives any objection to venue in such court and consents to service of process by registered or certified mail, return receipt requested, at the last known address of such party.

WILEY OPEN ACCESS TERMS AND CONDITIONS
Wiley Publishes Open Access Articles in fully Open Access Journals and in Subscription journals offering Online Open. Although most of the fully Open Access journals publish open access articles under the terms of the Creative Commons Attribution (CC BY) License only, the subscription journals and a few of the Open Access Journals offer a choice of Creative Commons Licenses. The license type is clearly identified on the article.
The Creative Commons Attribution License
The Creative Commons Attribution License (CC-BY) allows users to copy, distribute and transmit an article, adapt the article and make commercial use of the article. The CC-BY license permits commercial and non-
Creative Commons Attribution Non-Commercial License
The Creative Commons Attribution Non-Commercial (CC-BY-NC)License permits use, distribution and reproduction in any medium, provided the original work is properly cited and is not used for commercial purposes.(see below)

Creative Commons Attribution-Non-Commercial-NoDerivs License
The Creative Commons Attribution Non-Commercial-NoDerivs License (CC-BY-NC-ND) permits use, distribution and reproduction in any medium, provided the original work is properly cited, is not used for commercial purposes and no modifications or adaptations are made. (see below)
Use by commercial "for-profit" organizations
Use of Wiley Open Access articles for commercial, promotional, or marketing purposes requires further explicit permission from Wiley and will be subject to a fee.
Further details can be found on Wiley Online Library
http://olabout.wiley.com/WileyCDA/Section/id-410895.html

Other Terms and Conditions:

v1.10 Last updated September 2015

Questions? customercare@copyright.com or +1-855-239-3415 (toll free in the US) or +1-978-646-2777.

JOHN WILEY AND SONS LICENSE TERMS AND CONDITIONS

Oct 11, 2017

This Agreement between Mimi Gao ("You") and John Wiley and Sons ("John Wiley and Sons") consists of your license details and the terms and conditions provided by John Wiley and Sons and Copyright Clearance Center.

License Number	4205940438845
License date	Oct 11, 2017
Licensed Content Publisher	John Wiley and Sons
Licensed Content Publication	Angewandte Chemie International Edition
Licensed Content Title	Modulation of the Thermodynamic Signatures of an RNA Thermometer by Osmolytes and Salts
Licensed Content Author	Mimi Gao,Loana Arns,Roland Winter
Licensed Content Date	Jan 19, 2017
Licensed Content Pages	5
Type of use	Dissertation/Thesis
Requestor type	Author of this Wiley article
Format	Print and electronic
Portion	Full article
Will you be translating?	No
Title of your thesis / dissertation	Biophysical Insights into the High Pressure Sensitivity of Biomolecules
Expected completion date	Dec 2017
Expected size (number of pages)	200
Requestor Location	Mimi Gao Otto-Hahn-Straßße 6 TU Dortmund Faculty of Chemistry, PC1 Dortmund, 44227 Germany Attn: Mimi Gao
Publisher Tax ID	EU826007151
Billing Type	Invoice
Billing Address	Mimi Gao Otto-Hahn-Straßße 6 TU Dortmund Faculty of Chemistry, PC1 Dortmund, Germany 44227 Attn: Mimi Gao
Total	0.00 EUR
Terms and Conditions	

TERMS AND CONDITIONS

This copyrighted material is owned by or exclusively licensed to John Wiley & Sons, Inc. or one of its group companies (each a"Wiley Company") or handled on behalf of a society with which a Wiley Company has exclusive publishing rights in relation to a particular work (collectively "WILEY"). By clicking "accept" in connection with completing this licensing transaction, you agree that the following terms and conditions apply to this transaction (along with the billing and payment terms and conditions established by the Copyright

Clearance Center Inc., ("CCC's Billing and Payment terms and conditions"), at the time that you opened your RightsLink account (these are available at any time at http://myaccount.copyright.com).

Terms and Conditions

- The materials you have requested permission to reproduce or reuse (the "Wiley Materials") are protected by copyright.

- You are hereby granted a personal, non-exclusive, non-sub licensable (on a stand-alone basis), non-transferable, worldwide, limited license to reproduce the Wiley Materials for the purpose specified in the licensing process. This license, **and any CONTENT (PDF or image file) purchased as part of your order,** is for a one-time use only and limited to any maximum distribution number specified in the license. The first instance of republication or reuse granted by this license must be completed within two years of the date of the grant of this license (although copies prepared before the end date may be distributed thereafter). The Wiley Materials shall not be used in any other manner or for any other purpose, beyond what is granted in the license. Permission is granted subject to an appropriate acknowledgement given to the author, title of the material/book/journal and the publisher. You shall also duplicate the copyright notice that appears in the Wiley publication in your use of the Wiley Material. Permission is also granted on the understanding that nowhere in the text is a previously published source acknowledged for all or part of this Wiley Material. Any third party content is expressly excluded from this permission.

- With respect to the Wiley Materials, all rights are reserved. Except as expressly granted by the terms of the license, no part of the Wiley Materials may be copied, modified, adapted (except for minor reformatting required by the new Publication), translated, reproduced, transferred or distributed, in any form or by any means, and no derivative works may be made based on the Wiley Materials without the prior permission of the respective copyright owner.**For STM Signatory Publishers clearing permission under the terms of the STM Permissions Guidelines only, the terms of the license are extended to include subsequent editions and for editions in other languages, provided such editions are for the work as a whole in situ and does not involve the separate exploitation of the permitted figures or extracts,** You may not alter, remove or suppress in any manner any copyright, trademark or other notices displayed by the Wiley Materials. You may not license, rent, sell, loan, lease, pledge, offer as security, transfer or assign the Wiley Materials on a stand-alone basis, or any of the rights granted to you hereunder to any other person.

- The Wiley Materials and all of the intellectual property rights therein shall at all times remain the exclusive property of John Wiley & Sons Inc, the Wiley Companies, or their respective licensors, and your interest therein is only that of having possession of and the right to reproduce the Wiley Materials pursuant to Section 2 herein during the continuance of this Agreement. You agree that you own no right, title or interest in or to the Wiley Materials or any of the intellectual property rights therein. You shall have no rights hereunder other than the license as provided for above in Section 2. No right, license or interest to any trademark, trade name, service mark or other branding ("Marks") of WILEY or its licensors is granted hereunder, and you agree that you shall not assert any such right, license or interest with respect thereto

- NEITHER WILEY NOR ITS LICENSORS MAKES ANY WARRANTY OR REPRESENTATION OF ANY KIND TO YOU OR ANY THIRD PARTY, EXPRESS, IMPLIED OR STATUTORY, WITH RESPECT TO THE MATERIALS OR THE ACCURACY OF ANY INFORMATION CONTAINED IN THE MATERIALS, INCLUDING, WITHOUT LIMITATION, ANY IMPLIED WARRANTY OF MERCHANTABILITY, ACCURACY, SATISFACTORY QUALITY, FITNESS FOR A PARTICULAR PURPOSE, USABILITY,

INTEGRATION OR NON-INFRINGEMENT AND ALL SUCH WARRANTIES ARE HEREBY EXCLUDED BY WILEY AND ITS LICENSORS AND WAIVED BY YOU.

- WILEY shall have the right to terminate this Agreement immediately upon breach of this Agreement by you.
- You shall indemnify, defend and hold harmless WILEY, its Licensors and their respective directors, officers, agents and employees, from and against any actual or threatened claims, demands, causes of action or proceedings arising from any breach of this Agreement by you.
- IN NO EVENT SHALL WILEY OR ITS LICENSORS BE LIABLE TO YOU OR ANY OTHER PARTY OR ANY OTHER PERSON OR ENTITY FOR ANY SPECIAL, CONSEQUENTIAL, INCIDENTAL, INDIRECT, EXEMPLARY OR PUNITIVE DAMAGES, HOWEVER CAUSED, ARISING OUT OF OR IN CONNECTION WITH THE DOWNLOADING, PROVISIONING, VIEWING OR USE OF THE MATERIALS REGARDLESS OF THE FORM OF ACTION, WHETHER FOR BREACH OF CONTRACT, BREACH OF WARRANTY, TORT, NEGLIGENCE, INFRINGEMENT OR OTHERWISE (INCLUDING, WITHOUT LIMITATION, DAMAGES BASED ON LOSS OF PROFITS, DATA, FILES, USE, BUSINESS OPPORTUNITY OR CLAIMS OF THIRD PARTIES), AND WHETHER OR NOT THE PARTY HAS BEEN ADVISED OF THE POSSIBILITY OF SUCH DAMAGES. THIS LIMITATION SHALL APPLY NOTWITHSTANDING ANY FAILURE OF ESSENTIAL PURPOSE OF ANY LIMITED REMEDY PROVIDED HEREIN.
- Should any provision of this Agreement be held by a court of competent jurisdiction to be illegal, invalid, or unenforceable, that provision shall be deemed amended to achieve as nearly as possible the same economic effect as the original provision, and the legality, validity and enforceability of the remaining provisions of this Agreement shall not be affected or impaired thereby.
- The failure of either party to enforce any term or condition of this Agreement shall not constitute a waiver of either party's right to enforce each and every term and condition of this Agreement. No breach under this agreement shall be deemed waived or excused by either party unless such waiver or consent is in writing signed by the party granting such waiver or consent. The waiver by or consent of a party to a breach of any provision of this Agreement shall not operate or be construed as a waiver of or consent to any other or subsequent breach by such other party.
- This Agreement may not be assigned (including by operation of law or otherwise) by you without WILEY's prior written consent.
- Any fee required for this permission shall be non-refundable after thirty (30) days from receipt by the CCC.
- These terms and conditions together with CCC's Billing and Payment terms and conditions (which are incorporated herein) form the entire agreement between you and WILEY concerning this licensing transaction and (in the absence of fraud) supersedes all prior agreements and representations of the parties, oral or written. This Agreement may not be amended except in writing signed by both parties. This Agreement shall be binding upon and inure to the benefit of the parties' successors, legal representatives, and authorized assigns.
- In the event of any conflict between your obligations established by these terms and conditions and those established by CCC's Billing and Payment terms and conditions,

these terms and conditions shall prevail.

- WILEY expressly reserves all rights not specifically granted in the combination of (i) the license details provided by you and accepted in the course of this licensing transaction, (ii) these terms and conditions and (iii) CCC's Billing and Payment terms and conditions.

- This Agreement will be void if the Type of Use, Format, Circulation, or Requestor Type was misrepresented during the licensing process.

- This Agreement shall be governed by and construed in accordance with the laws of the State of New York, USA, without regards to such state's conflict of law rules. Any legal action, suit or proceeding arising out of or relating to these Terms and Conditions or the breach thereof shall be instituted in a court of competent jurisdiction in New York County in the State of New York in the United States of America and each party hereby consents and submits to the personal jurisdiction of such court, waives any objection to venue in such court and consents to service of process by registered or certified mail, return receipt requested, at the last known address of such party.

WILEY OPEN ACCESS TERMS AND CONDITIONS
Wiley Publishes Open Access Articles in fully Open Access Journals and in Subscription journals offering Online Open. Although most of the fully Open Access journals publish open access articles under the terms of the Creative Commons Attribution (CC BY) License only, the subscription journals and a few of the Open Access Journals offer a choice of Creative Commons Licenses. The license type is clearly identified on the article.
The Creative Commons Attribution License
The Creative Commons Attribution License (CC-BY) allows users to copy, distribute and transmit an article, adapt the article and make commercial use of the article. The CC-BY license permits commercial and non-
Creative Commons Attribution Non-Commercial License
The Creative Commons Attribution Non-Commercial (CC-BY-NC)License permits use, distribution and reproduction in any medium, provided the original work is properly cited and is not used for commercial purposes.(see below)

Creative Commons Attribution-Non-Commercial-NoDerivs License
The Creative Commons Attribution Non-Commercial-NoDerivs License (CC-BY-NC-ND) permits use, distribution and reproduction in any medium, provided the original work is properly cited, is not used for commercial purposes and no modifications or adaptations are made. (see below)
Use by commercial "for-profit" organizations
Use of Wiley Open Access articles for commercial, promotional, or marketing purposes requires further explicit permission from Wiley and will be subject to a fee.
Further details can be found on Wiley Online Library
http://olabout.wiley.com/WileyCDA/Section/id-410895.html

Other Terms and Conditions:

v1.10 Last updated September 2015

Questions? customercare@copyright.com or +1-855-239-3415 (toll free in the US) or +1-978-646-2777.

JOHN WILEY AND SONS LICENSE
TERMS AND CONDITIONS

Oct 11, 2017

This Agreement between Mimi Gao ("You") and John Wiley and Sons ("John Wiley and Sons") consists of your license details and the terms and conditions provided by John Wiley and Sons and Copyright Clearance Center.

License Number	4205810687884
License date	Oct 11, 2017
Licensed Content Publisher	John Wiley and Sons
Licensed Content Publication	ChemPhysChem
Licensed Content Title	Crowders and Cosolvents—Major Contributors to the Cellular Milieu and Efficient Means to Counteract Environmental Stresses
Licensed Content Author	Mimi Gao,Christoph Held,Satyajit Patra,Loana Arns,Gabriele Sadowski,Roland Winter
Licensed Content Date	Sep 27, 2017
Licensed Content Pages	1
Type of use	Dissertation/Thesis
Requestor type	Author of this Wiley article
Format	Print and electronic
Portion	Figure/table
Number of figures/tables	3
Original Wiley figure/table number(s)	Figure 1, Figure 4, Figure 6
Will you be translating?	No
Title of your thesis / dissertation	Biophysical Insights into the High Pressure Sensitivity of Biomolecules
Expected completion date	Dec 2017
Expected size (number of pages)	200
Requestor Location	Mimi Gao Otto-Hahn-Straßße 6 TU Dortmund Faculty of Chemistry, PC1 Dortmund, 44227 Germany Attn: Mimi Gao
Publisher Tax ID	EU826007151
Billing Type	Invoice
Billing Address	Mimi Gao Otto-Hahn-Straßße 6 TU Dortmund Faculty of Chemistry, PC1 Dortmund, Germany 44227 Attn: Mimi Gao
Total	0.00 EUR
Terms and Conditions	

TERMS AND CONDITIONS

- NEITHER WILEY NOR ITS LICENSORS MAKES ANY WARRANTY OR REPRESENTATION OF ANY KIND TO YOU OR ANY THIRD PARTY, EXPRESS, IMPLIED OR STATUTORY, WITH RESPECT TO THE MATERIALS OR THE ACCURACY OF ANY INFORMATION CONTAINED IN THE MATERIALS, INCLUDING, WITHOUT LIMITATION, ANY IMPLIED WARRANTY OF MERCHANTABILITY, ACCURACY, SATISFACTORY QUALITY, FITNESS FOR A PARTICULAR PURPOSE, USABILITY, INTEGRATION OR NON-INFRINGEMENT AND ALL SUCH WARRANTIES ARE HEREBY EXCLUDED BY WILEY AND ITS LICENSORS AND WAIVED BY YOU.

- WILEY shall have the right to terminate this Agreement immediately upon breach of this Agreement by you.

- You shall indemnify, defend and hold harmless WILEY, its Licensors and their respective directors, officers, agents and employees, from and against any actual or threatened claims, demands, causes of action or proceedings arising from any breach of this Agreement by you.

- IN NO EVENT SHALL WILEY OR ITS LICENSORS BE LIABLE TO YOU OR ANY OTHER PARTY OR ANY OTHER PERSON OR ENTITY FOR ANY SPECIAL, CONSEQUENTIAL, INCIDENTAL, INDIRECT, EXEMPLARY OR PUNITIVE DAMAGES, HOWEVER CAUSED, ARISING OUT OF OR IN CONNECTION WITH THE DOWNLOADING, PROVISIONING, VIEWING OR USE OF THE MATERIALS REGARDLESS OF THE FORM OF ACTION, WHETHER FOR BREACH OF CONTRACT, BREACH OF WARRANTY, TORT, NEGLIGENCE, INFRINGEMENT OR OTHERWISE (INCLUDING, WITHOUT LIMITATION, DAMAGES BASED ON LOSS OF PROFITS, DATA, FILES, USE, BUSINESS OPPORTUNITY OR CLAIMS OF THIRD PARTIES), AND WHETHER OR NOT THE PARTY HAS BEEN ADVISED OF THE POSSIBILITY OF SUCH DAMAGES. THIS LIMITATION SHALL APPLY NOTWITHSTANDING ANY FAILURE OF ESSENTIAL PURPOSE OF ANY LIMITED REMEDY PROVIDED HEREIN.

- Should any provision of this Agreement be held by a court of competent jurisdiction to be illegal, invalid, or unenforceable, that provision shall be deemed amended to achieve as nearly as possible the same economic effect as the original provision, and the legality, validity and enforceability of the remaining provisions of this Agreement shall not be affected or impaired thereby.

- The failure of either party to enforce any term or condition of this Agreement shall not constitute a waiver of either party's right to enforce each and every term and condition of this Agreement. No breach under this agreement shall be deemed waived or excused by either party unless such waiver or consent is in writing signed by the party granting such waiver or consent. The waiver by or consent of a party to a breach of any provision of this Agreement shall not operate or be construed as a waiver of or consent to any other or subsequent breach by such other party.

- This Agreement may not be assigned (including by operation of law or otherwise) by you without WILEY's prior written consent.

- Any fee required for this permission shall be non-refundable after thirty (30) days from receipt by the CCC.

- These terms and conditions together with CCC's Billing and Payment terms and conditions (which are incorporated herein) form the entire agreement between you and WILEY concerning this licensing transaction and (in the absence of fraud) supersedes all prior agreements and representations of the parties, oral or written. This Agreement

may not be amended except in writing signed by both parties. This Agreement shall be binding upon and inure to the benefit of the parties' successors, legal representatives, and authorized assigns.

- In the event of any conflict between your obligations established by these terms and conditions and those established by CCC's Billing and Payment terms and conditions, these terms and conditions shall prevail.

- WILEY expressly reserves all rights not specifically granted in the combination of (i) the license details provided by you and accepted in the course of this licensing transaction, (ii) these terms and conditions and (iii) CCC's Billing and Payment terms and conditions.

- This Agreement will be void if the Type of Use, Format, Circulation, or Requestor Type was misrepresented during the licensing process.

- This Agreement shall be governed by and construed in accordance with the laws of the State of New York, USA, without regards to such state's conflict of law rules. Any legal action, suit or proceeding arising out of or relating to these Terms and Conditions or the breach thereof shall be instituted in a court of competent jurisdiction in New York County in the State of New York in the United States of America and each party hereby consents and submits to the personal jurisdiction of such court, waives any objection to venue in such court and consents to service of process by registered or certified mail, return receipt requested, at the last known address of such party.

WILEY OPEN ACCESS TERMS AND CONDITIONS

Wiley Publishes Open Access Articles in fully Open Access Journals and in Subscription journals offering Online Open. Although most of the fully Open Access journals publish open access articles under the terms of the Creative Commons Attribution (CC BY) License only, the subscription journals and a few of the Open Access Journals offer a choice of Creative Commons Licenses. The license type is clearly identified on the article.

The Creative Commons Attribution License

The Creative Commons Attribution License (CC-BY) allows users to copy, distribute and transmit an article, adapt the article and make commercial use of the article. The CC-BY license permits commercial and non-

Creative Commons Attribution Non-Commercial License

The Creative Commons Attribution Non-Commercial (CC-BY-NC)License permits use, distribution and reproduction in any medium, provided the original work is properly cited and is not used for commercial purposes.(see below)

Creative Commons Attribution-Non-Commercial-NoDerivs License

The Creative Commons Attribution Non-Commercial-NoDerivs License (CC-BY-NC-ND) permits use, distribution and reproduction in any medium, provided the original work is properly cited, is not used for commercial purposes and no modifications or adaptations are made. (see below)

Use by commercial "for-profit" organizations

Use of Wiley Open Access articles for commercial, promotional, or marketing purposes requires further explicit permission from Wiley and will be subject to a fee.

Further details can be found on Wiley Online Library

http://olabout.wiley.com/WileyCDA/Section/id-410895.html

Other Terms and Conditions:

v1.10 Last updated September 2015